2022

Identification of biomarkers for the prediction of radiation toxicity in prostate cancer patients

Daniel Cullen
Technological University Dublin, daniel.cullen3@proton.me

Identification of biomarkers for the prediction of radiation toxicity in prostate cancer patients

Daniel Cullen

Radiation and Environmental Science Centre

Technological University Dublin

Supervised by:

Prof Fiona Lyng

Dr Aidan Meade

Prof Orla Howe

Abstract

The success of radiotherapy in tumour control depends on the total dose given. However, the tolerance of the normal tissues surrounding the tumour limits this dose. It is not known why some patients develop radiation toxicity and, currently, it is not possible to predict before treatment which patients will experience adverse effects. Thus, there is an unmet clinical need for a new test to identify patients at risk of radiation toxicity. The aim of this study was to determine if spectral variations in blood lymphocytes from PCa patients may suggest Raman spectral bands that could be used in future research to identify spectral features associated with radiosensitivity.

Blood samples were collected retrospectively from 42 patients enrolled on the Cancer Trials Ireland ICORG 08-17 study who had undergone radiotherapy for prostate cancer and had shown either severe or no/minimal late radiation toxicity in follow-up. Radiation response was assessed following *in-vitro* irradiation using Raman micro-spectroscopy in addition to the G2 chromosomal radiosensitivity assay and the γH2AX DNA damage assay. A partial least squares discriminant analysis model was developed to classify patients using known radiation toxicity scores. Following this retrospective study, blood samples were collected prospectively from 51 patients also enrolled on the ICORG 08-17 study. These samples were collected *prior to* radiotherapy and these patients were categorised based on severe or no/minimal late radiation toxicity in follow-up. Radiation response was assessed following *in-vitro* irradiation using Raman micro-spectroscopy in addition to the G2 chromosomal radiosensitivity assay and the γH2AX DNA damage assay.

A partial least squares discriminant analysis model was developed to predict radiation toxicity. Finally, blood samples were collected prospectively *prior to* radiotherapy from another 30 patients enrolled on the Northern Ireland Cancer Trials Centre SPORT study for prostate cancer and these patients were also categorised based on severe or no/minimal late radiation toxicity in follow-up. Radiation response was assessed following *in-vitro* irradiation using Raman micro-spectroscopy in addition to the citrulline assay. A partial least squares discriminant analysis model was again developed to predict radiation toxicity.

Prediction of radiation toxicity outcome could not be achieved based on late radiation toxicity in the cohort of prostate cancer patients enrolled on the ICORG 08-17 study, but some success in predicting radiation toxicity could be achieved based on late radiation toxicity in the cohort of prostate cancer patients enrolled on the Northern Ireland Cancer Trials Centre SPORT study. The patients from the ICORG 08-17 study will be followed up at 6 monthly intervals until Year 9 however, and those from the SPORT study will be followed up every 6 months for up to 5 years with a minimum annual follow-up from 5-10 years, allowing the models to be updated as patient clinical status changes. In the future, this technology may have potential to lead to individualized patient radiotherapy by identifying patients that are at risk of radiation toxicity.

Declaration

I certify that this report which I submit for examination, is entirely my own work and has not been taken from the work of others, save to the extent that such work has been cited and acknowledged within the text of my own work. This report was prepared according to the regulations for postgraduate study by research of the Technological University Dublin (TU Dublin) and has not been submitted in whole or in part for another award in any other third level institution. The work presented in this report conforms to the principles and requirements of the TU Dublin's guidelines for ethics in research.

Signature: 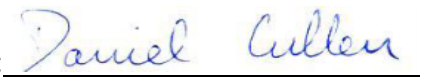 Date: 08/02/2022

Acknowledgements

I would like to extend my gratitude to my PhD supervisors, Prof Fion Lyng, Dr Aidan Meade and Prof Orla Howe for their guidance, patience, and selfless use of time. For this I am immensely thankful.

I would also like to thank Jade Monaghan, Dr Dinesh Medipally, Dr Jane Bryant and Dr Adrian Maguire for their support and assistance throughout the course of this work.

Abbreviations

53BP1	p53-binding protein 1
ADL	Activities of daily living
ADT	Androgen-deprivation therapy
AIF	Apoptosis-inducing factor
APAF-1	Apoptosis-activating factor-1
Ape1	Apurinic/apyrimidinic endonuclease 1
ATG	Autophagy-related
ATM	Ataxia telangiectasia mutated protein
ATR	Ataxia telangiectasia and Rad3-related protein
AUC	Area under the receiver operating characteristic curve
Bak	Bcl-2 homologous antagonist/killer protein
Bax	Bcl-2-associated X protein
Bid	BH3-interacting domain death agonist
CaF_2	Calcium fluoride
CCD	Charge-coupled device
CCL2	Chemokine ligand 2
CD	Cluster of differentiation
Cdc	Cell division cycle
CDK	Cyclin-dependent kinase
CDKI	Cyclin-dependent kinase inhibitor
Chk	Checkpoint kinase
CLS-R	Classical least squares regression

ctb	Chromatid break
ctBP	C-terminal-binding protein
ctg	Chromatid gap
ctm	Chromatid minute
ctIP	c-terminal-binding protein-interacting protein
CV	Cross-validation
CXCL8	CXC motif chemokine ligand 8
DDR	DNA damage response
DISC	Death-inducible signalling complex
DNA	Deoxyribonucleic acid
DNA-PKcs	DNA-dependent protein kinase catalytic subunit
DPBS	Dulbecco’s phosphate buffered saline
DSB	Double strand break
DVC	Dose volume constraints
E2F-TF	E2F-transcription factor
EBRT	External beam radiotherapy
EMR	Electromagnetic radiation
FBS	Foetal bovine serum
FN	False negative
FP	False positive
G0	Gap 0
G1	Gap 1
G2	Gap 2
GAAD	GZMA-activated DNase

GAG	Glycosaminoglycan
GI	Gastro-intestinal
GZMA	Granzyme A
GU	Genito-urinary
GWAS	Genome wide association studies
HMG2	3-hydroxy-3-methylglutaryl-coenzyme 2
HR	Homologous repair
HRS	Hyper-radiosensitivity
IAP	Inhibitor of apoptosis proteins
IL-1	Interleukin-1
IL-2	Interleukin-2
IL-6	Interleukin-6
IL-8	Interleukin-8
IMRT	Intensity modulated radiotherapy
IP-10	Interferon-inducible protein 10
IPSM	Institute of Physical Sciences in Medicine
IRR	Increased radioresistance
LDA	Linear discriminant analysis
LET	Linear energy transfer
LIG4	Ligase 4
LINAC	Linear accelerator
LQ	Linear quadratic
M	Mitotic
MCP-1	Monocyte chemoattractant protein-1

MEC	Mucoepidermoid carcinoma
MFI	Mean fluorescent intensity
MN	Micronuclei
MNT	Micronucleus test
Mre11	Meiotic recombination protein 11
MRN	Mre11-Rad50-Nbs1
MTT	3-(4,5 dimethylthiazol-2-yl)-2,5-diphenyl tetrazolium bromide
MU	Monitor units
NBS	Nijmegen breakage syndrome
Nbs1	Nijmegen breakage syndrome protein 1
NCI-CTCAE	National Cancer Institute Common Terminology Criteria for Adverse Events
NHEJ	Non-homologous end-joining
NIST	National Institute of Standards and Technology
NSCLC	Non-small-cell lung carcinoma
NTCP	Normal tissue complication probability
OAR	Organs at risk
PA	Pleomorphic adenoma
PBMC	Peripheral blood mononuclear cells
PC	Principal component
PCa	Prostate cancer
PCA	Principal component analysis
PI	Propidium iodide
PLS	Partial least squares

PLS-DA	Partial least squares-discriminant analysis
PLS-R	Partial least squares-regression
PSA	Prostate-specific antigen
PTV	Planning target volumes
PTX3	Pentraxin 3
Rb	Retinoblastoma
RILA	Radiation-induced CD8 T-lymphocyte assay
RNA	Ribonucleic acid
RNS	Reactive nitrogen species
ROC	Receiver operating characteristic
ROS	Reactive oxygen species
RPA	Replication protein A
RT	Radiotherapy
RTOG	Radiation Therapy Oncology Group
S	Synthesis
SABR	Stereotactic ablative body RT
SET	Su(var)3-9, enhancer-of-zeste and trithorax
SG	Savitzky-Golay
Smac	Second mitochondria-derived activator of caspase
SNP	Single nucleotide polymorphism
SNR	Signal-to-noise ratio
SRM	Standard reference material
SSB	Single strand break
TCP	Tumour control probability

TF	Transcription factor
TGFβ1	Transforming growth factor beta 1
TN	True negative
TNFR	Tumour necrosis factor receptor
TNFα	Tumour necrosis factor alpha
TP	True positive
UV	Ultra-violet
WT	Wartin’s tumour
XLF	X-ray repair cross-complementing protein 4-like factor
XRCC	X-ray repair cross-complementing protein

List of Figures

Figure 1.12: The cell cycle and the cyclin-CDK complexes associated with each phase that regulate its progression (Doolittle, 2014).

Figure 1.13: DNA damage signalling during the G1 phase. ATM-dependent activation of the tumour suppressor gene, p53, upregulates p21 resulting in inhibition of the G1-phase cyclin-CDK complexes and therefore Rb phosphorylation, preventing the transition to S-phase (Shaltiel *et al*., 2015).

Figure 1.14: DNA damage signalling during the S (left) and G2 (right) phases. ATR and ATM are activated in response to DNA damage and activate Chk1 and Chk2 via phosphorylation, respectively. Chk1 and Chk2 phosphorylate and inactivate the cell division cycle phosphatases Cdc25A and Cdc25C, halting cell cycle transitions (Shaltiel *et al*., 2015).

Figure 1.15: The homologous recombination (HR) and non-homologous end-joining (NHEJ) DNA repair pathways (Brandsma and Gent, 2012).

Figure 1.16: Extrinsic (left) and intrinsic (right) apoptotic pathways. Cell death signals initiate the intrinsic pathway causing the release of proapoptotic proteins from the mitochondrial intermembrane space into the cytosol which results in apoptosome complex formation. Caspase-9 is activated triggering the caspase cascade causing cleavage of numerous cytosolic and/or nucleic substrates and promoting cell death. Smac and Omi are also released stimulating caspase activation by neutralising apoptosis proteins (IAPs) inhibitors while AIF and endonuclease G participate in chromatin condensation and DNA fragmentation. The extrinsic pathway is initiated by the binding death ligand to a death receptor followed by the creation of the death-inducible signalling complex (DISC) which results in the activation caspase-8 which activates caspase-3 cleaving of target proteins leading to apoptotic cell death. In type II apoptotic cells, caspase-8 cleaves Bid which induces the translocation, oligomerisation and insertion of Bax/Bak into the mitochondrial outer membrane. The release of several proteins results in apoptosome complex formation and activation of the caspase cascade (Orrenius *et al*., 2011).

Figure 6.6: Correlation plot of fitted components from CLS-R model. Moderate to strong correlation coefficients were observed, primarily between the lipid components.

Figure 6.7: (A) PCA scatter plot showing discrimination of grade 0-1 and 2+ toxicity patients. Confidence ellipses were generated at the 95% confidence level. (B) PCA scatter plot showing the discrimination of grade 0-1 (represented by •) and grade 2+ (represented by **x**) toxicity patients with patient spectra coloured according to the 2 clusters identified following a *K*-means cluster analysis.

Figure 6.8: Cross-validated sensitivity and specificity of a PLSDA model developed on spectra. Fitted lines are intended as a guide to the eye, rather than implying a particular mathematical relationship.

List of Tables

Table of Contents

Chapter 1 - Introduction

1.1 Prostate Cancer

Prostate cancer (PCa) is the second most commonly diagnosed cancer in men, after lung cancer, and the fourth most frequently occurring cancer overall (Sung *et al*., 2021; Ferlay *et al.*, 2015; Baade *et al.*, 2009). In 2020, 1.4 million cases worldwide (7.3 % of total cancer cases) were diagnosed and approximately 375,304 deaths occurred (Sung *et al*., 2021). Northern and Western Europe have the highest incidence rates of PCa (age-standardised rate of 83.4 and 77.6 per 100,000 respectively) and thus PCa represents a prominent health burden in Europe (Sung *et al*., 2021). In Ireland, specifically, a rate of 141 cases per 100,000 occurred between 2015 and 2017 accounting for 29.2% of all invasive cancers in men in Ireland and representing one of the highest incidence rates of PCa in Europe (National Cancer Registry, 2018).

PCa is a multifactorial disease and as such, there are genetic, biological, environmental and lifestyle risk factors associated with it (Adjakly *et al.*, 2015; Cuzick *et al.*, 2014; Gann 2002). Of all the risk factors associated with this disease however, age is the most significant (Cuzick *et al.*, 2014). The proportion of men diagnosed with PCa before the age of 50 is very low and in the vast majority of cases, it is diagnosed at age 65 and beyond (Adjakly *et al.*, 2015). PCa is generally detected using a digital rectal exam and a serum prostate-specific antigen (PSA) test and then confirmed via transrectal ultrasonography and a histopathological examination with immunohistochemical staining of needle biopsy samples (Chang *et al.*, 2014; Qu *et al.*, 2014; Stone *et al*., 2007; Jiang *et al.*, 2005). During the histopathological examination, a modified Gleason grading system is used to reflect the difference between the normal and cancerous tissue (Delahunt *et al.*, 2012).

This grading system assigns a score (1-5) to the most common histological pattern and the most differentiated histological pattern (Epstein *et al.*, 2016; Kir *et al.*, 2016). The grade increases as the level of malignancy, and thus cancer aggressiveness, increases (Tabesh *et al.*, 2007). The two scores are then added together to give an overall score and the higher the score, the worse the prognosis (Epstein *et al.*, 2016; Delahunt *et al.*, 2012). The tumour will then be staged using the TNM classification system (see Table 1.1) which assesses the primary tumour (T), regional lymph nodes (N) and metastases (M) using information from the diagnostic tests (Brierley *et al*., 2016).

Table 1.1: The TNM Classification System (Brierley *et al*., 2016)

Primary Tumour (T)	
TX	Tumour cannot be examined
T0	No evidence of tumour
T1	Clinically inapparent tumour
T1a	Incidental histological finding in 5% or less of resected tissue
T1b	Incidental histological finding in more than 5% of resected tissue
T1c	Tumour identified via needle biopsy
T2	Tumour confined to prostate
T2a	Tumour involves a half of one lobe or less
T2b	Tumour involves more than a half of one lobe but not both lobes
T2c	Tumour involves both lobes
T3	Tumour extends beyond prostatic capsule
T3a	Extension including microscopic bladder neck involvement
T3b	Tumour invading seminal vesicle(s)
T4	Tumour is fixed or invading adjacent structures other than the seminal vesicles
Regional Lymph Nodes (N)	
NX	Lymph nodes cannot be examined
N0	No metastasis in lymph nodes evident
N1	Metastasis in lymph nodes evident
Distant Metastasis (M)	
MX	Distant metastasis cannot be examined
M0	No distant metastasis evident
M1	Distant metastasis evident
M1a	Non-regional lymph nodes(s)
M2b	Bone(s)
M3c	Other site(s)

In addition, patients with localised PCa are typically divided into low-, intermediate- and high-risk groups based on Gleason score, T stage and PSA level as shown in Table 1.2 (Mottet *et al.*, 2014; Cancer Research UK, 2017). Using this information, the most appropriate treatment options can then be selected for the patient (Cancer Research UK, 2017).

Table 1.2: Risk Groups for Localised PCa (Mottet *et al.*, 2014; Cancer Research UK, 2017)

	Low-risk	**Intermediate-risk**	**High-risk**
Definition	PSA < 10ng/ml and T1-T2a and GS < 7	PSA 10-20ng/ml or T2b or GS 7	PSA > 20ng/ml or T2c-T4 or GS > 7

1.1.1 Radiotherapy

The treatment for PCa is dependent upon an individual's particular circumstance with tumour stage, Gleason score, age, general health and PSA levels all being taken into consideration to design the course of treatment accordingly for the best anticipated prognosis (Cancer Research UK, 2017). A number of modes of treatment are available for PCa and these include radiotherapy (RT), radical prostatectomy, chemotherapy and hormone therapy (Ku *et al.*, 2015; Chang *et al.*, 2014; Beaton *et al.*, 2013; Ringborg *et al.*, 2003). RT is, however, the most significant non-surgical method of treatment and is highly cost-effective, contributing to only 5% of the total annual cost of cancer care (Ringborg *et al.*, 2003), while treating 50% of PCa patients worldwide, with 60% of these treated with curative intention (Begg *et al.*, 2011; Barnett *et al.*, 2009; Delaney *et al.*, 2005).

RT involves the use of ionising radiation, a physical agent which forms ions and deposits energy in the tissue through which it passes resulting in cancer cell death through a variety of mechanisms (Baskar *et al.*, 2012). The biological target of this high-energy radiation is primarily DNA, damage to which can prevent further proliferation of growing cancer cells, particularly if the damage is in the form of DNA double-strand breaks (DSBs) (Baskar *et al.*, 2012; Jackson and Bartek, 2009). This damage can occur either through radiation directly interacting with DNA or via free radicals, which are primarily created via the ionisation of cellular water molecules, which then interact with DNA (Baskar *et al.*, 2012). The two most common mechanisms of cell death induced by ionisation radiation are apoptosis and mitotic catastrophe (Baskar *et al.*, 2012), with necrosis (Proskuryakov and Gabai, 2010) and autophagy (Baskar *et al.*, 2012) less frequently observed. In addition to cell death, 'premature' senescence may also be induced by ionising radiation (Schmitt, 2007; Roninson, 2003).

In addition, studies by Ghosh *et al*. (2015), Desai *et al*. (2013) and Postow *et al.* (2012) suggest that signals induced by the RT treatment could transform a tumour into an immunogenic antigen, thereby eliciting an immune response from the host that contributes to the RT response. Radiation may be delivered to the target area through an internally deposited radioactive source or external beams (Brown *et al.*, 2011). In the former, termed brachytherapy, radioactive sources such as iridium are employed, which are sealed in seeds or catheters (Baskar *et al.*, 2012; Brown *et al.*, 2011; Sathya *et al.*, 2005). For intermediate- and high-risk PCa patients, external-beam RT (EBRT) is the most common mode of clinical RT (Baskar *et al.*, 2012; Hanks *et al.*, 2003; Bolla *et al.*, 2002; Lawton *et al.*, 2001).

This form of RT involves delivering high-energy radiation to the target site using a beam of high energy X-rays which is produced in a linear accelerator (Baskar *et al.*, 2012; Brown *et al.*, 2011). Various EBRT techniques exist for use in PCa treatment of which the most common are: (a) 3D conformal RT, where the shape of the radiation beams are altered to conform to the tumour; (b) intensity modulated RT (IMRT), which varies the dose delivered to localised regions of the tumour; (c) image guided RT, which involves the use of imaging techniques to position patients so that radiation treatment can be delivered more accurately (Zelefsky *et al.*, 2012; De Meerleer *et al.*, 2007; Geinitz *et al.*, 2005). RT may also be applied as a monotherapy or in combination with other treatment modalities such as surgery, chemotherapy, or hormone therapy (Chang *et al.*, 2014; Beaton *et al.*, 2013). For high-risk PCa patients, RT in conjunction with androgen-deprivation therapy (ADT) is considered the treatment of choice (Dal Pra *et al.*, 2010) with randomised trials suggesting that ADT improves patient outcomes (Jones *et al.*, 2011; Bolla *et al.*, 2010; Widmark *et al.*, 2009; D'Amico *et al.*, 2008).

ADT involves the use of drugs that inhibit the stimulation of PCa by testosterone (Schmidt-Hansen *et al.*, 2014). These drugs block the production of luteinising releasing hormone from the hypothalamus, subsequently resulting in the blocking of follicle-stimulation hormone and luteinising hormone that stimulate the testicular production of testosterone (Schmidt-Hansen *et al.*, 2014; Gomella, 2009). The aim of RT is to eradicate malignant tumours while minimising the damage to surrounding normal tissues which could result in irreversible toxic side effects (Igdem, 2015; Brown *et al.*, 2011; Barnett *et al.*, 2009).

This balance between cure and adverse treatment outcomes can be described by models of tumour control probability (TCP) and of normal tissue complication probability (NTCP). As shown in figure 1.1, the probability of tumour control increases as radiation dose increases. As a small volume of normal tissue is inevitably included in the field of radiation however, the probability of radiation toxicity also increases as radiation dose increases. As a result, RT schedules aim to maximise TCP while minimising NTCP through appropriate choice of treatment dose (Ray *et al*., 2015; Nahum and Uzan, 2012; Barnett *et al*., 2009).

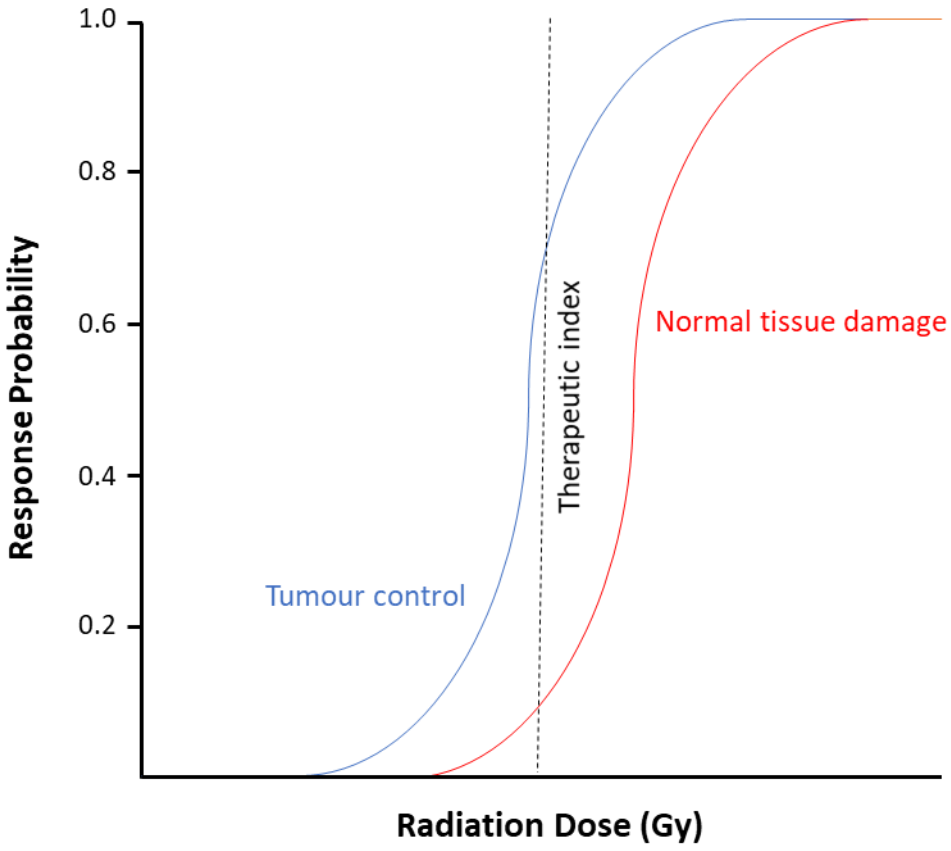

Figure 1.1: Tumour (blue) and normal tissue (red) control probability curves. The dotted line shows a theoretical dose that gives a tumour control probability of ~70% and a ~10% probability of normal tissue damage (Ray *et al*., 2015).

Curative RT treatment strategies also generally involve dividing the total radiation dose into daily fractions given over a number of weeks to reduce normal tissue damage while maximising TCP (Igdem, 2015; Baskar *et al.*, 2012). For example, a typical fractionation regime for PCa would involve a total dose of 78 Gy divded into daily 2 Gy fractions (Yu, 2017). This fractionation approach takes advantage of the 5 Rs of RT allowing for improved tumour cell death and normal tissue repair between each treatment fraction (Igdem, 2015; Baskar *et al.*, 2012).

1.1.2 The 5 Rs of Radiotherapy Response

The 5 Rs of RT provide a short list of the mechanisms which are important in determining the biological tissue response to standard clinical RT (Pajonk *et al.*, 2010; Steel *et al.*, 1989). These mechanisms are repopulation, reoxygenation, redistribution, repair of sub-lethal damage and intrinsic radiosensitivity.

- Repopulation refers to the proliferative response of surviving cells between successive RT fractions, resulting in increasing radiation tolerance with prolonged treatment time (Boustani *et al.*, 2019; Dörr, 2019). This is an important factor in RT treatment because while normal cells repopulate at a steady rate, tumour cells show an accelerated repopulation rate that results in a reduction of treatment efficacy (Zips, 2019; Yang *et al.*, 2014; Dörr, 2019; Kim and Tannock, 2005). Reducing the overall treatment time by increasing the fraction dose and reducing the number of fractions may help to eliminate clonogenic tumour cell repopulation (Herskind *et al.*, 2017; Ciervide *et al.*, 2012).

- Reoxygenation refers to the processes through which surviving hypoxic tumour cells become better oxygenated during RT (Horsman *et al.*, 2019). Hypoxic tumour cells occur in most tumours and are believed to be an important factor in treatment failure as they are much less sensitive to radiation than normally-oxygenated cells (Horsman *et al.*, 2019; Nias, 2000). Permitting reoxygenation of hypoxic tumour cells between successive RT fractions may improve treatment outcome as it can increase tumour radiosensitivity (Boustani *et al*., 2019; Pajonk *et al.*, 2010).

- Redistribution refers to the exhibition of differential radiosensitivity in cells in different phases of the cell cycle (Zips, 2019; Pawlik and Keyomarsi, 2004). According to the law of Bergonié and Tribondeau, the radiosensitivity of biological tissue is directly proportional to the mitotic activity of its cells and indirectly proportional to the level of differentiation of its cells. Thus, cells in the DNA synthesis (S) phase, and in particular, late S phase, tend to be the most radioresistant while cells in the mitotic (M) phase and very late gap 2 (G2) phase tend to be the most sensitive (Boustani *et al*., 2019; Zips, 2019; Pawlik and Keyomarsi, 2004). Cell cycle progression of surviving tumour cells between successive RT fractions allows for the redistribution of the radioresistant S-phase cells into one of the more sensitive cell cycle phases, thereby increasing the probability of tumour cell death during subsequent RT fractions (Zips, 2019; Nias, 2000).

- Repair refers to the process by which the function of normal cells is restored (Boustani *et al*., 2019; Horsman *et al.*, 2019). As mentioned, the biological target of RT is the DNA of the tumour cells.

Tumour cell death by ionising radiation is based on the creation of unrepairable lesions in the DNA of these cells either by direct interaction or by the production of free radicals (Baskar *et al.*, 2012; Pajonk *et al.*, 2010). Most of the radiation-induced DNA damage is sub-lethal and can be repaired at lower doses however, but the accumulation of such sub-lethal damage at higher doses, can result in lethality (Pajonk *et al.*, 2010). Sub-lethal damage repair is a process that requires oxygen and nutrients which makes damage more likely to accumulate in hypoxic tumour cells than in well-oxygenated normal cells (Hall and Giaccia, 2019). Allowing time for repair of sub-lethal damage between successive RT fractions takes advantage of this effect (Herskind *et al.*, 2017; Pajonk *et al.*, 2010).

- Intrinsic radiosensitivity accounts for the differential radiation-induced response exhibited by tumour cells in a manner that is correlated with the cell phenotype and genotype, as well as other environmental factors (Marcu *et al.*, 2015). A wide variation in intrinsic radiosensitivity exists between tumours, even between those of similar histological type and origin, and the overall response of tumours to RT is influenced by this intrinsic radiosensitivity (Marcu *et al.*, 2015; Begg, 2009).The origins of this intrinsic radiosensitivity appear to be related in part to the genetic instability of individual tumours which leads to variability in RT response (Marcu *et al.*, 2015). On a molecular level however, intrinsic radiosensitivity is poorly understood (Marcu *et al.*, 2015; Harrington *et al.*, 2007). Yet, despite this lack of understanding, attempts have still been made to clinically assess individual radiosensitivity (discussed in section *1.5 Assays of Clinical Radiosensitivity*).

1.1.3 Cell Survival Models

Cell killing is the most important process in understanding the biological response to radiation and the most common representation of this relationship between radiation and cell killing is the linear-quadratic (LQ) model shown in figure 1.2 (Hall and Giaccia, 2019; Jones *et al*., 2001). The LQ model is thus the model of choice to describe cell survival curves in radiobiology as it provides a practically useful explanation of fractionation and radiation dose-rate effects observed at the macroscopic level (Joiner, 2019). The model can be applied to both tumour and normal tissues and is thus particularly useful for evaluating how alterations in radiation delivery patterns can affect the overall therapeutic response (Hall and Giaccia, 2019; Joiner, 2019; Dale, 2004).

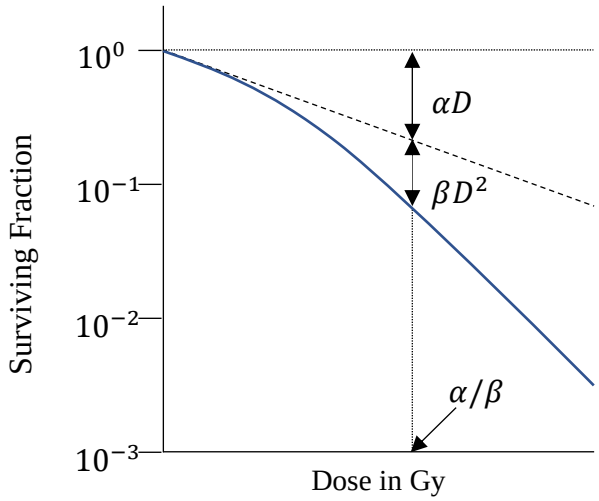

Figure 1.2: The linear-quadratic model where experimental data is fitted to a linear-quadratic function. This model describes two components of cell killing. The first, the linear component, is proportional to dose (αD), while the second, the quadratic component, is proportional to the square of the dose (βD^2). The dose at which point the linear and quadratic model components are equal is described as the ratio α/β (Hall and Giaccia, 2019; Joiner, 2019).

The LQ model assumes that there are two components to cell killing by radiation – type A damage and type B damage (Hall and Giaccia, 2019; Dale, 2004). Type A damage occurs as a result of a single ionising event and type B damage occurs as a result of two, separate sub-lethal ionising events which interact to cause lethal damage (Hall and Giaccia, 2019; Dale, 2004). Type A damage is represented by the linear component of the cell survival curve and type B damage is represented by the quadratic component of the cell survival curve (Hall and Giaccia, 2019; Dale, 2004). The LQ model can be expressed as:

$$SF_D = e^{-\alpha D - \beta D^2} \quad \textbf{(1.1)}$$

where SF_D represents the surviving fraction of cells at a particular dose D, α represents the probability of lethality due to type A damage and β represents the probability of lethality due to type B damage (Hall and Giaccia, 2019; Joiner, 2019; Joiner and Bentzen, 2019). Furthermore, type A and type B damage contributions to cell killing are equal at a dose which is equal to the ratio of α to β (Hall and Giaccia, 2019; Dale, 2004). It is this ratio that provides a quantitative metric of the sensitivity of a tumour or normal tissue to alterations in dose-rate or fractionation (Dale, 2004). It has been shown however, that the LQ model is less effective in modelling the relationship between dose and cell survival at doses below 1 Gy (Marples and Collis, 2008; Bonner, 2004). Two phenomena, hypersensitivity (HRS) and increased radioresistance (IRR), give rise to the deviation from the LQ model at doses between 0 and 1 Gy (Marples and Collis, 2008; Bonner, 2004). HRS refers to the sub-LQ cell survival values observed in cells at radiation doses less than ~0.2 Gy while IRR refers to the abrupt return of cell survival values to LQ values observed over the ~0.2 Gy to 0.6 Gy range (Marples and Collis, 2008; Bonner, 2004).

As a result of this change in survival response, cell survival cannot be predicted below 1 Gy by simply back-extrapolating measurements made at higher doses using the LQ model (Marples and Collis, 2008). A modified form of the LQ model, known as the induced repair model (see figure 1.3) was therefore proposed by Joiner (2002) given as:

$$SF_{(D,\,D_c)} = \exp\{-\alpha_r \left(1 + \left({}^{\alpha_s}/_{\alpha_r} - 1\right) e^{-{}^{D}/_{D_c}}\right) D - \beta D^2\} \qquad \textbf{(1.2)}$$

where α_s is the low-dose α value describing the HRS region, α_r is the low-dose α value describing the IRR region and D_c is the dose at which the transition from HRS to IRR begins (Joiner, 2019; Marples and Collis, 2008; Steel, 2007). From this equation, it can be seen that when $D \gg D_c$, $\exp(-D/D_c)$ approaches zero and the equation is reduced to the LQ expression with parameters α_r and β (Joiner, 2019; Steel, 2007). Furthermore, at very low doses, where $D \ll D_c$, $\exp(-D/D_c)$ approaches 1 and the equation again reduces to the LQ expression but with parameters α_s and β (Joiner, 2019; Steel, 2007).

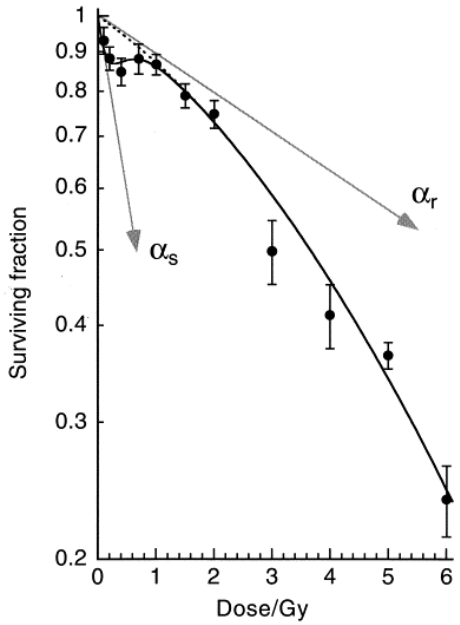

Figure 1.3: Fitting of the induced model and linear-quadratic models is represented by the solid line and dashed line, respectively. At doses <1 Gy, the linear quadratic model, which has an initial slope α_r, significantly underestimates irradiation effect. Doses <1 Gy are better described by the induced repair model using a far steeper slope represented by α_s (Joiner, 2019; Short *et al*., 1999).

The underlying mechanisms behind this low-dose behaviour of surviving cells are not fully understood however, but several studies suggest that the low-dose behaviour of cells is linked to the early G2/M checkpoint and that the ataxia telangiectasia mutated protein (ATM) may play a key role (Krueger *et al*., 2010; Xue *et al*., 2009; Marples *et al*., 2004). ATM is an important molecule in DSB repair induction, and it appears to have a threshold of activation at ~0.2 Gy (Krueger *et al*., 2010; Xue *et al*., 2009). At doses below 0.2 Gy, ATM is not activated resulting in a failure of the early G2/M checkpoint function and low DSB repair which in turn leads to induced cell death and mutation producing an HRS response (Xue *et al*., 2009). At doses above 0.2 Gy however, ATM is activated, leading to early G2/M cell cycle arrest and blocking of mitotic entry which allows for DNA repair, thereby reducing cell death and producing IRR outcomes (Xue *et al*., 2009). While the mechanisms behind HRS and IRR responses are not entirely clear, studies by Słonina *et al*. (2007) and Harney *et al*. (2004) suggest that these responses are individually variable and so may be useful as a means of characterising individual radiosensitivity.

1.2 Interaction of Radiation with Matter

1.2.1 Absorption of Ionising Radiation

Radiation may be categorised as directly or indirectly ionising and the intensity of this ionisation can be measured in terms of linear energy transfer (LET) which is the amount of energy transferred to a material per unit length of track (Nias, 2000). Directly ionising radiation (particulate radiation) disrupts the atomic structure of the chemical and biological materials thorough which it passes (Hall and Giaccia, 2019; Desouky *et al*., 2015). Examples of directly ionising radiation include energetic electrons, protons, α-particles and heavy charged particles.

Indirectly ionising radiation (electromagnetic or photonic radiation) does not produce biological and chemical damage in the same manner (Hall and Giaccia, 2019; Desouky *et al.*, 2015; Gazda and Coia, 2005). Instead, they impart energy to electrons within the absorber, creating fast-moving charged particles capable of producing chemical and biological damage (Hall and Giaccia, 2019; Desouky *et al.*, 2015). Examples of indirectly ionising radiation include light in the far ultra-violet (UVC) region, γ-rays and X-rays (Hall and Giaccia, 2019; Gazda and Coia, 2005). In the present study, indirectly ionising radiation, specifically X-ray radiation, was used for cellular irradiation. An X-ray photon can be completely absorbed by the material through which it passes by depositing its energy in what is referred to as photoelectric interaction, or it may be scattered from its original course, depositing part of its energy in what is known as the Compton process (Hall and Giaccia, 2019; Desouky *et al.*, 2015; Gazda and Coia, 2005).

An X-ray photon may also interact with the electrostatic field surrounding nuclei with a high atomic number in a manner that results in its energy being converted to matter, producing an electron and a positron in pair production (Morse and Wolfe, 2013; Saha, 2001). During the photoelectric interaction (as shown in figure 1.4), a photon relinquishes the entirety of its energy to a tightly bound electron in one of the atomic orbitals (generally the outer shell) causing the electron to be ejected from the atom and to pass into the surrounding matter (Desouky *et al.*, 2015; Gazda and Coia, 2005). This creates a vacancy in the atomic shell which may be filled by an electron from an outer orbital of the same atom or by a free electron from outside the atom (Hall and Giaccia, 2019).

This also can also result in a change of energy state of the electron with the difference in energy emitted as a photon of characteristic X-rays (Hall and Giaccia, 2019). In soft tissue however, this characteristic radiation is of little biological consequence as it has low energy (Hall and Giaccia, 2019).

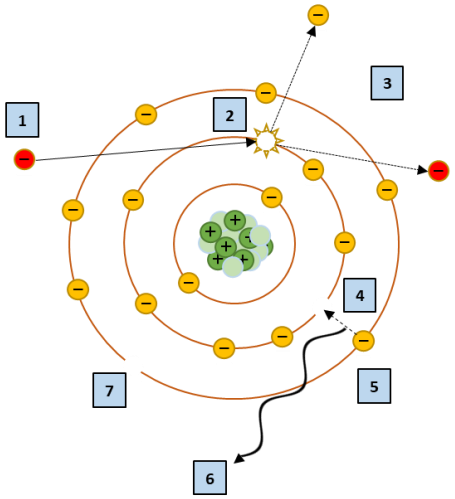

Figure 1.4: The photoelectric effect. (1) An incoming photon imparts its energy to an electron in one of the atomic orbitals. (2) The electron is ejected from the atom. (3) The ejected electron imparts the atom with an energy equivalent to that imparted by the photon. (4) An inner vacancy in the atomic shell is created as a result. (5) The vacancy is filled by an electron. (6) The electron sheds its excess energy as it fills the void. (7) A vacancy is left in the outer shell (Hall and Giaccia, 2019; Desouky *et al.*, 2015; Gazda and Coia, 2005).

The pair production process (see figure 1.5) occurs when the X-ray photon energy is greater than twice the mass energy of the electron (1.022 MeV) (Burmeister and Joiner, 2019; Gazda and Coia, 2005; Saha, 2001). The photon interacts with the electric field surrounding the nucleus of the absorbing atoms with high atomic number (Gazda and Coia, 2005). The photon relinquishes its energy to the nucleus and an electron and positron are produced (Burmeister and Joiner, 2019; Gazda and Coia, 2005; Saha, 2001). The positron ionises until it combines with a free electron resulting in the generation of two photons which scatter in opposite directions (Gazda and Coia, 2005).

The electron produced can result in the ionisation and excitation of other surrounding atoms (Mundt *et al*., 2003). Moreover, while pair production is not the most significant radiation absorption mechanism, it is does occur to a certain extent in routine RT (Burmeister and Joiner, 2019; Gazda and Coia, 2005; Saha, 2001).

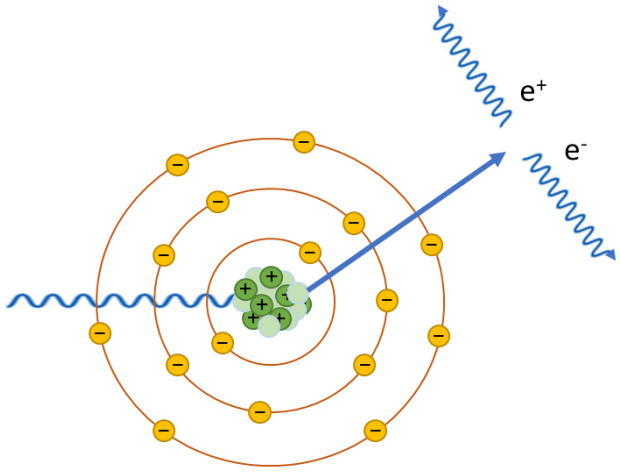

Figure 1.5: Pair production. A high energy photon interacts with the electric field surrounding the nucleus. The photon imparts its energy to the nucleus producing an electron and positron. The positron ionises until it combines with a free electron resulting in the generation of two photons which scatter in opposite directions (Gazda and Coia, 2005; Saha, 2001).

During the Compton process (see figure 1.6), a photon transfers only a portion of its energy (0 - 80 %) in the form of kinetic energy to a loosely bound orbital electron (Hall and Giaccia, 2019; Gazda and Coia, 2005). This produces a fast electron while the photon, now with lower energy, is deflected and continues on a different path from its original where it can take part in further interactions (Hall and Giaccia, 2019; Desouky *et al.*, 2015; Gazda and Coia, 2005). The production of a fast electron can result in the ionisation of other atoms, the breaking of important chemical bonds and the initiation of the chain of events that result in biological damage (Hall and Giaccia, 2019; Gazda and Coia, 2005).

Thus, the Compton process is of significant biological consequence and at high energies characteristic of a linear accelerator used in RT, this process is the dominant absorption mechanism (Hall and Giaccia, 2019; Gazda and Coia, 2005).

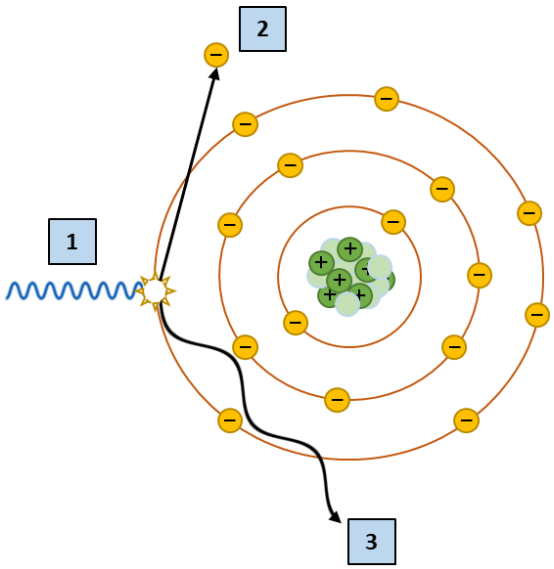

Figure 1.6: The Compton process. (1) An incoming photon interacts with an electron of the outer orbital and imparts a portion of its energy to the electron causing it to be ejected from orbit. (2) The ejected, or Compton, electron leaves the atom with the imparted energy. (3) The photon follows an altered path with less energy than prior to the collision. (Hall and Giaccia, 2019).

1.2.2 Direct and Indirect Effects of Ionising Radiation

The chemical and biological effects of ionising radiation occur primarily from damage to DNA, the critical target of RT (Hall and Giaccia, 2019; Kim *et al.*, 2014). As previously mentioned, ionising radiation, whether directly or indirectly ionising, can interact directly or indirectly with DNA (Hall and Giaccia, 2019; Kim *et al.*, 2014; Baskar *et al.*, 2012). With direct action, radiation hits the DNA molecule directly, exciting or ionising the atoms of the molecule, disrupting the structure and causing single-strand breaks (SSBs) or DSBs (Desouky *et al.*, 2015; Lomax *et al.*, 2013). These breaks, if unrepaired, may then result in cell death or mutation.

Direct action is most common in high LET radiations such as α-particles and with high radiation doses (Hall and Giaccia, 2019; Desouky *et al.*, 2015). The dominant action for indirect ionising radiation such as X-rays however, is indirect action (Hall and Giaccia, 2019). With indirect action, radiation interacts with non-nucleic acid-associated atoms and molecules, producing free radicals that can diffuse to, and interact with the DNA molecule (Hall and Giaccia, 2019; Desouky *et al.*, 2015; Kim *et al.*, 2014). Free radicals carry a highly chemically reactive unpaired electron in their outer shell which can react with DNA molecules resulting in molecular structural damage (Desouky *et al.*, 2015; Kim *et al.*, 2014; Lomax *et al.*, 2013). The vast majority of X-ray radiation-induced damage results from indirect action due to the high water content (~70 %) of cells (Hall and Giaccia, 2019; Saha, 2013; Von Sontag, 2006). The interaction of a photon of X-rays with a water molecule can cause the water molecule to become ionised which can be expressed as:

$$H_2O \xrightarrow{Radiation} H_2O^+ \cdot + e^- \qquad \textbf{(1.3)}$$

where $H_2O^+ \cdot$ is an ion radical (the dot represents an unpaired electron) and e^- is an ejected electron (Hall and Giaccia, 2019; Nias, 2000). This resulting ion radical then reacts with another molecule of water to form a highly reactive hydroxyl radical, a reactive oxygen species (ROS). This can be expressed as:

$$H_2O^+ \cdot + H_2O \rightarrow 2H^+ + 2OH \cdot \qquad \textbf{(1.4)}$$

where $OH \cdot$ is the highly reactive hydroxyl radical and H^+ is a highly reactive hydrogen atom (McMillan and Steel, 2002; Nias, 2000).

In addition, the ejected or fast electron (e^-) can become hydrated by other water molecules producing another reactive water species:

$$e^- + H_2O \rightarrow e^-_{aq} \quad \textbf{(1.5)}$$

where e^-_{aq} is the hydrated electron (Kumar *et al.*, 2016; McMillan and Steel, 2002). A hydrogen radical may also be produced through the reaction of a highly reactive hydrogen atom with a hydrated electron:

$$e^-_{aq} + H^+ \rightarrow H\cdot \quad \textbf{(1.6)}$$

where $H\cdot$ is the hydrogen radical (Nias, 2000). Furthermore, hydroxyl radicals may also react with one another to form hydrogen peroxide:

$$OH\cdot + OH\cdot \rightarrow H_2O_2 \quad \textbf{(1.7)}$$

where H_2O_2 is the ROS, hydrogen peroxide (Nias, 2000). These primary water radiolysis products ($OH\cdot$, e^-_{aq}, $H\cdot$ and H_2O_2) can all damage DNA molecules but most of the damage is caused by the hydroxyl radical (Hall and Giaccia, 2019; Von Sontag, 2006). In addition to the damage caused by these products, damage can also occur as a result of reactive nitrogen species (RNS) and other species (Wardman, 2009). The result of this indirect action is the cleavage of the DNA backbone and oxidative damage of DNA bases producing SSBs and DSBs and the resulting biological effect may be expressed seconds, days, months or even years later (Hall and Giaccia, 2019; Desouky *et al.*, 2015; Cadet and Wagner, 2013).

1.2.3 Radiation-induced DNA Damage

DNA is a large molecule consisting of two opposite, or complementary, strands held together by hydrogen bonds between the four nitrogenous bases thymine, cytosine, adenine and guanine forming a double helical structure, as shown in figure 1.7 (Travers and Muskhelishvili, 2015; Pray, 2008). The ‘backbone’ of each strand is comprised of alternating deoxyribose sugar and phosphate units and attached to this backbone are the aforesaid bases (Pray, 2008). Thymine and cytosine are pyrimidines and adenine and guanine are purines (Pray, 2008). The bases of opposite DNA strands must be complementary as adenine and thymine pair exclusively and guanine and cytosine also pair exclusively (Hall and Giaccia, 2019; Pray, 2008). The order of these bases defines the genetic code and thus any damage to the bases, strands or bonds involved can have significant biological consequences if it cannot be repaired.

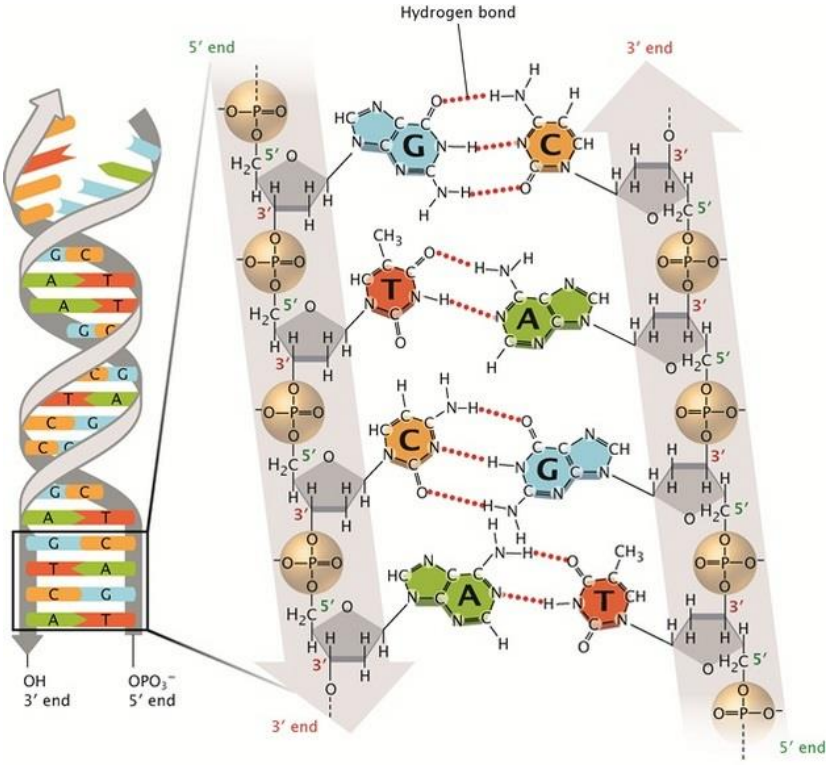

Figure 1.7: Two-dimensional representation (left) and chemical structure (right) of DNA (Pray, 2008).

There are numerous forms of DNA damage, such as nucleotide or base modifications, base dimerisation and crosslinking, though the two primary types of DNA damage associated with ionising radiation which lead to cell death are SSBs and DSBs (Sage and Shikazono, 2017; Bernstein *et al*., 2013). SSBs (as shown in figure 1.8A) are readily repaired using the opposite intact DNA strand as a template (Hall and Giaccia, 2019; Vignard *et al*., 2013; McMillan and Steel, 2002) and so do not lead readily to cell death. Furthermore, if both strands of a DNA molecule are broken but the breaks are well separated (as shown in figure 1.8B), they are also readily repaired because they are handled separately (Hall and Giaccia, 2019; Eccles *et al*., 2011).

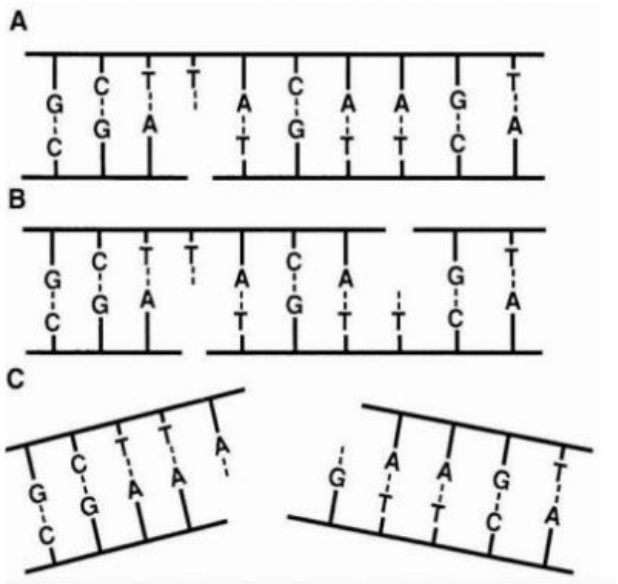

Figure 1.8: Diagram of single- and double-strand DNA breaks: **A** – single strand break, **B** – well separated breaks in both strands, **C** – double strand break (Hall and Giaccia, 2019).

Conversely however, if the breaks of both DNA strands are opposite one another or are separated by only a few base pairs, a DSB can occur causing cleavage into two pieces as shown in figure 1.8C (Hall and Giaccia, 2019; Cannan and Pederson, 2016; Eccles *et al*., 2011). DSBs are difficult to repair and unrepaired or mis-repaired DSBs can be problematic (West and Barnett, 2011). An approximate 40 DSBs are induced in mammalian cells per 1-2 Gy of ionising radiation and most are repaired with approximately one DSB per unit dose remaining unrepaired. This single unrepaired DSB can be lethal to the cell if it triggers programmed cell death or inactivates a crucial gene (West and Barnett, 2011; Martin *et al*., 2010; McMillan and Steel, 2002). There are numerous kinds of DSBs and these vary depending on the distance between breaks and the end groups produced from the break (Hall and Giaccia, 2019).

1.3 DNA Damage Recognition and Response

The DNA damage response (DDR) system (see figure 1.9) is a highly complicated and regulated system that determines cell fate following radiation-induced DNA damage (Vens *et al*., 2019; Wouters and Begg, 2009). It is a group of elaborately interconnected signalling pathways involving DNA damage sensors and transducers which ultimately affect the cell cycle and trigger a signalling cascade which determines the fate of the cell (Vens *et al*., 2019; Wouters and Begg, 2009).

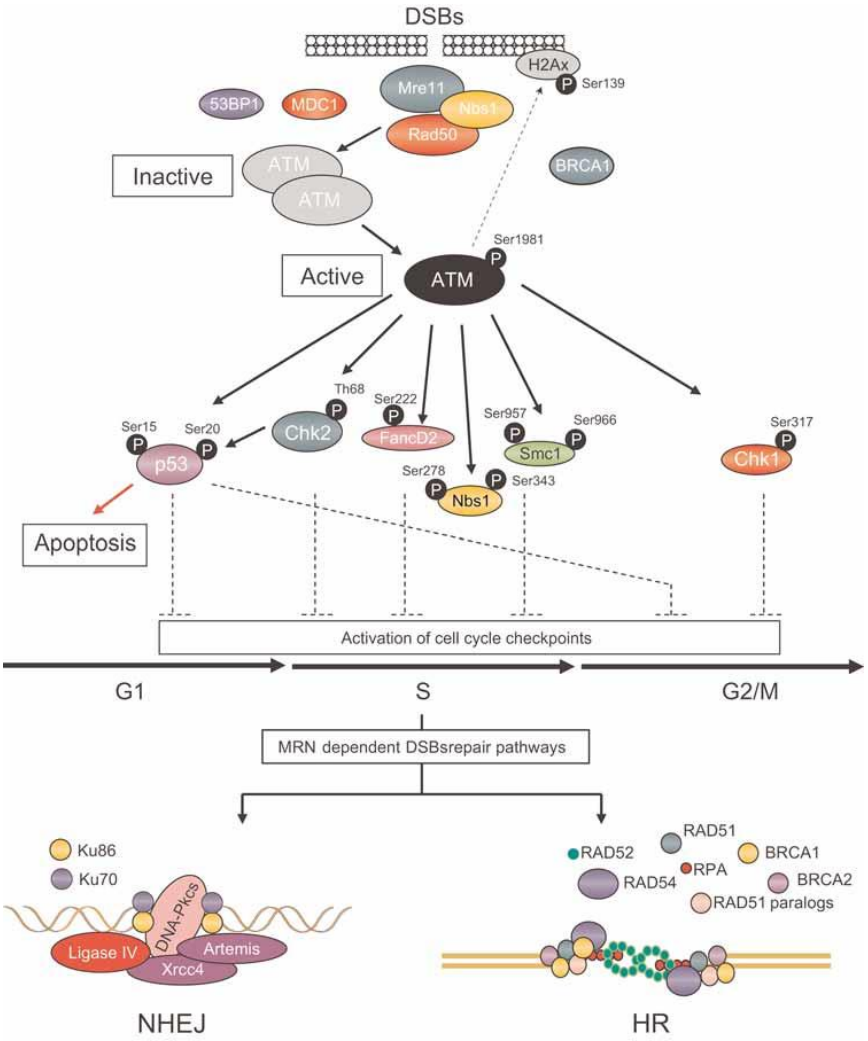

Figure 1.9: Overview of the DNA damage response system. DNA double-strand breaks phosphorylate ATM which in turn phosphorylates various substrates involved in a cascade of events including apoptosis and cell cycle checkpoint activation. These substrates can inhibit the cell cycle at various points allowing nonhomologous-end-joining (NHEJ) or homologous recombination (HR) cell repair. The substrates shown are not an exhaustive list and depict only some of the known ATM substrates (Frappart and McKinnon, 2006).

1.3.1 DNA Damage Sensors

The initial cell response to DSBs involves the localisation of various proteins to the DNA damage site forming clusters often referred to as foci (Podhorecka *et al*., 2010; Kouzarides, 2007; Taverna *et al*., 2007). It is thought that these foci provide a platform from which DNA repair and signalling of other effector molecules can occur (Vens *et al*., 2019; Podhorecka *et al*., 2010; Wouters and Begg, 2009).

One of the earliest events in DDR, occurring within minutes, is the phosphorylation of the subtype of histone H2A called H2AX, which is distributed randomly throughout the chromatin (Podhorecka *et al*., 2010; Kuo and Yang, 2008; Rogakou *et al*., 1998). The phosphorylated form of H2AX, referred to as γH2AX, is thought to act as a docking site for many of the relocalised proteins involved in DSB repair and to promote the formation of foci (Ferlazzo *et al*., 2017; Podhorecka *et al*., 2010). Cells engineered to be deficient in H2AX show significant defects in the formation of foci and demonstrate radiosensitivity (Vens *et al*., 2019; Wouters and Begg, 2009). Thus, γH2AX appears to play a major role in radiation-induced DSB repair. The phosphorylation of H2AX can occur through three pathways but only two appear to play a role in radiation-induced DSBs (Vens *et al*., 2019; Yan *et al*., 2011; Podhorecka *et al*., 2010; Wouters and Begg, 2009).

- The first is the ATM-MRN pathway (see figure 1.10). ATM is the main molecule responsible for H2AX phosphorylation in response to radiation-induced DSBs (Maréchal and Zou, 2013; Durocher and Jackson, 2001). ATM is normally present in the cell in an inactive form however and thus its recruitment to the DSB site requires a DSB sensor tri-protein complex comprised of meiotic recombination protein 11 (Mre11), Rad50 and Nijmegen breakage syndrome protein 1 (Nbs1), known as the MRN complex (Srivastava *et al*., 2009; Dupré *et al*., 2006). The Rad50 component of the MRN complex detects the DSB and binds to it (Moreno-Herrero *et al*., 2005). The Nbs1 component then binds ATM, recruiting it to the DSB site where it is activated and can phosphorylate H2AX (Vens *et al*., 2019; Wouters and Begg, 2009; Falck *et al*., 2005; You *et al*., 2005).

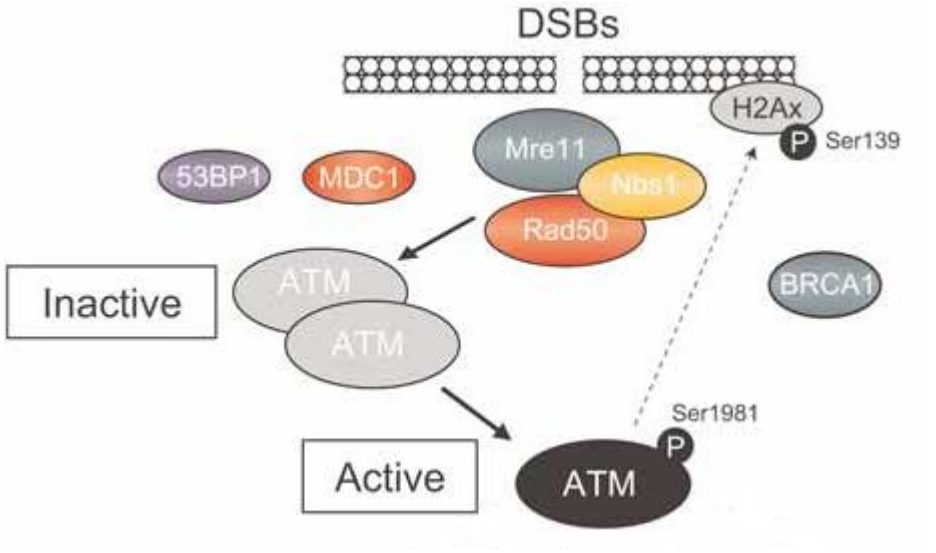

Figure 1.10: Overview of the MRN-ATM signalling pathway. DNA double-strand breaks activate ATM via phosphorylation which involves sensing of the DNA break by the MRN complex and recruiting ATM to the break site where it is activated and can phosphorylate H2AX. The phosphorylated H2AX then functions as a platform on which proteins involved in double-strand break repair concentrate (Frappart and McKinnon, 2006).

- H2AX phosphorylation and thus foci formation can also occur through the DNA-PKcs-Ku pathway, as shown in figure 1.11 (Tu *et al*., 2013; An *et al*., 2010). This involves the phosphorylation of H2AX by the catalytic subunit of DNA-dependent protein kinase referred to as DNA-PKcs (Tu *et al*., 2013; An *et al*., 2010). DNA-PKcs is structurally similar to ATM and, like ATM, it is incapable of acting as a sensor of DSBs (Vens *et al*., 2019; Wouters and Begg, 2009). Thus, the Ku70-Ku80 protein complex carries out this sensor function, binding directly to the DSB and recruiting DNA-PKcs to the site where it can phosphorylate H2AX (An *et al*., 2010; Falck *et al*., 2005; Meek *et al*., 2004). The activation of ATM and DNA-PKCs leads not only to the phosphorylation of H2AX but to the phosphorylation of hundreds of other cellular proteins in response to DNA damage (Matsuoka *et al*., 2007).

The phosphorylation of all these proteins results in the activation of various different downstream effector pathways, the most important of which are cell cycle checkpoint activation, DNA repair and cell death (Vens *et al*., 2019; Wouters and Begg, 2009).

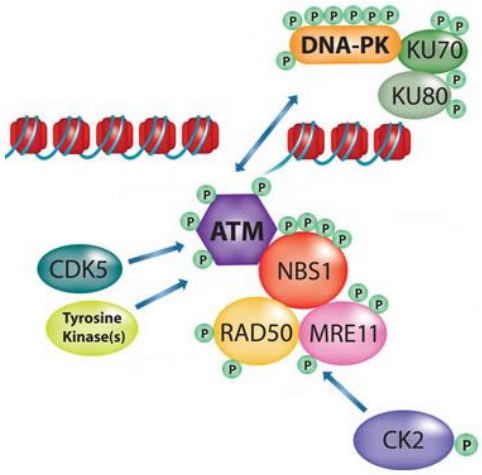

Figure 1.11: Phosphorylation of H2AX by the catalytic subunit of DNA-dependent protein kinase referred to as DNA-PKcs. DNA-PKcs is incapable of acting as a sensor of double-strand breaks however, and the Ku70-Ku80 protein complex carries out this sensor function, binding directly to the DSB and recruiting DNA-PKcs to the site where it can phosphorylate H2AX (Bhatti *et al*., 2011).

1.3.2 Cell Cycle Checkpoint Activation

The cell-cycle checkpoint activation pathway is a major DDR effector pathway. The cell cycle consists of four distinct phases, the gap 1 (G1) phase, the S-phase, the G2-phase and the M-phase, as well as a 'resting' or gap 0 (G0) phase as shown in figure 1.12 (Wenzel and Singh, 2018; Barnum and O'Connell, 2016; Nias, 2000). DNA replication occurs during the S-phase and the cell undergoes division during the M-phase. The G1 and G2 phases prepare the cell for the S-phase and M-phase respectively (Barnum and O'Connell, 2016; Nias, 2000). During the G1-phase the cell undergoes a period of growth and produces proteins necessary for DNA replication in the S-phase (Bähler, 2005; Cooper, 2000).

During the G2-phase the cell again undergoes a period of growth and checks the duplicated DNA for errors before dividing in the M-phase (Cooper, 2000). Following M-phase, the cell may enter the G0-phase before re-entering the G1-phase (Nias, 2000).

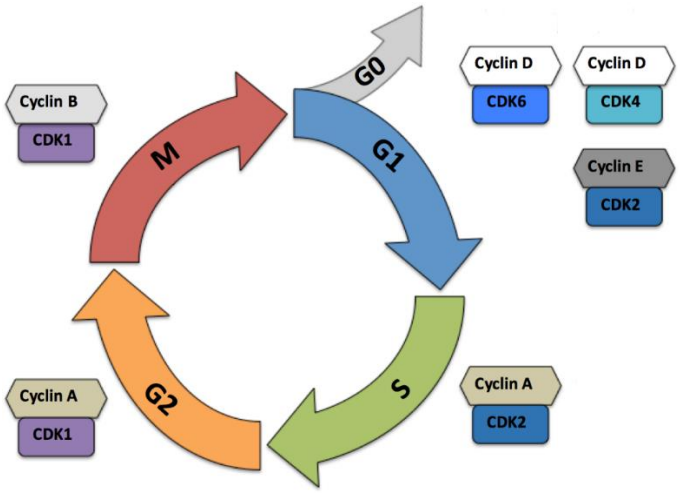

Figure 1.12: The cell cycle and the cyclin-CDK complexes associated with each phase that regulate its progression (Doolittle, 2014).

The exposure of a cell to ionising radiation causes delays in the progress of the cell through the G1, S and G2 phases due to the activation of DNA damage checkpoints (Nickoloff, 2017; Kastan and Bartek, 2004). These checkpoints are discrete points in the cell cycle that prevent or slow progression of the cell into the next phase (Barnum and O'Connell, 2016; McMillan and Begg, 2002). The primary biological aim of this delayed progression is to allow time for DNA damage repair to take place (Vens *et al*., 2019; Wouters and Begg, 2009; Bartek and Lukas, 2007). All progression through the cell cycle is controlled by cyclin-dependent kinases (CDKs) which phosphorylate other proteins to activate the mechanisms needed for cell cycle progression (Wenzel and Singh, 2018; Barnum and O'Connell, 2016). CDKs are only active when associated with their cyclin partners and specific cyclin-CDK complexes are functional at each cell cycle phase (Vens *et al*., 2019; Barnum and O'Connell, 2016; Wouters and Begg, 2009; Nias, 2000).

Inhibition of these cyclin-CDK complexes is therefore necessary for the activation of cell cycle checkpoints and for radiation. This can occur via two main mechanisms (Vens *et al*., 2019; Wouters and Begg, 2009). The first is by activation of proteins called CDK inhibitors (CDKIs) which directly inhibit cyclin-CDK complexes and the second is by affecting the phosphorylation status and activity of the CDK protein itself (Vens *et al*., 2019; Wouters and Begg, 2009; McMillan and Begg, 2002). The DDR system activates four specific checkpoints in response to irradiation taking place at different points in the cell cycle and these are the G1 arrest checkpoint, the S-phase checkpoint, the G2 early checkpoint and the G2 late checkpoint which are summarised in Table 1.3 (Vens *et al*., 2019; Wouters and Begg, 2009; Cooper, 2000).

Table 1.3: Summary of cell cycle checkpoint system.

Checkpoint	Primary signalling proteins	Applies to cells irradiated in	Features
G1	ATM, p53, p21	G1	Prevents/delays S-phase entry
S	ATM, Chk2, Cdc25A/Cdc25C	S	Slows progression through S-phase
G2 early	ATM, Chk2, Cdc25A/Cdc25C	G2	Prevents/delays M-phase entry
G2 late	ATR, Chk1, Cdc25A/Cdc25C	G1/S	Accumulation of cells in G2

The G1 arrest checkpoint occurs at the transition between the G1 and S phases and thus has an important role in deciding if cell division should be initiated (Bertoli *et al*., 2013; McMillan and Begg, 2002). The transition from G1- to S-phase is controlled by the E2F transcription factor (E2F-TF) which acts as a regulator of many genes involved in DNA replication initiation (Bertoli *et al*., 2013; Burkhart and Sage, 2008; McMillan and Begg, 2002). It is kept in an inactive state by binding to the retinoblastoma (Rb) protein (Burke *et al*., 2012; Burkhart and Sage, 2008).

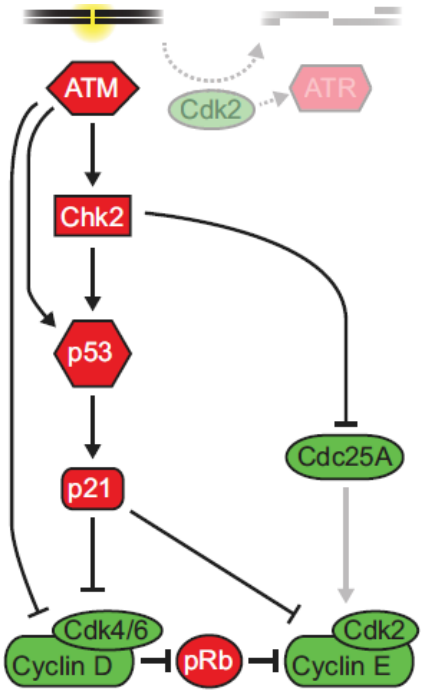

Figure 1.13: DNA damage signalling during the G1-phase. ATM-dependent activation of the tumour suppressor gene, p53, upregulates p21 resulting in inhibition of the G1-phase cyclin-CDK complexes and therefore Rb phosphorylation, preventing the transition to S-phase (Shaltiel *et al*., 2015).

As the cell normally transitions from G1- to S-phase, the Rb protein is phosphorylated by G1-phase cyclin-CDK complexes causing its release from the E2F-TF, allowing the E2F-TF to function and initiate S-phase (Burke *et al*., 2012; Burkhart and Sage, 2008). Irradiation causes ATM-dependent activation of the tumour suppressor gene, p53, and this upregulates the CDKI p21 resulting in inhibition of the G1-phase cyclin-CDK complexes and therefore Rb phosphorylation (as shown in figure 1.13), preventing the transition to S-phase (Burke *et al*., 2012; Burkhart and Sage, 2008). The S-phase, G2 early, and G2 late checkpoints are all activated through a similar process controlled by the related checkpoint kinase's (Chk) 1 and 2 (Bartek *et al*., 2004). As shown in figure 1.14, ataxia telangiectasia and Rad3-related protein (ATR) and ATM, which are activated in response to DSBs, phosphorylate and thus activate Chk1 and Chk2, respectively (Nickoloff, 2017; Shaltiel *et al*., 2015; McMillan and Begg, 2002).

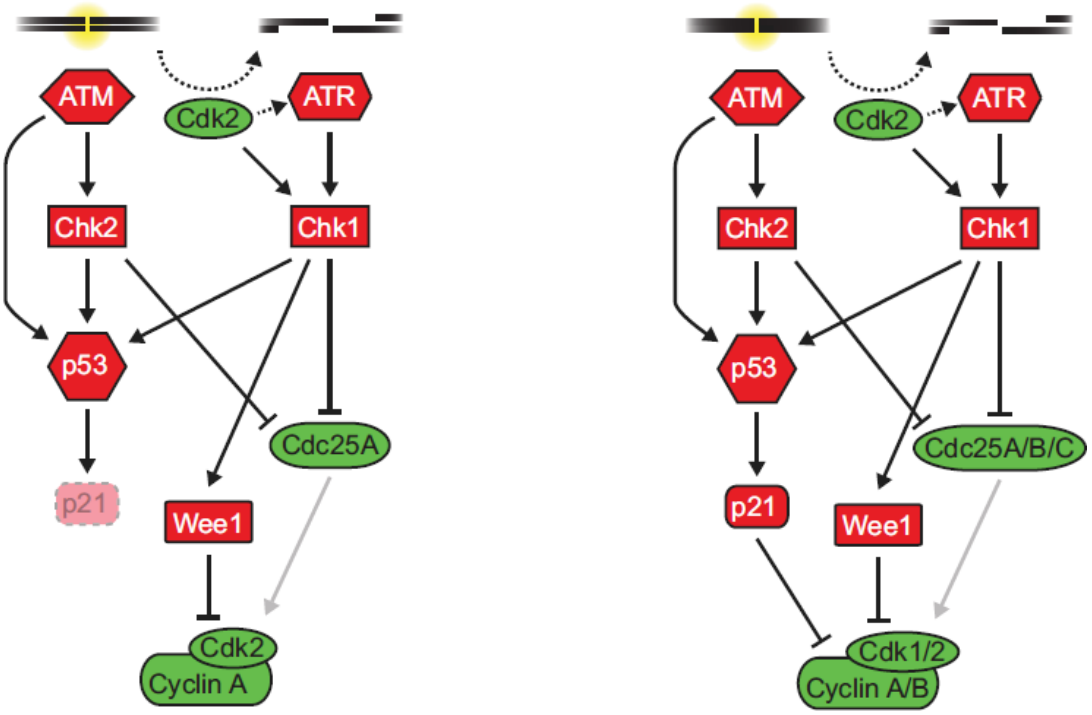

Figure 1.14: DNA damage signalling during the S (left) and G2 (right) phases. ATR and ATM are activated in response to DNA damage and activate Chk1 and Chk2 via phosphorylation, respectively. Chk1 and Chk2 phosphorylate and inactivate the cell division cycle phosphatases Cdc25A and Cdc25C, halting cell cycle transitions (Shaltiel *et al*., 2015).

Once activated, Chk1 and Chk2 phosphorylate and thus inactivate the cell division cycle (Cdc) phosphatases Cdc25A and Cdc25C (Shaltiel *et al*., 2015; Illiakis *et al*., 2003). The inactivation of Cdc25A/C prevents either from dephosphorylating and activating the cyclin-CDK complexes necessary for cell cycle phase transitions (Shaltiel *et al*., 2015; Illiakis *et al*., 2003). The S-phase and G2 early checkpoints are both ATM-Chk2-Cdc25A/C-dependent while the G2 late checkpoint is ATM-independent and instead, ATR-Chk1-Cdc25A/C-dependent (Shaltiel *et al*., 2015; Falck *et al*., 2001). Cells irradiated in S-phase demonstrate a dose-dependent reduction in the rate of DNA synthesis and as a result, the time needed for DNA replication significantly increases (Vens *et al*., 2019; Wouters and Begg, 2009).

The G2 early checkpoint is activated by relatively low radiation doses and rapidly prevents entry into M-phase resulting in a short-term decrease in the number of cells undergoing mitosis following irradiation (Vens *et al*., 2019; Wouters and Begg, 2009). The G2 late checkpoint on the other hand imposes a long-term G2 delay observed following the irradiation of cells during the G1 or S phases (Vens *et al*., 2019; Wouters and Begg, 2009). These cells may experience short G1 and S-phase checkpoints but then experience a second, longer dose-dependent delay at the G2 checkpoint hours later (Vens *et al*., 2019; Wouters and Begg, 2009). Thus, an accumulation of cells in G2-phase can occur following irradiation. It has been suggested that mutations in the genes that regulate cell cycle checkpoint activation which cause failure of checkpoints could influence overall cellular radiosensitivity but there is little evidence to support this (Vens *et al*., 2019; Wouters and Begg, 2009; McMillan and Begg, 2002). The ATR-dependent G2 late checkpoint is an exception however, as ATR inhibitors preventing the activity of this checkpoint have been shown to cause radiosensitisation (Vens *et al*., 2019; Wouters and Begg, 2009; McMillan and Begg, 2002).

1.3.3 DNA Repair Pathways

Once cell cycle progression has been halted after the detection of DNA damage, repair of the damage can proceed (Bartek and Lukas, 2007). For DSBs, repair can occur through two main pathways, the homologous recombination (HR) pathway or the non-homologous end joining (NHEJ) pathway (Natarajan and Takeda, 2017; Brandsma and Gent, 2012; Jackson, 2002). HR requires a homologous stretch of DNA to act as a template for accurate repair, which the sister chromatid provides in the S and G2 phases (Natarajan and Takeda, 2017; Brandsma and Gent, 2012; Polo and Jackson, 2011).

The first step in the HR pathway, as shown in figure 1.15, is the resection of the broken DNA ends by the MRN complex in conjunction with c-terminal-binding protein (ctBP)-interacting protein (ctIP) and other exonucleases to create single-stranded regions needed for subsequent strand invasion (Natarajan and Takeda, 2017; Stracker and Petrini, 2011; Sartori *et al*., 2007). The single stranded regions are then coated with replication protein A (RPA) which removes secondary structures (Brandsma and Gent, 2012; Sugiyama *et al*., 1997). RPA is then replaced by Rad51 to form a nucleoprotein filament that searches the sister chromatid for the homologous sequence and, in conjunction with many other proteins, catalyses strand invasion (Brandsma and Gent, 2012; Sugiyama *et al*., 1997). A 'D-loop' is formed and synthesis of a new strand for each broken strand occurs using the intact sequence as a template (Vens *et al*., 2019; Brandsma and Gent, 2012; Wouters and Begg, 2009). The D-loop is then resolved by cutting the DNA at the crossover points (Holiday junctions) by resolvases (Vens *et al*., 2019; Brandsma and Gent, 2012; Wouters and Begg, 2009).

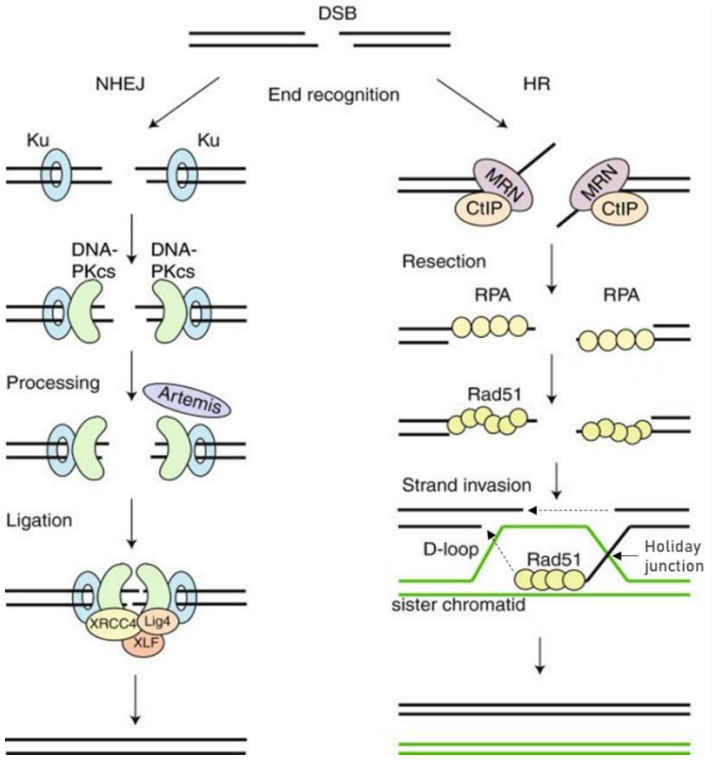

Figure 1.15: The homologous recombination (HR) and non-homologous end-joining (NHEJ) DNA repair pathways (Brandsma and Gent, 2012).

NHEJ involves joining two DNA DSB ends together without the need for homologous DNA sequences and can occur in all phases of the cell cycle (Brandsma and Gent, 2012; Lieber, 2008). It is a relatively simple repair pathway and proceeds faster than HR (Vens *et al*., 2019; Brandsma and Gent, 2012; Wouters and Begg, 2009). It is, however, less accurate than HR and can result in small insertions or deletions at the site of repair (Natarajan and Takeda, 2017; Lieber, 2008). As shown in figure 1.15, the first step in the NHEJ pathway is the binding of Ku70-Ku80 to both ends of the break which protects the ends from degradation by exonucleases and recruits DNA-PKcs to the damage site (Brandsma and Gent, 2012; Ciccia and Elledge, 2010). If necessary, the ends can be cleaned up or processed by nucleases, such as Artemis, or filled in by DNA polymerases, such as polymerase μ or polymerase λ, to create compatible ends more suitable for ligation (Lieber, 2010; Jeggo and Lobrich, 2005).

Finally, a ligation complex is formed consisting of DNA ligase 4 (LIG4), X-ray repair cross-complementing protein (XRCC) 4 and XRCC4-like factor (XLF) which joins the broken ends of DNA together (Vens *et al*., 2019; Wouters and Begg, 2009; Ahnesorg *et al*., 2006; Buck *et al*., 2006).

1.3.4 Cell Death and Mitotic Catastrophe

Following irradiation, the DDR system may forgo DNA repair and initiate cell death through several controlled processes including necrosis, autophagy, and apoptosis, as well as through mitotic catastrophe and premature senescence (Galluzzi *et al*., 2012; Kroemer *et al*., 2005; Okada and Mak, 2004). These processes can each be distinguished at the molecular and morphological level, and each may be a potential contributor to radiosensitivity in certain cells and in certain contexts (Wouters, 2019; Okada and Mak, 2004).

Necrosis

Necrosis was previously believed to be an inappropriate or accidental cell death mechanism that occurred under extremely unfavourable conditions such as extreme alterations in pH, ion imbalance and energy loss (Wouters, 2019; Galluzzi *et al*., 2012). Emerging research, however, has demonstrated that necrosis can occur in a highly controlled and genetically regulated manner, though the mechanisms are yet to be fully understood (Berghe *et al*., 2014; Galluzzi *et al*., 2012). Moreover, numerous forms of interconnected necrotic cell death processes exist including necroptosis, oxytosis, ferroptosis and pyroptosis (Berghe *et al*., 2014).

It is not clear how necrotic cell death is controlled by the cell following irradiation, though its frequency does differ between various cell types indicating the sensitivity of its activation may be controlled (Wouters, 2019).

Autophagy

Autophagy refers to a lysosome-dependent degradation process (Galluzzi *et al*., 2012; Mizushima, 2011). During autophagy, an isolation membrane is formed in the cytoplasm which grows and engulfs cytosolic cargo to form a cytoplasm-filled vacuole known as an autophagosome (Tait *et al*., 2014; Klionsky, 2007). The autophagosome fuses with a lysosome resulting in the degradation of the engulfed material into primary components that can be recycled to fuel metabolism (Wouters, 2019; Tait *et al*., 2014). It is a complex process controlled by more than 20 known genetic products, collectively known as autophagy-related (ATG) proteins, and has yet to be fully understood (Yu *et al*., 2018; Klionsky, 2007). Apoptosis and mitotic catastrophe are the two most important cell death mechanisms that occur following irradiation (Eriksson and Stigbrand, 2010).

Apoptosis

Apoptosis can occur via two key pathways (see figure 1.16) – the *extrinsic*, or receptor-mediated pathway, and the *intrinsic*, or mitochondria-mediated, pathway (Winter *et al*., 2014; Galluzzi *et al*., 2012; Orrenius *et al*., 2011). In the *intrinsic* pathway, cell death signals, such as those resulting from the DDR, can act directly or indirectly on the mitochondria. This causes the release of proapoptotic proteins from the mitochondrial intermembrane space into the cytosol (Orrenius *et al*., 2011; Taylor *et al*., 2008; Saelens *et al*., 2004; Cande *et al*., 2002).

These proapoptotic proteins may include cytochrome-c, apoptosis-inducing factor (AIF), second mitochondria-derived activator of caspase (Smac), Omi and endonuclease G (Orrenius *et al*., 2011; Saelens *et al*., 2004; Cande *et al*., 2002). The release of cytochrome-c results in the formation of a cytosolic apoptosome complex with apoptosis-activating factor-1 (APAF-1) and procaspase-9 in the presence of deoxyadenosine triphosphate (Orrenius *et al*., 2011; Saelens *et al*., 2004). Procaspase-9 is activated triggering the caspase cascade via procaspase-3 activation which results in the cleavage of numerous cytosolic and/or nucleic substrates and promoting cell death (Orrenius *et al*., 2011; Saelens *et al*., 2004; Degterev *et al*., 2003). Moreover, the release of Smac and Omi stimulates caspase activation by neutralising inhibitor of apoptosis proteins (IAPs) while AIF and endonuclease G are translocated to the nucleus to participate in chromatin condensation and fragmentation of DNA (Orrenius *et al*., 2011; Saelens *et al*., 2004).

The *extrinsic* pathway is initiated by the binding of an extracellular death ligand, generated by an immune cell for example, to a surface receptor such as cluster of differentiation (CD) 95 or tumour necrosis factor receptor (TNFR) 1 and followed by the creation of the death-inducible signalling complex (DISC) which results in the activation of procaspase-8 (Orrenius *et al*., 2011; Taylor *et al*., 2008; Riedl and Shi, 2004). In type I, or mitochondria-independent apoptotic cells, caspase-8 activates procaspase-3 cleaving of target proteins leading to apoptotic cell death (Orrenius *et al*., 2011). In type II, or mitochondria-dependent, apoptotic cells, cross-talk between the two pathways occurs (Orrenius *et al*., 2011; Fulda and Debatin, 2006).

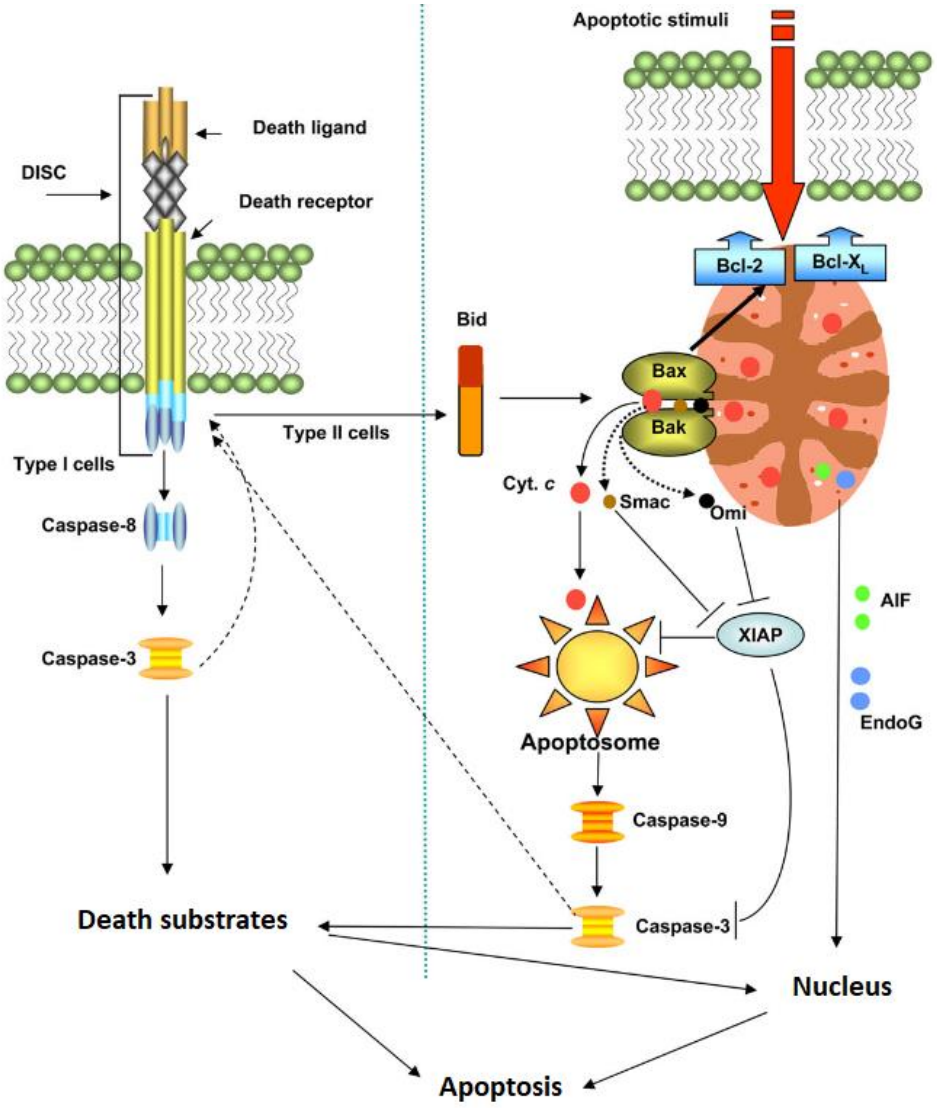

Figure 1.16: Extrinsic (left) and intrinsic (right) apoptotic pathways. Cell death signals initiate the intrinsic pathway causing the release of proapoptotic proteins from the mitochondrial intermembrane space into the cytosol which results in apoptosome complex formation. Caspase-9 is activated, triggering the caspase cascade causing cleavage of numerous cytosolic and/or nucleic substrates and promoting cell death. Smac and Omi are also released stimulating caspase activation by neutralising apoptosis proteins (IAPs) inhibitors while AIF and endonuclease G participate in chromatin condensation and DNA fragmentation. The extrinsic pathway is initiated by the binding death ligand to a death receptor followed by the creation of the death-inducible signalling complex (DISC) which results in the activation caspase-8 which activates caspase-3 cleaving of target proteins leading to apoptotic cell death. In type II apoptotic cells, caspase-8 cleaves Bid which induces the translocation, oligomerisation and insertion of Bax/Bak into the mitochondrial outer membrane. The release of several proteins results in apoptosome complex formation and activation of the caspase cascade (Orrenius *et al*., 2011).

Caspase-8 cleaves Bid (BH3-interacting domain death agonist) which induces the translocation, oligomerisation and insertion of Bax (Bcl-2-associated X protein) and/or Bak (Bcl-2 homologous antagonist/killer protein) into the outer membrane of the mitochondria (Orrenius *et al*., 2011; Fulda and Debatin, 2006). The release of several proteins, including cyctochrome-c, results in the formation of a cytosolic apoptosome complex leading to activation of the caspase cascade (Orrenius *et al*., 2011; Saelens *et al*., 2004).

A third, *caspase-independent*, apoptotic pathway has also been described as shown in figure 1.17 (Fan *et al*., 2003). This granzyme A (GZMA)-mediated pathway involves the delivery of GZMA into the cytoplasm through perforin-mediated pores (Orrenius *et al*., 2011). GZMA can then activate GZMA-activated DNase (GAAD) by cleaving SET (Su(var)3-9, enhancer-of-zeste and trithorax), HMG2 (3-hydroxy-3-methylglutaryl-coenzyme 2) and Ape1 (apurinic/apyrimidinic endonuclease 1) of the GAAD inhibitor complex located in the endoplasmic reticulum (Orrenius *et al*., 2011). Once activated GAAD translocates into the nucleus where it induces DNA strand breaks (Orrenius *et al*., 2011).

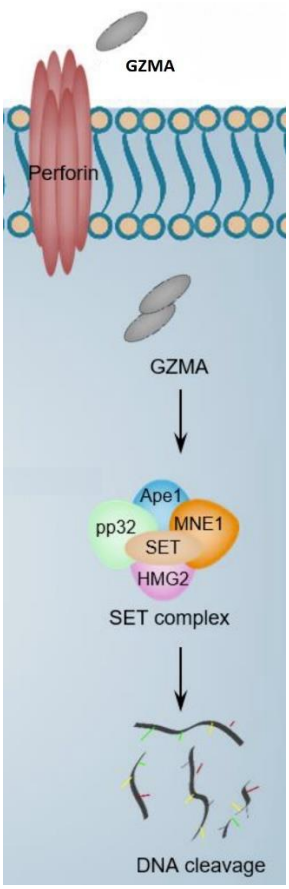

Figure 1.17: Granzyme A (GZMA)-mediated pathway. This pathway involves the delivery of GZMA into the cytoplasm via perforin-mediated pores which activates DNase by cleaving SET, HMG2 and Ape1 when then translocates into the nucleus where it induces DNA strand breaks (Eldeeb *et al*., 2018).

Mitotic Catastrophe

Mitotic catastrophe refers to cell death following, or resulting from, aberrant mitosis (Wouters, 2019; Castedo *et al*., 2004). Morphologically, it is associated with giant, multinucleated cell accumulation and the presence of micronuclei, nucleoplasmic bridges, nuclear buds and chromosome aberrations as shown in figure 1.18 (Wouters, 2019; Migliore *et al*., 2014, Driessens *et al*., 2003; Nabha *et al*., 2002). Furthermore, it is believed to occur when cells progress through mitosis in an inappropriate manner due to cells entering the phase with mis-repaired or unrepaired DNA damage (Wouters, 2019; Castedo *et al*., 2004).

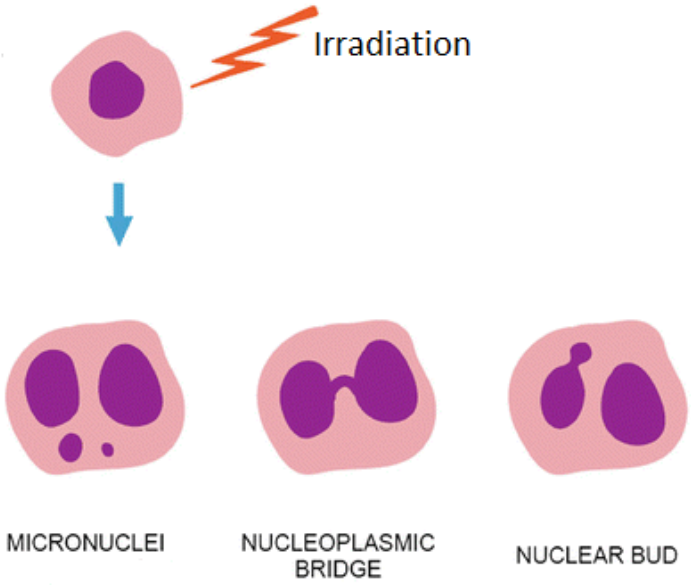

Figure 1.18: Multinucleated cells occurring from chromosomal damage and aberrant mitosis and the resulting nuclear anomalies (Migliore *et al.*, 2014).

Mitotic catastrophe is common in cells following irradiation as they frequently exhibit a range of different chromosome aberrations when they enter mitosis (Wouters, 2019). Death may occur from a physical inability to replicate and correctly separate genetic material or from the loss of genetic material, depending on the types of chromosome aberrations present (Wouters, 2019; Cogswell *et al*., 2000). Mitotic catastrophe may also serve to trigger apoptosis, senescence, autophagy or necrosis (independent of the initial radiation-induced damage) when cell fusion, polyploidy or cytokinesis failure results from the attempt to undergo mitosis (Castedo *et al*., 2004; Chu *et al*., 2004). The aforementioned G2 early and late checkpoints exist to prevent mitotic catastrophe and cells that show checkpoint activation defects or genetic alterations in cyclin-CDK complexes can enter mitosis prematurely and die via mitotic catastrophe (Wouters, 2019; Yoshikawa *et al*., 2001). This failure to prevent mitotic entry is believed to account for much of the increased radiosensitivity observed in ATM-deficient cells (Wouters, 2019).

Senescence

Cellular senescence is a process that enforces proliferative arrest on a cell (Childs *et al*., 2015). It is generally associated with the cellular aging process, but premature senescence can occur due to stresses such as radiation-induced DNA damage (Childs *et al*., 2015; Campisi and d'Adda di Fagagna, 2007). As with necrosis, the pathways governing this form of cell death are only partially understood but it appears to involve ATM-dependent activation of p53 which upregulates the CDKI p21 to prevent S-phase entry as previously discussed (Takahashi *et al*., 2006; Beauséjour *et al*., 2003; Alcorta *et al*., 1996). In this case however, the cell cycle arrest is permanent (Childs *et al*., 2015). These cells may then be removed by the immune system as they can invoke an inflammatory response through senescence-associated secretory phenotype protein secretion (Childs *et al*., 2015; Hoenicke and Zender, 2012).

1.3.5 Genomic Instability and Carcinogenesis

Genomic instability is another possible outcome following DNA damage initiated by ionising radiation and it is a hallmark of carcinogenesis (Nickoloff, 2017; Little, 2003). It is a non-targeted radiation effect that occurs in the progeny of irradiated cells and includes various cellular alterations such as chromosomal modification, micronucleus formation, reduced subcloning efficiency and changes in mutation rate (Maxwell *et al*., 2008; Sadikovic *et al*., 2008; Limoli *et al*., 1997). It is frequently associated with the loss of cell cycle control and modification to DNA repair processes but can occur due to a variety of cellular alterations (Little, 2003). Genomic instability most commonly occurs as a result of the mis-repair of endogenous or exogenous DNA damage, particularly following error prone NHEJ (Natarajan and Takeda, 2017; Nickoloff, 2017; Lieber, 2008; Little, 2003).

Some HR events can also cause genomic instability (Shen and Nickoloff, 2007; Weinstock *et al*., 2006). For example, a non-sister homologous sequence which is not 100 % identical may be used for HR resulting in the transfer of divergent sequence information to a broken chromosome, a process known as gene conversion (Nickoloff, 2002). The molecular mechanisms underpinning radiation-induced genomic instability are not well understood. Work by Newhauser and Durante (2011) and Little *et al*. (2008) suggests that ATM activation of cell survival pathways can result in cells with only partially repaired DNA damage being protected, resulting in genomic instability, the accumulation of mutations and eventually, late carcinogenesis. Further on-going work aims to identify the driver genes responsible for genomic instability which could potentially act as therapeutic targets (Ben-David, 2015).

1.4 Radiation Toxicity

Pelvic radiation toxicity, both gastro-intestinal (GI) and genito-urinary (GU), is an ongoing point of significant interest in the field of oncology and it is considered that this condition is untreatable until an understanding of the etiology and pathogenesis is understood (Durankus *et al*., 2020). The exposure of normal tissue surrounding a tumour to ionising radiation is inevitable in the normal course of RT and, as a result, all patients undergoing treatment will experience toxicity to some extent (West and Barnett, 2011). The mechanisms involved in the development of toxic side effects are complex, involving multiple pathways and molecular cross-talk (as shown in figure 1.19), and are not completely understood (Durankus *et al*., 2020; Kim *et al*., 2014). The first pathway involves the water radiolysis products which cause oxidative damage resulting in cell death and parenchymal and vascular tissue damage (Kim *et al*., 2014).

More recently however, two further pathways have been identified, involving (a) the production of pro-inflammatory cytokines and chemokines and (b) implicating the innate immune response in resultant tissue damage (Kim *et al*., 2014).

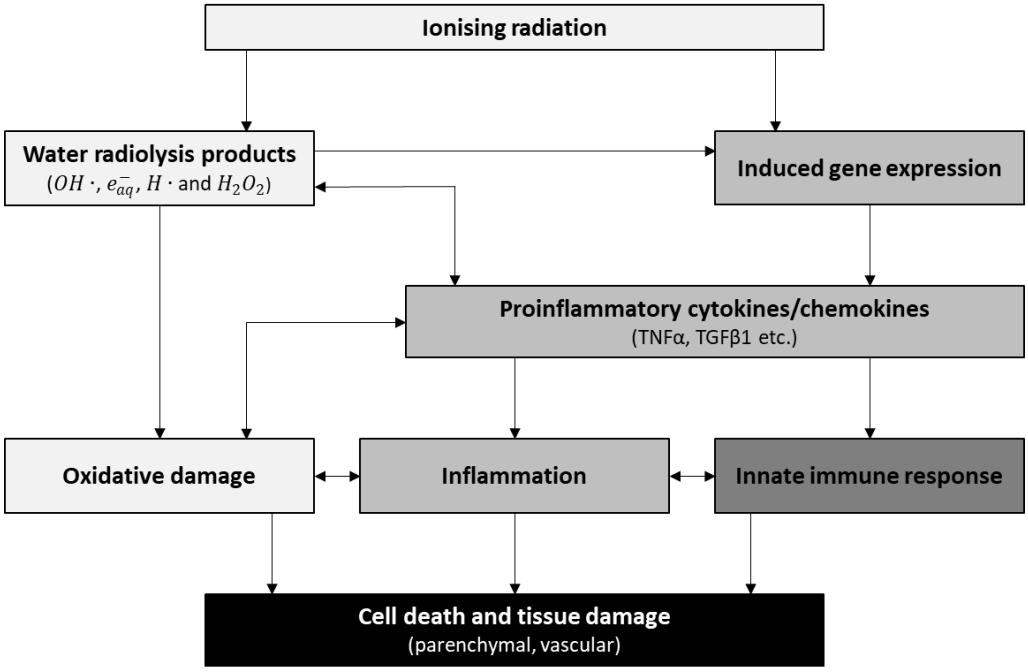

Figure 1.19: Pathways involved in the development of radiation toxicity (Kim *et al*., 2014).

Toxic side effects resulting from cell death and tissue damage typically occur locally in irradiated areas and are variable, numerous and site-dependent (West and Barnett, 2011). Moreover, the severity of toxic side effects varies from minor to severe and their duration varies from weeks (acute) to the remainder of the patients lifetime (chronic) (West and Barnett *et al*., 2011). In PCa treatment specifically, there is a risk of GI and/or GU toxicity.

1.4.1 Pathophysiology of GI and GU Toxicity

GI Toxicity

The epithelial lining of the GI tract is one of the most rapidly proliferating tissues in the body and the intestinal stem cells of the crypts found in this lining mediate the regeneration of intestinal and colonic tissues (see figure 1.20) (van der Flier and Clevers, 2009). Within hours after irradiation, the epithelial cells in the crypt may undergo apoptosis triggered by DNA damage leading to the shrinkage of the crypts (Dörr, 2019; Inagaki-Ohara *et al*., 2001; Merritt *et al*., 1994). When this occurs to a significant proportion of crypts in a region of the intestine, damage to the intestinal epithelium results due to inadequate replacement of surface epithelial cells (Shadad *et al*., 2013; Erickson *et al*., 1994).

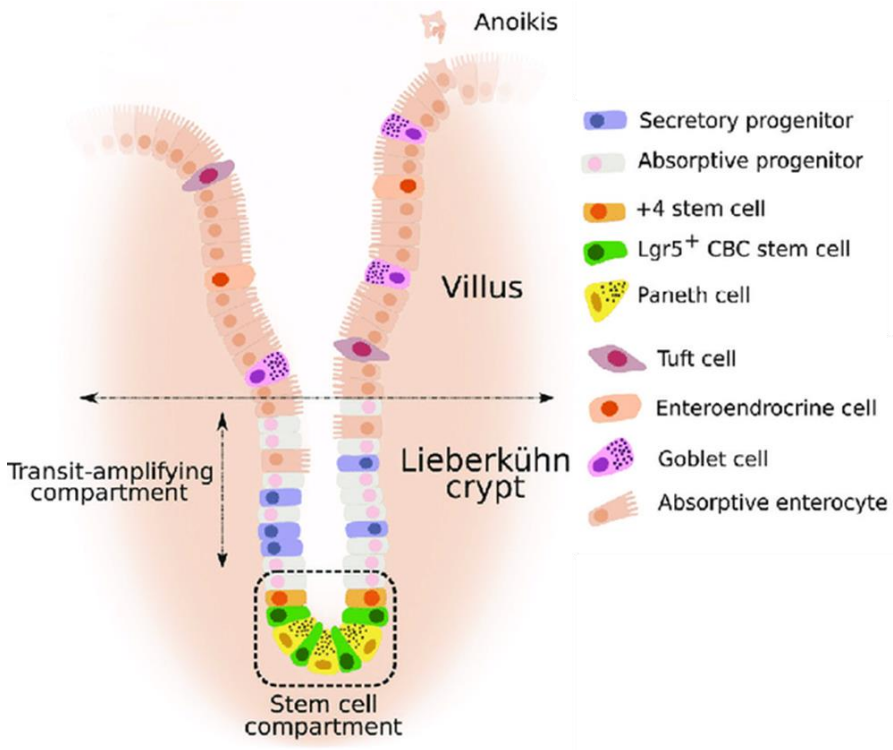

Figure 1.20: Intestinal epithelium schematic representation. Renewal of the intestinal epithelium is driven by stem cells at the bottom of the crypt which give rise to progenitor cells. These progenitor cells subsequently differentiate into mature cell types required for normal function (Gleizes *et al*., 2018).

Normal barrier function is therefore lost resulting in fluid loss and the exposure of normally sterile lamina propria to micro-organisms which trigger an acute inflammatory response associated with immune cell infiltration (Shadad *et al*., 2013; Erickson *et al*., 1994). The infiltration of immune cells leads to the loss of epithelial cells and the enzymatic degradation of the extracellular matrix of the lamina propria (Velcheti and Punekar, 2021; Rieder *et al*., 2007). After the cessation of RT, this acute inflammatory process continues but the crypts can start to regenerate through highly complex and poorly understood mechanisms (Leibowitz *et al*., 2021; Hovdenak *et al*., 2000). This leads to the restoration of the epithelial barrier which is then followed by the resolution of the inflammatory response (Leibowitz *et al*., 2021; Hovdenak *et al*., 2000). In some patients however, the inflammatory response becomes exaggerated leading to chronic adverse effects such as necrosis and rectal bleeding (Stone *et al*., 2003; Denham and Hauer-Jensen, 2002).

GU Toxicity

GU toxicity is more common than GI toxicity but the mechanisms of its pathophysiology are even less well understood (Cozma *et al*., 2021; Spratt *et al*., 2012). It results from bladder-tissue damage at multiple levels and early symptoms are believed to be caused by radiation-induced damage to the glycosaminoglycan (GAG) layer of the uroepithelium (Zwaans *et al*., 2016; Smit and Heyns, 2010). The GAG layer is a hydrophilic mucosal layer which acts as a protective barrier against noxious substances and solutes in urine (Payne *et al*., 2013; Smit and Heyns, 2010; Lavazzo *et al*., 2007). The loss of this protective layer results in urinary components infiltrating the bladder wall engendering further injury and inducing an inflammatory response (Jaal and Dörr, 2006).

In most cases these symptoms are largely self-resolved but, as with GI toxicity, certain individuals experience chronic adverse effects such as dysuria and reduced bladder contractility (Zwaans *et al*., 2016). Damage to the vasculature and smooth-muscle cells of the bladder results in an influx of fibroblasts and the deposition of collagen, which may be an influence (Zwaans *et al*., 2016; Liberman *et al*., 2014; Tibbs, 1997).

1.4.2 Acute and Late Toxic Outcomes

The severity of GI and GU toxicity can be graded using different methods, but the two most commonly used systems are the National Cancer Institute Common Terminology Criteria for Adverse Events (NCI-CTCAE) grading system and the Radiation Therapy Oncology Group (RTOG) grading system. Using the NCI-CTCAE system, 15 adverse events associated with GI and/or GU toxicity such as proctitis, rectal bleeding and dysuria, are considered and a grade of 0-4 is assigned for each adverse event depending on the severity of the signs and symptoms of the event (see Table 1.4).

The RTOG system however, assigns a grade of 0-4 based on the type and/or severity of adverse events as shown in Table 1.5 (Hunter *et al*., 2012; Cox and Stetz, 1995). Furthermore, toxic side effects are generally divided into acute and late effects (Hall and Giaccia, 2019). Acute toxic side effects arise during or within weeks of therapy are generally expected, but late toxic effects that arise several months to several years later are the main cause for concern (Barnett *et al*., 2009). Acute radiation toxicity results from the death of a large volume of cells and typically occurs within a few days or weeks of irradiation in rapidly proliferating tissues such as the GI tract and skin (Hall and Giaccia, 2019; Barnett *et al*., 2009). Acute toxic side effects are generally reversible and are not usually a dose-limiting factor (Barnett *et al*., 2009).

Table 1.4: Common Terminology Criteria for Adverse Events (v3.0).

Adverse Event	0	1	2	3	4
Fatigue	None	Mild fatigue over baseline	Moderate or causing difficulty performing some activities of daily living (ADL)	Severe fatigue interfering with ADL	Disabling
Diarrhoea	None	Increase of <4 stools per day over baseline; mild increase in ostomy output compared to baseline	Increase of 4-6 stools per day over baseline; IV fluids indicated <24 hrs; moderate increase in ostomy output compared to baseline; not interfering with ADL	Increase of ≥7 stools daily over baseline; incontinence; IV fluids ≥24 hrs; hospitalisation; severe increase in ostomy output compared to baseline; interfering with ADL	Life-threatening consequences (e.g. haemodynamic collapse)
Constipation	None	Occasional or intermittent symptoms; occasional use of stool softeners, laxatives, dietary modification or enema	Persistent symptoms with regular use of laxatives or enemas indicated	Symptoms interfering with ADL; constipation with manual evacuation indicated	Life-threatening (e.g. obstruction, toxic megacolon)
Rectal pain	None	Mild pain not interfering with function	Moderate pain; pain or analgesic interfering with function but not with ADL	Severe pain; pain or analgesics severely interfering with ADL	Disabling
Proctitis	None	Rectal discomfort, intervention not indicated	Symptoms not interfering with ADL; medical intervention indicated	Stool incontinence or other symptoms interfering with ADL; operative intervention indicated	Life-threatening consequences (e.g. perforation)
Rectal bleeding	None	Mild, intervention (other than iron supplements) not indicated	Symptomatic and medical intervention or minor cauterisation indicated	Transfusion, interventional radiology, endoscopic or operative intervention indicated; radiation therapy (i.e. haemostasis or bleeding)	Life-threatening consequences; major urgent intervention indicated
Urinary frequency/ urgency	Normal	Increase in frequency or nocturia up to 2x normal; enuresis	Increase >2x normal but <hourly	≥1x/hr; urgency; catheter indicated	-
Dysuria (pain on urination)	None	Mild pain not interfering with function	Moderate pain; pain or analgesic interfering with function but not interfering with ADL	Severe pain; pain or analgesic severely interfering with ADL	Disabling

Table 1.5: Gastrointestinal and genitourinary toxicity grading system developed by the Radiation Therapy Oncology Group (Cox and Stetz, 1995).

Grade	Gastrointestinal Toxicity	Genitourinary Toxicity
0	None	None
1	Mild diarrhoea, mild cramping, bowel movement 5 times daily, slight rectal discharge or bleeding	Slight epithelial atrophy, minor telangiectasia
2	Moderate diarrhoea and colic, bowel movement >5 times daily, excessive rectal mucus or intermittent bleeding	Moderate frequency of urination, generalized telangiectasia, intermittent macroscopic haematuria
3	Obstruction or bleeding requiring surgery	Severe frequency of urination and dysuria, severe generalized telangiectasia, frequent haematuria, reduction in bladder capacity (<150 cc)
4	Necrosis, perforation, fistula	Necrosis, contracted bladder (capacity <100 cm^3), severe haemorrhagic cystitis

Late radiation toxicity can be irreversible and life-threatening, and the risk of its occurrence is the main limiting factor in PCa treatment (Beaton *et al*., 2013; Barnett *et al*., 2012; Vasireddy *et al*., 2010). Furthermore, the extended time-frame of its development (>3 months) inhibits its titration against radiation dose (Ohri *et al*., 2012; Barnett *et al*., 2009; Cox and Stetz, 1995). Late toxic effects can have a severe impact on patients' health-related quality of life and lead to further complications such as second malignancies. Methods to prevent late radiation toxicity in PCa patients are thus critical as many of its symptoms can be more harmful than the initial tumour treated (Kim *et al*., 2014).

1.5 Assays of Clinical Radiosensitivity

Radiosensitivity is a broad term applied to individuals, organs, tissues and cells (Foray *et al*., 2012; West and Barnett, 2011). For the purposes of this study however, radiosensitivity is defined as the capacity of an irradiated individual, organ, tissue or cell to exhibit a specific toxic reaction to radiation exposure, as put forward by Foray *et al*. (2012). Radiosensitivity varies between cell types, as well as between cells from different individuals (West and Barnett, 2011). Moreover, individuals also differ in their intrinsic radiosensitivity, and this may be associated with cellular radiosensitivity and/or genetic instability (Foray *et al*., 2012; West and Barnett, 2011). The study of genetic syndromes related to mutations in the genes of DNA repair pathways such as ataxia telangiectasia, LIG4 syndrome and Nijmegen breakage syndrome (NBS), as shown in Table 1.6, provided early insight into individual variations in radiosensitivity (Foray *et al*., 2012; West and Barnett, 2011).

Table 1.6: Mutated genes involved in individual radiosensitivity identified from genetic syndromes.

Genetic Syndrome	Associated Mutated Gene	Reference
Ataxia telangiectasia	ATM	Jeggo and Lavin, 2009; Taylor *et al*., 1975
Ataxia telangiectasia-like disorder	Mre11	Matsumoto *et al*., 2011
LIG4 syndrome	LIG4	O' Driscoll *et al*., 2004
Nijmegen breakage syndrome	NBN	Christiakov *et al*., 2008

Other genes of interest in radiosensitivity include the downstream effectors of cellular response to radiation-induced damage discussed in section *1.3.1 DNA Damage Sensors*. Furthermore, as ROS are also important in cellular response to radiation-induced damage, genes which encode antioxidants involved in scavenging these ROS are also of interest and studies have shown altering antioxidant levels can change cellular radiosensitivity (Aykin-Burns *et al*., 2011; Kuptsova *et al*., 2008; Epperly *et al*., 2000).

In addition, genetic differences which predispose individuals to increased levels of ROS may predispose individuals to radiation toxicity (Kuptsova *et al*., 2008). Cytokines such as transforming growth factor beta 1 (TGFβ1) and tumour necrosis factor alpha (TNFα) which are upregulated in response to irradiation and involved in the development of fibrosis associated with radiation toxicity may also be of interest (Bentzen, 2006). However, thus far, there is little evidence for a direct role in either individual or cellular radiosensitivity (West and Barnett, 2011). Several studies have also investigated single nucleotide polymorphisms (SNPs) but with limited success (discussed in section *1.5.5 Radiogenomics*). To date, no markers of tumour response to treatment or predictors of late radiation toxicity are in clinical use. Research on various predictive assays has been ongoing for several years but the results are, thus far, conflicting.

1.5.1 Cell-based Assays

One of the earliest methods proposed for assessing cellular response to RT is the clonogenic, or cell survival, assay (Torres-Roca and Stevens, 2008). It involves the removal of cells from the tumour, placing them in a defined growth environment and testing their ability to produce a colony of 50 or more cells after irradiation at 2 Gy (Joiner, 2019; Torres-Roca and Stevens, 2008). The fraction of surviving cells following 2 Gy irradiation, referred to as SF2, is then determined by simply calculating the ratio of the plating efficiency of the irradiated sample against an unirradiated sample (Joiner, 2019). A cell survival curve (previously discussed in section *1.1.3 Low Dose Models for Cell Survival*) can then be plotted of the surviving fraction against radiation dose to estimate the sensitivity of cells to radiation dose (Joiner, 2019).

Studies by Björk-Eriksson *et al*. (2000) and West *et al*. (1997) have found SF2 to be an important correlate of clinical response to RT in cervical cancer and head and neck cancer, respectively. Conversely however, studies by Stausbøl-Gren and Overgaard, (1999) and Eschwege *et al*. (1997) have not found this to be the case in head and neck cancer. In addition, Taghian *et al*. (1993) did not find SF2 to be an important correlate of clinical response to RT in glioblastoma patients. Due to the invasive nature of tumour biopsies however, fibroblast and lymphocyte clonogenic assays have been investigated as alternatives. Early studies by Burnet *et al*. (1992) and Geara *et al*. (1992) using fibroblasts obtained from skin biopsies of breast cancer patients and head and neck cancer patients, respectively, found *in-vitro* cellular radiosensitivity was indicative of *in-vivo* normal tissue response. Fibroblast clonogenic assays however, take 2-3 months for radiosensitivity data to be obtained (West *et al*., 2001). Using lymphocyte clonogenic assays, on the other hand, radiosensitivity data can be obtained within 2-3 weeks (Dunne *et al*., 2003; West *et al*., 2001).

Studies by Ramsay and Birrell (1995) and West *et al*. (2001) using lymphocyte samples from breast cancer patients and cervical cancer patients, respectively, found the lymphocyte clonogenic assay correlated to clinical response to RT. Conversely however, a study by Geara *et al*. (1992) on head and neck cancer patients and breast cancer patients found no significant correlation between the lymphocyte clonogenic assay and clinical RT response. Despite some success and a reduced time frame compared to the fibroblast clonogenic assay, the lymphocyte clonogenic assay is still time consuming and there is a need to develop a more rapid method of measuring radiosensitivity in time to better plan individual RT treatment (Dunne *et al*., 2003).

An alternative to the clonogenic assay is the 3-(4,5 dimethylthiazol-2-yl)-2,5-diphenyl tetrazolium bromide (MTT) assay (Joiner, 2019; Buch *et al*., 2012). This assay is more commonly used to study chemosensitivity and drug toxicity but with careful attention to technical factors, it is reported to be capable of yielding a measure of radiosensitivity (Joiner, 2019; Buch *et al*., 2012). It is based on the production of dark-coloured formazan dye through the reduction of the tetrazolium salt MTT by metabolically active cells (Hansen and Bross, 2010). After an incubation period, crystals are formed by the water-insoluble formazan dye which can be dissolved in an organic solvent and quantified using a microplate reader (Buch *et al*., 2012). The absorbance readings obtained are related to the quantity of cells and thus provide the possibility of using the MTT assay as a cellular proliferation assay to assess cell growth following irradiation using cell survival curves (Buch *et al*., 2012; Price and McMillan, 1990). Studies by Slavotinek *et al*. (1994) and Wasserman and Twentyman (1988) found good correlation between the MTT assay and the clonogenic assay when assessing radiosensitivity in lymphoblastoid cell lines and murine solid tumours, respectively.

Moreover, Buch *et al*. (2012) found a strong correlation between the clonogenic assay and a multiple MTT assay approach using human non-small-cell lung carcinoma (NSCLC) cell lines, human glioblastoma cell lines and rat glioblastoma cell lines. In addition, Kim *et al*. (2008) showed that the MTT assay has potential for assessing clinical radiosensitivity in colon cancer cell lines. Conversely however, Banasiak *et al*. (1999) found a poor correlation between the MTT assay and the clonogenic assay when assessing radiosensitivity in a panel of human bladder cancer cell lines and a ureteral cell line.

Furthermore, the MTT assay is prone to variations due to cell density and interference from reducing compounds, elevated medium pH and light (Joiner, 2019; Riss *et al*., 2013). In addition, it is reported that the assay lacks specificity and mostly reflects growth inhibition and not a loss of cell viability (Mirzayans *et al*., 2017; Riss *et al*., 2013) rendering it highly prone to misinterpretation (Mirzayans *et al*., 2017). Another cell-based assay, which has shown great promise, is the radiation-induced T-lymphocyte apoptosis (RILA) assay. This assay involves culturing whole blood samples before and after irradiation followed by lysing of red blood cells and labelling of T-lymphocytes, typically with a CD4 or CD8 antibody and propidium iodide (PI) (Talbot *et al*., 2019). Flow cytometry is then used to define the labelled lymphocytes as apoptotic based on reduced PI staining (Talbot *et al*., 2019). A RILA score can then derived from the difference in apoptotic cells between irradiated and non-irradiated as a percent, with a lower score indicating greater radiosensitivity (Talbot *et al*., 2019).

One study by Ozsahin *et al*. (2005) found a strong association between RILA assay score and late toxic effects in a group of mixed cancer patients with CD8 T-lymphocytes proving more sensitive and more specific than CD4 T-lymphocytes. Moreover, another study by Schnarr *et al*. (2009) on PCa patients found the RILA assay to have some potential in identifying late radiation toxicity when using a total lymphocyte population but not when using CD4 or CD8 T-lymphocytes. Schnarr and colleagues observed that PCa patients with late toxic effects did not consistently display the lowest RILA scores. In contrast, studies by Azria *et al*. (2015) and Vandevoorde *et al*. (2016) on breast cancer patients found the RILA score of CD8 T-lymphocytes to be strongly predictive of late fibrosis and overall toxicity, respectively.

Moreover, another study by Veldwijk *et al*. (2019) found a strong association between the RILA score of CD4 T-lymphocytes and both fibrosis and telangiectasia in breast cancer patients. Conversely however, studies by Finnon *et al*. (2012) and Greve *et al*. (2012) showed no association between late toxic effects and the RILA assay in breast cancer patients and PCa patients, respectively. The RILA assay does show promise in predicting radiation response, but the current protocol is relatively slow, labour intensive and requires significant technical expertise.

1.5.2 Cytogenetic-based Assays

The micronucleus test (MNT) is another assay that shows some potential as a method for assessing radiosensitivity. Micronuclei (MN) are extra-nuclear bodies containing damaged whole chromosomes and/or damaged chromosome fragments formed during mitosis, but which were not incorporated into the nucleus (Luzhna *et al*., 2013; Encheva *et al*., 2012). MN may be induced by defects in cell repair machinery and the accumulation of DNA damage and chromosomal aberrations as a result of various clastogenic agents including ionising radiation (Luzhna *et al*., 2013; Encheva *et al*., 2012). The MNT determines the frequency of radiation-induced MN in cells to serve as an indicator of radiosensitivity (Encheva *et al*., 2012).

A study by Streffer *et al*. (1986) found this assay to be an effective measure of radiosensitivity in rectal tumours while a study by Sprung *et al*. (2005) using fibroblast and lymphoblast cell lines found the assay to be capable of detecting a significant proportion of radiosensitive cancer patients. Conversely, studies by Johansen *et al*. (1998) and Encheva *et al*. (2012) on fibroblasts in breast cancer patients and lymphocytes in gynaecological cancer patients, respectively, did not find the MNT to be an effective measure of radiosensitivity.

In addition, Vral *et al*. (2004) reported poor reproducibility when applying the MNT due to intra-individual variation and Joiner (2009) reported that the reliability of the assay is limited by the fact that diploid, polyploid and aneuploid cells tolerate genetic loss differently and MN formation varies as a consequence.

The G2 chromosomal radiosensitivity assay is another cytogenetic assay that has become popular for assessing clinical radiosensitivity. This assay involves culturing and irradiating cells to a low dose *in-vitro* before arresting the cells in metaphase for microscopic analysis of radiation-induced chromosomal aberrations. The number of aberrations are counted per 100 metaphases to provide a radiation-induced G2 score. Spontaneous aberrations are accounted for by subtracting the G2 score for an unirradiated control from the irradiated sample. The assay can be applied to any dividing cell population but it is most often applied to peripheral blood lymphocytes (Bryant *et al*., 2002). Moreover, this assay is faster than other techniques, taking only 3-5 days to obtain data, and good reproducibility can be achieved (Vral *et al*., 2004).

Studies by Poggioli *et al*. (2010), Howe *et al*. (2005) and Baeyens *et al*. (2002) on lymphocytes in breast cancer patients have shown that the G2 chromosomal radiosensitivity assay could be an appropriate prognostic method to define individual radiosensitivity. Conversely however, studies by Finnon *et al*. (2012) and Barber *et al*. (2000) on lymphocytes in breast cancer patients found this assay to have little predictive value for the risk of developing late side effects to RT. Furthermore, a study by Brzozowska *et al*. (2012) using the G2 chromosomal radiosensitivity assay on lymphocytes in PCa patients showed a poor correlation between G2 score and *in-vitro* radiosensitivity.

In addition, a major disadvantage of the G2 chromosomal radiosensitivity assay is the use of an arbitrary cut-off value to define radiosensitivity, such as the commonly used 90th percentile of radiation-induced G2 scores from a healthy population (Vral *et al*., 2004).

1.5.3 DNA Damage Assays

Assaying the levels of DNA damage-induced nuclear foci in response to ionising radiation has also been shown as a potential method for predicting radiosensitivity. These foci represent complexes of signalling and repair proteins which localise to DNA strand breaks (Hall and Giaccia, 2019; Podhorecka *et al*., 2010). The most commonly assayed proteins for foci formation are p53-binding protein 1 (53BP1) and γH2AX (Hall and Giaccia, 2019; Habash *et al*., 2017). As a predictive marker of radiosensitivity however, the phosphorylated histone, γH2AX, is more commonly used (Hall and Giaccia, 2019). The γH2AX DNA damage assay involves incubating cells with an antibody specific for γH2AX and then detecting binding of this antibody with a fluorescently-tagged secondary antibody.

Flow cytometry or fluorescent microscopy can then be used to locate and quantify the intensity of the fluorescent tag. A study by Bourton *et al*. (2011) found the γH2AX DNA damage assay to be a potentially robust and rapid method to predict acute and late radiation toxicity using lymphocytes from a variety of cancer patients. Moreover, studies by Chua *et al*. (2011) and Vandevoorde *et al*. (2016) on lymphocytes from breast cancer patients found a correlation between *in-vitro* radiosensitivity and late radiation toxicity using the γH2AX DNA damage marker.

Conversely, radiosensitivity studies using lymphocytes by Werbrouck *et al*. (2010) on a variety of cancer patients, Vasireddy *et al*. (2010) on gynaecological cancer patients, Finnon *et al*. (2012) on breast cancer patients and Brzozowska *et al*. (2012) on PCa patients found this assay to have a poor predictive performance.

1.5.4 Plasma-based Assays

Pro-inflammatory cytokines have been implicated in radiation-related tissue damage and inflammation and have shown some potential as an indicator of cell and tissue toxicity (Di Maggio *et al*., 2015; Christensen *et al*., 2009). Radiation exposure initiates a programmed response aimed at promoting tissue repair which involves the production and regulation of pro-inflammatory cytokines and research suggests that circulating cytokine levels may prove to be an important indicator of radiation toxicity (Stanojković *et al*., 2020). Studies by Stanojković *et al*. (2020) and Christensen *et al*. (2009) on prostate cancer patients found that patient profiles correlated with radiation-induced GU toxicity. Stanojković *et al*. (2020) observed increased levels of circulating interleukin-2 (IL-2) and interleukin-6 (IL-6) during RT and these elevated cytokine levels were associated with higher grades of acute GU toxicity.

Christensen *et al*. (2009) found that elevated levels of circulating IL-2, IL-6 and interferon-γ were associated with increased GI while RT-induced changes in levels of circulating interleukin-1 (IL-1) and interferon-γ were associated with increased GU toxicity. In contrast, a study by Bedini *et al*. (2018) on prostate cancer patients found that plasma levels of IL-1, IL-6, CXC motif chemokine ligand 8 (CXCL8), chemokine ligand 2 (CCL2) and pentraxin 3 (PTX3) were not significantly associated with acute or late GI toxicity. Bedini *et al*. (2018) did, however, find that plasma levels of TNFα were higher in patients exhibiting multiple late GI toxicity symptoms.

Furthermore, a study by Siva *et al*. (2014) on NSCLC found that plasma cytokine concentration levels were significantly different in patients who developed severe lung toxicity compared to those that did not. Specifically, severe lung toxicity was associated with depressed levels of interferon-inducible protein 10 (IP-10), monocyte chemoattractant protein-1 (MCP-1), Eotaxin and IL-6 post-irradiation. Lastly, a study by Stenmark *et al*. (2012) on lung cancer patients found that elevated levels of plasma interleukin-8 (IL-8) were significantly correlated with radiation-induced lung toxicity development while increased plasma levels of TGFβ1 were weakly correlated with radiation-induced lung toxicity. Plasma-based pro-inflammatory cytokine assays have shown some potential in determining radiation toxicity outcomes in lung and prostate cancer patients. Studies on cytokine assays however, have primarily focused on acute, as opposed to late, radiation toxicity. Moreover, these assays can be both labour intensive and time consuming.

The citrulline assay is another plasma-based assay. This assay measures L-citrulline concentration levels which has been shown in recent years to be a potential measure of intestinal toxicity. L-citrulline is a non-protein amino acid synthesized from glutamine by enterocytes primarily in the liver and the small intestine (Jäckel *et al*., 2021; Barzał *et al*., 2014; van de Poll *et al*., 2007; Crenn *et al*., 2003). L-citrulline synthesized by the enterocytes of the liver is metabolised locally in the urea cycle however, while L-citrulline synthesized by the enterocytes of the small intestine is absorbed into the bloodstream (Crenn *et al*., 2008; Windmueller and Spaeth, 1981). Once L-citrulline is released into the bloodstream, it is primarily metabolised to arginine in the kidneys (Crenn *et al*., 2003).

Therefore, as plasma L-citrulline derived from the small intestine reflects a reduction in intestinal enterocyte mass, it is considered a biomarker of intestinal toxicity (Crenn *et al*., 2003). Studies of humans with villous atrophy of the small intestinal mucosa, short bowel syndrome and coeliac disease found that plasma L-citrulline concentration is related to the severity of intestinal lesions (Basso *et al*., 2014; Jianfeng *et al*., 2005; Crenn *et al*., 2003; Crenn *et al*., 2000). In addition, several studies using pre-clinical non-rodent animal models (i.e. dogs, minipigs and non-human primates), found L-citrulline concentration to be a potential biomarker for small intestine toxicity (Shin *et al*., 2019; Gerou-Ferriani *et al*., 2018; Carr *et al*., 2017; Jones *et al*., 2015; Shim *et al*., 2014; Dossin *et al*., 2011).

A recent study by Jäckel *et al*. (2021) using dogs and rats, found that plasma L-citrulline concentration correlated well with histopathological findings such as enterocyte loss, villous atrophy and intestinal crypt necrosis, and with clinical signs such as diarrhoea and bloody faeces. It was noted however, that factors such as drug treatment may induce physiological alterations that influence L-citrulline metabolism and any interpretations of plasma L-citrulline concentration should be made in light of this (Jäckel *et al*., 2021). An earlier study by Onal *et al*. (2011) involving humans with prostate and endometrial cancer patients found that plasma L-citrulline concentration levels changed significantly during RT treatment within RTOG intestinal toxicity grades. Onal *et al*. (2011) found that plasma L-citrulline concentration was significantly reduced after 3 weeks of RT, treatment end, and 4 months post-RT. Positive correlations were found between plasma L-citrulline concentration and mean bowel dose, as well as between plasma L-citrulline concentration and intestinal toxicity (Onal *et al*., 2011). Another earlier study by Wedlake *et al*. (2008) involving patients with mixed pelvic malignancies found that plasma L-citrulline concentration was significantly decreased between baseline levels and 4-5 weeks of RT.

Furthermore, Wedlake *et al*. (2008) found, that within the Grade 2+ toxicity group, a subgroup of patients experienced a greater degree of toxicity and a significant decrease in plasma L-citrulline concentration was observed in this subgroup. Lastly, a study by Lutgens *et al*. (2004) involving patients with haematological malignancies had gut toxicity assessed using the citrulline assay. Lutgens *et al*. (2004) found that plasma L-citrulline concentration could be used as a quantitative parameter for intestinal damage and that the time course for plasma L-citrulline concentration agreed with the known kinetics of intestinal epithelial gut damage following RT and chemotherapy.

The findings of these studies advocate reasonably that plasma L-citrulline concentration is a marker of intestinal damage and a potential marker for intestinal toxicity. Further studies involving human subjects are required however, and thresholds need to be defined whereby a change in plasma L-citrulline concentration would indicate an unacceptable level of toxicity is occurring (Jäckel *et al*., 2021; Wedlake *et al*., 2008).

1.5.5 Radiogenomics

Radiogenomic approaches to predicting individual radiosensitivity have also been investigated but have yielded conflicting results. Early studies investigated the associations between SNPs, chosen based on their association with DDR, and late radiation toxicity (Herskind *et al*., 2016). SNPs are small alterations in DNA nucleotide sequences and have been shown to be potential indicators of late tissue response to RT. They can be detected using numerous methods such as the restriction fragment length polymorphism method or polymerase chain reaction-based methods. Studies by Andreassen *et al*. (2006), Andreassen *et al*. (2003), Quarmby *et al*. (2003) and Giotopoulos *et al*. (2007) on breast cancer patients found associations between late tissue response and SNPs in genes such as ATM, XRCC3, TGFβ1 and XRCC1, respectively.

A larger study by Andreassen *et al*. (2006) however, failed to find an association between late tissue response and SNPs in these 4 genes. In addition, a study by De Ruyck *et al*. (2006) found no significant association between late tissue response and SNPs in the gene TGFβ1. Due to the complex biological pathways involved in various adverse endpoints however, individual risk of developing late toxicity is likely determined by variation in multiple genes (Andreassen, 2010; Andreassen and Alsner, 2009). Thus, genome-wide association studies (GWAS) have been applied to find associations between common genetic variants and risk of late toxicity development (Herskind *et al*., 2016). GWAS involve examining SNPs across the entire genome and can involve the detection of hundreds or even thousands of SNPs at a time typically using DNA microarrays. One such study by Barnett *et al*. (2014) on prostate and breast cancer patients found numerous SNPs associated with various individual toxicity endpoints such as late faecal incontinence and urinary frequency as well as several associated with overall toxicity.

Another GWAS by Fachal *et al*. (2014) on PCa patients found evidence of an association between the TANC1 gene and overall toxicity with the exact SNP responsible unknown. Furthermore, a GWAS study on PCa patients by Kerns *et al*. (2016) identified two SNPs, associated with urinary frequency and decreased urinary stream, expressed in tissues adversely affected by pelvic RT including bladder, kidney, rectum and small intestine tissues. Another more recent PCa study by Oh *et al*. (2017) using a novel multi-SNP predictive model based on machine learning algorithms found that predictive models involving hundreds of SNPS which yield clinically useful RT risk stratification could be produced. Finally, a recent meta-analytical GWAS study on PCa patients by Kerns *et al*. (2019) found 3 SNPs associated with rectal bleeding, haematuria and decreased urinary stream furthering understanding of common genetic variants in radiation toxicity.

Despite these initial findings however, genomic approaches to predicting individual radiosensitivity are expensive and labour intensive. Moreover, most genomic studies aimed at predicting individual radiosensitivity have been severely underpowered to detect SNPs and while they have shown some potential they are extremely demanding in terms of sample size requiring multinational radiogenomic studies in very large cohorts (Kerns *et al*., 2019; Andreassen and Alsner, 2009; McCarthy and Hirschhorn, 2008).

1.6 Summary and Objectives

RT is used to treat approximately 50% of all cancer patients and the success of RT in tumour control depends not only on the total dose given, but the tolerance of the normal tissues surrounding the tumour. It is not known why some patients develop radiation toxicity and, currently, it is not possible to predict before treatment which patients will experience adverse effects as a result of RT. Thus, there is an unmet clinical need for a new test to identify patients at risk of radiation toxicity. The radiobiological assays discussed in section *1.5 Assays of Clinical Radiosensitivity* have shown some success in identifying patients at risk of radiation toxicity but have so far yielded conflicting results. In addition, these assays can be labour intensive, time-consuming, expensive, prone to misinterpretation and limited in reliability. Here, an approach based on an optical spectroscopic technique, Raman micro-spectroscopy, is proposed. The primary aim of this study was to determine if spectral variations in blood lymphocytes from PCa patients may suggest Raman spectral bands that could be used in future research to identify spectral features associated with radiosensitivity.

To achieve this aim, the following objectives were set forth:

1) Assess the ability of Raman micro-spectroscopy to identify patients with grade 0-1 and grade 2+ toxicity retrospectively.

2) Assess the ability of Raman micro-spectroscopy to predict radiation toxicity outcome in PCa patients.

3) Investigate the spectral difference between patients with grade 0-1 and grade 2+ toxicity.

4) Compare the spectral data with biological DNA damage assay, G2 chromosomal radiosensitivity assay and citrulline assay data.

In chapter 2, the theory behind Raman spectroscopy is introduced, in addition to the applications of Raman spectroscopy in the field of radiation biology. This chapter also introduces the methods used to analyse the data in the subsequent chapters. Chapter 4 outlines the application of Raman micro-spectroscopy to analyse lymphocytes taken *following* RT from PCa patients enrolled on the Cancer Trials Ireland ICORG 08-17 study in order to classify patients based on radiation toxicity grade. Chapters 5 and 6 outline the application of Raman micro-spectroscopy to analyse lymphocytes taken *prior to* commencing RT in order to predict radiation toxicity outcome in PCa patients enrolled on the Cancer Trials Ireland ICORG 08-17 study (in chapter 5) and in a separate cohort of PCa patients enrolled on the Northern Ireland Cancer Trials Centre SPORT study (in chapter 6). A summary of the findings from these studies is provided in chapter 7.

Chapter 2 - Raman Micro-spectroscopy and Data Analysis

As mentioned in section *1.5 Assays of Clinical Radiosensitivity*, research on predictive assays of normal tissue radiosensitivity has been ongoing for several years and has so far yielded conflicting results. The present study aims to take a new approach using Raman micro-spectroscopy which has advantages over cell-based and genomic assays in terms of minimal sample preparation, speed and cost. Moreover, there have been numerous studies showing the potential of Raman spectroscopy for disease screening and diagnosis with very promising results (discussed in section *2.6 Applications of Raman Spectroscopy in Radiobiology*).

2.1 The Raman Effect

When a molecule is irradiated with electromagnetic radiation (EMR) of energy $h\nu$, the energy may be transmitted, absorbed or scattered (Colthup *et al.*, 1990). Most of the energy that is scattered is via Rayleigh scattering, an elastic effect where the rotational and vibrational energies of the molecule remain unchanged and thus, the energy and the frequency of the scattered photon is equal to that of the incident photon (Colthup *et al.*, 1990). Another form of scattering known as Raman scattering may also occur (Long, 2002; Colthup *et al.*, 1990). This is an inelastic process where the rotational and vibrational energy of the molecule changes by an amount ΔE_m and, in order for energy to be conserved, the energy of the scattered photon must be different from that of the incident photon by an amount equal to ΔE_m (Colthup *et al.*, 1990). This can be expressed as:

$$h\nu_i - h\nu_s = \Delta E_m \qquad \textbf{(2.1)}$$

where $h\nu_i$ represents the incident photon and $h\nu_s$ represents the scattered photon (Colthup *et al.*, 1990).

If energy is gained by the molecule, ΔE_m will be positive resulting in Stokes scattering and if energy is lost by the molecule, ΔE_m will be negative resulting in anti-Stokes scattering (Long, 2002; Colthup *et al.*, 1990). Figure 2.1 shows an example of an energy level diagram for molecular scattering where the energy difference, ΔE_m, between the vibrational ground state $(n = 0)$ of the electronic ground state (E_0) and the first vibrational state $(n = 1)$ is represented by $h\nu_m$ (Collette and Williams, 2002; Colthup *et al.*, 1990).

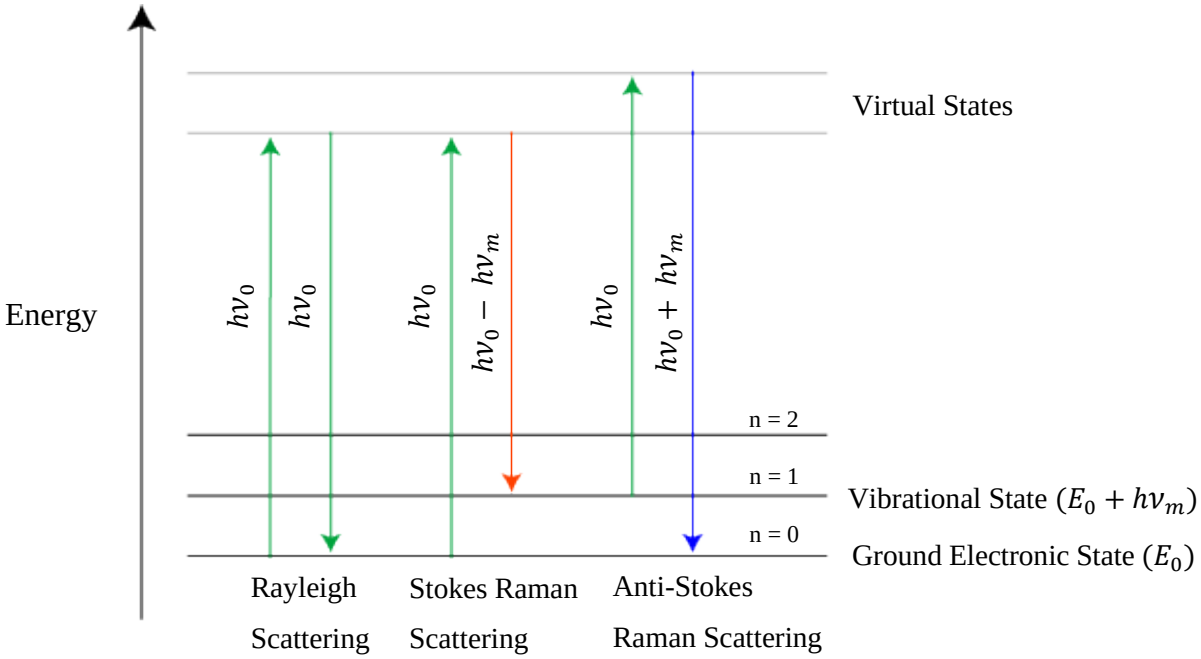

Figure 2.1: Diagrammatic representation of energy transfer in Rayleigh, Stokes and anti-Stokes scattering (Collette and Williams, 2002).

When a molecule in the ground vibrational state $(n = 0)$ of the ground electronic state (E_0) is irradiated with a laser at frequency ν_0 with energy $h\nu_0$, the molecule absorbs the photon energy and is excited to a virtual state (Collette and Williams, 2002; Colthup *et al.*, 1990). These virtual states represent an electronically polarised state resulting from the oscillating field of the beam as opposed to stable quantised energy levels (Collette and Williams, 2002).

The molecule loses energy as the virtual state decays and a scattered photon is emitted to make up for this energy loss (Collette and Williams, 2002; Colthup *et al.*, 1990). In the case of Rayleigh scattering, the energy of the emitted photon is equal to that of the incident laser beam ($h\nu_0$) and the molecule returns to its initial state (E_0 where $n = 0$ in this example). With Stokes Raman scattering, energy is absorbed from the incident beam by the molecule in the form of vibrational motion and thus the emitted photon energy upon decay of the virtual state is of lower energy ($h\nu_0 - h\nu_m$) than that of the incident beam (Collette and Williams, 2002; Colthup *et al.*, 1990). The molecule is therefore left possessing more vibrational energy than it did prior to irradiation by the laser beam and so it falls to the first excited vibrational level ($n = 1$) of the ground electronic state (Collette and Williams, 2002; Colthup *et al.*, 1990).

With anti-Stokes Raman scattering, the molecule is initially in the first excited energy level ($n = 1$) and is raised to a virtual state on absorption of the incident photon energy (Collette and Williams, 2002; Colthup *et al.*, 1990). Upon decay of this virtual state, the loss of energy is made up for by the emission of a scattered photon with higher energy ($h\nu_0 + h\nu$) than that of the incident beam (Collette and Williams, 2002; Colthup *et al.*, 1990). The molecule is therefore left possessing less vibrational energy than it did prior to irradiation by the laser beam and so it falls to the ground vibrational level ($n = 0$) of the ground electronic state (Collette and Williams, 2002; Colthup *et al.*, 1990). At or near room temperature, molecules populate the ground vibrational state ($n = 0$) more heavily than higher vibrational energy levels such as $n = 1$ (Collette and Williams, 2002; Colthup *et al.*, 1990).

Thus, a higher number of molecules exhibit Stokes Raman scattering than anti-Stokes scattering and this difference increases as the vibrational energy level spacing increases (Collette and Williams, 2002; Colthup *et al.*, 1990). For this reason, most Raman spectroscopy instruments, including the one used in the present study, record Stokes Raman scattering only (Collette and Williams, 2002).

2.2 Polarisability and the Raman Selection Rule

The Raman scattering phenomenon only occurs in molecules with the capacity to undergo a change in polarisability which can be viewed as the deformability of the electron cloud in a molecule resulting from the interaction of light and matter (Ferraro *et al.*, 2003; Colthup *et al.*, 1990). It is a material characteristic that depends on the nature and structure of the molecular bonds (Ferraro *et al.*, 2003). When placed in an electric field, electrons are displaced relative to the protons and this separation of charge is referred to as an induced dipole moment (Colthup *et al.*, 1990). The strength of this induced dipole moment (μ) is given by:

$$\mu = \alpha E \qquad \textbf{(2.2)}$$

where α is the polarisability and E is the strength of the electric field of the applied EMR (Larkin, 2011; Colthup *et al.*, 1990). This external electric field varies with time t and oscillates at frequency ν with amplitude E_0 (Willock, 2009; Colthup *et al.*, 1990). This can be given as:

$$E = E_0 \cos 2\pi\nu t \qquad \textbf{(2.3)}$$

This external oscillating electric field will induce an oscillating dipole moment in the molecule, the frequency of which will be the same as that of the electric field (Willock, 2009; Colthup *et al.*, 1990). This is given as:

$$\mu = \alpha E_0 cos 2\pi \nu t \quad \textbf{(2.4)}$$

The polarisability of a molecule depends on its geometry and elemental composition and thus the polarisability will itself be dependent on time and change as the molecule vibrates (Willock, 2009; Colthup *et al.*, 1990). In the case of a diatomic molecule for example, the molecular shape is compressed and extended during vibration and as the electron cloud is not identical at extremes of the vibration, an alteration in polarisability occurs (Colthup *et al.*, 1990). For small changes, the polarisability can be expanded using a Taylor series:

$$\alpha = \alpha_0 + \frac{\partial \alpha}{\partial Q} Q + \ldots \quad \textbf{(2.5)}$$

where α_0 is the equilibrium polarisability, $\partial\alpha/\partial Q$ is the derivative of the polarisability with respect to Q, a normal coordinate which, in the case of a diatomic molecule, would be $r - r_e$ (Colthup *et al.*, 1990). The normal coordinate Q also periodically varies and this can be given as:

$$Q = Q_0 cos 2\pi \nu_0 t \quad \textbf{(2.6)}$$

where Q_0 is a constant (the maximum value for Q) and ν_0 is the frequency of the normal coordinate vibration (Willock, 2009; Colthup *et al.*, 1990).

Combining equations 2.5 and 2.6 yields:

$$\alpha = \alpha_0 + \frac{\partial \alpha}{\partial Q} Q_0 cos 2\pi \nu_0 t \quad \textbf{(2.7)}$$

and substituting this value for α into equation 2.4 produces:

$$\mu = \alpha_0 E_0 cos2\pi\nu t + \frac{\partial\alpha}{\partial Q} Q_0 E_0 (cos2\pi\nu_0 t)(cos2\pi\nu t) \quad \textbf{(2.8)}$$

Finally, a standard trigonometric identity can be applied:

$$cosA\ cosB = \frac{1}{2}[\cos(A - B) + \cos(\mathrm{A} + \mathrm{B})] \quad \textbf{(2.9)}$$

This allows equation 2.8 to be written as:

$$\mu = \alpha_0 E_0 cos2\pi\nu t + \frac{\partial\alpha}{\partial Q}\frac{Q_0 E_0}{2}[cos2\pi(\nu - \nu_0)t + cos2\pi(\nu + \nu_0)t] \quad \textbf{(2.10)}$$

It can be seen from equation 2.10 that the induced dipole moment (μ) oscillates at the component frequencies ν, $\nu - \nu_0$, and $\nu + \nu_0$ giving rise to, respectively, Rayleigh, Stokes and anti-Stokes scattering (Willock, 2009; Colthup *et al.*, 1990). It can also be seen that Stokes and anti-Stokes Raman scattering depend on a change in polarisability ($\partial\alpha/\partial Q$). If a molecular vibration results in no change in polarisability, $\partial\alpha/\partial Q = 0$ then no Raman scattering is observed (Larkin, 2011; Willock, 2009; Colthup *et al.*, 1990) giving rise to the Raman selection rule:

$$\frac{\partial\alpha}{\partial Q} \neq 0 \quad \textbf{(2.11)}$$

When a change in polarisability occurs during vibration, so $\partial\alpha/\partial Q \neq 0$, the frequency of the incident light is shifted by plus or minus the molecular vibration frequency (Willock, 2009; Colthup *et al.*, 1990). For anti-Stokes Raman scattering, there is an increase in frequency while for Stokes Raman scattering there is a decrease in frequency and measuring this difference in frequency gives the vibrational frequency of a molecular bond (Willock, 2009; Keller and Mahadevan-Jansen., 2006).

As a result of this occurrence, Raman spectroscopy can be used to identify an extensive range of molecules and to characterise the molecular make-up of biological samples such as biofluids, cells and tissues, by furnishing their spectroscopic fingerprint (Auner *et al*., 2018; Kong *et al.*, 2015; Read and Whiteley, 2015; Schie and Huser, 2013). Moreover, biochemical alterations in cells and tissues that may arise from, or give rise to, a disease or other debilitating condition, can result in prominent changes in a Raman spectrum (Auner *et al*., 2018; Kong *et al.*, 2015). Thus, the ability of Raman spectroscopy to detect such biochemical changes, gives rise to its potential as a prognostic and diagnostic tool (Auner *et al*., 2018; Kong *et al.*, 2015).

2.3 Raman Micro-spectroscopy Instrumentation

For the present study, all Raman spectroscopic measurements were taken using a Horiba Jobin Yvon LabRam HR800 micro-spectroscopy system. Figure 2.2 shows a schematic diagram of this system, which can accommodate both an internal and external laser source. Lasers are ideal sources of excitation for Raman spectroscopy as they are highly monochromatic and extraneous lines are much weaker than other excitation sources (Ferraro *et al.*, 2003). Moreover, they have small diameters and can be focused on sample areas as small as ~2 μm making them ideal for analysing cells (Ferraro *et al.*, 2003). For the present study, an external solid-state diode excitation laser source was used. The external laser light enters the spectrometer via a pinhole opening before it passes through a clean-up filter that permits only the laser line of interest (660 nm in this case) to enter the rest of the system (Ferraro *et al.*, 2003; Pelletier, 1999). The laser light is then deflected by a system of mirrors and through a wheel filter that is used to adjust the power level of the laser (Sil *et al.*, 2017).

Another mirror then reflects the laser light through a beam splitter and an objective lens which focuses it onto the sample. The beam splitter can also be used for illumination of the sample through the objective lens for bright-field microscopic imaging using a mounted camera.

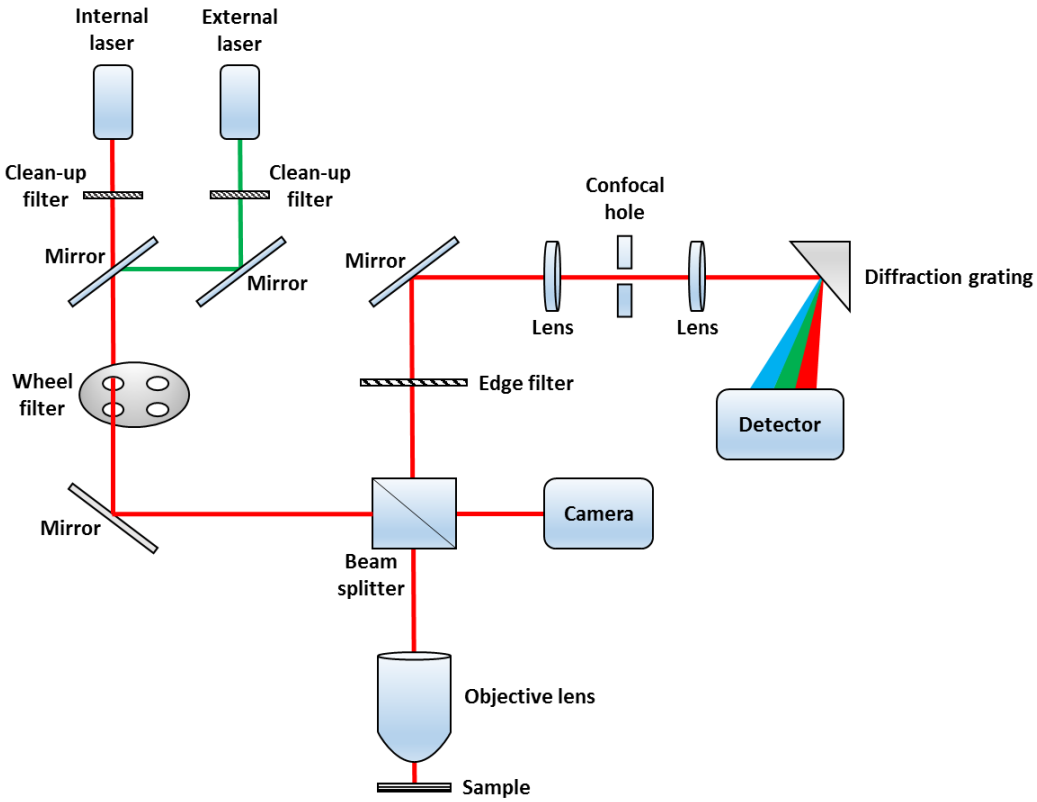

Figure 2.2: Schematic diagram of the Horiba Jobin Yvon LabRam HR800 system.

Back-scattered light from the sample enters the spectrometer through to the edge filter. The edge filter blocks Rayleigh scattered light, allowing only Raman scattered light to pass through to the rest of the system (Weeks and Huser, 2010). A mirror deflects this Raman scattered light through a lens which guides the light through an adjustable confocal pinhole aperture that controls depth spatial resolution and blocks any scattering that occurs outside the desired depth of focus (Wu *et al.*, 2011; Pelletier, 1999).

The scattered light then passes through another lens which focuses the light onto a diffraction grating. This diffraction grating splits the light into its constituent wavelengths, and these are directed onto a thermoelectrically-cooled charge-coupled device (CCD) array detector. This CCD detector is a silicon-based semiconductor comprised of an array of photosensitive elements (Ferraro *et al*., 2003). These elements detect photons and generate photoelectrons, storing them as small charges (Ferraro *et al*., 2003; Adar, 2001). These charges are converted into measurable voltages which are then digitised and transferred to the control computer in the form of a spectrum (Ferraro *et al*., 2003; Adar, 2001). In the resulting spectrum, the x-axis is the wavenumber ($\tilde{\nu}$ in units of cm^{-1}) of the Raman shift (i.e. which is related to the energy difference between the incident light and the scattered light) and the y-axis is the intensity of the scattered light.

2.4 Raman Spectral Pre-processing

Pre-processing of Raman spectral data is important to improve the accuracy and stability of measurements for later analysis (Shaver, 2001). The most commonly applied pre-processing steps include smoothing and denoising, baseline and background subtraction and normalisation (Shaver, 2001). One of the most common and difficult issues in Raman spectral analysis is the low signal-to-noise ratio (SNR) obtained (Lin *et al*., 2012; Shaver, 2001). When the SNR is low, unwanted spectral features may engulf the characteristic sample peaks, making them difficult to detect and unsuitable for subsequent analysis (Lin *et al*., 2012; Shaver, 2001). Smoothing a spectrum using an appropriate filter can improve the SNR of the spectrum and enhance the extraction of a biochemical fingerprint for the sample (Shaver, 2001). In the present study, a Savitzky-Golay (SG) filter was used to smooth and denoise spectra.

A SG filter is a popular choice for smoothing and denoising spectra as it is capable of preserving the peaks and valleys of a spectrum while filtering out unwanted high frequency noise (see figure 2.3) (Schafer, 2011; Awal *et al*., 2011).

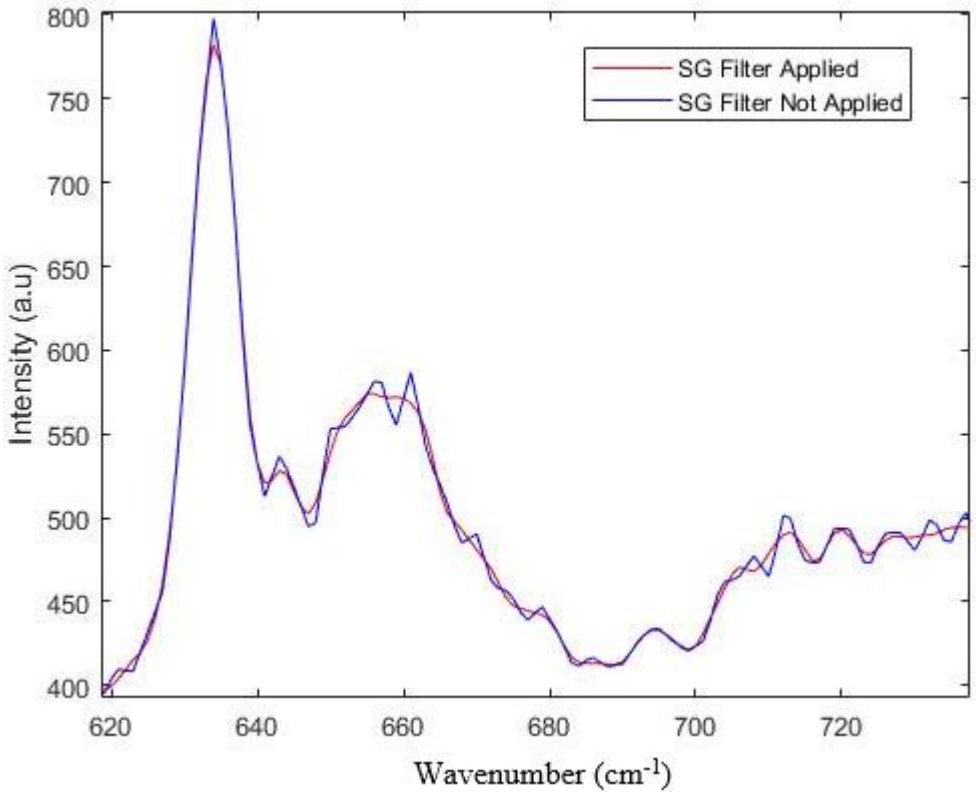

Figure 2.3: Region of a Raman spectrum with (red) and without (blue) a Savitzky-Golay (SG) filter applied (window size: 15; polynomial degree: 5).

Application of a SG filter involves fitting a small window of wavenumbers to a polynomial of an appropriate degree using a least square technique to create a digital filter (Villarroel *et al*., 2011). A small window size results in poor smoothing, however, and a large window size can result in degradation of spectral resolution causing weak spectral features to be distorted (Chen *et al*., 2014). Thus, there is a trade-off between smoothing and spectral resolution which must be considered when choosing the window size and polynomial degree (Chen *et al*., 2014).

Another common issue in Raman spectral analysis is the background contribution which can make it difficult to distinguish the presence and position of bands (Shaver, 2001). Backgrounds in Raman spectroscopy can arise from luminescent processes, such as fluorescence or phosphorescence, from non-laser-induced emissive processes, such as those of room light, and/or non-analyte sources, such as substrates and instrument optics (Shaver, 2001). Optimising experimental conditions can significantly reduce background contributions but many Raman spectra still contain some level of background contribution (Shaver, 2001). Numerous methods exist for background removal but one common approach, as used in the present study, is the rubberband baseline correction as shown in figure 2.4.

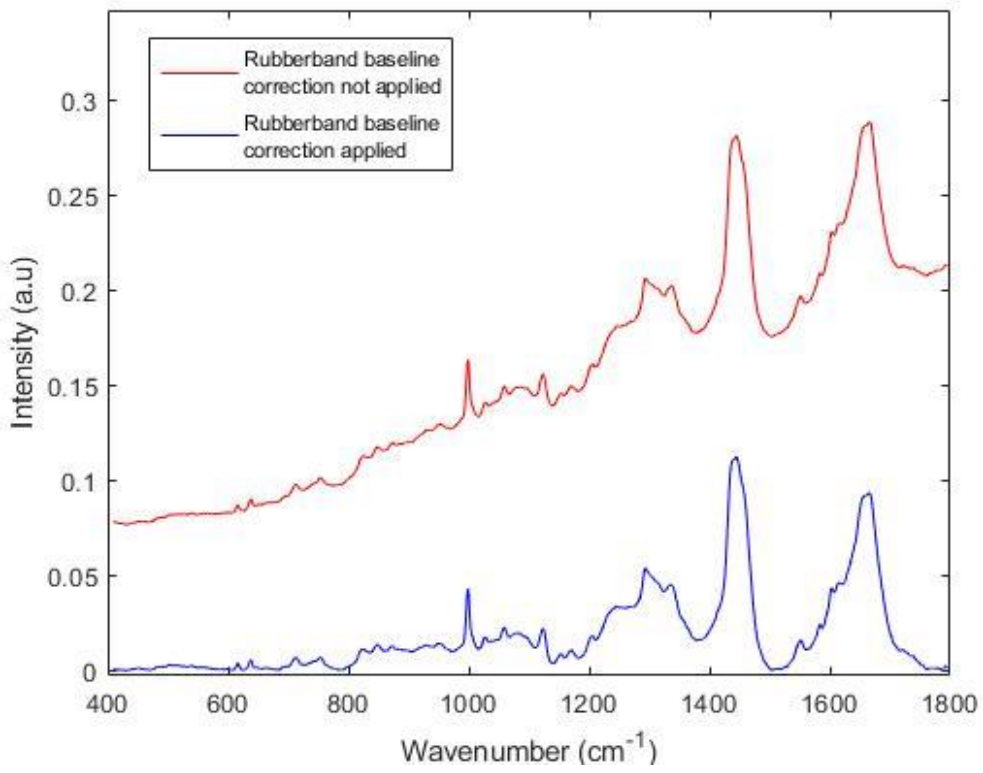

Figure 2.4: Raman spectrum with (blue) and without (red) rubberband baseline correction.

This function identifies the convex hull of the signal using a set of local minima throughout the spectrum and creates a baseline by connecting these minima using straight lines (Liu *et al*., 2017; Wartewig, 2003). Any points not lying on the baseline are discarded and a smoothed baseline is created (Baek *et al*., 2015; Wartewig, 2003). Another major source of systematic error in Raman spectral analysis arises from total intensity variations (Shaver, 2001). Variations in various sample properties, such as opacity and density, can result in changes in observed intensity (Shaver, 2001). Thus, normalisation of a spectrum to some known or constant value can be essential for more stable analysis and the detection of small changes in spectral variables (Rencher and Christensen, 2012; Shaver, 2001).

Normalisation is a scaling process where each variable is divided by a scaling factor which is different for each variable (Rencher and Christensen, 2012; van den Berg, 2006). One commonly applied scaling factor is the unit-vector length which was used in the present study. Unit-vector length normalisation involves dividing the components of a vector by its length and it has shown to be effective for Raman spectrum normalisation (van den Berg, 2006; Shaver, 2001). In addition to the above pre-processing techniques, it is recommended, where possible, to use a multiline spectrum measurement from a reference sample to adjust for non-linearities of the instrument calibration (Byrne *et al*., 2011). Typically used reference samples for this purpose include neon light, poly(ethylene terephthalate) and 1,4-Bis (2-methylstyryl) benzene (Liu *et al*., 2016). The Raman spectra from these samples contain numerous sharp peaks at well-known wavenumber locations. A polynomial function can be used to fit the Raman spectrum peak positions and adjust the wavenumber positions of sample spectra to the reference, producing a wavenumber calibrated spectrum.

Figures 2.5 and 2.6 show a Raman spectrum pre- and post-calibration, respectively, with a multiline spectrum measurement from a 1,4-Bis (2-methylstyryl) benzene sample.

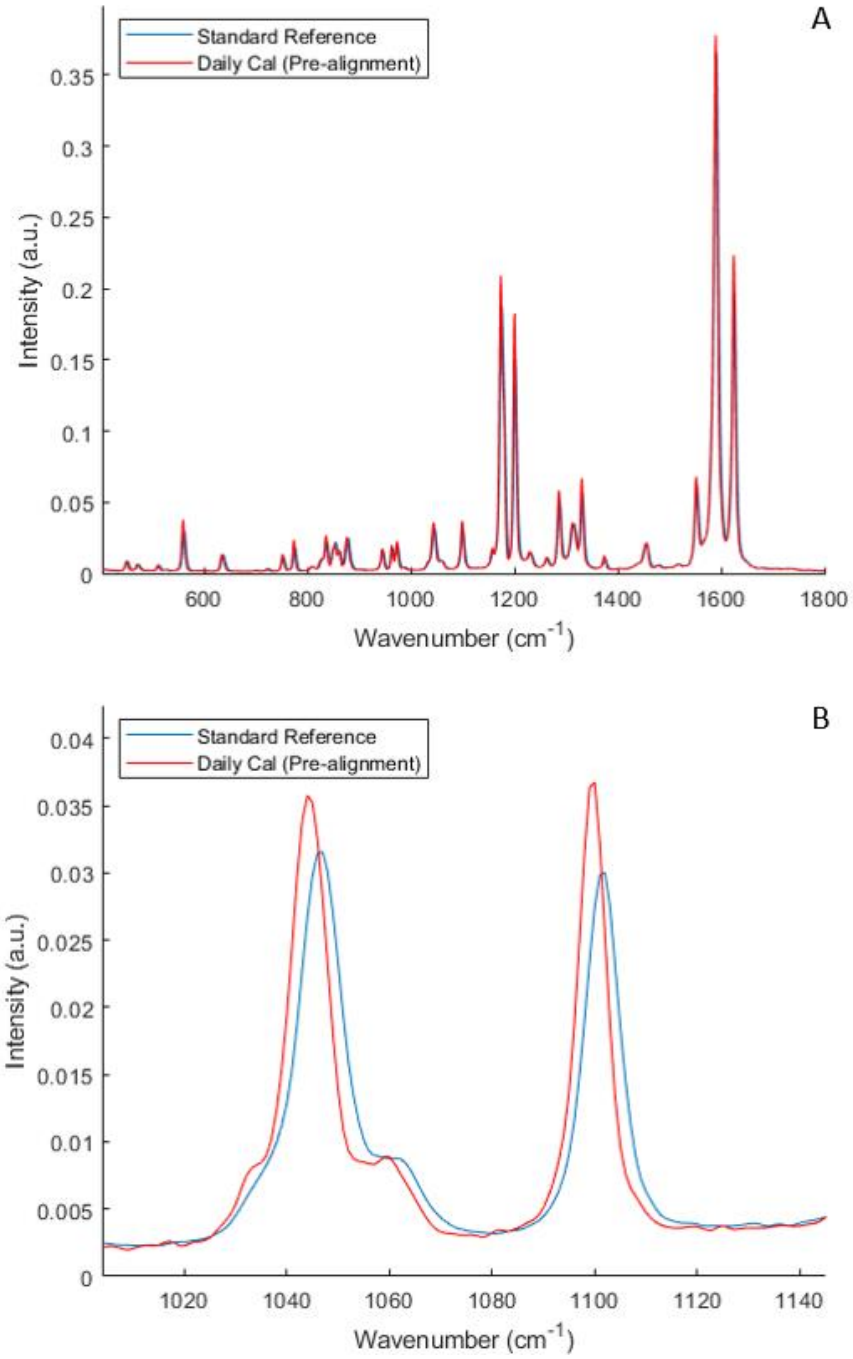

Figure 2.5: Daily 1,4-Bis (2-methylstyryl) benzene calibration spectrum pre-alignment using a standard reference spectrum of 1,4-Bis (2-methylstyryl) benzene. A – Low wavenumber region, B – Close-up of peaks at 1046 and 1102 cm^{-1} highlighting misalignment.

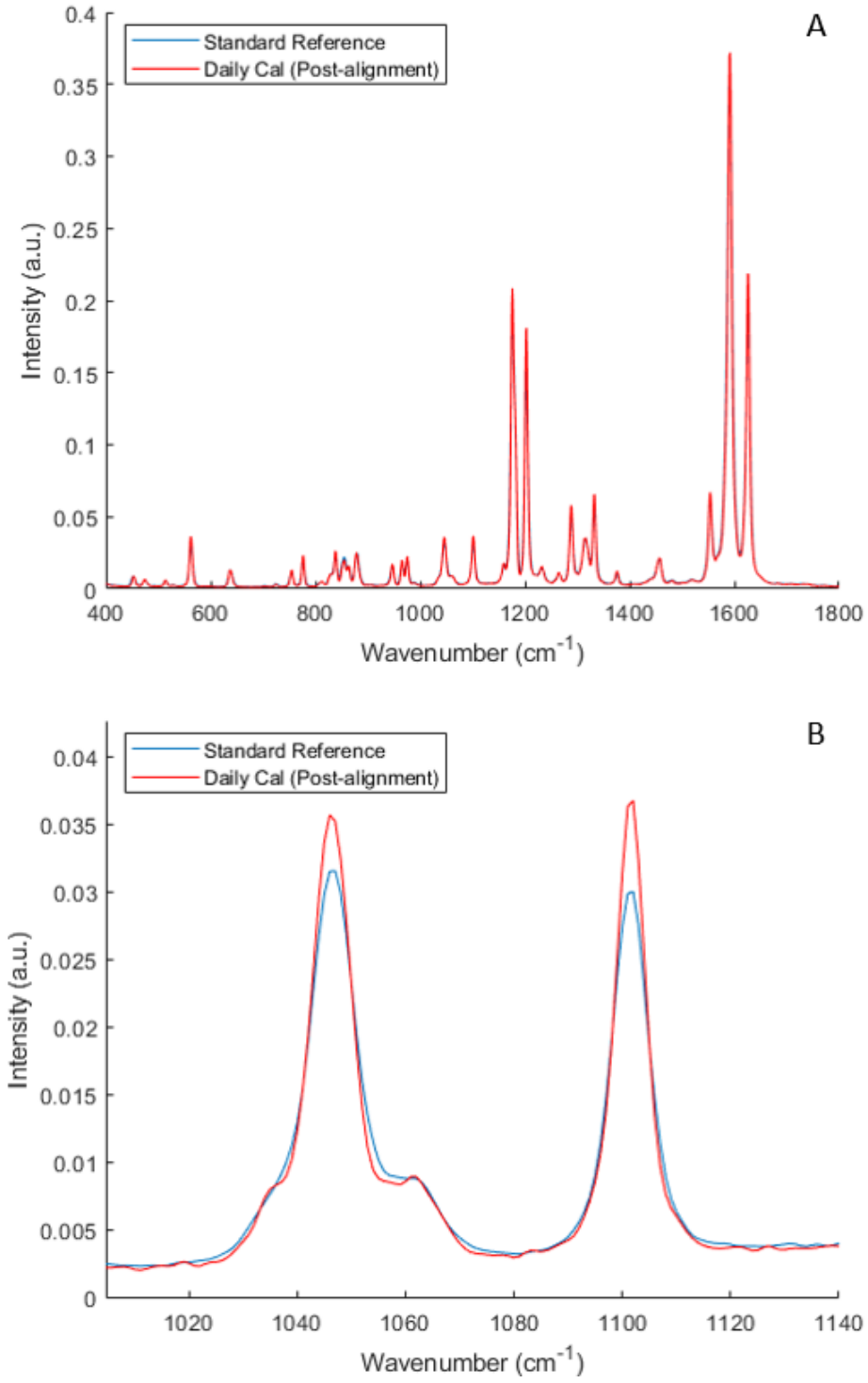

Figure 2.6: Daily 1,4-Bis (2-methylstyryl) benzene calibration spectrum post-alignment using a standard reference spectrum of 1,4-Bis (2-methylstyryl) benzene. A – Low wavenumber region, B – Close-up of peaks at 1046 and 1102 cm^{-1} highlighting alignment.

Furthermore, it is also recommended, where possible, to adjust for intensity variations to reduce systematic error in Raman spectral analysis (Butler *et al*., 2016; Choquette *et al*., 2007). This is most commonly achieved by recording a spectrum of a broadband intensity standard such as those provided by the National Institute of Standards and Technology (NIST) (Butler *et al*., 2016; Choquette *et al*., 2007). The intensity correction procedure can be described by the following equation:

$$S_{Corr}(\Delta v) = C_{SRM}(\Delta v) \times S_{Meas}(\Delta v) \quad \textbf{(2.12)}$$

where $S_{Corr}(\Delta v)$ is the intensity-corrected spectrum, $C_{SRM}(\Delta v)$ is the correction curve, $S_{Meas}(\Delta v)$ is the Raman measurement to be corrected and (Δv) is the wavenumber in units of Raman shift (cm^{-1}). The correction curve can be obtained by dividing a measured spectrum of the reference material by a 'true' spectrum of the reference material provided by NIST.

2.5 Multivariate Data Analysis

As biological datasets typically have more variables than samples (known as the 'small n large p problem') and as Raman spectra are comprised of a high number of overlapping features, multivariate statistical analysis and statistical learning algorithms are necessary for summarizing and modelling the resulting data. There are a wide range of multivariate analysis and statistical learning techniques available but those chosen for the present study are well established and have been shown to work well in past research on similar data.

2.5.1 K-means Cluster Analysis

K-means cluster analysis is a partitioning technique used to find cluster and cluster centres in an unlabelled dataset (Wehrens, 2011; Hastie *et al*., 2009). The *K*-means algorithm consists of two steps, and it is initialised by choosing a random number of cluster centres (Wehrens, 2011; Hastie *et al*., 2009). The following two-steps are then iterated:

1) An object's distance to all cluster centres is calculated and it is assigned to the closest centre (e.g. based on Euclidean distance). This is done for all objects.

2) The cluster centres are replaced by the computed means, or centroids, of all the objects assigned to them.

Once all objects have been assigned to a cluster, each object is examined to see if it is closer to the centroid of another cluster than it is to the centroid of the cluster to which it is initially assigned (Wehrens, 2011; Hastie *et al*., 2009; Rencher, 2002). If this is found to be the case, the object is moved to the new cluster and the two cluster centroids are re-calculated (Wehrens, 2011; Hastie *et al*., 2009; Rencher, 2002). These steps are iterated until convergence, where no further improvement is possible (Wehrens, 2011; Hastie *et al*., 2009; Rencher, 2002). The *K*-means algorithm is sensitive to the initial choice of cluster centre numbers, and it may be necessary to repeat the process with another number of cluster centres (Rencher, 2002). If convergence is achieved extremely slowly, or different choices of cluster centre number produce significantly different final clusters, this may suggest that there are no natural clusters within the data (Rencher, 2002).

The *K*-means partitioning algorithm can also be used to improve on other techniques such as hierarchical cluster analysis or principal component analysis (Rencher, 2002). One of the aforesaid techniques is first used and the number of resulting clusters determines the number of cluster centres to choose for the *K*-means analysis (Rencher, 2002). In the present case, principal component analysis was used to determine the number of cluster centres to initialise the *K*-means algorithm.

2.5.2 Principal Component Analysis

Principal component analysis (PCA) is a well-known and widely applied unsupervised statistical technique. PCA is used to analyse a data matrix representing observations described by a number of dependent variables that are, generally, covariant (Abdi and Williams, 2010). In the present case, the matrix contains spectral data where objects (individual spectra) are measurements of a large number of variables (wavenumbers). The main aim of PCA is to identify the features that explain as much of the total variation in the dataset as possible using as few features as possible (Pechenizkiy *et al.*, 2006).

It involves the extraction of a lower dimensional space by transforming the original coordinate system from a data matrix into a new set of orthogonal features known as principal components (PCs) which represent the underlying structure of the data (Pechenizkiy *et al.*, 2006) and removes inter-variable covariance. It operates by calculating the eigenvectors and eigenvalues of the covariance matrix of the original data to identify a set of new variables or PCs where the first PC encapsulates the largest proportion of variance in the data, and each successive PC describes reducing proportions of variance. Each PC is statistically independent to the others.

Importantly, in order that the PCs describe variance in the data, it must be 'mean centred' by subtraction of its mean prior to calculation of the covariance matrix (Awad and Khanna, 2015). As a rule of thumb, the number of PCs considered should describe at least 90% of the total variance in a dataset (Varmuza and Filzmoser, 2009). Beyond this, the PCs are usually associated with noise within the data. The values of the PCs are known as factor scores and these may be (geometrically) interpreted as the projections of the original data onto the PCs (Abdi and Williams, 2010). The decomposition of a matrix, *X*, of spectral data into matrices of its PCs, *Q*, and scores, *F*, can therefore be represented by the following equation:

$$X = Q^T F \quad \textbf{(2.13)}$$

2.5.3 Classical Least Squares Regression

Classical least squares regression (CLS-R) is a supervised fitting method used to approximate the weighted contributions of a set of input measurements to a sample measurement. CLS-R assumes that any complex measurement, a spectrum in the present case, is the weighted sum of all the base components that contribute to that measurement (Mark and Workman, 2010). This can be mathematically represented by the following equation:

$$A = a_1 bc_1 + a_2 bc_2 + a_3 bc_3 \ldots \quad \textbf{(2.14)}$$

where *A* is the sample spectrum measurement, *a* represents a component spectrum, *b* represents the pathlength and *c* represents the weighting coefficient (Mark and Workman, 2010). However, as the pathlength is the same in the present case for all components within the sample of interest, the above equation can be simplified to:

$$A = a_1 c_1 + a_2 c_2 + a_3 c_3 \ldots \quad \textbf{(2.15)}$$

This equation is only valid for a single wavelength however and needs to be adapted to all wavelengths in the spectral range of interest (Mark and Workman, 2010). Thus, the above equation becomes:

$$A_j = a_{1j}c_1 + a_{2j}c_2 + a_{3j}c_3 \ldots \quad \textbf{(2.16)}$$

where A_j is the sample spectrum measurement at the *j*th wavelength and a_j represents a component spectrum at the *j*th wavelength (Mark and Workman, 2010). Furthermore, in identifying *c* for each component spectrum to determine the make-up of A_j, the error in the determination of A_j must be defined (Mark and Workman, 2010). The error can be represented by the following equation:

$$E_j = A_j - (a_{1j}c_1 + a_{2j}c_2 + a_{3j}c_3 \ldots) \quad \textbf{(2.17)}$$

where E_j is the error associated with the *j*th wavelength and as the least square principle involves minimising the sum-squared error in the determination of values for A_j across *j*th wavelengths, this equation becomes:

$$\sum_j E_j^2 = \sum_j (A_j - a_{1j}c_1 - a_{2j}c_2 - a_{3j}c_3 \ldots)^2 \quad \textbf{(2.18)}$$

The sum-of-squared-errors is minimised by taking the derivative of the above equation with respect to each weighted coefficient (Mark and Workman, 2010). For example, for c_1 we get:

$$\frac{d(\sum_j E_j^2)}{dc_1} = 2 \times \sum_j (A_j - a_{1j}c_1 - a_{2j}c_2 - a_{3j}c_3 \ldots) \times \sum_j a_{1j} \quad \textbf{(2.19)}$$

Each derivative obtained for each component spectrum is set equal to zero and divided by 2 (Rencher and Christensen, 2012; Mark and Workman, 2010). For the above equation we get:

$$\sum_j (A_j - a_{1j}c_1 - a_{2j}c_2 - a_{3j}c_3 \ldots) \times \sum_j a_{1j} = 0 \quad \textbf{(2.20)}$$

After distributing the summations and multiplying through, this equation becomes:

$$\sum_j a_{1j}A_j - \sum_j a_{1j}a_{1j}\,c_1 - \sum_j a_{1j}a_{2j}\,c_2 - \sum_j a_{1j}a_{3j}c_3 \ldots = 0 \qquad \textbf{(2.21)}$$

Finally, the above equation can be rearranged to become:

$$\sum_j a_{1j}A_j = \sum_j a_{1j}a_{1j}\,c_1 - \sum_j a_{1j}a_{2j}\,c_2 - \sum_j a_{1j}a_{3j}c_3 \ldots \qquad \textbf{(2.22)}$$

Plugging known spectra for each component a_1, a_2, a_3…, and a measured sample spectrum A into the expressions generated and solving them by treating them as simultaneous equations, the weighted coefficients c_1, c_2, c_3…, can be obtained (Mark and Workman, 2010). It is important to note however, that collinearity between fitted components may skew the fit (Stone *et al*., 2007). Collinearity may occur, for example, where an amino acid and a protein containing that amino acid are included in the model (Stone *et al*., 2007). Thus, care is necessary when interpreting the model results.

2.5.4 Partial Least Squares-Discriminant Analysis

Partial least squares-discriminant analysis (PLSDA) is one of the most commonly applied classification techniques in chemometrics (Brereton and Lloyd, 2014). It is a popular choice in fields where large amounts of data are generated, including metabolomics, proteomics, genomics and spectroscopy and it is particularly useful where a dataset contains more variables than samples as in the present case (Christin *et al*., 2013; Szymanska *et al*., 2012; Blekherman *et al*., 2011; Wehrens, 2011; Boulesteix and Strimmer, 2007; Oksman-Caldentey and Inze, 2004). As a multi-class linear classifier, the aim of PLSDA is to maximise the covariance between independent variables (spectral wavenumbers) and the corresponding dependent variables (class) within multidimensional data.

It does so by identifying a hyperplane that divides the multidimensional feature space into distinct regions (each corresponding to a class) with as small an error as possible (Brereton and Lloyd, 2014). This new lower-dimensional feature space allows for the prediction of the dependent variable using a reduced number of factors known as PLS components (Gromski *et al*., 2015). These PLS components describe the behaviour of the dependent variables and span the lower-dimensional feature space onto which the independent variables are projected (Gromski *et al*., 2015). For a given set of samples I, a data matrix X represents a set of analytical measurements from a sample set, and the vector Y represents a set of numerical labels denoting the class of each sample (Brereton and Lloyd, 2014).

PLSDA is derived from PLS-regression (PLS-R) and requires the production of a regression model between the data matrix X and the vector Y (Brereton and Lloyd, 2014; Wold *et al*., 2001). In PLS-R, Y is a set containing continuous values but in PLSDA, Y is a set of discrete values, with a number of levels corresponding to the number of classes (Brereton and Lloyd, 2014). For a two-class problem, these two levels are simply group A and group B. The fundamental equations for PLSDA are:

$$X = TP + E \quad \textbf{(2.23)}$$

$$Y = TQ + f \quad \textbf{(2.24)}$$

where T represents the matrix of PLS components, or score matrix, P and Q each represent a matrix of regression coefficients (loadings) for X and Y respectively, and E and f are residual error terms (Brereton and Lloyd, 2014). During standard execution of PLS, the data matrix X is mean centred and if there are an equal number of samples in each class, Y is centred by default (Brereton and Lloyd, 2014).

However, where the number of samples in each group is unequal, as in the present case, the standard PLS approach will not usually produce the most appropriate decision boundary as the boundary may be shifted towards the larger group, increasing the misclassification of samples from this group (Brereton and Lloyd, 2014). This issue can be solved by weight centring the X matrix by subtracting the average of the means of the two classes A and B (i.e. $(\bar{x}_A + \bar{x}_B)/2$) from the columns of X (Brereton and Lloyd, 2014). The columns of X are no longer centred but the centre of gravity of X and Y is now equal (Brereton and Lloyd, 2014). It is essential to account for such issues in order to define a suitable decision threshold for the model and to avoid misleading prediction outcomes (Brereton and Lloyd, 2014). When building the PLSDA model, the PLS weight vector w is first calculated by:

$$w = X'Y \tag{2.25}$$

The matrix of PLS components, T, is then determined as follows:

$$T = \frac{Xw}{\sqrt{\sum w^2}} \tag{2.26}$$

The matrix of X loadings, P, and the matrix of Y loadings, Q, can then be computed by:

$$P = \frac{T'X}{\sum T^2} \tag{2.27}$$

$$Q = \frac{Y'T}{\sum T^2} \tag{2.28}$$

A residual data matrix is then determined by subtracting the effect of the new PLS component from X as follows:

$$X^{resid} = X - TP \tag{2.29}$$

Finally, a residual value for Y can be determined by:

$$Y^{resid} = Y - TQ \quad \textbf{(2.30)}$$

Once the PLSDA model has been built, the value of Y can be predicted for the original data, for unknown samples and for test samples used during cross-validation (Brereton and Lloyd, 2014). The relationship between X and Y can be shown by:

$$Y = Xb + f = TQ + f \quad \textbf{(2.31)}$$

where b is a regression coefficient vector of dimensions $J \times 1$ that can be estimated as follows:

$$b = W(PW)^{-1}Q \quad \textbf{(2.32)}$$

The unknown or test sample value can thus be predicted by:

$$\hat{Y} = \mathrm{x}b \quad \textbf{(2.33)}$$

If the value of $\hat{Y} > 0$, the sample belongs to group A and if $\hat{Y} < 0$, the sample belongs to group B (Brereton and Lloyd, 2014).

2.5.5 K-fold Cross-validation

Cross-validation (CV) is one of the simplest and most widely used methods for optimising and assessing the performance of a predictive model (Hastie *et al.*, 2009). Ideally, with sufficient data, a validation set is set aside and used to test the predictive ability of the model (Wehrens, 2011; Hastie *et al.*, 2009). When data are scarce however, such as in the present study, this approach may result in very crude error estimates and the model quality may be suboptimal and unrepresentative of a typical model based on the available data (Wehrens, 2011; Hastie *et al.*, 2009).

K-fold CV, also known as leave-multiple-out CV, is a valid strategy that can be used to finesse the problem (Wehrens, 2011; Hastie *et al.*, 2009). This involves randomly shuffling the data before splitting it into *K* approximately equal-sized fractions (James *et al.*, 2017; Wehrens, 2011; Hastie *et al.*, 2009). As an example, a schematic of one iteration of K = 5 CV is illustrated as shown in figure 2.7.

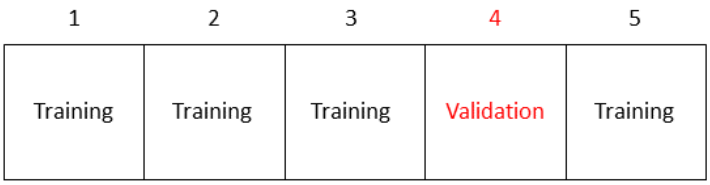

Figure 2.7 Data fragments when *K* = 5 during *K*-fold CV.

For the *k*th iteration (fraction 4 in figure 2.7), the model is fitted to the remaining *K*-1 data fractions and the classification performance of the fitted model is calculated when applied to the *k*th fraction of the data (James *et al.*, 2017; Hastie *et al.*, 2009). This is repeated for each fraction ($k = 1, 2, \ldots, K$) and the mean squared error is averaged across all *k* trials (James *et al.*, 2017; Hastie *et al.*, 2009). While there are no formal rules when choosing a value for *K*, $K = 5$ and $K = 10$ are typically used as these values have been shown empirically to render error rates free from very high variance and excessively high bias (James *et al.*, 2017; Wehrens, 2011; Hastie *et al.*, 2009).

2.5.6 Classification Performance Metrics

Classification performance metrics are useful measures of classification model quality built from confusion matrices which provide a summary of correctly and incorrectly identified class members as shown in Table 2.1.

Table 2.1: General confusion matrix for binary classification

	Predicted Positive	**Predicted Negative**
Actual Positive	True positive (TP)	False negative (FN)
Actual Negative	False positive (FP)	True negative (TN)

The number of TP cases refers to the number of cases correctly identified as positive and the number of TN cases refers to the number of cases correctly identified as negative. Furthermore, the number of FP cases refers to the number of negative cases misclassified as positive or, in the present study, the number of grade 0-1 cases misclassified as grade 2+ cases. Conversely, the number of FN cases refers to the number of positive cases misclassified as negative or, in the present study, the number of grade 2+ cases misclassified as grade 0-1 cases. Two of the most commonly used metrics in binary classification evaluation are *sensitivity* and *specificity*. Sensitivity estimates the probability that a positive label is true and can be derived as follows:

$$Sensitivity = \frac{TP}{TP+FN} \quad \textbf{(2.35)}$$

Specificity, on the other hand, estimates the probability that a negative label is true and can be derived as follows:

$$Specificity = \frac{TN}{TN+FP} \quad \textbf{(3.36)}$$

The closer the sensitivity and specificity values are to 1, the better the classification performance of the model. These two measures evaluate a classification model's positive and negative classification performance separately however and thus some measure of overall performance is necessary. Accuracy is the most commonly used metric to give an overall assessment of the performance of a binary classifier (Bekkar *et al*., 2013). It evaluates the overall efficacy of a model by estimating the probability that a class label is true (Bekkar *et al*., 2013).

Accuracy can be derived as follows:

$$Accuracy = \frac{TP+TN}{TP+TN+FP+FN} \quad \textbf{(2.37)}$$

As with sensitivity and specificity, the closer the resulting value is to 1, the better the overall classification performance of the model. However, accuracy is a poor measure of classification performance in the case where a significant degree of class imbalance occurs. The overall performance of a classification model can be evaluated and represented graphically through a receiver operating characteristic (ROC) curve. The ROC curve is defined as a plot of the TP rate as a function of the FP rate or, sensitivity as a function of 1-specificity for various decision thresholds (Jokiel-Rokita and Topolnicki, 2020; Bekkar *et al*., 2013). From the ROC curve, the area under the ROC curve (AUC) can be estimated to give a summary indication of model performance in a single metric (Bekkar *et al*., 2013).

The AUC of a model is equivalent to the probability that the model will rank a randomly selected positive instance higher than a randomly selected negative instance (Fawcett, 2006). It is typically estimated using a geometric approach called the trapezoidal method where linear interpolation between each ROC curve point is carried out (Bekkar *et al*., 2013). Table 2.2 shows a suggested scale for interpreting AUC values. Sensitivity, specificity, accuracy and AUC values were calculated in the present study to give an evaluation of the PLSDA model's classification performance.

Table 2.2: Interpretation of AUC values (Ludemann *et al*., 2006)

AUC Value	Model Performance
0.5 – 0.6	Fail
0.6 – 0.7	Poor
0.7 – 0.8	Fair
0.8 – 0.9	Good
0.9 – 1.0	Excellent

2.6 Applications of Raman Spectroscopy in Radiobiology

Raman spectroscopy has a number of features that make it an advantageous tool in medical diagnostics. For example, molecular information can be obtained without the need for labels such as dyes, stains or fluorescent markers (Ellis *et al.*, 2013; Kong *et al.*, 2015). In addition, it is non-invasive, generally non-destructive, possesses a high molecular sensitivity and is relatively unperturbed by the presence of water thereby allowing biofluids and cells within aqueous settings to be analysed (Clemens *et al.*, 2014; Ellis *et al.*, 2013; Kong *et al.*, 2015).

Moreover, it is a rapid method for analysis that requires little sample preparation and a low volume sample. In recent years, there have been numerous studies showing the potential of Raman spectroscopy in the screening and diagnosis of various diseases with promising results using cells, tissues and biofluids (Kong *et al*., 2015). Recent studies have also shown the potential of Raman spectroscopy to characterise radiation response of normal and tumour cells irradiated *in-vitro* and of tumour tissue irradiated *in-vivo*. Radiation-induced biochemical changes were found to be detectable using Raman spectroscopy in *in-vitro* studies on keratinocytes (HaCaT cell line) and normal lymphocytes by Meade *et al*. (2016) and Maguire *et al*. (2015a), respectively.

Meade *et al*. (2016) found changes in spectral features following irradiation associated with DNA, RNA and amide I, using Raman spectroscopy in conjunction with PCA followed by linear discriminant analysis (LDA). This study demonstrated the sensitivity of Raman spectroscopy to radiation-induced effects across a range of radiation doses from low to high (0-5 Gy) and both HRS and IRR were observed in the HaCaT cell line at low radiation doses.

Maguire *et al*. (2015a) found changes in spectral features associated with DNA, RNA, proteins and lipids using Raman spectroscopy in conjunction with PCA followed by LDA with DNA damage confirmed using the γH2AX DNA damage assay. This study demonstrated the ability of Raman spectroscopy to detect alterations in spectral profiles at doses as low as 0.05 Gy in as little as 1 hr post-exposure. Inter-individual variability in classification performance was observed between unirradiated and irradiated lymphocytes however, with higher sensitivity and specificity for some donors suggesting more pronounced changes in spectral features of their lymphocytes following *in-vitro* irradiation. Moreover, an *in-vitro* study by Yasser *et al*. (2014) applied Raman spectroscopy in conjunction with PCA to examine the differences between oral cancer cell lines and radioresistant sublines irradiated to 2 Gy.

Yasser *et al*. (2014) found differences in spectral features associated with proteins, lipids and nucleic acids and demonstrated the ability of Raman spectroscopy to distinguish between radioresistant sublines and parental lines with only minor overlap suggesting an altered spectral profile acquired by the radioresistant cells following radiation exposure. This study showed the potential of Raman spectroscopy to predict radioresistance.

Radiation-induced biochemical changes were also found to be detectable using Raman spectroscopy in a study on NSCLC xenografts and human tumour cells by Harder *et al*. (2015) and Matthews *et al*. (2011), respectively. Using Raman spectroscopy combined with PCA, Harder *et al*. (2015) showed distinct radiation-related Raman signatures associated with carbohydrate, protein, lipid and nucleic acid spectral features in human NSCLC tumour xenografts irradiated *in-vivo*.

A significant increase in glycogen spectral features was also observed in the irradiated tumours in comparison to unirradiated tumours for doses of 5 and 15 Gy during this study. Matthews *et al*. (2011) found radiation-induced spectral changes associated with nucleic acids, lipids, amino acids and conformation protein structures between unirradiated and irradiated and human tumour cell samples cultured *in-vitro* following PCA of Raman spectral profiles. These spectral changes were found to increase with radiation dose (over the range from 0-50 Gy) and incubation time following exposure (over the period from 0-120 hr). This study also demonstrated that cell cycle progression can be a large source of variability within a dataset, and this may interfere with discriminating samples based on radiation-induced biochemical changes.

A study by Jafarzadeh *et al*. (2018) examining biochemical alterations in irradiated breast cancer cells using Raman spectroscopy in combination with numerous discriminant analysis techniques, including PCA, LDA and genetic algorithm discriminant analysis, found differences in spectral features associated with DNA, lipids, proteins, phenylalanine, amide I and carotenoid. Significant molecular and structural alterations were observed following irradiation of cells *in-vitro* at 2 Gy but longer post-irradiation times showed that the cells relaxed to their initial state. At a dose of 4 Gy however, more serious irreversible changes were seen in these cells.

A more recent study by Meade *et al*. (2019) found Raman spectroscopy capable of predicting γH2AX DNA damage assay mean fluorescent intensity (MFI) when using peripheral blood lymphocytes from PCa patients cultured *ex-vivo* and irradiated from 0-0.5 Gy. This study demonstrated the ability of Raman spectroscopy to provide an estimate of the level of DNA damage in humans using PLS-R and support vector regression, with the latter regression technique outperforming the former, suggesting a non-linear relationship between DNA damage measurements and spectral measurements.

Another recent *in-vitro* study, by Lasalvia *et al.* (2019), evaluating the effects of proton irradiation on non-tumorigenic human breast cells, found that Raman spectroscopy could clearly detect radiobiological effects at doses as low as 0.5 Gy. Furthermore, Raman spectral analysis showed that DNA/RNA damage increases with time and a trend in relation to dose, similar to that found in commonly used radiobiological assays such as the MTT and clonogenic assays, could also be observed in the Raman spectra. In addition, Santosh *et al*. (2019), used Raman spectroscopy to examine microenvironmental differences between treatment-resistant and treatment-sensitive tumours. Distinct differences in lipid and collagen content in the tumour microenvironment were observed in Raman spectra following irradiation to 2 Gy with consistently greater alterations observed in the treatment-sensitive tumours.

A much more recent *in-vitro* study, by Milligan *et al*. (2021), using prostate, lung and breast cancer cell lines irradiated from 0-10 Gy, demonstrated that Raman spectroscopy in conjunction with non-negative matrix factorisation, could be used to identify radiation-induced biochemical changes and distinguish between radiosensitive and radioresistant cell lines as a result.

Differences in phosphatidylcholine, arginine, glucose and asparagine were observed between radiosensitive and radioresistant cell lines, with glycogen and phosphatidylcholine standing out as the two most distinguishing factors. Finally, an *in-vitro* study by Qiu *et al.* (2020) on human nasopharyngeal cancer cells using Raman spectroscopy with PCA and LDA, found alterations in lipids and DNA bases and prominent alterations in intracellular proteins, following irradiation to 2.3 Gy. In particular, bands associated with tyrosine and tryptophan differed significantly between the irradiated and unirradiated groups. These studies, while by no means an exhaustive list, demonstrate the ability of Raman spectroscopy to identify the biochemical alterations that occur in cells following exposure to radiation. Thus, Raman spectroscopy may have potential as an assay for the prediction of late normal tissue toxicity by investigating spectral differences in lymphocytes from PCa patients.

Raman spectroscopy is not without limitations, however. The Raman effect is quite weak and thus requires a very sensitive and well optimized instrument to detect it. Moreover, impurities, such as red blood cells, which are common in some biological samples can cause fluorescence which may saturate the Raman spectrum. Moreover, while Raman spectroscopy is generally non-destructive, some sample types may be damaged through intense laser radiation. This damage can be offset by choosing a less intense laser line and the optimization of various parameters such as acquisition time and filter setting but this does not always solve the problem. The most prominent limitation, however, is the lack of molecular specificity. Biological assays, such as those mentioned in section *1.5 Assays of Clinical Radiosensitivity*, typically target very specific molecules within a cell or tissue, while a Raman spectrum is a superposition of all the molecules that make up the cell or tissue.

Fitting algorithms can be used to improve molecular specificity however, but these do not approach the level of specificity observed in single-point or multiplex biological assays. During optimization of a Raman assay however, biological assays could potentially be used following the use of a fitting algorithm, to confirm the molecules responsible for any differentiation in spectra.

Chapter 3 – Materials and Methods

3.1 Patients and Sample Preparation

3.1.1. Ethical Approval

Two hundred and fifty two patients were enrolled on the Cancer Trials Ireland (formerly the All-Ireland Co-operative Oncology Research Group) ICORG 08-17 study, ICTRP ID: NCT00951535; A Prospective Phase II Dose Escalation Study Using IMRT for High Risk N0 M0 Prostate Cancer), a prospective, phase II non-randomised controlled clinical study where the primary endpoint is to determine if dose escalation up to 81 Gy using IMRT for high risk localised PCa can provide PSA relapse-free survival similar to that previously reported (Alicikus *et al*., 2011). The studies outlined in chapters 4 and 5 were approved as a translational sub-study to CTrial-IE 08-17 and were also approved by the Research Ethics Committee and all research was performed in accordance with relevant guidelines and regulations. Informed consent was obtained from all participants.

For these patients, PSA levels and toxicities (which were graded according to the NCI-CTCAE grading system), have been recorded prior to treatment, during treatment and at follow up. Patients are followed up at 2 months post-RT, 8 months post-RT and at 6 monthly intervals until Year 9. All patients were prescribed either 6 months or 3 years of neo-adjuvant/adjuvant hormone therapy. Of the 147 patients who had been followed up 18-24 months post-RT, 56 patients were identified with grade 2+ GU or GI late radiation toxicity and of these, 25 patients consented to participate in, and provide a blood sample for, the retrospective study outlined in chapter 4. These patients were matched with 17 patients who showed no/minimal (grade 0-1) late radiation toxicity who also had been followed up for at least 18 months post-RT.

Patient groups were matched as far as practicable based on age, tumour stage, Gleason score, PSA level and RT volume/dose metrics. Furthermore, 51 of the 252 patients consented to participate in, and provide a blood sample for, the prospective study outlined in chapter 5. To date, of these 51 patients who had been followed up 26-38 months post-RT, samples were obtained for 35 patients and 17 showed no/minimal (grade 0-1) late radiation toxicity in follow-up while 18 showed severe (grade 2+) GU or GI late radiation toxicity in follow-up.

In addition, 30 patients were enrolled on the Northern Ireland Cancer Trials Centre SPORT study, ICTRP ID: NCT 03253978; A Randomised Feasibility Study Evaluating Stereotactic Prostate Radiotherapy In High-Risk Localised Prostate Cancer With or Without Elective Nodal Irradiation, a prospective, randomised feasibility controlled clinical study where the primary objective is to compare prostate-only stereotactic ablative body RT (SABR) to prostate and pelvic SABR in men with high-risk localised PCa. The study outlined in chapter 6 was approved as a sub-study to the SPORT study and was also approved by the Research Ethics Committee and all research was performed in accordance with relevant guidelines and regulations. Informed consent was obtained from all participants. For these patients, PSA levels and toxicities (which were graded according to the RTOG grading system), have been recorded prior to treatment, during treatment and at follow up. Patients are followed up at 6 weeks, 3 months, 6 months, 9 months, 12 months and every 6 months up to 5 years with a minimum annual follow-up from 5-10 years. Of the 30 patients who had been followed up 6-24 months post-RT, 4 patients were identified with grade 2+ GU or GI late radiation toxicity and consented to participate in, and provide a blood sample for, the prospective study outlined in chapter 6.

These patients were matched with 23 patients who showed no/minimal (grade 0-1) late radiation toxicity who also had been followed up for 6-24 months post-RT. No toxicity data was obtained for the remaining 3 patients. Healthy volunteers (n = 42) were a cohort of both males and females, all between the ages of 21 and 70 recruited from the staff of TU Dublin. All patient data from each study was associated with anonymised study numbers to maintain patient confidentiality.

3.1.2 Cell Culturing

Throughout this study, 20 ml fresh whole blood was drawn from either healthy volunteers or PCa patients into lithium-heparin tubes. Peripheral blood mononuclear cells (PBMCs) were isolated within 24 hrs of collection. A total of 6 ml of Dulbecco's modified phosphate buffered saline (DPBS) (Sigma Aldrich LLC, St Louis, MO) was added to 6 ml of heparinised blood, mixed by gentle inversion and overlaid onto 15 ml of Histopaque (Sigma Aldrich LLC). Samples were centrifuged at 400 g for 30 min at room temperature. The PBMC layer was removed using a pipette and the rest of the contents were discarded. PBMCs were washed by adding 10 ml of DPBS (Sigma Aldrich LLC) and gently mixed by inversion. Samples were washed a total of three times. Finally, cells were pelleted by centrifugation at 250 g for 5 min at room temperature. Supernatant was discarded and the cell pellet was resuspended in 3 ml of full media (RPMI + 12.5 % (v/v) FBS + 2 mM L-glutamine; Sigma Aldrich LLC) supplemented with 2.5% (v/v) phytohaemagglutinin (PAA Laboratories Ltd, Sommerset, UK). A total of 1 ml of cell suspension was transferred to a T25 flask containing 4 ml of full media. A total of 3 flasks were prepared for each donor. Flasks were placed horizontally and incubated for 72 hrs at 37˚C and 5% CO_2 to allow separation of lymphocytes and monocytes by plastic adherence.

3.1.3 Sample Irradiation

The *in-vitro* cultured lymphocytes were irradiated in their flasks to 0.05 Gy and 0.5 Gy with an 6 MV X-ray linear accelerator (LINAC) at St. Luke's Hospital, Dublin. An unirradiated sample was also prepared (0 Gy). The dose rate was approximately 1.5 Gy/min and was determined from a distance corrected measurement of the in-beam axial dose at an 80 cm source to chamber distance. This was measured using a secondary standard ionization chamber within a water equivalent phantom. The LINAC was calibrated in accordance with the 1990 Institute of Physical Sciences in Medicine (IPSM) code of practice (Lillicrap *et al.*, 2002) by the Medical Physics Department at St. Lukes Hospital such that 100 monitor units (MU, a measure of 'beam on' time) delivered a dose of 0.1 Gy at 1.4 cm deep in water positioned 100 cm from the source in a 10×10 cm^2 field. In order to achieve a uniform irradiation of flasks in practice, the irradiation conditions were altered from those at calibration.

A 30×35 cm^2 field was used to deliver each dose. The flasks were also positioned 10 cm deep in a water equivalent phantom 90 cm from the source. At 90 cm from the source, 100 MU delivers a dose of 0.0812 Gy at 10 cm deep in water for a 10×10 cm^2 field. The number of MU required to deliver each of the doses outlined above must be corrected for the different scatter conditions present within the larger field size (30×35 cm^2). A correction factor of 1.1372 was therefore applied, which is the ratio of the field area of a large field to a smaller one. Thus, at 90 cm from the source, 100 MU delivers a dose of 92.34 cGy (81.2×1.1372) and so the delivery of 0.05 Gy and 0.5 Gy required 6 MU and 55 MU, respectively. The calculated doses were verified using Gafchromic EBT3 film (Ashland Inc., NJ).

3.1.4 Slide Preparation for Raman Micro-spectroscopy

Following irradiation, the samples were placed in an incubator at 37˚C for 60 min, at which time cells were centrifuged at 250 g for 5 min and fixed using 4% paraformaldehyde (AppliChem GmbH, Darmstadt, Germany) in DPBS (Sigma Aldrich LLC). From the suspension, 40 µl was drop cast onto calcium fluoride (CaF_2) slides. The slides were then washed three times in deionised water and the samples were allowed to dry for Raman micro-spectroscopic measurements.

3.2 DNA Damage and Radiosensitivity Assays

3.2.1 γH2AX DNA Damage Assay

Following irradiation, a parallel set of cells to those used for Raman micro-spectroscopy were stored at -20˚C. These were later permeabilised in 200-1000 µl of 0.25% (v/v) Triton X-100 (VWR Chemicals, Radnor, PA) in DPBS and incubated for 5 min at room temperature. The permeabilisation solution was removed and the cells were resuspended in 200 µl of blocking solution (2% (w/v) bovine serum albumin (Sigma-Aldrich LLC) in DPBS (Sigma-Aldrich LLC)) and incubated for 30 min at room temperature. The blocking solution was removed, and the cells were resuspended in 150 µl of primary antibody solution (Anti-phospho-histone H2AX; Millipore, Billerica, MA) and incubated for 2 hrs at room temperature. Washing was performed three times in 500 µl of DPBS (Sigma Aldrich LLC) before 150 µl of secondary antibody solution (Alexa Fluor 488; Invitrogen, Carlsbad, CA) was added. The cells were incubated at room temperature for 1 hr in the dark and washing was performed again three times in 500 µl DPBS (Sigma Aldrich LLC).

The relative fluorescence, or MFI, due to green Alexa Fluor 488 dye was measured using an Accuri C6 flow cytometer (BD Biosciences, Berkshire, UK). A minimum of 10,000 events per sample was recorded. Debris and cell aggregates were removed from the analysis using forward and side scatter characteristics. The MFI for the 0.05 Gy and 0.5 Gy doses were normalised using the MFI for the 0 Gy to account for spontaneous aberrations. Finally, a series of unpaired two-tailed Student's *t*-tests were carried out to determine if there was a statistically significant difference between the two patient toxicity groups.

3.2.2 G2 Chromosomal Radiosensitivity Assay

Following irradiation, whole blood cultures were incubated with 200 µl of Colcemid® (1 µg/ml stock; Roche Diagnostics GmbH, Mannheim, Germany) at 37˚C and 5% CO_2 for 1 hr to arrest cells in metaphase. The samples were centrifuged at 250 g for 10 min. The supernatant was removed and 5 ml of ice cold 0.075 mM KCl (Sigma Aldrich LLC) was added to lyse the red blood cells. The samples were incubated on ice for 20 min to prevent chromatid damage repair. The samples were centrifuged at 250 g for 10 min. The supernatant was removed, and the extracted chromosomes were fixed with 3:1 methanol:acetic acid (*methanol:* Sigma Aldrich LLC; *acetic acid:* AppliChem GmbH). The samples were stored at 4˚C until needed. Slides were prepared by pre-cleaning in methanol (Sigma Aldrich LLC) 24 hrs prior to use and then washing and storing in deionised water. Two to three drops of the cell suspension were dropped onto the slides from a height and heat fixed. Slides were stained using a 3 % Giemsa solution (Sigma Aldrich LLC) prepared in a pH 6.8 buffer (VWR Chemicals) for 20 min. Slides were washed in deionised water and left to dry before being mounted in Coverquick® (VWR Chemicals).

The number of chromosomal aberrations per 100 cells was recorded microscopically to give a G2 score for each patient at each dose. The G2 scores for the 0.05 Gy and 0.5 Gy doses were normalised using the G2 score for the 0 Gy to account for spontaneous aberrations. Frequency plots were generated using the resulting scores and the 90^{th} percentile cut-off value was calculated using the G2 scores of healthy controls from a previous in-house study. Finally, a series of unpaired two-tailed Student's *t*-tests were used to determine if there was a statistically significant difference between the two patient groups.

3.3 Raman Spectral Acquisition and Analysis

3.3.1 Raman Spectral Measurements of Lymphocytes

Raman micro-spectroscopy was performed using a Horiba Jobin Yvon Labram HR800 UV micro-spectroscopy system (Horiba UK Ltd, Middlesex, UK) equipped with a solid-state diode laser. The system detector was calibrated daily using the 520.7cm^{-1} of silicon. A 660 nm laser line was chosen for sample excitation based on previous in-house studies (Maguire *et al*., 2015a; Maguire *et al*., 2015b). A 100× objective (numerical aperture = 0.95) and a diffraction grating of 300 lines/mm (centred at 1450 cm^{-1}) were used. The laser intensity was set to 100 % and the confocal hole was set to 100 μm. A total of 50 spectra from each of the unirradiated (0 Gy) and irradiated samples (0.05 Gy and 0.5 Gy) were collected from each patient sample. Spectra were recorded with a 20 second integration time and averaged over 3 integrations. Each spectrum was recorded using a 4 × 4 μm raster scan of the centre of each cell.

Three spectra of 1,4-Bis (2-methylstyryl) benzene (Sigma Aldrich LLC) and three spectra of NIST Standard Reference Material (SRM) no. 2245 were also recorded along with each sample for the purpose of wavenumber and intensity calibration. These spectra were recorded with a 0.3 second integration time. The temperature of the room was equilibrated to 18˚C for all measurements.

3.3.2 Raman Spectral Pre-processing

All sample spectra were wavenumber calibrated using 1,4-Bis (2-methylstyryl) benzene standard spectra and intensity calibrated using NIST SRM no. 2245 spectra via in-house developed calibration procedures in the Matlab 2017a environment. Baseline correction was performed using a rubberband baseline subtraction, all spectra were lightly smoothed using a SG filter (2^{nd} order, 15-point window) and inter-sample averaging of spectra within each patient sample was also conducted to produce approximately 5 representative spectra per patient within each class. This had the effect of both improving the signal to noise ratio and execution time of the models. All spectra were then vector normalized. All analysis was conducted in Matlab with the PLS Toolbox v.8.0 (Eigenvector Research Inc.).

3.3.3 Raman Spectral Analysis

The specific Raman spectral analysis approaches used for each study are specified in sections *4.2.7 Raman Spectral Acquisition and Analysis, 5.2.7 Raman Spectral Acquisition and Analysis and 6.2.5 Raman Spectral Acquisition and Analysis* for chapters 4, 5 and 6, respectively.

3.3.4 Model Development

PLSDA models were built independently from spectral datasets of lymphocytes irradiated with 0 Gy, 0.05 Gy and 0.5 Gy. To investigate whether the Raman spectra at any dose contained differentiating signals allowing the classification of patients according to radiation toxicity, PLSDA models were trained with spectra at that dose using 90% of the patients from each toxicity class and validated with the remaining 10% of patients. Patients were randomised between the training and validation sets automatically at the start of each algorithm development phase. A total of 20 independent models were constructed with an increasing number of latent variables, with the classification accuracy, sensitivity and specificity evaluated at the point in each model at which the sensitivity and specificity were optimised. The performance metrics shown were averaged across all independently cross-validated models.

Chapter 4 – Raman Micro-spectroscopy of Lymphocytes for the Identification of Prostate Cancer Patients with Late Radiation Toxicity Following Radiotherapy

Adapted from: Cullen, D, *et al*. Raman spectroscopy of lymphocytes for the identification of prostate cancer patients with late radiation toxicity following radiotherapy. *Translational Biophotonics* 2020; **2**(4), doi:10.1002/tbio.201900035

4.1 Introduction

As discussed in chapter 1, despite recent technological advances to conform the dose of radiation to the tumour, normal tissue is always irradiated during RT and this can lead to the development of acute or late toxicity for the patient. Research on predictive assays of normal tissue radiosensitivity has been ongoing for several years and has so far yielded conflicting results. The aim of the present study was to evaluate Raman micro-spectroscopy as an assay for identification of late normal tissue toxicity by investigating spectral differences in lymphocytes from PCa patients with severe late toxicity (grade 2+) and those with no/minimal late toxicity (grade 0-1). *In-vitro* cellular radiosensitivity was also assessed in parallel using the G2 chromosomal radiosensitivity assay, which measures the number of chromosomal aberrations induced by radiation in lymphocytes in the G2-phase of the cell cycle and the γH2AX assay, which measures DNA damage.

4.2 Materials and Methods

4.2.1 Patient Samples

Clinical details of both patient groups are shown in Table 4.1. Figure 4.1 shows an overview of the patient identification, sample processing, *in-vitro* irradiation and subsequent assays.

Table 4.1: Clinical features of grade 0-1 and grade 2+ patient groups. Data are number of patients unless otherwise stated

	Grade 0-1 (n= 17)	**Grade 2+ (n= 25)**
Age (years)		
Mean	68	68
Median	67	70
Range	54-81	52-78
Time to onset of grade 2+ toxicity (months)		
Mean	N/A	23
Median	N/A	16
Range	N/A	10-47
PSA (ng/ml)		
Mean	16.4	13.1
Median	14.5	11.6
T Stage		
T1c to T2a	4 (24%)	4 (16%)
T2b to T2c	1 (6%)	4 (16%)
T3a	7 (41%)	12 (48%)
T3b to T3c	5 (29%)	5 (20%)
Gleason score		
7	6 (35%)	10 (40%)
8	5 (29%)	8 (32%)
9	5 (29%)	6 (24%)
10	1 (6%)	1 (4%)
Planned duration of hormones		
6 months	1 (6%)	7 (28%)
36 months	16 (94%)	18 (72%)
RT Dose/ fractions		
75.6/ 42	0 (0%)	1 (4%)
81.0/ 45	17 (100%)	24 (96%)
DVCs (median)*		
Rectum_V50	37.2	38.3
Rectum_V70	15.5	15.6
Bladder_V40	17.2	27.6
Bladder_V65	5.8	11.8

**V50=volume of structure that received 50 Gy*

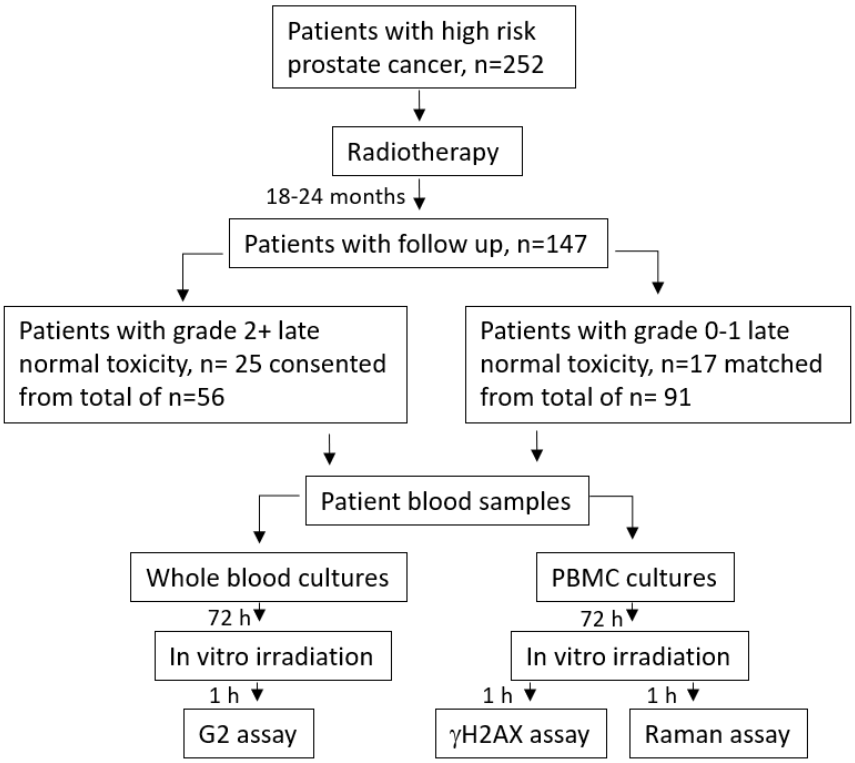

Figure 4.1: Schematic showing an overview of the patient identification, sample processing, *in-vitro* irradiation, G2 assay, γH2AX assay and Raman assay.

4.2.2 Cell Culturing

Cell culturing was carried out as described in section *3.1.1 Cell Culturing*.

4.2.3 Sample Irradiation

Sample irradiation was carried out as described in section *3.1.2 Sample Irradiation*.

4.2.4 Slide Preparation for Raman micro-spectroscopy

Calcium fluoride slide preparation was carried out as described in section *3.1.3 Slide Preparation for Raman micro-spectroscopy*.

4.2.5 γH2AX DNA Damage Assay

The γH2AX DNA damage assay was carried out as described in section *3.2.1 γH2AX DNA Damage Assay*.

4.2.6 G2 Chromosomal Radiosensitivity Assay

The G2 chromosomal radiosensitivity assay was carried out as described in section *3.2.2 G2 Chromosomal Radiosensitivity Assay*.

4.2.7 Raman Spectral Acquisition and Analysis

Raman spectral acquisition was carried out as described in section *3.3.1 Raman Spectral Measurements of Lymphocytes* and Raman spectral pre-processing was carried out as described in section *3.3.2 Raman Spectral Pre-processing*. Mean spectra were generated for both the grade 0-1 and grade 2+ toxicity groups and difference spectra were obtained by subtracting the mean spectra for the grade 0-1 group from the mean spectra for the grade 2+ group. Unpaired two-tailed Student's *t*-tests were then applied across all wavenumbers to identify statistically significant spectral differences between the two groups using a significance level (α) of 0.05. Mean and difference spectra in conjunction with unpaired two-tailed Student's *t*-tests ($\alpha = 0.05$) were also used to examine differences in irradiation dose response in each group. Model development was carried out as described in section *3.3.4 Model Development*.

4.3 Results

4.3.1 γH2AX DNA Damage Assay

Figure 4.2 shows the increase in γH2AX fluorescence 1 hr after *in-vitro* irradiation for the grade 0-1 and grade 2+ patients (Grade 0-1 mean = 1.0±0.7 and 1.2±1.0 at 0.05 and 0.5, respectively; Grade 2+ mean = 2.6±4.0 and 2.0±2.7 at 0.05 Gy and 0.5, respectively).

Both groups showed an increase in γH2AX fluorescence at each dose with a more pronounced increase in the grade 2+ group at both 0.05 Gy and 0.5 Gy. However, the difference was not statistically significant due to the high level of inter-individual variation particularly in the grade 2+ group.

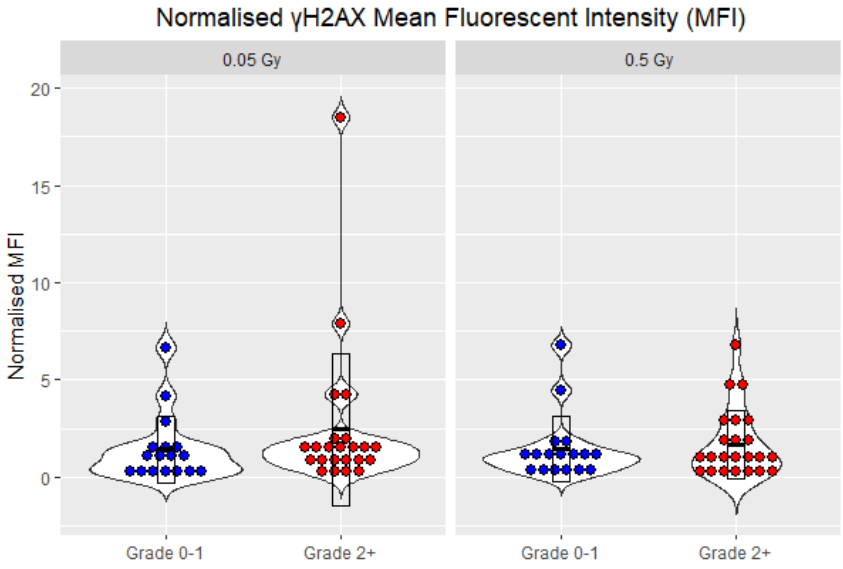

Figure 4.2: Relative increase in γH2AX fluorescence 1 hr after *in-vitro* irradiation to 0.05 Gy and 0.5 Gy for grade 0-1 and grade 2+ patients. The error bars indicate the standard deviation.

4.3.2 G2 Chromosomal Radiosensitivity Assay

For both the grade 0-1 and the grade 2+ patients, the number of spontaneous aberrations was very low (mean 7.2±5.4, range 0-20, for grade 0-1 patients and mean 9.4±7, range 0-28, for grade 2+ patients). Figure 4.3 shows the radiation-induced G2 scores for the grade 0-1 and grade 2+ patients. Significant inter-individual variation in G2 radiosensitivity was observed in both groups, with more variability in the grade 2+ group. The mean G2 score was 113± 35.1 (range 32-188, %CV 30.8) for grade 0-1 patients and 152±59.7 (range 60-268, %CV 38.8) for grade 2+ patients but there was no statistically significant difference in G2 score between the two groups. The grade 2+ group however, showed a very different distribution to the grade 0-1 group with a bimodal distribution (p=0.0001).

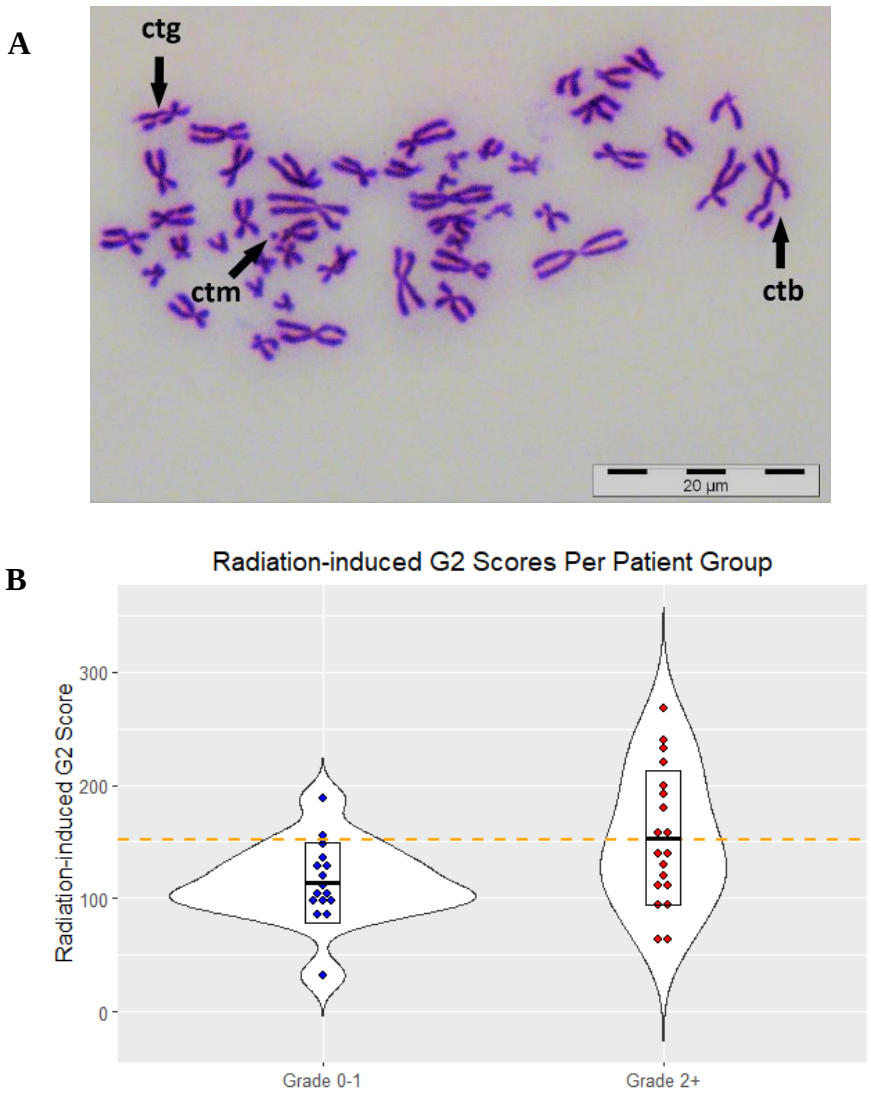

Figure 4.3: (A) Giemsa stained metaphase spread showing chromosomal aberrations such as chromatid break (ctb), chromatid gap (ctg) and chromatid minute (ctm). (B) Radiation-induced G2 scores for grade 0-1 and grade 2+ patients. The error bars indicate the standard deviation.

4.3.3 Radiation response of lymphocytes from Grade 0-1 and Grade 2+ patients

To investigate the radiation response of the lymphocytes from grade 0-1 and grade 2+ patients to *in-vitro* irradiation, the difference spectra of unirradiated and irradiated lymphocytes were calculated for each patient group separately. Figure 4.4 shows the mean spectra of unirradiated and irradiated lymphocytes from grade 0-1 and grade 2+ patients and the difference spectra of unirradiated and irradiated lymphocytes for each patient group.

The shaded regions show where the spectra of the irradiated lymphocytes were found to be significantly different to the unirradiated lymphocytes (α=0.05). Summaries of the band changes for the grade 0-1 and grade 2+ patients following irradiation are provided in Table 4.2 and 4.3, respectively. In general, changes in nucleic acids, proteins and lipids were observed after irradiation to 0.05 and 0.5 Gy in lymphocytes from grade 0-1 and grade 2+ patients with more significant differences observed between unirradiated and irradiated lymphocytes from grade 2+ patients.

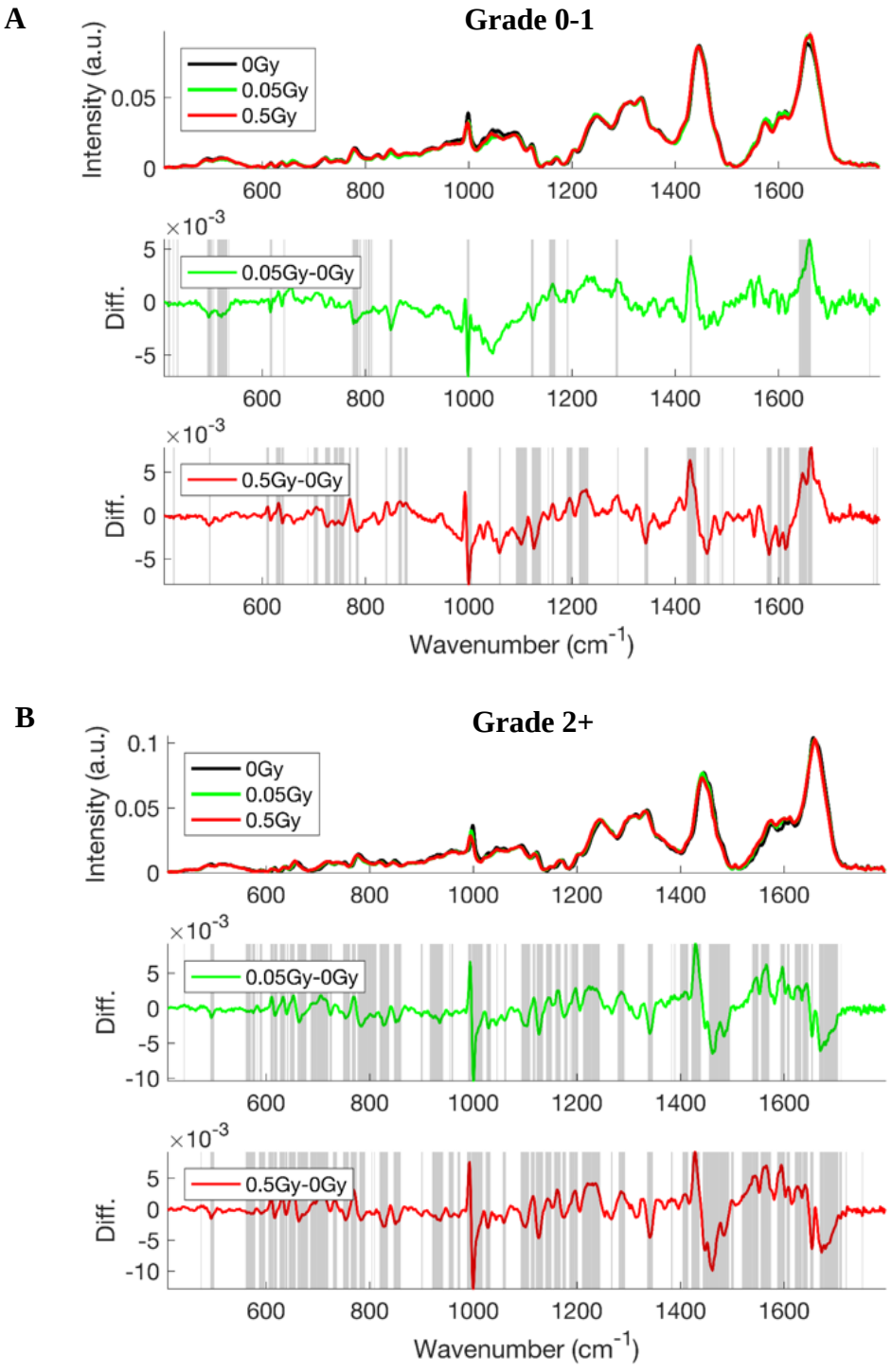

Figure 4.4: Lymphocyte response to 0.05 Gy and 0.5 Gy in (A) grade 0-1 and (B) grade 2+ patient groups. Top panels display the mean spectra (with a shaded region around each mean spectrum indicating the standard error on the mean for that class) and bottom panels display the difference between the spectrum of the unirradiated and irradiated cells. Shading within the middle and bottom panels represents regions of the spectrum that were found to be significantly different (two-tailed unpaired t-test with α=0.05).

Table 4.2: Summary of band changes and associated tentative assignments between spectra from unirradiated and irradiated lymphocytes from grade 0-1 patients

Band (cm^{-1})	**Δ 0 v 0.05 Gy**	**Band assignment**	**References**
775-786	↑	O-P-O stretching and U, T, C ring breathing in RNA/DNA	Chan *et al*. (2006)
812	↓	Phosphodiester	Ruiz-Chica *et al*. (2004)
850	↓	Tyrosine	Shetty *et al*. (2006)
999	↓	ν C-C skeletal modes	Deng *et al*. (2005)
1158-1168	↑	C-C and C-N stretching in proteins, carbohydrates	Notingher *et al*. (2004)
1288	↑	Phosphodiester groups in nucleic acids	Dukor (2002)
1431	↑	Unassigned	N/A
1640-1660	↑	Amide I, T, G and C ring breathing	Agarwal *et al*. (2006); Chan *et al*. (2006); Shetty *et al*. (2006); Frank *et al*. (1995)
Band (cm^{-1})	**Δ 0 v 0.5 Gy**	**Band assignment**	**References**
722-730	↓	A ring breathing	Chan *et al*. (2006)
739-758	↓	T ring breathing	Chan *et al*. (2006)
770	↑	Unassigned	N/A
787	↓	Phosphatidylserine	Krafft *et al*. (2005)
841	↑	Saccharides	Krafft *et al*. (2005)
865-881	↑	Hydroxyproline, saccharides, tryptophan	Shetty *et al*. (2006); Cheng *et al*. (2005)
998-1006	↓	Phenylalanine, ν C-C skeletal modes	Malini *et al*. (2006); Cheng *et al*. (2005); Deng *et al*. (2005)
1061	↓	Phospholipids, lipids, C-C stretching in carbohydrates	Faolain *et al*. (2005); Huang *et al*. (2005); Notingher *et al*. (2004)
1091-1113	↑	ν PO_2^- (nucleic acids)	Krafft *et al*. (2005); Notingher *et al*. (2004)
1121-1140	↑	ν C-O (carbohydrates)	Shetty *et al*. (2006); Notingher *et al*. (2004)
1189-1201	↑	Nucleic acids and phosphates	Andrus and Strickland (1998)
1215-1230	↑	Amide III (β-structure)	Stone *et al*. (2004); Lakshimi *et al*. (2002); Gniadecka *et al*. (1997)
1289	↑	Unassigned	N/A
1343	↓	CH_3CH_2 wagging, glucose	Krafft *et al*. (2005); Frank *et al*. (1995)
1422-1441	↑	Deoxyribose, CH_2 deformation;	Krafft *et al*. (2005); Ruiz-Chica *et al*. (2004); Frnak *et al*. (1995)
1457	↓	Deoxyribose	Cheng *et al*. (2005); Ruiz-Chica *et al*. (2004)

1460-1480	↓	Deoxyribose, CH_2/CH_3deformation;	Cheng *et al*. (2005); Ruiz-Chica *et al*. (2004)
1487	↓	Guanine	Ruiz-Chica *et al*. (2004)
1578-1587	↓	Guanine, adenine, phenylalanine	Notingher *et al*. (2004); Ruiz-Chica *et al*. (2004); Huang *et al*. (2003a)
1599-1607	↓	Phenylalanine, tyrosine	Chan *et al*. (2006); Cheng *et al*. (2005); Huang *et al*. (2003a); Lakshimi *et al*. (2002)
1611-1622	↓	C=C modes of tyrosine and tryptophan, phenylalanine	Chan *et al*. (2006); Cheng *et al*. (2005); Stone *et al*. (2004); Stone *et al*. (2002)
1639-1667	↑	Amide I, T, G and C ring breathing	Agarwal *et al*. (2006); Chan *et al*. (2006); Stone *et al*. (2004)

Table 4.3: Summary of band changes and associated tentative assignments between spectra from unirradiated and irradiated lymphocytes from grade 2+ patients

Band (cm^{-1})	**Δ 0 v 0.05 Gy**	**Band assignment**	**References**
662-678	↓	G, T ring breathing in RNA/DNA, C-S stretching of cystine	Cheng *et al*. (2005); Notingher *et al*. (2004); Stone *et al*. (2002)
689-719	↑	C-N of membrane phospholipid, choline group, cholesterol	Krafft *et al*. (2005); Stone *et al*. (2004)
750-761	↓	Tryptophan, DNA	Shetty *et al*. (2006); Binoy *et al*. (2004); Notingher *et al*. (2004); Stone *et al*. (2004)
766-772	↓	Pyramidine ring breathing mode	Farguharson *et al*. (2005)
770-812	↓	Phosphodiester, O-P-O stretching in DNA/RNA, U, T, C ring breathing in RNA/DNA	Chan *et al*. (2006); Notingher *et al*. (2004); Ruiz-Chica *et al*. (2004)
821-838	↓	Phosphodiester, O-P-O stretching in DNA/RNA	Ruiz-Chica *et al*. (2004); Stone *et al*. (2004); Stone *et al*. (2002)
849-861	↓	Hydroxyproline, proline, tyrosine	Chan *et al*. (2006); Cheng *et al*. (2005); Huang *et al*. (2003a)
921-942	↓	C-C stretching of proteins, proline, hydroxyproline	Cheng *et al*. (2005); Stone *et al*. (2004); Huang *et al*. (2003a); Stone *et al*. (2002); Frank *et al*. (1995)
955	↓	Unassigned	N/A
961	↓	Unassigned	N/A
992-1018	↑	Phenylalanine	Malini *et al*. (2006); Cheng *et al*. (2005); Frank *et al*. (1995)
1027-1034	↓	Phenylalanine	Chan *et al*. (2006); Cheng *et al*. (2005); Huang *et al*. (2003a)
1046	↓	Unassigned	N/A
1062	↓	Unassigned	N/A
1161-1169	↑	Tyrosine, lipids	Cheng *et al*. (2005); Dukor (2002)

1176-1182	↓	Tyrosine, cytosine, guanine	Notingher *et al*. (2004); Ruiz-Chica *et al*. (2004); Stone *et al*. (2004)
1191-1203	↓	Amide III	Chan *et al*. (2006); Malini *et al*. (2006); Notingher *et al*. (2004)
1216-1244	↓	A, T, amide III and C-N stretching	Notingher *et al*. (2004); Stone *et al*. (2004); Dukor (2002); Naumann (1998)
1281-1291	↑	Phosphodiester, cytosine	Ruiz-Chica *et al*. (2004); Dukor (2002)
1340-1347	↓	CH_3CH_2 wagging, guanine, glucose	Krafft *et al*. (2005); Notingher *et al*. (2004); Frank *et al*. (1995)
1382	↑	Unassigned	N/A
1390	↑	Unassigned	N/A
1402-1415	↑	C=C stretching	Notingher *et al*. (2004)
1424-1440	↑	Deoxyribose, CH_2 deformation	Krafty *et al*. (2005); Hanlon *et al*. (2000)
1457-1497	↓	DNA, A, G ring breathing modes, deoxyribose	Chan *et al*. (2006); Malini *et al*. (2006); Ruiz-Chica *et al*. (2004); Stone *et al*. (2004)
1540-1550	↑	Amide II, tryptophan	Stone *et al*. (2004); Dukor (2002); Stone *et al*. (2002)
1557-1572	↑	Tryptophan, tyrosine	Cheng *et al*. (2005); Lau *et al*. (2003); Lakshimi *et al*. (2002)
1593-1602	↑	C=N and C=C stretching, amide I, phenylalanine	Chan *et al*. (2006); Sigurdsson *et al*. (2004); Huang *et al*. (2003a); Dukor (2002); Naumann (1998)
1610	↑	Cytosine	Ruiz-Chica *et al*. (2004)
1623-1646	↑	Amide I	Faolain *et al*. (2005); Dukor (2002); Lakshimi *et al* (2002)
1655	↓	Amide I	Schulz and Baranska (2007); Shetty *et al*. (2006); Cheng *et al*. (2005); Viehoever *et al*. (2003); Frank *et al*. (1995)
1669-1704	↓	C=C stretching, amide I	Faolain *et al*. (2005); Krafft *et al*. (2005); Kaminaka *et al*. (2002); Lakshimi *et al*. (2002); Hanlon *et al*. (2000)
Band (cm^{-1})	**Δ 0 v 0.5 Gy**	**Band assignment**	**References**
660-680	↓	G, T ring breathing in RNA/DNA, C-S stretching of cystine	Chan *et al*. (2006); Cheng *et al*. (2005); Notingher *et al*. (2004); Stone *et al*. (2002)
700-720	↑	C-N of membrane phospholipid, choline group, cholesterol, DNA	Krafft *et al*. (2005); Binoy *et al*. (2004); Stone *et al*. (2002)
740-760	↓	Tryptophan, DNA	Shetty *et al*. (2006): Cheng *et al*. (2005); Binoy *et al*. (2004); Stone *et al*. (2004); Huang *et al*. (2003); Stone *et al*. (2002)
770-780	↑	Phosphatidylinositol, uracil ring breathing	Farguharson *et al*. (2005); Krafft *et al*. (2005)

820-850	↓	Phosphodiester, O-P-O stretching in DNA/RNA, proline, tyrosine	Cheng *et al*. (2005); Notingher *et al*. (2004); Ruiz-Chica *et al*. (2004); Stone *et al*. (2004); Stone *et al*. (2002)
920-940	↓	C-C backbone	Stone *et al*. (2004); Lau *et al*. (2003); Stone *et al*. (2002); Frank *et al*. (1995)
1000-1020	↓	Phenylalanine	Chan *et al*. (2006); Malini *et al*. (2006); Cheng *et al*. (2005); Frank *et al*. (1995)
1100-1140	↓	C-N and C-C stretching of proteins, lipids	Chan *et al*. (2006); Shetty *et al*. (2006); Cheng *et al*. (2005); Notingher *et al*. (2004); Stone *et al*. (2004); Huang *et al*. (2003a); Stone *et al*. (2002)
1160-1180	↓	Tyrosine, cytosine, guanine	Cheng *et al*. (2005); Notingher *et al*. (2004); Ruiz-Chica *et al*. (2004)
1200-1240	↑	Amide III, hydroxyproline, tyrosine, tryptophan	Cheng *et al*. (2005); Notingher *et al*. (2004); Stone *et al*. (2004); Stone *et al*. (2002); Frank *et al*. (1995)
1250-1270	↓	A, T, C, G, amide III, C-C and C-N stretching	Kateinen *et al*. (2007); Chan *et al*. (2006); Ruiz-Chica *et al*. (2004); Stone *et al*. (2004); Naumann (1998); Frank *et al*. (1995)
1320-1350	↓	CH_3CH_2 wagging of nucleic acids	Lau *et al*. (2005); Huang *et al*. (2003b); Viehoever *et al*. (2003); Stone *et al*. (2002)
1410-1430	↑	A, G of RNA/DNA, deoxyribose	Chan *et al*. (2006); Notingher *et al*. (2004); Ruiz-Chica *et al*. (2004)
1450-1490	↓	DNA, A, G ring breathing modes, deoxyribose, CH_2/CH_3 deformation of lipids	Chan *et al*. (2006); Malini *et al*. (2006); Cheng *et al*. (2005); Ruiz-Chica *et al*. (2004)
1510-1620	↑	Nucleic acids, phenylalanine, tryptophan	Chan *et al*. (2006); Ruiz-Chica *et al*. (2004); Stone *et al*. (2004); Huang *et al*. (2003a); Dukor (2002); Stone *et al*. (2002); Mahadevan-Jansen and Richards-Kortum (1997); Fung *et al*. (1996)
1690-1710	↓	Amide I, C=O in lipids	Lakshimi *et al*. (2002); Shaw and Mantsch (1999)

4.3.4 Spectral difference between lymphocytes from Grade 0-1 and Grade 2+ patients

Next, the spectral difference between lymphocytes from grade 0-1 and grade 2+ patients was investigated to determine if intrinsic biochemical differences could be identified. Figure 4.5 shows mean and difference spectra of unirradiated lymphocytes from the grade 0-1 and grade 2+ patients.

The shaded regions represent where the difference was found to be statistically significant (α=0.05). A summary of the band changes and assignments is shown in Table 3.2. Increases in bands associated with some vibrations of DNA, RNA, proteins, carbohydrates and carotenoids were observed in grade 2+ patients when compared to grade 0-1 patients. Decreases in bands associated with saccharides, lipids, proteins and other vibrations associated with DNA and RNA were observed in grade 2+ patients when compared to grade 0-1 patients.

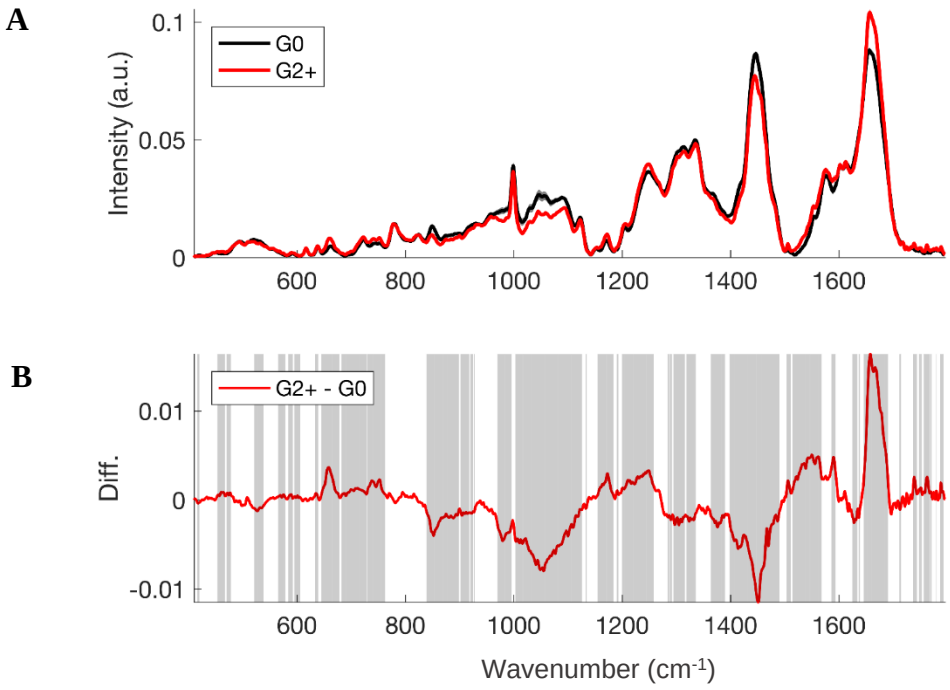

Figure 4.5: (A) Mean spectra of unirradiated lymphocytes from grade 0-1 patients (black) and grade 2+ patients (red). The shaded region around each spectrum indicates the standard error on the mean for each class. (B) Difference spectrum of unirradiated lymphocytes from grade 0-1 and grade 2+ patients. Shading represents regions of the spectrum that were found to be significantly different (two-tailed unpaired t-test with α=0.05).

Table 4.4: Summary of band changes and associated tentative assignments between spectra from lymphocytes from grade 0-1 and grade 2+ patients

Band (cm^{-1})	Δ G0-1 v G2+	Band assignment	References
649-678	↑	G, T ring breathing, C-S stretch in cytosine	Chan *et al*. (2006); Notingher *et al*. (2004); Stone *et al*. (2004)
685-730	↑	C-N of membrane phospholipid, choline group, cholesterol, DNA	Krafft *et al*. (2005); Binoy *et al*. (2004); Stone *et al*. (2004); Stone *et al*. (2002)
732-762	↑	T ring breathing, symmetric breathing of trytophan	Shetty *et al*. (2006); Cheng *et al*. (2005); Krafft *et al*. (2005); Stone *et al*. (2004); Huang *et al*. (2003); Stone *et al*. (2002)
835-898	↑	Saccharides, tyrosine, hydroxyproline, proline	Shetty *et al*. (2006); Cheng *et al*. (2005); Krafft *et al*. (2005); Stone *et al*. (2004); Huang *et al*. (2003)
903-927	↓	C-C skeletal modes	Stone *et al*. (2004); Stone *et al*. (2002)
971-996	↓	C-C skeletal modes	Notingher *et al*. (2004); Lakshimi *et al*. (2002); Frank *et al*. (1995)
1004-1126	↑	Phenylalanine ring breathing, various lipid modes ($–PO_2^-$, ν C-C, ν C-O), ν C-O carbohydrate, triglycerides, fatty acids	Cheng *et al*. (2005); Krafft *et al*. (2005); Notingher *et al*. (2004); Stone *et al*. (2004); Huang *et al*. (2003); Silveira *et al*. (2002)
1156-1184	↑	Cytosine, guanine, phenylalanine, tyrosine	Chan *et al*. (2006); Cheng *et al*. (2005); Ruiz-Chica *et al*. (2004); Lakshimi *et al*. (2002)
1193	↑	Unassigned	N/A
1202-1258	↑	Hydroxyproline, tyrosine; Amide III, tryptophan	Chan *et al*. (2006); Notingher *et al*. (2004); Stone *et al*. (2004); Dukor (2002); Frank *et al*. (1995)
1285-1292	↓	Cytosine	Ruiz-Chica *et al*. (2004)
1295-1316	↓	Lipid CH deformation, fatty acids	Kateinen *et al*. (2007); Cheng *et al*. (2005); Stone *et al*. (2004); Huang *et al*. (2003a); Dukor (2002); Hanlon *et al*. (2000)
1320-1335	↓	CH_3CH_2 twisting, bending and/or twisting of collagen/DNA	Lau *et al*. (2005); Huang *et al*. (2003a); Huang *et al*. (2003b); Viehoever *et al*. (2003)
1366-1390	↓	A, T, G ring breathing of DNA/RNA	Chan *et al*. (2006)
1399-1490	↓	A and G ring breathing, CH deformation, deoxyribose	Chan *et al*. (2006); Kolijenovic *et al*. (2005); Krafft *et al*. (2005); Notingher *et al*. (2004); Ruiz-Chica *et al*. (2004)
1503-1566	↑	Cytosine, carotenoid, tryptophan, amide II	Ruiz-Chica *et al*. (2004); Stone *et al*. (2004); Huang *et al*. (2003); Dukor (2002); Stone *et al*. (2002); Mahadevan-Jansen and Richards-Kortum (1997)

1586-1593	↑	Phenylalanine, hydroxyproline, C=N and C=C stretching	Cheng *et al*. (2005); Naumann (1998)
1625-1639	↑	Amide I	Faolain *et al*. (2005); Dukor (2002); Lakshimi *et al*. (2002)
1646-1692	↑	Amide I	Shetty *et al*. (2006); Faolain *et al*. (2005); Stone *et al*. (2004); Viehoever *et al*. (2003); Stone *et al*. (2002); Frank *et al*. (1995)
1714	↑	Unassigned	N/A
1738-1770;	↑	Lipids, phospholipids, triglycerides	Shetty *et al*. (2006); Huang *et al*. (2003a); Dukor (2002); Lakshimi *et al*. (2002); Silveira *et al*. (2002); Mordechai *et al*. (1998)

4.3.5 Classification of Grade 0-1 versus Grade 2+ Patients

Classifications of lymphocyte spectra from grade 0-1 and grade 2+ patients were performed to investigate if the two patient groups could be discriminated. PLSDA models were developed as described earlier. Independent models were built using spectra of unirradiated and irradiated lymphocytes. The resulting accuracies, sensitivities and specificities are provided in Table 4.3 and are calculated for the cross-validated PLSDA model. An example of the cross-validation performance of the PLSDA model is shown in Figure 4.6.

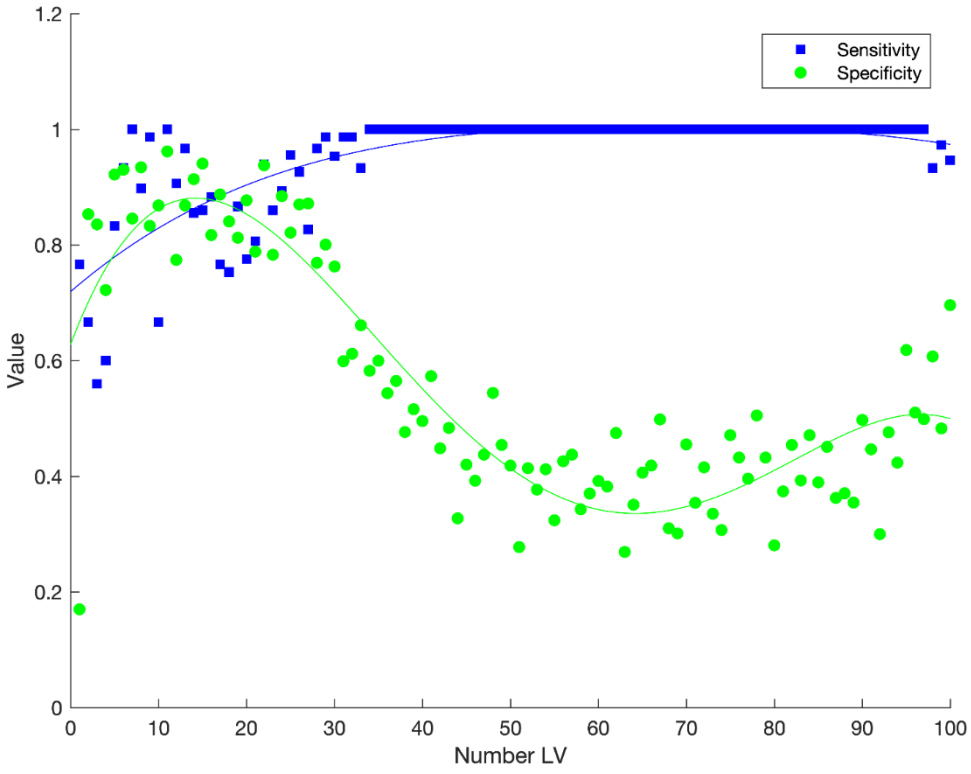

Figure 4.6: Cross-validated sensitivity and specificity of a PLSDA model developed on spectra at 0 Gy. Fitted lines are intended as a guide to the eye, rather than implying a particular mathematical relationship.

Table 4.5: Accuracies, sensitivities and specificities for the PLSDA classification of grade 0-1 versus grade 2+ patients using spectra from unirradiated (0 Gy) and irradiated (0.05 Gy and 0.5 Gy) lymphocytes. The figures in brackets indicate the standard deviation over multiple evaluations for that particular metric.

Dose (Gy)	Sensitivity	Specificity	Accuracy	num LV*
0	0.95 (0.03)	0.92 (0.03)	0.93	13
0.05	0.72 (0.03)	0.70 (0.07)	0.71	9
0.5	0.74 (0.06)	0.70 (0.08)	0.72	6

*Number of latent variables

The optimised PLSDA models performed relatively well for the unirradiated lymphocytes with an accuracy, sensitivity and specificity of 0.93, 0.95 and 0.92, respectively. Poorer performance was achieved for the irradiated lymphocytes. While the model complexity (indicated by the number of latent variables selected by the cross-validated model) is relatively high for the models at 0 Gy, the generalizability of these models to unseen data, i.e., data that has not been used for model development, reinforces the view that the models are being developed on real and consistent Raman signals observed in the data. Figure 4.7 depicts an exemplary ROC which was calculated for the models on spectra at 0 Gy.

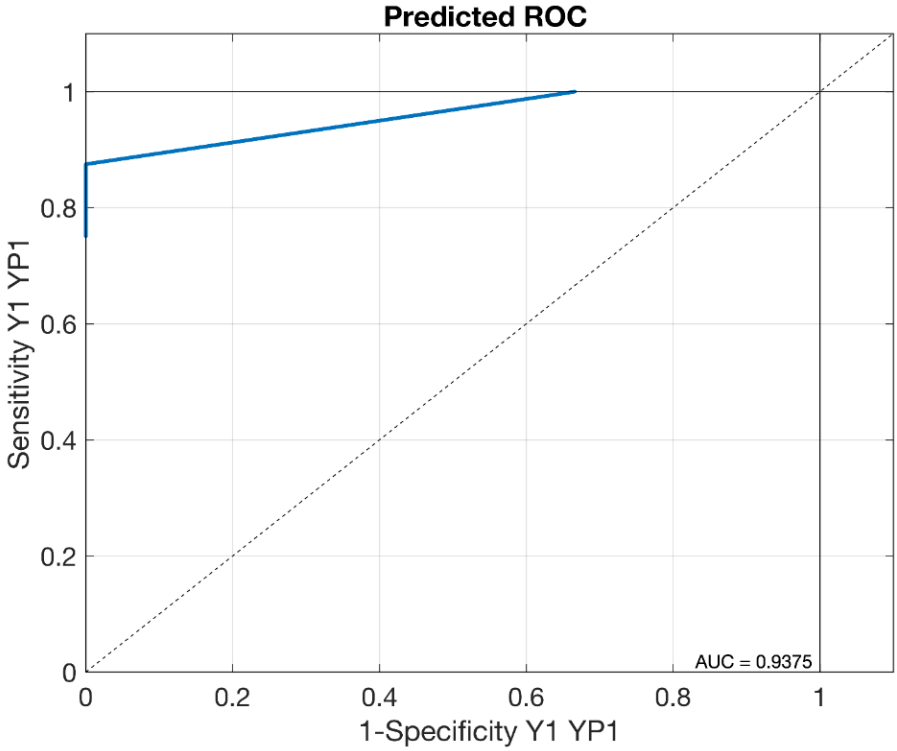

Figure 4.7: Receiver operator characteristic for a cross-validated PLSDA classification of grade 0-1 versus grade 2+ patient groups using spectra from unirradiated (0 Gy) lymphocytes. AUC indicates the area under the curve.

An additional analysis was also carried out whereby the class is randomly assigned to the spectra input to the model at training, as described by Westerhuis *et al*. (2008). The same training and testing methodology was then used and the results are depicted in Figure 4.8, where sensitivity and specificity average to 48% across the LV scale. This demonstrates that while the models reported here are relatively complex, a consistent and generalisable signal is identified and learnt by our PLSDA models.

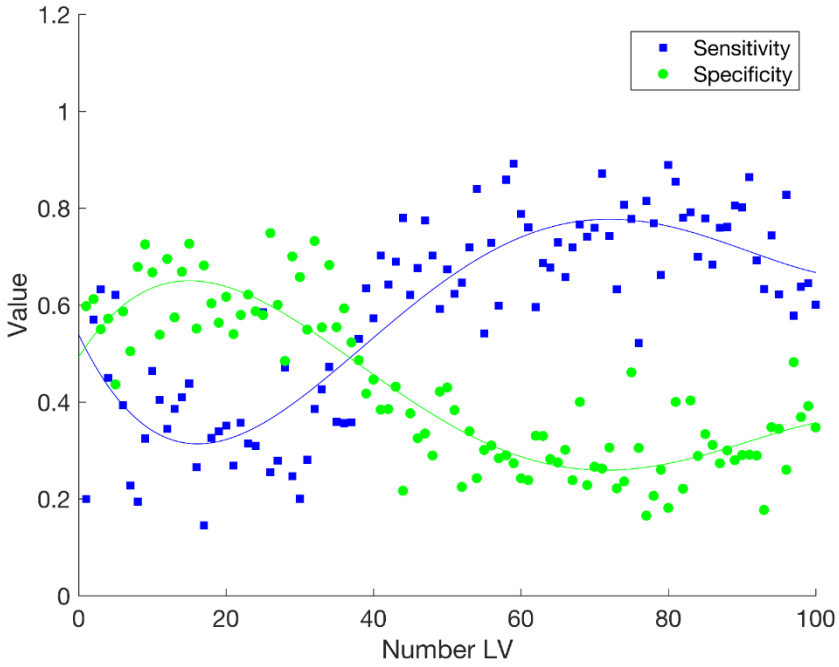

Figure 4.8: Cross-validated sensitivity and specificity of a PLSDA model in which class targets are randomized to test quality of PLSDA model developed on spectra at 0 Gy, according to a method proposed by Westerhuis *et al*. (2008). Overall classification accuracy averages in the region of 48% indicating that models are incapable of developing predictions when inappropriate classification targets are supplied.

4.4 Discussion

An increased mean G2 score was observed in the grade 2+ patients compared to the grade 0-1 patients but this was not statistically significant due to inter-individual variability. Previous studies by Finnon *et al*. (2012) for breast cancer patients and Brzozowska *et al*. (2012) for PCa patients also observed significant inter-individual variability in G2 radiosensitivity and no significant difference between patients with or without late adverse reactions. Our previous study established a radiosensitivity cut-off value of 132 using the 90th percentile of the G2 scores of healthy individuals (White *et al*., 2020).

This cut-off is in line with radiosensitivity cut-off values that have been reported previously (De Ruyck *et al*., 2008; Howe *et al*., 2005; Baeyens *et al*., 2002; Thierens *et al*., 2002; Vral *et al*., 2002; Baria *et al*., 2001; Scott *et al*., 1999). Using this G2 cut-off score of 132, only 27% of the grade 0-1 group compared to 60% of the grade 2+ group were above the radiosenstivity cut-off value. Although it would have been more relevant to carry out the G2 assay on PBMC cultures for this study as PBMC cultures were used for the γH2AX assay and the Raman assay, it was decided to use whole blood cultures as these are routinely used for the G2 assay and because our previous study establishing the radiosensitivity cut-off value of 132 had used whole blood cultures. In addition, white blood cell counts would have been very informative, but unfortunately as only one-off blood samples were available for the study, not enough material remained for these additional tests.

An increase in γH2AX fluorescence was observed for both groups 1 hr following *in-vitro* irradiation at each dose but again no statistically significant difference was found between the two groups due to the high level of inter-individual variability particularly in the grade 2+ group. Although previous studies have shown correlations between residual γH2AX fluorescence (>6 hrs post-irradiation) and late normal tissue toxicity (Vandevoorde *et al*., 2016; Bourton *et al*., 2011; Chua *et al*., 2011), γH2AX fluorescence was assessed at 1 hr post-irradiation in the present study to allow direct comparsion to the well established G2 assay. Inter-individual variability in the early damage response may explain the lack of correlation to late normal tissue toxicity, but other studies have failed to show correlations between residual γH2AX fluorescence and late normal tissue toxicity (Brzozowska *et al*., 2012; Finnon *et al*., 2012; Werbrouck *et al*., 2010).

In addition, a study by Felgentreff *et al*. (2021) demonstrated that the damage response capacity of lymphocyte subsets to irradation differs, particularly when comparing T- and B-lymphocytes to natural killer cells. As a result, any correlation between residual γH2AX fluorescence and late normal tissue toxicity may be masked by the differing responses of the lymphocyte subsets to irradiation and thus individual analyses of the lymphocyte subsets may be necessary to identify any relationship between residual γH2AX fluorescence and late normal tissue toxicity. Furthermore, although the flow cytometry γH2AX assay used here is not as sensitive as assays based on manual or automated foci scoring by microscopy, positive correlations between γH2AX fluorescence and late normal tissue toxicity have been found using both microscopy (Vandevoorde *et al*., 2016; Chua *et al*., 2011) and flow cytometry assays (Bourton *et al*., 2011).

The radiation response of the lymphocytes from grade 0-1 and grade 2+ groups was investigated. Similar responses in spectral regions associated with DNA, RNA, proteins and lipids were observed for the grade 0-1 and grade 2+ groups, correlating well with previous studies on normal and tumour cells irradiated *in-vitro* (Qiu *et al*., 2020; Meade *et al*., 2016; Harder *et al*., 2015; Maguire *et al*., 2015a; Matthews *et al*., 2011) and relating to DNA damage and cellular response to that damage. Interestingly, more significant differences between unirradiated and irradiated lymphocytes were observed in the grade 2+ group. This may be due to a more pronounced change in spectral features following *in-vitro* irradiation for the grade 2+ group. This correlates well with the results of the *in-vitro* cellular radiosensitivity assays where more pronounced effects were observed in the grade 2+ compared to the grade 0-1 group.

A previous study by Maguire *et al.* (2015a) using lymphocytes from healthy donors showed inter-individual variability in classification performance between unirradiated and irradiated lymphocytes with higher sensitivity and specificity for some donors suggesting more pronounced changes in spectral features of their lymphocytes following *in-vitro* irradiation. In the present study, the more pronounced effects were observed in the grade 2+ group, suggesting increased radiosensitivity compared to the grade 0-1 group.

Significant spectral differences associated with vibrations of DNA, RNA, carotenoids, carbohydrates, proteins, lipids and other cellular components were observed between the grade 0-1 and the grade 2+ groups. Classification of grade 0-1 versus grade 2+ groups yielded good accuracy using the PLSDA model. Significantly, a high classification accuracy was achieved for the unirradiated lymphocytes from each group. This suggests that *in-vitro* irradiation may not be required for the future prediction of patient toxicity and that the intrinsic spectral phenotype of the patient may be sufficient to discriminate on radiation toxicity.

Interestingly, the intrinsic spectral differences between patients with grade 0-1 and grade 2+ toxicity were related not only to DNA, which is normally assessed in *in-vitro* radiosensitivity assays, but also to proteins and lipids. It is important to note however, that late toxic effects as a result of hormone therapy may have had some influence on the results in the current study. While studies by Valicenti *et al*. (2003), Jani and Gratzle (2005) and Jani *et al.* (2005) have found that PCa patients that underwent both radiation and hormone therapy did not show an independent effect on the risk of late toxic side effects as a result of hormone therapy, a more recent study by Hata *et al.* (2021) suggests that hormone therapy may have an impact on toxicity outcome.

The findings of Hata *et al.* (2021) were related to acute toxicity outcomes only however, while the findings of Jani and Gratzle (2005) and Jani *et al.* (2005) were related to late toxic effects, suggesting that the findings in the present study may be interpreted independent of any toxic effects of hormone therapy. The findings of the present study, however, would need to be confirmed in a larger patient population and would need to be further validated in an independent set of patients.

4.5 Conclusion

In conclusion, this chapter presents, for the first time, the novel application of Raman micro-spectroscopy to identify RT patients with late normal tissue toxicity. Spectral differences were identified between lymphocytes from patients with severe (grade 2+) late radiation toxicity and those with no/minimal (grade 0-1) late radiation toxicity which allowed the classification of patients with a high degree of accuracy.

Chapter 5 – Raman Micro-spectroscopy for the Prediction of Prostate Cancer Patients at Risk of Late Radiation Toxicity Following Radiotherapy

5.1 Introduction

In chapter 4, it was shown that Raman micro-spectroscopic analysis of lymphocytes taken from PCa patients *following* RT allowed for classification of these patients based on their radiosensitivity. The aim of the present study was to evaluate Raman micro-spectroscopy as an assay for the prediction of late normal tissue toxicity by investigating spectral differences in lymphocytes obtained *prior to* treatment from PCa patients who later developed no or minimal toxicity (grade 0-1) or severe toxicity (grade 2+). *In-vitro* cellular radiosensitivity was again assessed in parallel using the G2 chromosomal radiosensitivity assay and the γH2AX DNA damage assay.

5.2 Materials and Methods

5.2.1 Patient Samples

Clinical details of both patient groups are shown in Table 5.1 and figure 5.1 shows an overview of the patient identification, sample processing, *in-vitro* irradiation and subsequent assays.

Table 5.1: Clinical features of grade 0-1 and grade 2+ patients. Data are number of patients unless otherwise stated.

	Grade 0-1 (n= 17)	**Grade 2+ (n= 18)**
Age (years)		
Mean	66.3	72.9
Median	65	71.5
Range	57-77	66-85
PSA (ng/ml)		
Mean	33.5	12.0
Median	41.0	9.1
T Stage		
T1c to T2a	4 (23.5 %)	2 (11.1 %)
T2b to T2c	3 (17.6 %)	2 (11.1 %)
T3a	5 (29.4 %)	11 (61.1 %)
T3b to T3c	4 (23.5 %)	3 (16.7 %)
T4	1 (5.9 %)	0 (0 %)
Gleason score		
6	0 (0 %)	1 (5.6 %)
7	4 (23.5 %)	4 (22.2 %)
8	8 (47.1 %)	8 (44.4 %)
9	5 (29.4 %)	5 (27.8 %)
Planned duration of hormones*		
6 months NSAA	1 (7.7 %)	2 (11.1 %)
36 months LHRH	13 (76.5 %)	9 (50 %)
6 months NSAA+36 months LHRH	2 (11.8 %)	4 (22.2 %)
RT dose/ fractions		
81.0/ 45	17 (100 %)	18 (100 %)

*** Data mssing for one grade 0-1 patient and three grade 2+ patients**

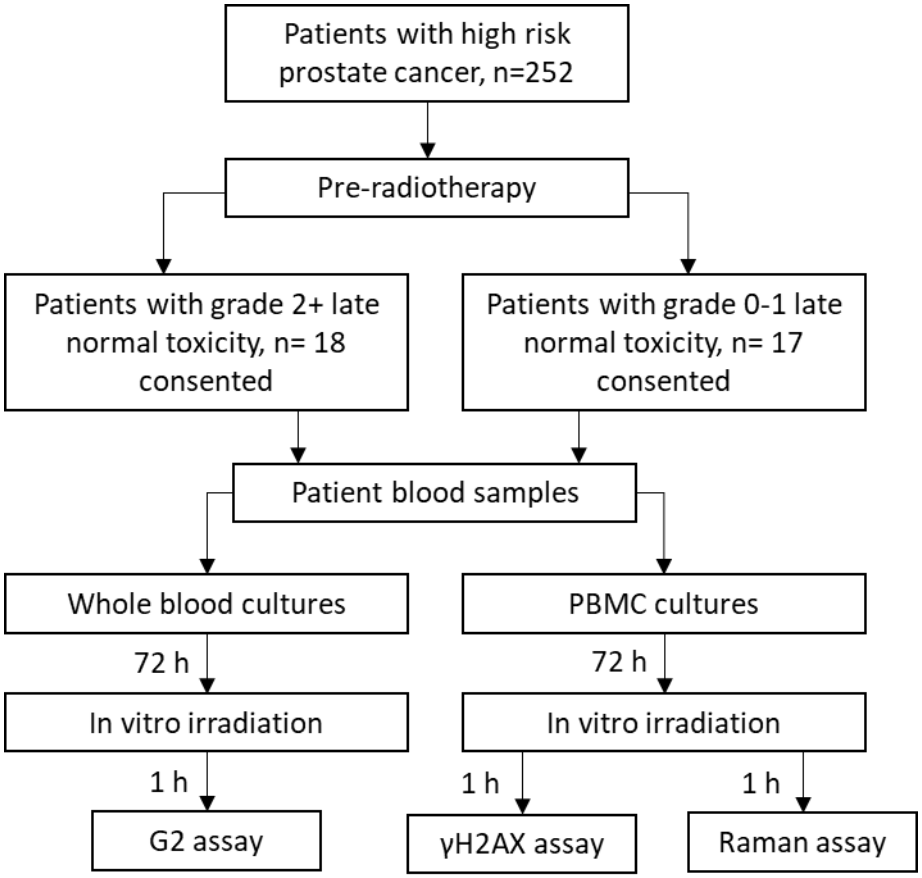

Figure 5.1: Schematic showing an overview of patient identification, sample processing, *in-vitro* irradiation, G2 assay, γH2AX assay and Raman assay.

5.2.2 Cell Culturing

Cell culturing was carried out as described in section *3.1.1 Cell Culturing*.

5.2.3 Sample Irradiation

Sample irradiation was carried out as described in section *3.1.2 Sample Irradiation*.

5.2.4 Calcium Fluoride Slide Preparation

Calcium fluoride slide preparation was carried out as described in section *3.1.3 Calcium Fluoride Slide Preparation*.

5.2.5 γH2AX DNA Damage Assay

The γH2AX DNA damage assay was carried out as described in section *3.2.1 γH2AX DNA Damage Assay*.

5.2.6 G2 Chromosomal Radiosensitivity Assay

The G2 chromosomal radiosensitivity assay was carried out as described in section *3.2.2 G2 Chromosomal Radiosensitivity Assay*.

5.2.7 Raman Spectral Acquisition and Analysis

Raman spectral acquisition was carried out as described in section *3.3.1 Raman Spectral Measurements of Lymphocytes* and Raman spectral pre-processing was carried out as described in section *3.3.2 Raman Spectral Pre-processing*. Mean spectra were generated for both the grade 0-1 and grade 2+ toxicity groups and difference spectra were obtained by subtracting the mean spectra for the grade 0-1 toxicity group from the mean spectra for the grade 2+ toxicity group. Unpaired two-tailed Student's *t*-tests were then applied across all wavenumbers to identify statistically significant spectral differences between the two groups ($\alpha = 0.05$). Mean and difference spectra in conjunction with unpaired two-tailed Student's *t*-tests ($\alpha = 0.05$) were also used to examine differences in irradiation dose response in each group. PCA and *K*-means cluster analysis was performed thereafter to explore variation within the dataset and identify any patterns present. Confidence ellipses were generated at the 95% confidence level for each PCA plot. Model development was carried out as described in section *3.3.4 Model Development*.

5.3 Results and Discussion

5.3.1 γH2AX DNA Damage Assay

Figure 5.2 shows the increase in γH2AX fluorescence 1 hr after *in-vitro* irradiation for the grade 0-1 and grade 2+ patients (Grade 0-1 mean = 1.3±1.2 and 1.2±0.9 at 0.05 and 0.5, respectively; Grade 2+ mean = 0.9±1.0 and 1.3±1.8 at 0.05 Gy and 0.5, respectively). The grade 0-1 patient group showed an increase in γH2AX fluorescence at both irradiation doses (0.05 Gy and 0.5 Gy) with a slightly more pronounced increase observed at the 0.5 Gy dose. The grade 2+ patient group on the other hand, showed slight decreases in γH2AX fluorescence at both irradiation doses. The differences observed were not statistically significant however (α = 0.05) due to the high level of inter-individual variation.

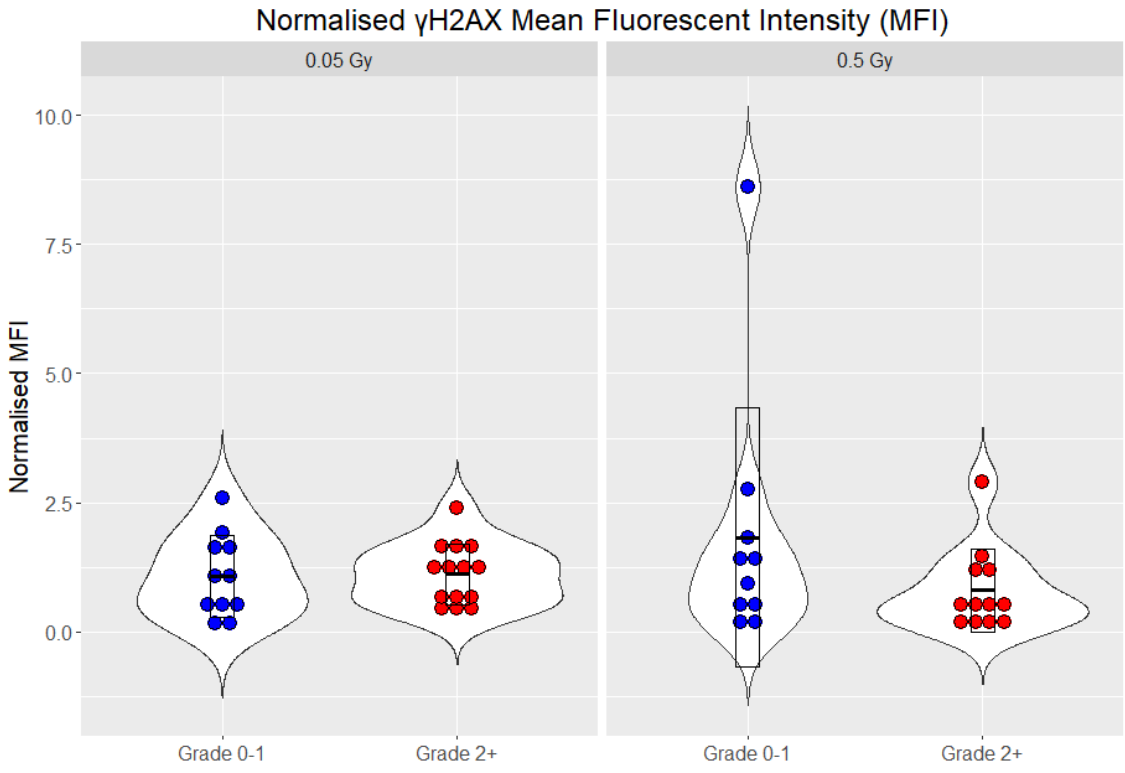

Figure 5.2: Relative increase in γH2AX fluorescence 1 hr after *in-vitro* irradiation to 0.05 Gy and 0.5 Gy for grade 0-1 and grade 2+ patients. The error bars indicate the standard deviation.

5.3.2 G2 Chromosomal Radiosensitivity Assay

Figure 5.3 shows the radiation-induced G2 scores for the grade 0-1 and grade 2+ patients irradiated at 0.5 Gy. The radiosensitivity cut-off value (90th percentile score) was calculated from healthy controls to be 132 aberrations per 100 metaphases. Individuals with a normalised G2 score exceeding this cut-off were considered radiosensitive. The mean G2 score was 145±56.4 (range 92-272, %CV 38.7) for grade 0-1 patients and 135±38.58 (range 48-234, %CV 28.4) for grade 2+ patients but there was no statistically significant difference in G2 score between the two groups. It was observed that the grade 0-1 group distribution was bimodal, indicating that there may be more than one population within the dataset. A Wilcoxon signed rank test was thus carried out which indicated that there may be two populations within the dataset (p = 0.0001; α = 0.05).

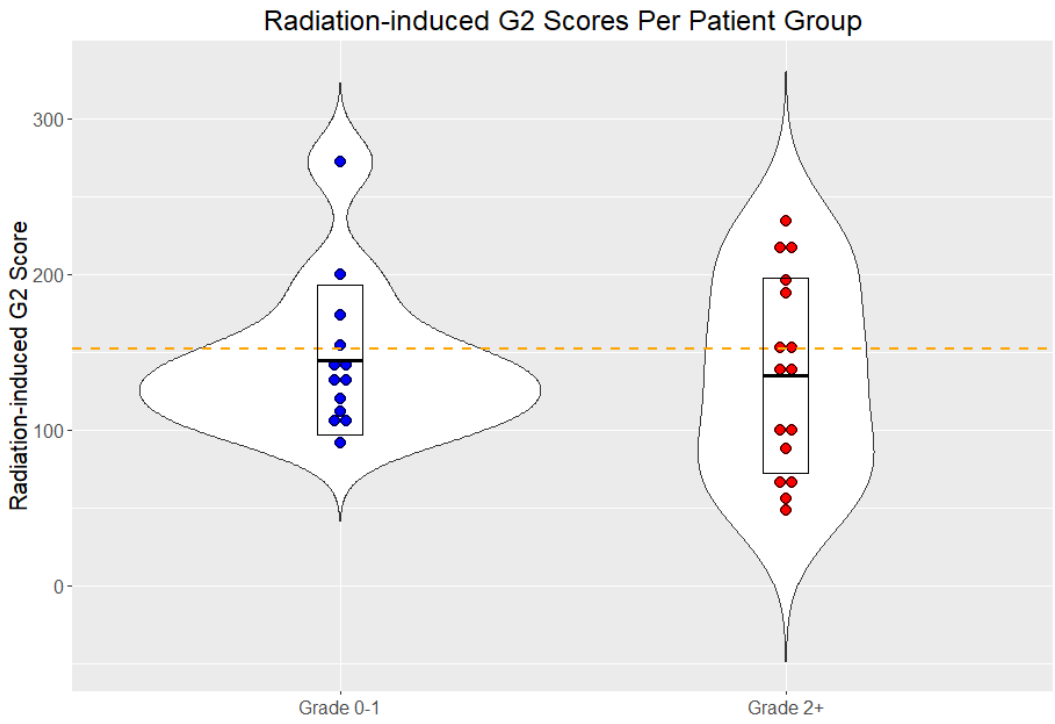

Figure 5.3: Radiation-induced G2 scores for grade 0-1 and grade 2+ patients. Orange dotted line shows the 90th percentile cut-off value of 132.

5.3.3 Radiation response of lymphocytes from Grade 0-1 and Grade 2+ patients

To investigate the radiation response of the lymphocytes from grade 0-1 and grade 2+ patients to *in-vitro* irradiation, the difference spectra of unirradiated and irradiated lymphocytes were calculated for each patient group separately. Figure 5.4 shows the mean spectra of unirradiated and irradiated lymphocytes from grade 0-1 and grade 2+ patients and the difference spectra of unirradiated and irradiated lymphocytes for each patient group. The shaded regions show where the spectra of the irradiated lymphocytes were found to be significantly different to the unirradiated lymphocytes (α=0.05). Summaries of the band changes for the grade 0-1 and grade 2+ patients following irradiation are provided in Table 5.2 and 5.3, respectively. Numerous significant changes in nucleic acids, proteins, carbohydrates and lipids were observed after irradiation to 0.05 and 0.5 Gy in lymphocytes from grade 0-1 patients. Conversely, very few significant changes were observed after irradiation to 0.05 and 0.5 Gy in lymphocytes from grade 2+ patients.

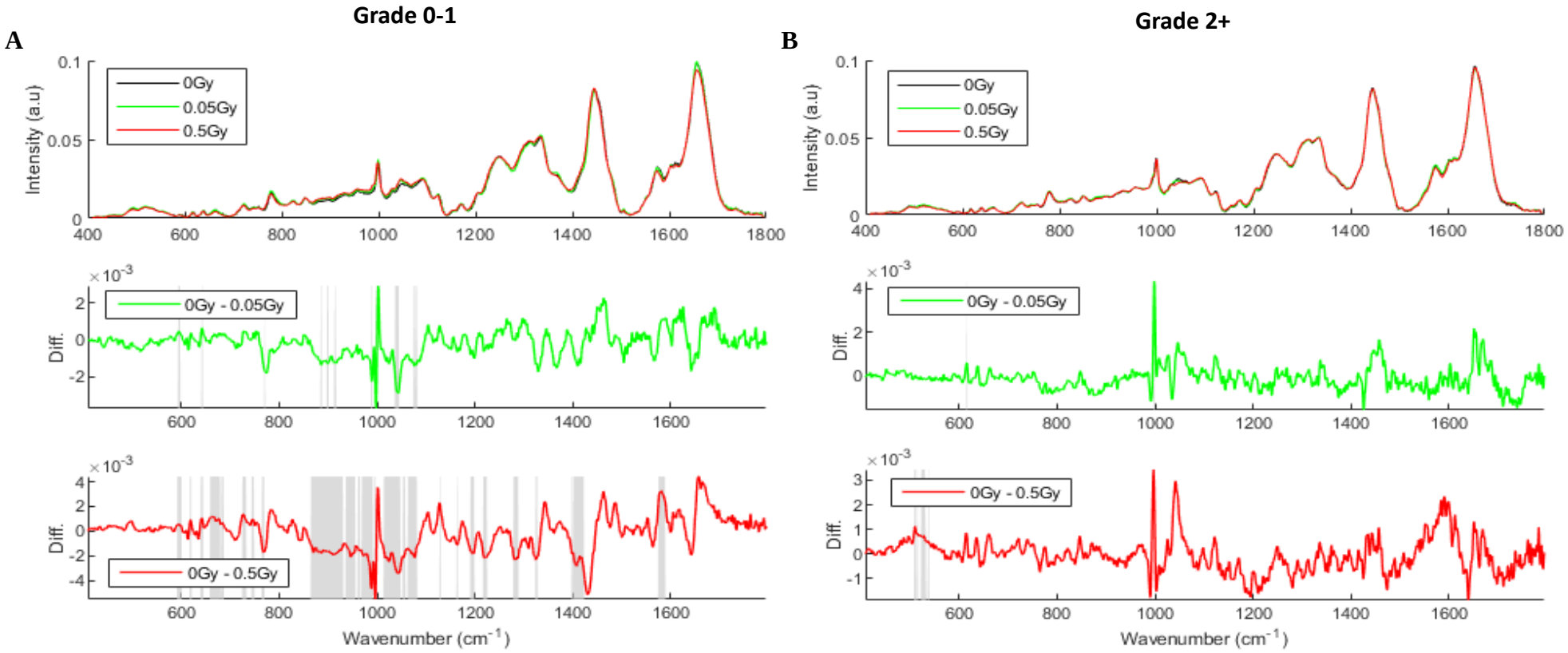

Figure 5.4: Lymphocyte response to 0.05 Gy and 0.5 Gy in (A) grade 0-1 and (B) grade 2+ patient groups. Top panels display the mean spectra (with a shaded region around each mean spectrum indicating the standard error on the mean for that class) and bottom panels display the difference between the spectrum of the unirradiated and irradiated cells. Shading within the middle and bottom panels represents regions of the spectrum that were found to be significantly different (two-tailed unpaired t-test with α=0.05).

Table 5.2: Summary of band changes and associated tentative assignments between spectra from unirradiated and irradiated lymphocytes from grade 0-1 patients

Band (cm^{-1})	**Δ 0 v 0.05 Gy**	**Band assignment**	**Reference**
593 – 598	↑	Phosphatidylinositol	Krafft *et al*. (2005)
641 – 644	↑	C-C twisting mode of tyrosine	Cheng *et al*. (2005); Stone *et al*. (2004)
769 – 772	↓	Unassigned	N/A
884 – 889	↓	Proteins, disaccharide	Shetty *et al*. (2006); Binoy *et al*. (2004)
898 – 900	↓	Monosaccharides, disaccharide	Shetty *et al*. (2006)
912 – 913	↓	Glucose	Krafft *et al*. (2005)
914 – 917	↓	Ribose vibration	Chan *et al*. (2006)
987 – 990	↓	Unassigned	N/A
996 – 999	↓	C-C, C-O ribose	Dukor (2002)
1036 – 1045	↓	Carbohydrates, proline	Dukor (2002); Frank *et al*. (1995)
1074 – 1078	↓	Lipids, phospholipids	Huang *et al*. (2003)
1079 – 1082	↓	Phospholipids, nucleic acids, carbohydrates, collagen	Malini *et al*. (2006); Gazi *et al*. (2003); Dukor (2002); Andrus & Strickland (1998)
Band (cm^{-1})	**Δ 0 v 0.5 Gy**	**Band assignment**	**Reference**
591 – 601	↑	Phosphatidylinositol	Krafft *et al*. (2005)
617 – 621	↑	C-C twisting mode of proteins	Stone *et al*. (2004); Frank *et al*. (1995); Stone *et al*. (2002)
639 – 645	↑	C-S stretching and C-C twisting of proteins	Frank *et al*. (1995)
658 – 680	↑	Ring breathing mode in DNA bases, C-S stretching of cytosine	Stone *et al*. (2004); Frank *et al*. (1995)
681 – 687	↑	Unassigned	N/A
724 – 733	↑	Adenine, phosphatidylserine, proline	Chan *et al*. (2006); Krafft *et al*. (2005); Notingher *et al*. (2004); Frank *et al*. (1995)
743 – 749	↓	DNA/RNA bases, tryptophan	Chan *et al*. (2006); Cheng *et al*. (2005); Huang *et al*. (2003a); Stone *et al*. (2002)
764 – 770	↓	Pyrimidine ring breathing mode	Farguharson *et al*. (2005)

864 – 931	↓	Ribose, deoxyribose, monosaccharides, disaccharides, proline, hydroxyproline, tryptophan	Chan *et al*. (2006); Shetty *et al*. (2006); Cheng *et al*. (2005); Ruiz-Chica *et al*. (2004); Stone *et al*. (2004)
935 – 956	↓	C-C stretching mode of proline, valine and protein backbone	Huang *et al*. (2003); Stone *et al*. (2002)
960 – 966	↓	Proteins	Huang *et al*. (2003a);
968 – 992	↓	Lipids, ribose, C-C stretching of proteins	Chan *et al*. (2006); Notingher *et al*. (2004); Dukor (2002)
994 – 998	↓	C-C, C-O ribose	Dukor (2002)
1013 – 1048	↓	Glycogen, phenylalanine, proline	Cheng *et al*. (2005); Dukor (2002); Frank *et al*. (1995)
1052 – 1058	↓	C-N stretching of proteins, lipids	Chan *et al*. (2006); Dukor (2002)
1062 – 1082	↓	Palmitic acid, fatty acids, triglycerides, carbohydrates	Krafft *et al*. (2005); Dukor (2002); Silveira *et al*. (2002)
1127 – 1130	↑	C-N stretching of proteins, C-O stretching of carbohydrates, lipids	Cheng *et al*. (2005); Notingher *et al*. (2004); Dovbeshko *et al*. (2000)
1162 – 1165	↓	Tyrosine	Cheng *et al*. (2005)
1190 – 1200	↓	Nucleic acids and phosphates	Andrus & Strickland (1998)
1216 – 1225	↓	C-N stretching, amide III, nucleic acids	Stone *et al*. (2004); Huang *et al*. (2003); Naumann (1998)
1278 – 1289	↓	Proteins, amide III, nucleic acids	Binoy *et al*. (2004); Stone *et al*. (2004); Dukor (2002); Andrus & Strickland (1998)
1323 – 1328	↓	Guanine, CH_3CH_2 wagging mode in purine bases of nucleic acids	Lau *et al*. (2005); Ruiz-Chica *et al*. (2004)
1397 – 1423	↓	Deoxyribose, ring breathing modes of DNA/RNA bases	Chan *et al*. (2006); Ruiz-Chica *et al*. (2004)
1574 – 1589	↑	Ring breathing modes of DNA/RNA bases, phenylalanine	Chan *et al*. (2006); Cheng *et al*. (2005); Huang *et al*. (2003a)

Table 5.3: Summary of band changes and associated tentative assignments between spectra from unirradiated and irradiated lymphocytes from grade 2+ patients

Band (cm^{-1})	**Δ 0 v 0.05 Gy**	**Band assignment**	**Reference**
615 – 618	↑	Protein C-C twisting	Chan *et al*. (2006)
996 – 999	↑	C-C, C-O ribose	Dukor (2002)
Band (cm^{-1})	**Δ 0 v 0.5 Gy**	**Band assignment**	**Reference**
508 – 513	↑	S-S disulphide stretching in collagen	Shetty *et al*. (2006); Cheng *et al*. (2005)
514 – 519	↑	Phosphatidylinositol	Lakshimi *et al*. (2002)
522 – 531	↑	S-S disulphide stretching in proteins, phosphatidylserine	Stone *et al*. (2004); Krafft *et al*. (2005); Stone *et al*. (2002)
532 – 534	↑	Unassigned	N/A
536 – 539	↑	Cholesterol ester	Krafft *et al*. (2005)

5.3.4 Spectral difference between lymphocytes from Grade 0-1 and Grade 2+ patients

Next, the spectral difference between lymphocytes from grade 0-1 and grade 2+ patients was investigated to determine if intrinsic biochemical differences could be identified. Figure 5.5 shows mean and difference spectra of unirradiated lymphocytes from the grade 0-1 and grade 2+ patients as well as the mean and difference spectra of lymphocytes irradiated to 0.05 Gy and 0.5 Gy. The shaded regions represent where the difference was found to be statistically significant ($\alpha = 0.05$). A summary of the band changes and assignments is shown in Table 5.4. Increases in bands associated with vibrations of carbohydrates were observed in grade 2+ patients when compared to grade 0-1 patients at 0 Gy. Decreases in bands associated with vibrations of DNA, RNA, proteins, and lipids were observed in grade 2+ patients when compared to grade 0-1 patients at 0 Gy.

At 0.05 Gy, decreases in bands associated with vibrations of DNA, RNA and proteins were observed in grade 2+ patients when compared to grade 0-1 patients with both increases and decreases observed for bands associated with vibrations of lipids between these two patient groups. At 0.5 Gy, decreases in bands associated with vibrations of DNA, RNA, carbohydrates and lipids were observed in grade 2+ patients when compared to grade 0-1 patients with both increases and decreases observed for bands associated with vibrations of proteins between the two patient groups.

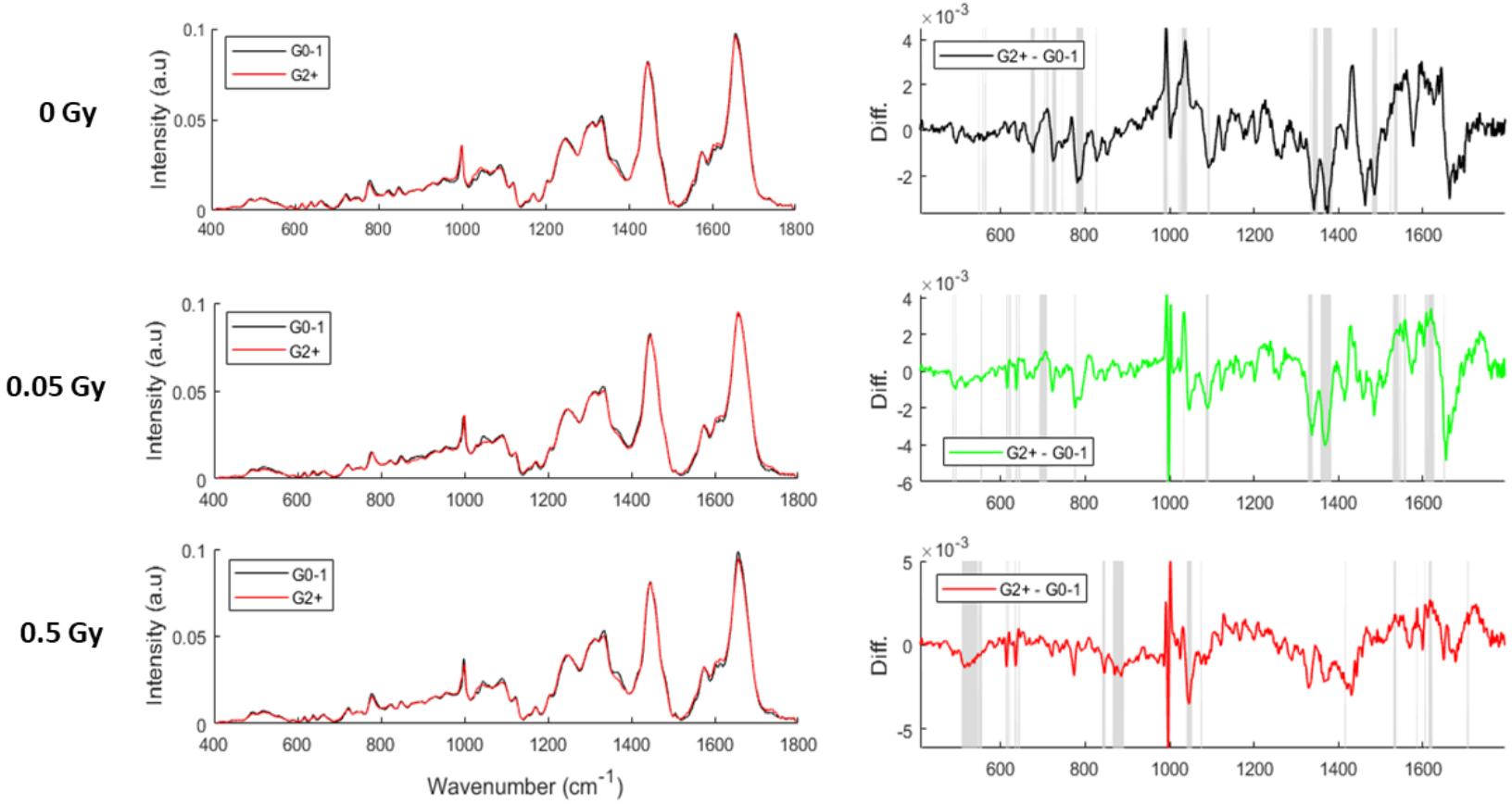

Figure 5.5: Mean (left) and difference (right) spectra of unirradiated and irradiated lymphocytes from grade 0-1 patients and grade 2+ patients. Shading represents regions of the spectrum that were found to be significantly different (two-tailed unpaired t-test with α=0.05).

Table 5.4: Summary of band changes and associated tentative assignments between spectra from lymphocytes from grade 0-1 and grade 2+ patients

Band (cm^{-1})	Δ G0-1 v G2+ at 0 Gy	Band assignment	Reference
548 – 550	↓	Cholesterol	Krafft *et al*. (2005)
557 – 560	↓	Unassigned	N/A
563 – 566	↓	Unassigned	N/A
670 – 681	↓	Ring breathing mode in DNA bases	Chan *et al*. (2006)
702 – 705	↑	Cholesterol, cholesterol ester	Krafft *et al*. (2005)
708 – 713	↑	Unassigned	N/A
721 – 732	↓	DNA, proline	Binoy *et al*. (2004); Frank *et al*. (1995)
745 – 747	↓	Thymine ring breathing mode	Chan *et al*. (2006)
778 – 796	↓	Thymine, cytosine, uracil, O-P-O stretching in DNA, phosphatidylserine	Chan *et al*. (2006); Krafft *et al*. (2005); Notingher *et al*. (2004)
825 – 828	↓	O-P-O stretching in DNA, proline, hydroxyproline, tyrosine, phosphodiester	Cheng *et al*. (2005); Ruiz-Chica *et al*. (2004); Stone *et al*. (2004)
985 – 996	↑	C-C, C-O ribose	Dukor (2002)
1021 – 1024	↑	Glycogen	Dukor (2002)
1026 – 1041	↑	Phenylalanine, carbohydrate residues, proline, phospholipids	Cheng *et al*. (2005); Notingher *et al*. (2004); Huang *et al*. (2003a); Dukor (2002); Stone *et al*. (2002); Frank *et al*. (1995)
1090 – 1095	↓	DNA, lipids	Chan *et al*. (2006); Malini *et al*. (2006)
1333 – 1336	↓	Nucleic acids, CH_3CH_2 twisting and wagging in collagen	Kateinen *et al*. (2007); Ruiz-Chica *et al*. (2004); Stone *et al*. (2004); Huang *et al*. (2003a); Stone *et al*. (2002)
1338 – 1351	↓	Nucleic acids, glucose	Krafft *et al*. (2005); Notingher *et al*. (2004); Mahadevan-Jansen & Richards-Kortum (1997); Fung *et al*. (1996)

1363 – 1385	↓	Ring breathing modes of DNA/RNA bases, tryptophan	Chan *et al*. (2006); Cheng *et al*. (2005); Ruiz-Chica *et al*. (2004); Stone *et al*. (2004)
1479 – 1492	↓	Adenine and guanine ring breathing modes, collagen	Chan *et al*. (2006); Stone *et al*. (2004); Kaminaka *et al*. (2001)
1522 – 1525	↑	Carotenoid	Mahadevan-Jansen & Richards-Kortum (1997)
1531 – 1540	↑	Unassigned	N/A
Band (cm-1)	**Δ G0-1 v G2+ at 0.05 Gy**	**Band assignment**	**Reference**
486 – 490	↓	Glycogen	Stone *et al*. (2004)
492 – 495	↓	Unassigned	N/A
552 – 556	↓	Unassigned	N/A
613 – 617	↓	Cholesterol ester	Krafft *et al*. (2005)
619 – 624	↓	C-C twisting mode of phenylalanine	Notingher *et al*. (2004); Stone *et al*. (2004); Stone *et al*. (2002)
635 – 639	↓	Methionine	Shetty *et al*. (2006)
642 – 646	↑	C-C twisting mode of tyrosine and phenylalanine	Cheng *et al*. (2005); Notingher *et al*. (2004); Stone *et al*. (2004)
691 – 710	↑	Cholesterol, cholesterol ester, methionine	Shetty *et al*. (2006); Krafft *et al*. (2005)
774 – 778	↓	Phosphatidylinositol	Krafft *et al*. (2005)
991 – 996	↑	C-C, C-O ribose	Dukor (2002)
997 – 1000	↑	Phenylalanine	Malini *et al*. (2006)
1032 – 1034	↓	CH_2CH_3 bending modes of collagen and phospholipids, phenylalanine, proline	Chan *et al*. (2006); Cheng *et al*. (2005); Huang *et al*. (2003a); Frank *et al*. (1995)
1085 – 1093	↓	DNA phosphate backbone vibration, C-C stretching	Chan *et al*. (2006); Stone *et al*. (2004)
1327 – 1339	↓	Phospholipids, nucleic acids, CH_3CH_2 twisting and wagging mode of collagen and lipids	Malini *et al*. (2006); Cheng *et al*. (2005); Huang *et al*. (2003a); Viehoever *et al*. (2003); Stone *et al*. (2002); Utzinger *et al*. (2001)
1357 – 1383	↓	Guanine, tryptophan, ring breathing modes of DNA/RNA bases	Chan *et al*. (2006); Cheng *et al*. (2005); Ruiz-Chica *et al*. (2004)

1528 – 1543	↑	Carotenoid	Mahadevan-Jansen & Richards-Kortum (1997)
1544 – 1548	↑	Amide II, tryptophan	Stone *et al*. (2004); Dukor (2002); Stone *et al*. (2002)
1554 – 1560	↑	Amide II, tryptophan	Cheng *et al*. (2005); Faolain *et al*. (2005); Lau *et al*. (2003)
1604 – 1627	↑	Phenylalanine, cytosine, tyrosine, tryptophan	Chan *et al*. (2006); Cheng *et al*. (2005); Ruiz-Chica *et al*. (2004); Huang *et al*. (2003a)
1649 – 1652	↓	Amide I	Malini *et al*. (2006); Caspers *et al*. (2001)
Band (cm^{-1})	**Δ G0-1 v G2+ at 0.5 Gy**	**Band assignment**	**Reference**
412 – 415	↓	Phosphatidyinositol	Krafft *et al*. (2005)
507 – 546	↓	Cysteine, cholesterol ester, Phosphatidyinositol, phosphatidylserine	Shetty *et al*. (2006); Krafft *et al*. (2005); Lakshimi *et al*. (2002)
547 – 556	↓	Cholesterol	Krafft *et al*. (2005)
612 – 616	↓	Cholesterol ester	Krafft *et al*. (2005)
618 – 621	↓	C-C twisting of phenylalanine	Notingher *et al*. (2004); Stone *et al*. (2004); Stone *et al*. (2002)
633 – 637	↓	Methionine	Shetty *et al*. (2006)
641 – 645	↑	C-C twisting of tyrosine and phenylalanine	Cheng *et al*. (2005); Notingher *et al*. (2004); Stone *et al*. (2004)
840 – 848	↓	Glucose, monosaccharides, disaccharides	Shetty *et al*. (2006); Stone *et al*. (2004)
865 – 892	↓	Ribose, deoxyribose, monosaccharides, polysaccharides, tryptophan, hydroxyproline, proline	Shetty *et al*. (2006); Cheng *et al*. (2005); Ruiz-Chica *et al*. (2004); Stone *et al*. (2004); Frank *et al*. (1995)
995 – 998	↑	C-C, C-O ribose	Dukor (2002)
1040 – 1053	↓	Carbohydrates, glycogen, C-N stretching of protein, proline	Chan *et al*. (2006); Binoy *et al*. (2004); Dukor (2002); Frank *et al*. (1995)
1074 – 1077	↓	Lipids	Malini *et al*. (2006)
1414 – 1417	↓	Unassigned	N/A
1530 – 1537	↑	Unassigned	N/A
1585 – 1587	↑	Phenylalanine, hydroxyproline	Cheng *et al*. (2005)

1604 – 1607	↑	Cytosine, phenylalanine, tyrosine	Chan *et al*. (2006); Notingher *et al*. (2004); Ruiz-Chica *et al*. (2004); Lakshimi *et al*. (2002)
1613 – 1623	↑	Tyrosine, tryptophan, phenylalanine	Chan *et al*. (2006); Cheng *et al*. (2005); Notingher *et al*. (2004); Huang *et al*. (2003a); Lakshimi *et al*. (2002)
1704 – 1708	↑	Unassigned	N/A

5.3.5 PCA and K-means Cluster Analysis of Grade 0-1 versus Grade 2+ Patients

Figure 5.6 shows the results following PCA of the unirradiated and irradiated lymphocyte spectra from the grade 0-1 and grade 2+ patients. Plots A, B and C show the score plots for 0 Gy, 0.05 Gy and 0.5 Gy respectively, while plots D, E and F show the PC1 loadings at 0 Gy, 0.05 Gy and 0.5 Gy, respectively and plots G, H and I show the PC2 loadings at 0 Gy, 0.05 Gy and 0.5 Gy, respectively. PC1 and PC2 were found to explain 55%, 52% and 65% of the variance from the unirradiated lymphocytes, the lymphocytes irradiated to 0.05 Gy and the lymphocytes irradiated to 0.5 Gy, respectively. The loadings plots of PC1 and PC2 indicate the spectral ranges explaining any differences within the score values. No discrimination was observed between the unirradiated lymphocyte spectra from the grade 0-1 and grade 2+ patients. Furthermore, no discrimination was observed between the lymphocyte spectra from the grade 0-1 and grade 2+ patients irradiated to 0.05 Gy or 0.5 Gy.

Figure 5.7 shows the results following *K*-means cluster analysis of the unirradiated and irradiated lymphocyte spectra from the grade 0-1 and grade 2+ patients (A-C). Following *K*-means cluster analysis, 3 clusters were observed in the spectra from the unirradiated lymphocytes, 4 clusters were observed in the spectra from the lymphocytes irradiated to 0.05 Gy and 3 clusters were observed in the spectra from the lymphocytes irradiated to 0.5 Gy. No clusters were observed based on radiation toxicity outcome. Lymphocyte spectra from 5 patients, however, were observed to form sub-clusters that became more distinct as the radiation dose increased (as shown in figure 5.7 A-C (i-v)). These sub-clusters did not correlate with any clinically measurable outcome including radiation toxicity grade, PSA measurement, Gleason score or tumour grade.

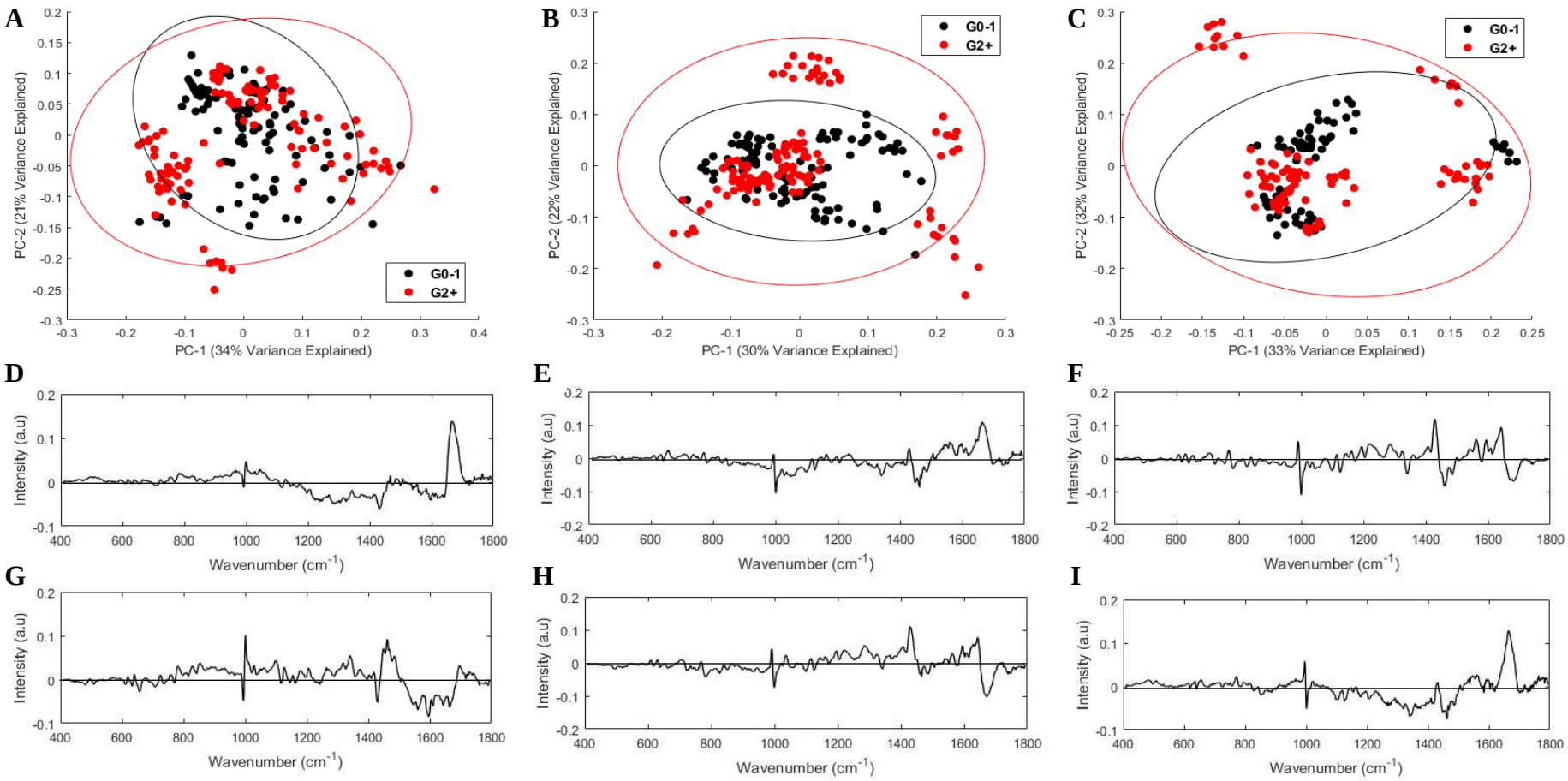

Figure 5.6: PCA scatter plots showing discrimination of grade 0-1 and 2+ toxicity patients at the 0 Gy (A), 0.05 Gy (B) and 0.5 Gy (C) dose following Raman analysis. Confidence ellipses were generated at the 95% confidence level for each PCA plot. Plots D, E and F show the PC1 loadings at 0 Gy, 0.05 Gy and 0.5 Gy, respectively, while plots G, H and I show the PC2 loadings at 0 Gy, 0.05 Gy and 0.5 Gy, respectively.

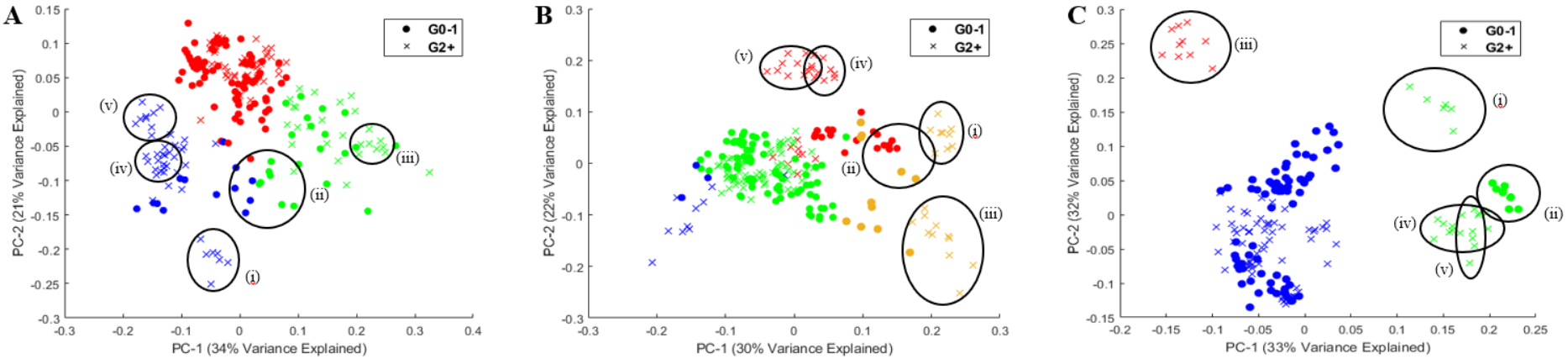

Figure 5.7: PCA scatter plots A, B and C show the discrimination of grade 0-1 (•) and 2+ (x) toxicity patients at the 0 Gy, 0.05 Gy and 0.5 Gy dose respectively, with patient spectra coloured according to the clusters identified following a *K*-means cluster analysis. Three clusters were observed at 0 Gy, four at 0.05 Gy and 3 at 0.5 Gy. The circled spectra represent five patients (i-v) that were observed to form distinct clusters as radiation dose increased.

5.3.6 Classification of Grade 0-1 versus Grade 2+ Patients

Classifications of unirradiated and irradiated lymphocyte spectra from grade 0-1 and grade 2+ patients were performed to investigate if the two patient groups could be discriminated. PLSDA models were developed as described earlier. Independent models were built using spectra of unirradiated and irradiated lymphocytes. The resulting sensitivities and specificities are provided in Table 6.5 and are calculated for the cross-validated PLSDA model. An example of the cross-validation performance of the PLSDA model is shown in Figure 5.8.

Table 5.5: Sensitivities and specificities for the PLSDA classification of grade 0-1 versus grade 2+ patients using spectra from unirradiated (0 Gy) and irradiated (0.05 Gy and 0.5 Gy) lymphocytes. The figures in brackets indicate the standard deviation over multiple evaluations for that particular metric.

Dose (Gy)	Sensitivity	Specificity	num LV*
0	0.51(0.39)	0.31(0.42)	15
0.05	0.56(0.35)	0.28(0.40)	10
0.5	0.56 (0.34)	0.23 (0.32)	20

*Number of latent variables

The optimised PLSDA models performed poorly for the unirradiated lymphocytes with a sensitivity and specificity of 0.51 and 0.31, respectively. Poor performance was also achieved for the irradiated lymphocytes.

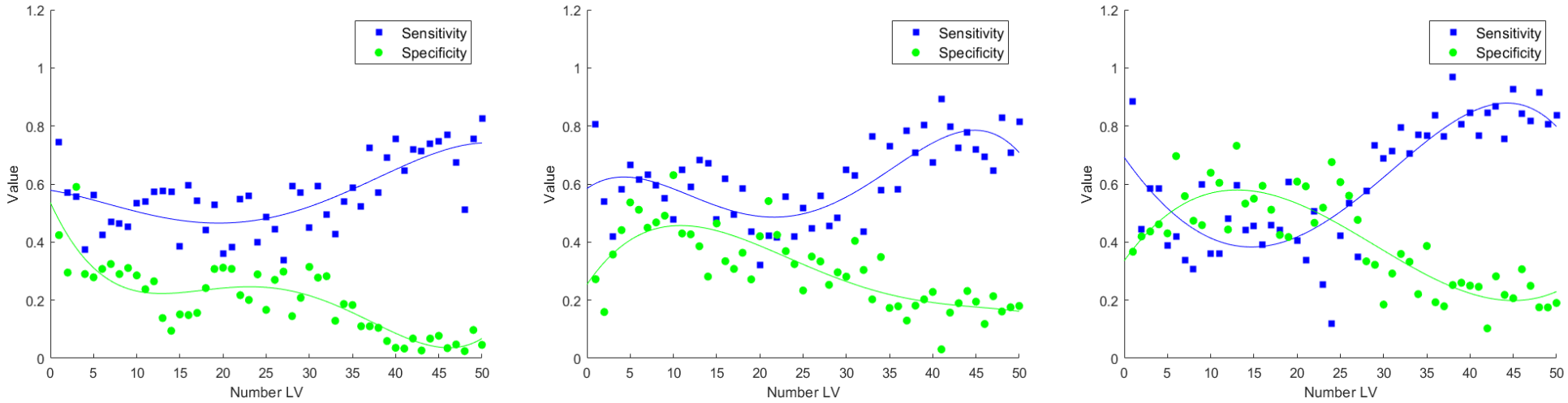

Figure 5.8: Cross-validated sensitivity and specificity of a PLSDA model developed on spectra at 0 Gy (A), 0.05 Gy (B) and 0.5 Gy (C). Fitted lines are intended as a guide to the eye, rather than implying a mathematical relationship.

5.4 Discussion

In contrast to the findings from the chapter 4 retrospective study, a decreased mean G2 score was observed in the grade 2+ patients compared to the grade 0-1 patients. This difference was again, not statistically significant however due to inter-individual variability, particularly in the grade 2+ group. Significant inter-individual variability in G2 radiosensitivity and no significant difference between patients with or without late adverse reactions has been observed in previous studies for PCa patients by Finnon *et al*. (2012) for breast cancer patients and Brzozowska *et al*. (2012), as previously discussed. Our previous study by White *et al*. (2020) established a radiosensitivity cut-off value of 132 using the 90th percentile of the G2 scores of healthy individuals which is in line with radiosensitivity cut-off values that have been reported previously (De Ruyck *et al*., 2008; Howe *et al*., 2005; Baeyens *et al*., 2002; Thierens *et al*., 2002; Vral *et al*., 2002; Baria *et al*., 2001; Scott *et al*., 1999). Using this G2 cut-off score of 132, 31% of the grade 0-1 group compared to 44% of the grade 2+ group were above the radiosenstivity cut-off value.

As with the retrospective study from chapter 4, whole blood cultures were used for the G2 assay in place of the PBMC cultures used for the γH2AX assay and the Raman assay, as whole blood cultures are routinely used for the G2 assay and because our previous study establishing the radiosensitivity cut-off value of 132 had used whole blood cultures. While, both groups from the chapter 4 retrospective study showed an increase in γH2AX fluorescence at each dose, only the grade 0-1 patient group showed an increase in γH2AX fluorescence at both irradiation doses following *in-vitro* irradiation. A low level of inter-individual variability was observed across each group.

Furthermore, as discussed in chapter 4, while previous studies have shown correlations between residual γH2AX fluorescence and late normal tissue toxicity later than 6 hrs post-irradiation (Vandevoorde *et al*., 2016; Bourton *et al*., 2011; Chua *et al*., 2011), γH2AX fluorescence was assessed at 1 hr post-irradiation in the present study to allow direct comparsion to the well established G2 assay. In addition, while inter-individual variability in the early damage response may have contributed to the lack of correlation to late normal tissue toxicity in the retrospective study, the present study shows no correlation despite low levels of inter-individual variability. Other previously mentioned studies have also failed to show correlations between residual γH2AX fluorescence and late normal tissue toxicity however (Brzozowska *et al*., 2012; Finnon *et al*., 2012; Werbrouck *et al*., 2010).

Again, while the flow cytometry γH2AX assay used in the present study is not as sensitive as assays based on manual or automated foci scoring by microscopy, positive correlations between γH2AX fluorescence and late normal tissue toxicity have been found using both microscopy (Vandevoorde *et al*., 2016; Chua *et al*., 2011) and flow cytometry assays (Bourton *et al*., 2011). The radiation response of the lymphocytes from grade 0-1 and grade 2+ groups was again investigated using Raman micro-spectroscopy. Responses in spectral regions associated with nucleic acids, proteins, carbohydrates and lipids were observed after irradiation to 0.05 and 0.5 Gy in lymphocytes from grade 0-1 patients. Very few significant changes were observed after irradiation to 0.05 and 0.5 Gy in lymphocytes from grade 2+ patients.

This observed outcome contrasts with the observations of chapter 4 as well as previous studies on normal and tumour cells irradiated *in-vitro* (Qiu *et al*., 2021; Meade *et al*., 2016; Harder *et al*., 2015; Maguire *et al*., 2015a; Matthews *et al*., 2011) and relating to DNA damage and cellular response to that damage. Unexpectedly, and in stark contrast to the findings of chapter 4, more significant differences between unirradiated and irradiated lymphocytes were observed in the grade 0-1 group than the grade 2+ group. The results from chapter 4 showed changes in nucleic acids, proteins and lipids observed after irradiation to 0.05 and 0.5 Gy in lymphocytes from grade 0-1 and grade 2+ patients with more significant differences observed between unirradiated and irradiated lymphocytes from grade 2+ patients. In the present study however, significant changes in nucleic acids, proteins, carbohydrates and lipids were observed after irradiation to 0.05 and 0.5 Gy in lymphocytes from grade 0-1 patients and very few significant changes were observed after irradiation to 0.05 and 0.5 Gy in lymphocytes from grade 2+ patients.

This may be due to patients within the grade 0-1 group who have yet to progress to grade 2+ toxicity as it can take 10 or more years for the results of this treatment side-effect to manifest themselves physically and to be clinically measurable. This correlates with the results of the *in-vitro* cellular radiosensitivity assays where more pronounced effects were observed in the grade 0-1 compared to the grade 2+ group. Classification of grade 0-1 versus grade 2+ groups yielded poor results using the PLSDA model and no clusters were observed based on radiation toxicity outcome using PCA or *K*-means cluster analysis.

Five patients however (one grade 0-1 and four grade 2+), were observed to form more distinct sub-clusters as radiation dose increased and while it appears these five patients are more sensitive to radiation dose, the clusters did not correlate with any clinically measurable outcome including radiation toxicity grade, PSA measurement, Gleason score or tumour grade.

5.5 Conclusion

In conclusion, while chapter 4 presented the novel application of Raman micro-spectroscopy to identify RT patients with late normal tissue toxicity, this chapter presents, for the first time, the application of Raman micro-spectroscopy to predict radiation toxicity outcomes in PCa patients before treatment. Spectral differences were identified between lymphocytes from patients with severe (grade 2+) late radiation toxicity and those with no/minimal (grade 0-1), but these differences were greater in the grade 0-1 group. Prediction could not be achieved based on late radiation toxicity and it may be too early to attempt prediction as the clinical status of a number of the grade 0-1 patients may progress to grade 2+ in the following years. These patients will be followed up at 6 monthly intervals until Year 9 however, allowing the models to be updated as patient clinical status changes.

Chapter 6 – Raman Micro-spectroscopy and Citrulline Level for the Prediction of Late Radiation Toxicity in Prostate Cancer Patients Following Radiotherapy

6.1 Introduction

While in chapter 4, it was found that Raman micro-spectroscopic analysis of lymphocytes taken from PCa patients *following* RT allowed for classification of these patients based on their radiosensitivity, it was shown in chapter 5 that Raman micro-spectroscopic analysis of lymphocytes taken from PCa patients *prior to* commencing RT did not allow for the prediction of radiation toxicity. The present study further evaluates Raman micro-spectroscopy as an assay for the prediction of late normal tissue toxicity by investigating spectral differences in lymphocytes obtained from PCa patients enrolled on the SPORT trial. Samples were obtained from patients *prior to* receiving RT treatment and who later developed no or minimal toxicity (grade 0-1) or severe toxicity (grade 2+). In addition, citrulline level was assessed as a potential radiation biomarker to predict late normal tissue toxicity. Following the results of chapters 4 and 5, no *ex-vivo* irradiation was carried out for the present study.

6.2 Materials and Methods

6.2.1 Patient Samples

Two 4 ml blood samples were collected in Vacutainer® EDTA blood collection tubes (BD, New Jersey) in duplicate from study participants. PBMCs were isolated as described in section *3.1.1 Cell Culturing* at the Centre for Cell Research and Cancer Biology and the School of Pharmacy, Queen's University Belfast.

The isolated PBMCs were then frozen in FBS (+10% dimethyl sulphoxide) and transported to TU Dublin on dry ice and subsequently stored at -80^{o}C. Before use, the samples were defrosted for 15 min at room temperature. Samples were centrifuged at 250 g for 5 min at room temperature and washed by adding 10 ml of DPBS (Sigma Aldrich LLC) and gently mixed by inversion. Samples were washed a total of three times. The PBMCs were then cultured as described in section *3.1.1 Cell Culturing.* Clinical details of both patient groups are shown in Table 6.1 and figure 6.1 shows an overview of the patient identification, sample processing and subsequent assays.

Table 6.1: Clinical features of grade 0-1 and grade 2+ patients. Data are number of patients unless otherwise stated.

	Grade 0-1 (n= 23)	**Grade 2+ (n= 4)**
Age (years)		
Mean	66.5	67.3
Median	67.0	69.5
Range	55-76	54-76
PSA (ng/ml)		
Mean	6.3	7.5
Median	3.78	6.0
T Stage		
T1c to T2a	7 (30.4 %)	2 (50.0 %)
T2b to T2c	3 (13.0 %)	0 (0 %)
T3a	13 (56.5 %)	2 (50.0 %)
Gleason score		
6	0 (0 %)	0 (0 %)
7	18 (78.2 %)	3 (75.0 %)
8	3 (13.0 %)	0 (0 %)
9	1 (4.4 %)	1 (25.0 %)
10	1 (4.4 %)	0 (0 %)
Prostate RT dose/ fractions		
36.0/ 5	23 (100 %)	4 (100 %)
Pelvis RT dose/ fractions		
25/ 5	12 (52.2 %)	2 (50 %)

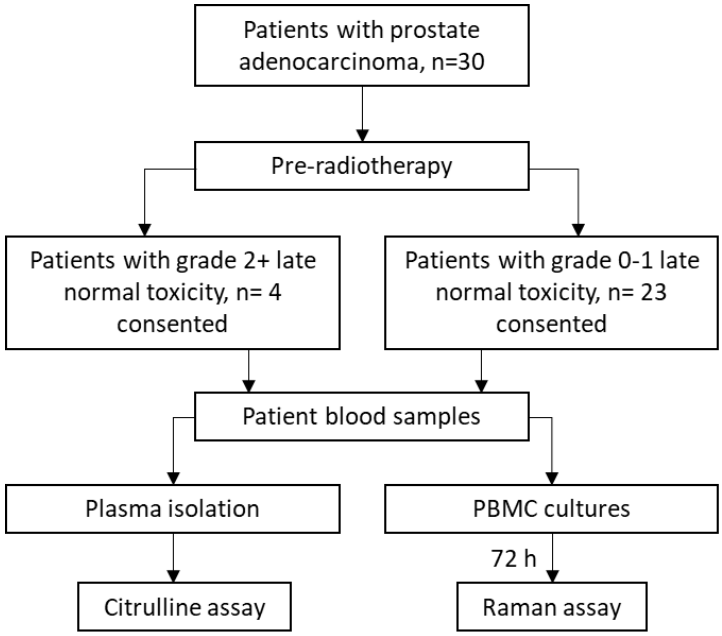

Figure 6.1: Schematic showing an overview of patient identification, sample processing, *in-vitro* irradiation, G2 assay, γH2AX assay and Raman assay.

6.2.2 Cell Culturing

Cell culturing was carried out as described in section *3.1.1 Cell Culturing*.

6.2.3 Calcium Fluoride Slide Preparation

Calcium fluoride slide preparation was carried out as described in section *3.1.3 Calcium Fluoride Slide Preparation*.

6.2.4 Citrulline Assay

The citrulline assay was carried out by the Cell Research and Cancer Biology and the School of Pharmacy, Queen's University Belfast. Briefly, two 4 ml peripheral venous blood samples were collected from each patient in Vacutainer® EDTA blood collection tubes. Patient samples were stored and transported on ice. Plasma was obtained via blood centrifugation at room temperature and the plasma citrulline concentration levels (μmol/l) were measured using high-performance liquid chromatography.

6.2.5 Raman Spectral Acquisition and Analysis

Raman spectral acquisition was carried out as described in section *3.3.1 Raman Spectral Measurements of Lymphocytes* and Raman spectral pre-processing was carried out as described in section *3.3.2 Raman Spectral Pre-processing*. Mean spectra were generated for both the grade 0-1 and grade 2+ toxicity groups and difference spectra were obtained by subtracting the mean spectra for the grade 0-1 toxicity group from the mean spectra for the grade 2+ toxicity group. Unpaired two-tailed Student's *t*-tests were then applied across all wavenumbers to identify statistically significant spectral differences between the two groups ($\alpha = 0.05$). PCA and *K*-means cluster analysis was performed thereafter to explore variation within the dataset and identify any patterns present. Confidence ellipses were generated at the 95% confidence level for each PCA plot. Following this, CLS-R was carried out using a spectral library of 28 pure biological components to investigate which biological molecules contributed to spectral differences between the patient toxicity groups. Model development was carried out as described in section *3.3.4 Model Development*.

6.3 Results

6.3.1 Citrulline Assay

Figure 6.2 shows the difference in citrulline levels for the grade 0-1 and grade 2+ patients pre-RT, 2 weeks into RT, 4 weeks into RT and 6 weeks post-RT. The grade 0-1 patient group showed higher citrulline levels overall at each time point (mean = 14.87±6.5, 14.78±8.2, 17.11±8.9 and 16.60±8.5, respectively), compared to the grade 2+ patient group (mean = 12.29±6.6, 8.23±2.0, 11.83±9.1 and 13.25±6.4).

The differences observed within and between the 2 patient groups were not statistically significant at any time point however ($\alpha = 0.05$). A high level of inter-individual variation was observed in both groups with a %CV of 43.9, 55.6, 52.2 and 51.2 for the grade 0-1 patient group and 53.9, 24.4, 77.3 and 48.3 for the grade 2+ patient group at pre-RT, 2 weeks into RT, 4 weeks into RT and 6 weeks post-RT, respectively.

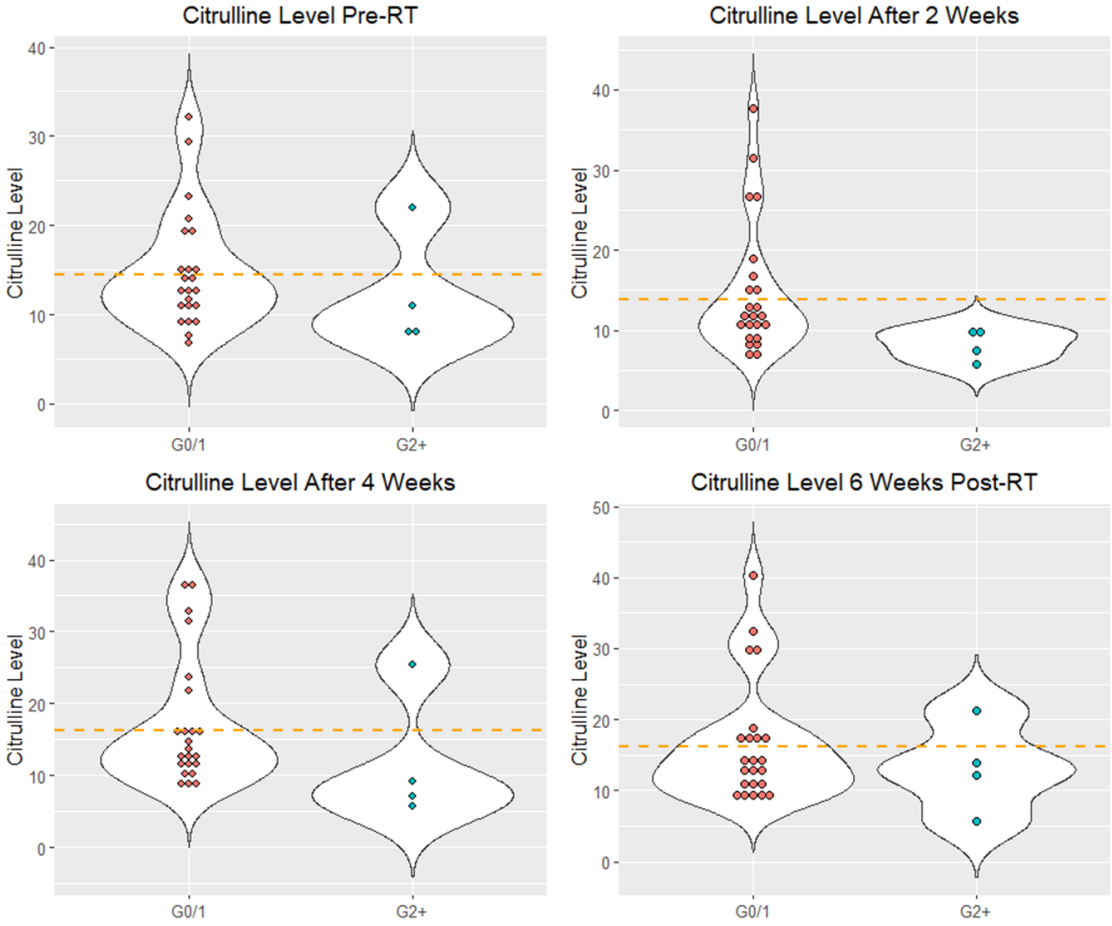

Figure 6.2: Citrulline levels (µmol/l) for grade 0-1 and grade 2+ patients pre-RT, 2 weeks into RT, 4 weeks into RT and 6 weeks post-RT. The orange dotted lines represent the mean citrulline value (14.48, 13.81, 16.32 and 16.10, respectively).

6.3.2 Spectral difference between lymphocytes from Grade 0-1 and Grade 2+ patients

As with the previous two studies, the spectral difference between lymphocytes from grade 0-1 and grade 2+ patients was investigated to determine if intrinsic biochemical differences could be identified. Figure 6.3 shows mean and difference spectra of lymphocytes from the grade 0-1 and grade 2+ patients. The shaded regions represent where the difference was found to be statistically significant ($\alpha = 0.05$). A summary of the band changes and assignments is shown in Table 6.2. Increases in bands associated with vibrations of carbohydrates, lipids and proteins were observed in grade 2+ patients when compared to grade 0-1 patient. Decreases in bands primarily associated with vibrations of DNA and RNA were observed in grade 2+ patients when compared to grade 0-1 patients.

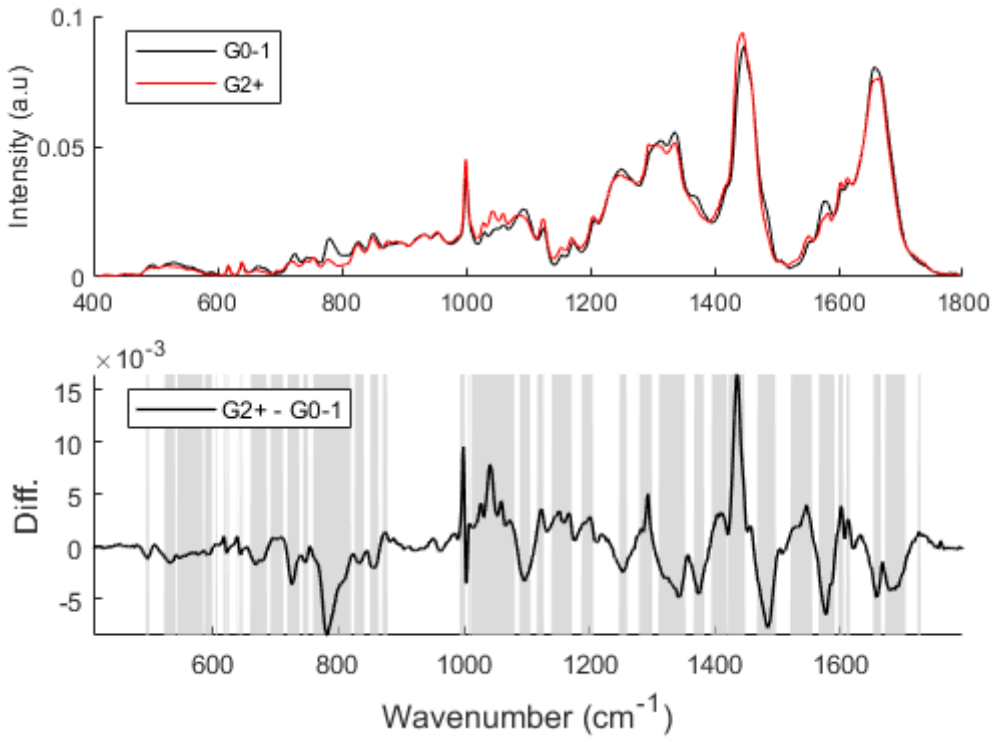

Figure 6.3: Mean (top) and difference (bottom) spectra of lymphocytes from grade 0-1 patients and grade 2+ patients. Shading represents regions of the spectrum that were found to be significantly different (two-tailed unpaired t-test with α=0.05).

Table 6.2: Summary of band changes and associated tentative assignments between spectra from lymphocytes from grade 0-1 and grade 2+ patients

Band (cm^{-1})	Δ G0-1 v G2+ 0 Gy	Band assignment	References
522-540	↓	S-S disulfide stretching in proteins, phosphatidylserine, cholesterol ester	Shetty *et al*. (2006); Krafft *et al*. (2005); Stone *et al*. (2004); Stone *et al*. (2002)
542-584	↓	Cholesterol, tryptophan, cytonsine, guanine, phosphatidylinositol	Krafft *et al*. (2005); Stone *et al*. (2004)
586-599	↓	Glycerol, phosphatidylinositol	Krafft *et al*. (2005)
604-607	↑	Glycerol	Krafft *et al*. (2005)
616-619	↑	C-C twisting of proteins	Chan *et al*. (2006)
621-625	↓	C-C twisting mode of phenylalanine	Notingher *et al*. (2004); Stone *et al*. (2004); Stone *et al*. (2002)
638-640	↑	C-S stretching and C-C twisting of proteins	Chan *et al*. (2006)
643-647	↓	C-C twisting mode of tyrosine and phenylalanine	Cheng *et al*. (2005); Notingher *et al*. (2004); Stone *et al*. (2004)
659-686	↓	C-S stretching mode of cystine, guanine, thymine, C-S stretching mode of cytosine	Chan *et al*. (2006); Cheng *et al*. (2005); Notingher *et al*. (2004); Stone *et al*. (2004); Stone *et al*. (2002)
691-712	↑	Cholesterol, cholesterol ester	Krafft *et al*. (2005)
718-738	↓	C-N of membrane phospholipid, DNA, C-C stretching, proline, phosphatidylserine, C-S stretching	Krafft *et al*. (2005); Binoy *et al*. (2004); Notingher *et al*. (2004); Stone *et al*. (2002); Frank *et al*. (1995)
743-752	↓	DNA, symmetric breathing of tryptophan, lactic acid	Chan *et al*. (2006); Cheng *et al*. (2005); Binoy *et al*. (2004); Huang *et al*. (2003a); Stone *et al*. (2002)
759-820	↓	Tryptophan, phosphatidylethanolamine, phosphatidylinositol, uracil, thymine, cytosine, O-P-O DNA backbone, phosphatidylserine, phosphodiester, proline, hydroxyproline	Chan *et al*. (2006); Shetty *et al*. (2006); Cheng *et al*. (2005); Krafft *et al*. (2005); Binoy *et al*. (2004); Notingher *et al*. (2004); Ruiz-Chica *et al*. (2004); Stone *et al*. (2004)
825-841	↓	Phosphodiester, O-P-O stretch of DNA/RNA, proline, hydroxyproline, tyrosine, saccharide	Chan *et al*. (2006); Shetty *et al*. (2006); Cheng *et al*. (2005); Krafft *et al*. (2005); Ruiz-Chica *et al*. (2004); Stone *et al*. (2004); Stone *et al*. (2002)

850-864	↓	Tyrosine, proline, hydroxyproline, glycogen, C-C stretching, phenylalanine, collagen, phosphatidic acid	Kateinen *et al*. (2007); Chan *et al*. (2006); Shetty *et al*. (2006); Cheng *et al*. (2005); Krafft *et al*. (2005); Binoy *et al*. (2004); Stone *et al*. (2004); Huang *et al*. (2003a); Stone *et al*. (2002)
870-878	↑	C-C stretching, hydroxyproline, tryptophan, phosphatidylcholine, sphingomyelin, phospholipids	Cheng *et al*. (2005); Krafft *et al*. (2005); Huang *et al*. (2003a); Frank *et al*. (1995)
993-1002	↑	C-O ribose, phenylalanine	Malini *et al*. (2006); Cheng *et al*. (2005); Dukor (2002); Frank *et al*. (1995)
1007-1011	↑	Phenylalnine, polysaccharides	Shetty *et al*. (2006); Naumann (1998)
1012-1081	↑	Glycogen, phenylalanine, C-O ribose stretching, proline, lipids, phospholipids, C-O stretching, C-C stretching, palmitic acid, fatty acid, triglycerides, glucose, collagen	Chan *et al*. (2006); Malini *et al*. (2006); Cheng *et al*. (2005); Faolain *et al*. (2005); Krafft *et al*. (2005); Seballos *et al*. (2005); Binoy *et al*. (2004); Notingher *et al*. (2004); Stone *et al*. (2004); Huang *et al*. (2003a); Dukor (2002); Silveira *et al*. (2002); Stone *et al*. (2002); Dovbeshko *et al*. (2000); Frank *et al*. (1995)
1088-1106	↓	DNA, lipids, phenylalanine, amide III	Chan *et al*. (2006); Malini *et al*. (2006); Shetty *et al*. (2006); Lakshimi *et al*. (2002); Ronen *et al*. (1990)
1116-1127	↑	Glucose, carotene, C-O band of ribose, C-C stretching of lipids and proteins, disaccharides	Malini *et al*. (2006); Cheng *et al*. (2005); Krafft *et al*. (2005); Stone *et al*. (2004); Huang *et al*. (2003a); Dukor (2002); Stone *et al*. (2002)
1139-1172	↑	Glycogen, carotenoid, C-C and C-N stretching of proteins, lipids, tyrosine, phenylalanine	Chan *et al*. (2006); Cheng *et al*. (2005); Huang *et al*. (2005); Stone *et al*. (2004); Huang *et al*. (2003a); Dukor (2002); Lakshimi *et al*. (2002); Stone *et al*. (2002); Hanlon *et al*. (2000)
1187-1206	↑	Nucleic acids, amide III, collagen, tyrosine, phenylalanine, hydroxyproline	Chan *et al*. (2006); Malini *et al*. (2006); Notingher *et al*. (2004); Stone *et al*. (2004); Dukor (2002); Lakshimi *et al* (2002); Dovbeshko *et al*. (2000); Andrus & Strickland (1998); Frank *et al*. (1995)
1247-1260	↓	Amide III, adenine, thymine, guanine, cytosine, lipids	Chan *et al*. (2006); Ruiz-Chica *et al*. (2004); Stone *et al*. (2004); Naumann (1998); Frank *et al*. (1995)

1279-1300	↑	Amide III, collagen, cytosine, nucleic acids and phosphates, palmitic acid, fatty acids, acyl chains, lipids	Shetty *et al*. (2006); Kolijenovic *et al*. (2005); Krafft *et al*. (2005); Ruiz-Chica *et al*. (2004); Stone *et al*. (2004); Dukor (2002); Lakshimi *et al*. (2002); Andrus & Strickland (1998)
1310-1353	↓	CH3/CH2 twisting mode of collagen/lipids, guanine, amide III, nucleic acids, adenine	Chan *et al*. (2006); Cheng *et al*. (2005); Ruiz-Chica *et al*. (2004); Stone *et al*. (2004); Huang *et al*. (2003a); Lakshimi *et al*. (2002); Stone *et al*. (2002)
1366-1383	↓	Phospholipids, guanine, lipids, thymine, guanine, adenine	Kateinen *et al*. (2007); Chan *et al*. (2006); Stone *et al*. (2004); Lakshimi *et al*. (2002)
1394-1420	↑	C=O symmetric stretch, CH2 deformation, aspartic and glutamic acid	Shetty *et al*. (2006); Faolain *et al*. (2005); Cheng *et al*. (2005)
1421-1448	↑	Guanine, adenine, CH deformation of DNA/RNA, proteins and lipids, deoxyribose, cholesterol, fatty acids	Chan *et al*. (2006); Ruiz-Chica *et al*. (2004); Notingher *et al*. (2004); Dukor (2002); Silveira *et al*. (2002); Hanlon *et al*. (2000)
1467-1497	↓	C=N stretching, amide II, guanine, adenine, DNA, collagen	Chan *et al*. (2006); Malini *et al*. (2006); Ruiz-Chica *et al*. (2004); Stone *et al*. (2004); Dukor (2002); Kaminaka *et al*. (2001); Naumann (1998)
1520-1555	↑	Carotenoid, carotene, amide II, tryptophan	Malini *et al*. (2006); Faolain *et al*. (2005); Stone *et al*. (2004); Huang *et al*. (2003a); Dukor (2002); Stone *et al*. (2002)
1565-1591	↓	Guanine, adenine, nucleic acids, phenylalanine, hydroxyproline	Chan *et al*. (2006); Cheng *et al*. (2005); Notingher *et al*. (2004); Ruiz-Chica *et al*. (2004); Huang *et al*. (2003a); Mahadevan-Jansen & Richards-Kortum (1997); Fung *et al*. (1996)
1596-1605	↑	Phenylalanine, tyrosine, cytosine	Chan *et al*. (2006); Cheng *et al*. (2005); Ruiz-Chica *et al*. (2004); Stone *et al*. (2004); Huang *et al*. (2003a); Stone *et al*. (2002)
1609-1615	↑	Cytosine, tyrosine, tryptophan	Chan *et al*. (2006); Cheng *et al*. (2005); Ruiz- Chica *et al*. (2004)

1652-1665	↓	Lipid, collagen, amide I, thymine, guanine, cytosine, fatty acids, lipids	Chan *et al*. (2006); Cheng *et al*. (2005); Notingher *et al*. (2004); Stone *et al*. (2004); Dukor (2002); Hanlon *et al*. (2000); Frank *et al*. (1995)
1671-1704	↓	Amide I, cholesterol, ceramide	Shetty *et al*. (2006); Faolain *et al*. (2005); Krafft *et al*. (2005); Lakshimi *et al*. (2002)
1723-1728	↑	Unassigned	N/A

6.3.4 CLS-R Analysis of Grade 0-1 versus Grade 2+ Patients

CLS-R analysis was applied to identify and quantify the relative concentrations of pure molecular species contributing to the differences in Raman spectra between the grade 0-1 patients and grade 2+ patients followed by *t*-tests to determine if these differences were significant (α=0.05). The list of pure molecular reference species used in this study are provided in Table 6.3 and were chosen based on the significant differences observed in the spectra depicted in Figure 6.3. Significant differences were observed for all molecular species included in the model. As shown in Figure 6.4, higher concentrations of myristic acid, tyrosine and uracil were observed in grade 2+ patients when compared to grade 0-1 patients. The residuals for the model are shown in Figure 6.5. In addition, higher concentrations of arachidonic acid and DNA were observed in grade 0-1 patients when compared to grade 2+ patients.

Table 6.3: Summary of pure molecular reference species used for CLS-R

Category	Molecular reference species
Proteins and associated compounds	Histone 2A, L-proline, phenylalanine, trans-4-hydroxy-L-proline, tyrosine, tryptophan
Lipids and fatty acids	Arachidonic acid, ceramide, cholesterol, L-alpha-lysophosphatidylcholine, linoleic acid, linolenic acid, lipoic acid, myristic acid, oleic acid, palmitic acid, PUFA, stearic acid, triglycerides
Nucleic acids and associated compounds	Adenine, cytosine, deoxyuridine, DNA, guanine, RNA, thymidine, thymine, uracil

(PUFA: Polyunsaturated fatty acids)

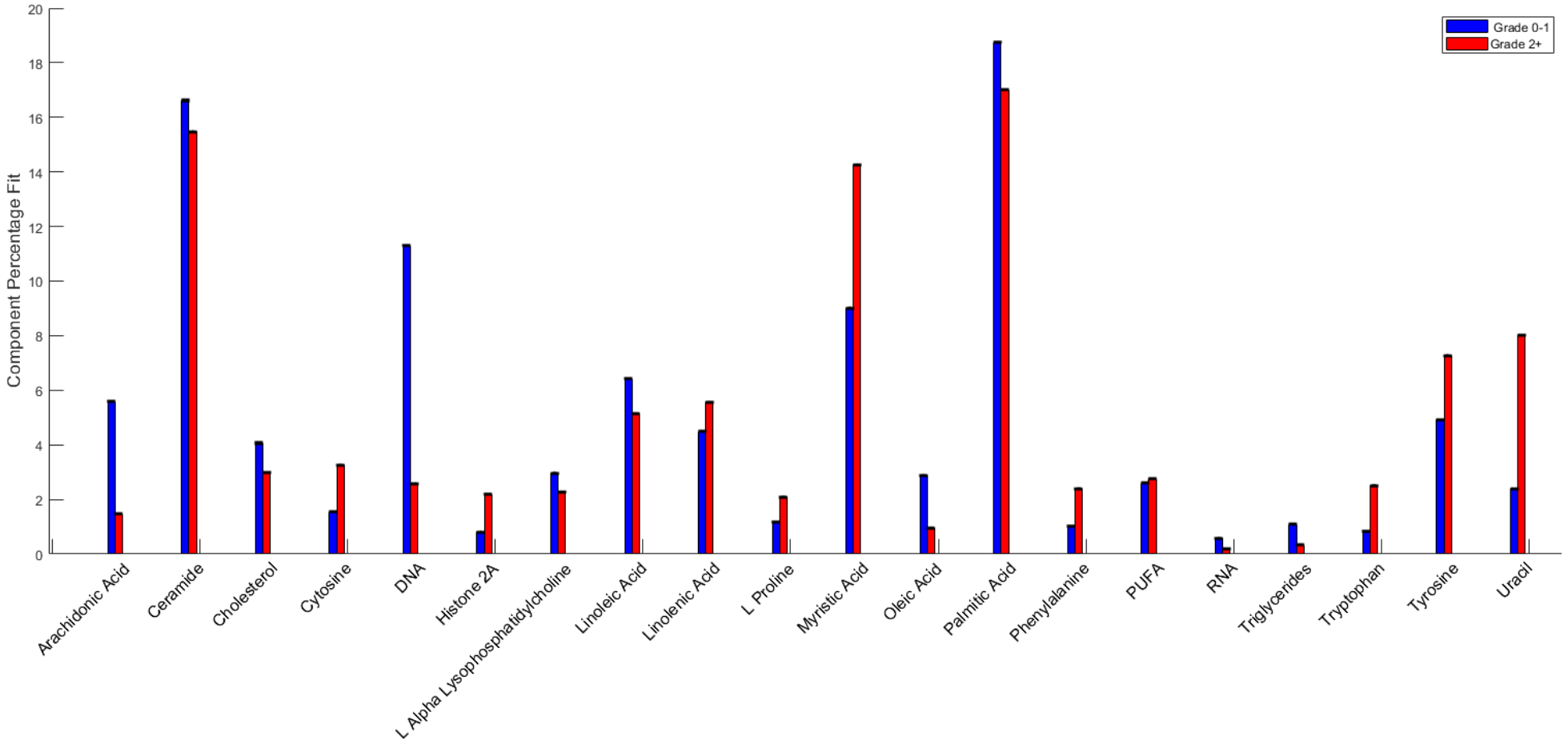

Figure 6.4: Relative concentrations of pure molecular species from classical least squares regression fitting of Raman spectra from grade 0-1 patients (blue) and grade 2+ patients (red). Error bars represent the root mean squared error. Significant differences were observed between the two patient groups for all molecular species included in the model. Furthermore, as the relative concentration of adenine, deoxyuridine, guanine, lipoic acid, stearic acid, thymidine, thymine and trans-4-hydroxy-L-proline were found to be very low, they could not be visualized with the other molecular species and have been excluded from the plot.

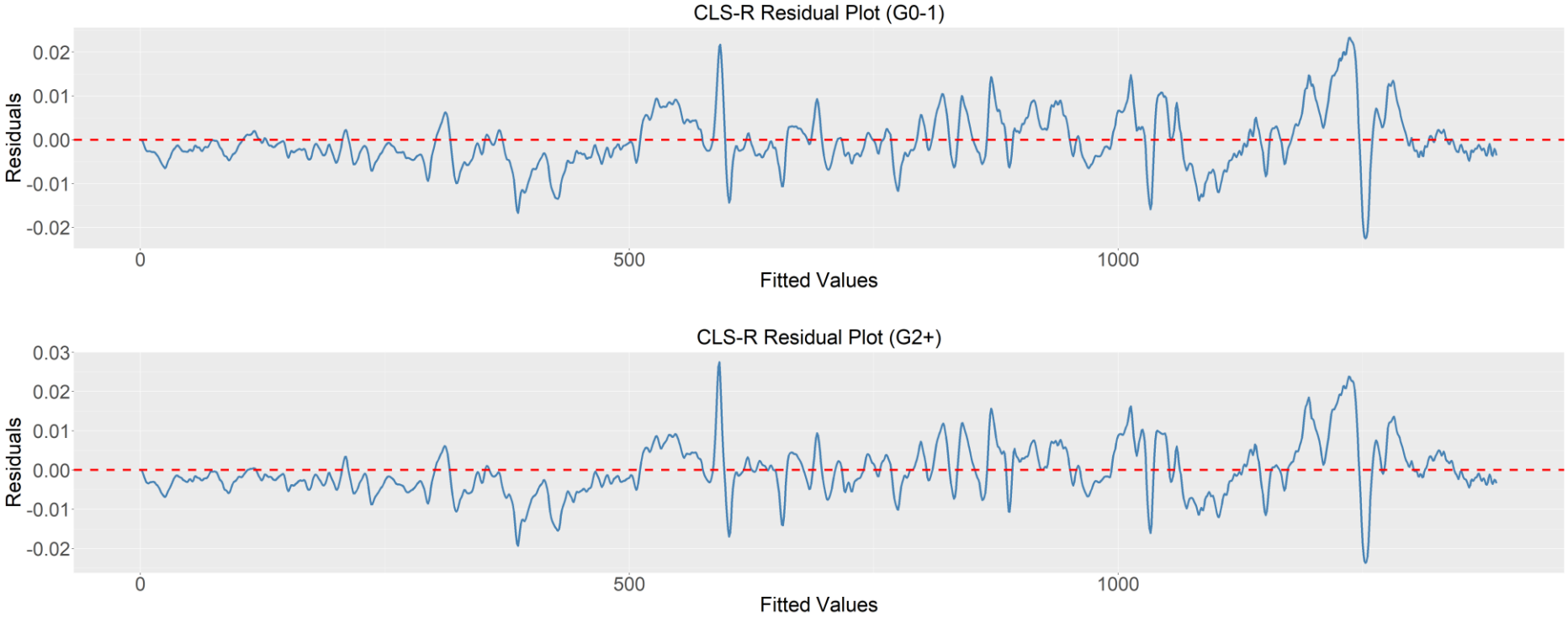

Figure 6.5: Residual plots following CLS-R fitting of pure molecular reference species to the grade 0-1 patient spectra (A) and the grade 2+ patient spectra (B). There are some minor spectral peaks remaining for both groups.

As discussed in Chapter 2 (section *2.5.3 Classical Least Squares Regression*), collinearity between fitted components may skew the fit (Stone *et al.*, 2007). Collinearity may occur, for example, where an amino acid and a protein containing that amino acid are included in the model (Stone *et al.*, 2007). Figure 6.6 shows a correlation plot of the fitted components to assess the collinearity between components. Numerous fitted components were found to have moderate to strong (0.7 – 1.0) positive correlation coefficients indicating collinearity. This was particularly evident between the lipid components.

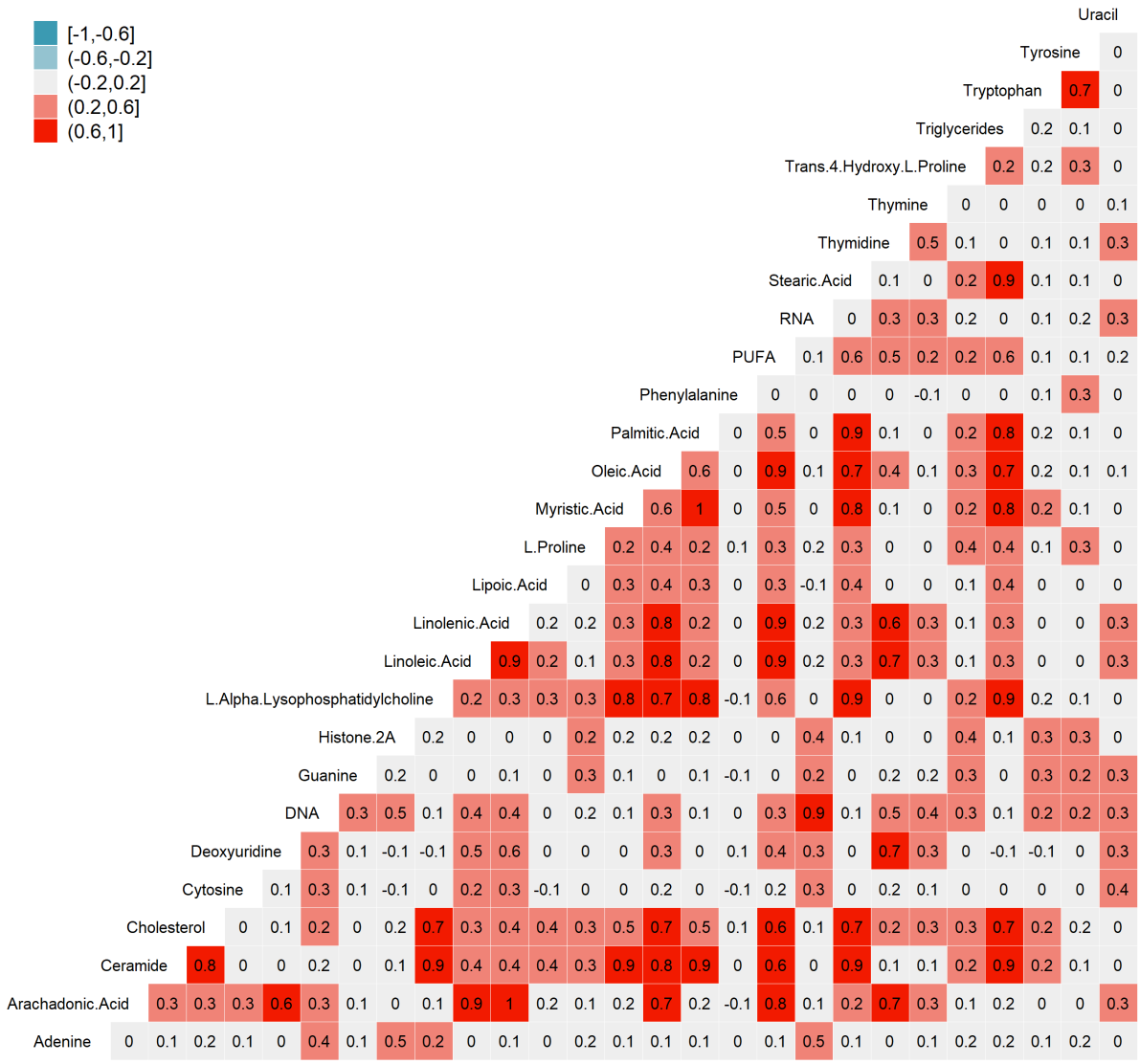

Figure 6.6: Correlation plot of fitted components from CLS-R model. Moderate to strong correlation coefficients were observed, primarily between the lipid components.

6.3.5 PCA and K-means Cluster Analysis of Grade 0-1 versus Grade 2+ Patients

Figure 6.7 shows the results following PCA of the lymphocyte spectra from the grade 0-1 and grade 2+ patients, as well as *K*-means cluster analysis of the lymphocyte spectra from the grade 0-1 and grade 2+ patients. PC1 and PC2 were found to explain 46% and 22% of the variance from the lymphocytes, respectively. No discrimination was observed between the lymphocyte spectra from the grade 0-1 and grade 2+ patients. Moreover, following *K*-means cluster analysis, 2 clusters were observed in the spectra from the lymphocytes. No clusters were observed based on radiation toxicity grade. Moreover, no observed cluster correlated with any other clinically measurable outcome including PSA measurement, Gleason score or tumour grade.

A

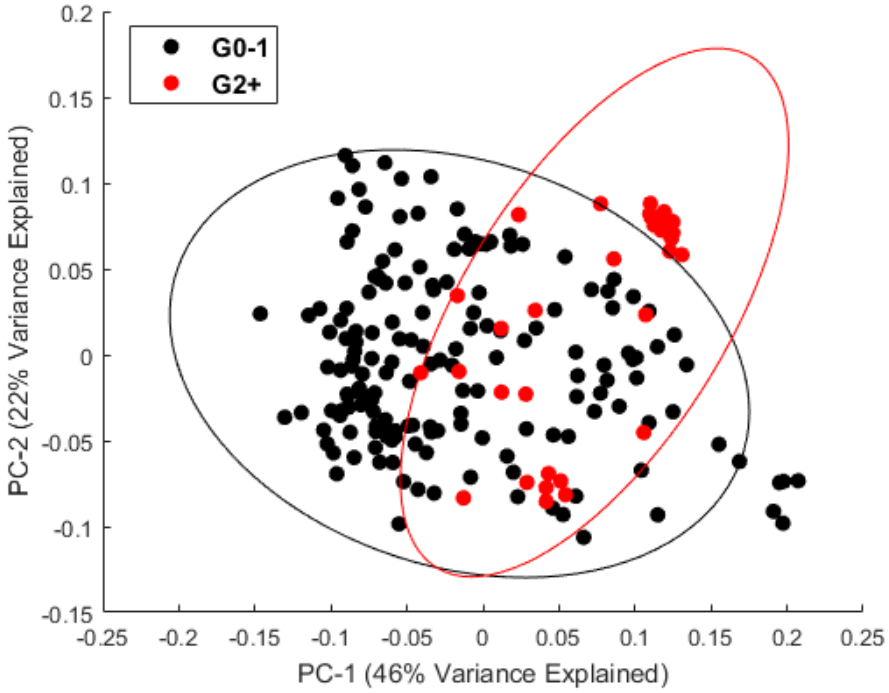

B

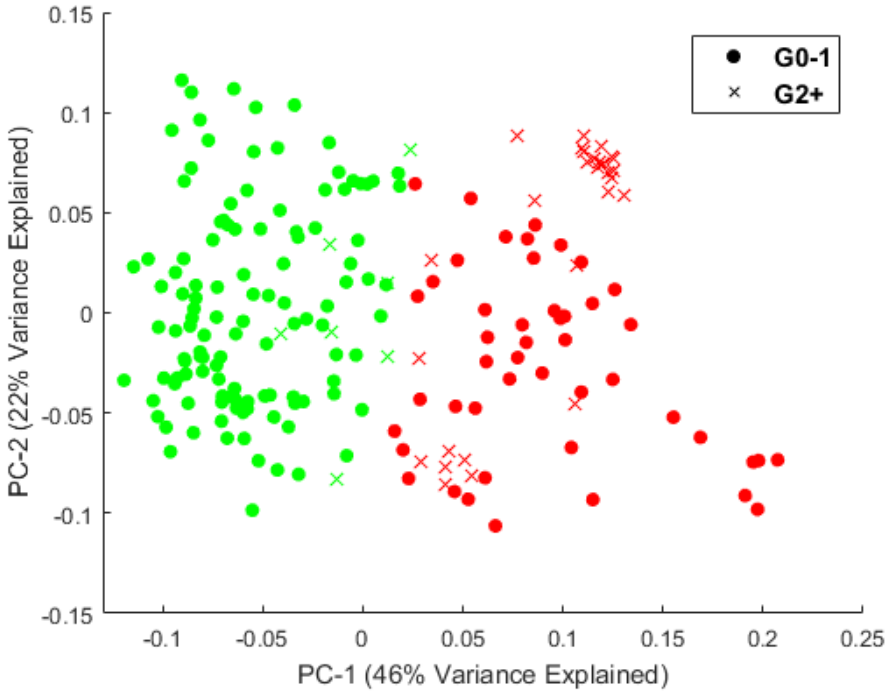

Figure 6.7: (A) PCA scatter plot showing discrimination of grade 0-1 and 2+ toxicity patients. Confidence ellipses were generated at the 95% confidence level. (B) PCA scatter plot showing the discrimination of grade 0-1 (represented by •) and grade 2+ (represented by x) toxicity patients with patient spectra coloured according to the 2 clusters identified following a *K*-means cluster analysis.

6.3.6 Classification of Grade 0-1 versus Grade 2+ Patients

As with the previous two studies, classifications of lymphocyte spectra from grade 0-1 and grade 2+ patients were performed to investigate if the two patient groups could be discriminated. PLSDA models were developed as described earlier. Independent models were built using spectra of lymphocytes. Due to the large imbalance between the two patient groups however, oversampling of the minority grade 2+ patient group was applied to the training set. Samples were randomly replicated from the grade 2+ patient group for each independent model after splitting the data into training and test sets. The resulting accuracies, sensitivities and specificities are provided in Table 6.4 and are calculated for the cross-validated PLSDA model. An example of the cross-validation performance of the PLSDA model is shown in Figure 6.8.

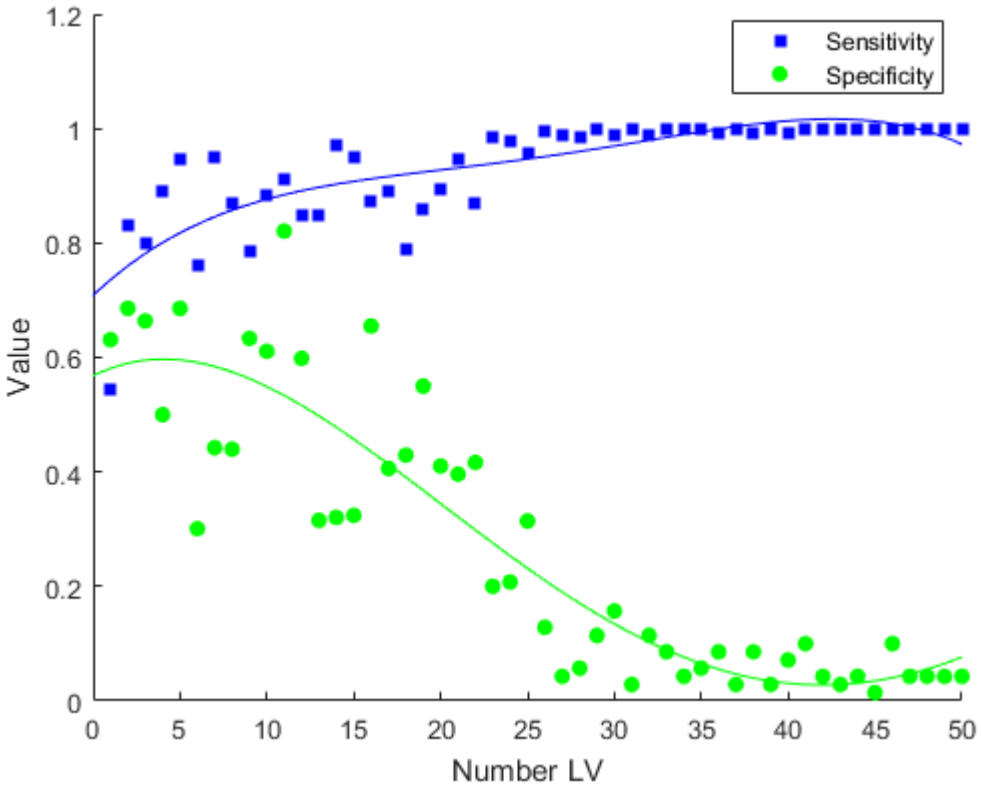

Figure 6.8: Cross-validated sensitivity and specificity of a PLSDA model developed on spectra. Fitted lines are intended as a guide to the eye, rather than implying a particular mathematical relationship.

Table 6.4: Accuracies, sensitivities and specificities for the PLSDA classification of grade 0-1 versus grade 2+ patients using spectra from lymphocytes. The figures in brackets indicate the standard deviation over multiple evaluations for that particular metric.

Sensitivity	Specificity	Accuracy	num LV*
0.91(0.10)	0.82(0.33)	0.89	11

*Number of latent variables

The optimised PLSDA models performed relatively well for the lymphocytes with an accuracy, sensitivity and specificity of 0.89, 0.91 and 0.82, respectively and while the model complexity is relatively high for the model (num LV = 11), the generalizability of this model to unseen data, reinforces the view that the model is being developed on real and consistent Raman signals observed in the data. The relatively high standard deviations, however, indicate that the model did not perform well across all instances.

6.4 Discussion

Contrary to the findings of Jäckel *et al.* (2021), Onal *et al.* (2011), Wedlake *et al.* (2008) and Lutgens *et al*. (2004), no significant difference in plasma citrulline concentration was observed between the grade 0-1 and grade 2+ toxicity patient groups at any of the timepoints examined due to inter-individual variability, particularly in the grade 0-1 group. Plasma citrulline concentration was observed to be lower overall for all patients with grade 2+ toxicity 2 weeks after RT commencement before increasing however. While the difference observed after 2 weeks was not significant, the pattern of a decreasing plasma citrulline concentration level after 2 weeks of RT followed by an increase at 4 weeks is consistent with the findings of Wedlake *et al.* (2008) and Lutgens *et al*. (2004).

Furthermore, this pattern is consistent with the pathogenesis of acute radiation toxicity where maximal histological inflammation occurs within the irradiated rectum within the first 2 weeks of RT with GI symptoms peaking within 3-5 weeks of RT commencement (Wedlake *et al.* 2008; Hovdenak *et al*., 2000; Sedgewick *et al*., 1994; Gelfand *et al*., 1968). Similar to chapter 4, and in contrast to chapter 5, significant intrinsic spectral differences were observed between patients with grade 0-1 and grade 2+ toxicity and these differences were related not only to DNA but also to proteins and lipids, correlating well with previous studies on normal and tumour cells irradiated *in-vitro* (Qiu *et al*., 2020; Meade *et al*., 2016; Harder *et al*., 2015; Maguire *et al*., 2015a; Matthews *et al*., 2011).

Moreover, as shown from the CLS-R analsyis, lymphocytes from patients with grade 2+ toxicity had much lower levels of DNA, arachidonic acid and oleic acid compared with the lymphocytes from patients with grade 0-1 toxicity and these differences were found to be significant. Lower levels of ceramide, cholesterol, L-α-lysophosphatidycholine, linoleic acid, palmitic acid, RNA and triglycerides were also observed in the lymphocytes from patients with grade 2+ toxicity in comparison to those from patients with grade 0-1 toxicity and these differences were also found to be significant. In addition, signficantly higher levels of tyrosine, tryptophan and phenylalanine were also observed in the lymphocytes from patients with grade 2+ toxicity in comparison to those from patients with grade 0-1 toxicity, correlating well with previous studies examining Raman spectral profiles of cells post-irradiation (Qiu *et al*., 2020, Jafarzadeh *et al*., 2018; Harder *et al*., 2015; Yasser *et al*., 2014; Matthews *et al*., 2011). In the present study however, these differences were observed without the need for irradiation.

Furthermore, the significant difference found in lysophosphatidycholine, a compound derived from phosphatidylcholine, corroborates the findings of Milligan *et al*. (2021) which suggested that phosphatidylcholine was an important variable in contributing to the classification of spectra as belonging to radiosensitive or radioresistant cell lines. Furthermore, the lymphocytes from patients with grade 0-1 toxicity showed lower levels of cytosine, histone 2A, linolenic acid, L-proline, myristic acid, phenylalanine, tryptophan, tyrosine and uracil.

It is important to note however, that collinearity between fitted components may skew the fit and care is necessary when interpreting the model results. Numerous fitted components were found to have moderate to strong positive correlation coefficients indicating collinearity between fitted components and this was particularly evident between the fitted lipid components. In addition, to achieve highly accurate fitting of spectral components, all biochemicals should be represented, have little to no noise in their spectra and be measured in a similar microenvironment. While the pure molecular reference species used here had an excellent SNR, it was not possible to represent all expected biochemicals or to obtain spectra for these biochemcials in a similar microenvironment to that of a lymphocyte. This difference in microenvironment may have resulted in Raman scattering less representative of the same biochemicals found in a lymphocyte microenvironment. It is also important to note that negative concentrations are also possible when using CLS-R without non-negative constraints, as in the present study, and non-negative least-squares and semi-parametric approaches may be more appropriate when applying CLS-R (Sowa *et al*., 2006). Thus, the pure molecular reference species identified here are highly approximate and tentative.

Some separation between the grade 0-1 versus grade 2+ groups was observed using PCA, however, a significant amount of overlap between the two groups was still evident. Moreover, following *K*-means cluster analysis, no clusters were observed that correlated with radiation toxicity grade or any other clinically measurable outcome including PSA measurement, Gleason score or tumour grade. Similar to the findings outlined in chapter 4, however, classification of grade 0-1 versus grade 2+ groups yielded good accuracy using the PLSDA model.

A high classification accuracy was achieved for the lymphocytes from each group. This further suggests that *in-vitro* irradiation may not be required for the future prediction of patient toxicity and that the intrinsic spectral phenotype of the patient may be sufficient to discriminate on radiation toxicity. It is important to note however, that the high standard deviations associated with the sensitivity and specificity of the PLSDA model indicate that the model is not a reliable indicator of radiotoxicity outcome in every instance, and the use of oversampling to handle the imbalance between patient groups in the dataset may also have had an influence on the model results by overfitting the data. Furthermore, as previously discussed, these findings would need to be confirmed in a larger patient population.

6.5 Conclusion

In summation, this chapter, as with the preceding chapter, presents the novel application of Raman micro-spectroscopy to predict radiation toxicity outcomes in PCa patients. Spectral differences, as found in chapter 4 and in contrast to chapter 5, were identified between lymphocytes from patients with severe (grade 2+) late radiation toxicity and those with no/minimal (grade 0-1).

Prediction could be achieved based on late radiation toxicity but the spectral analysis was not a reliable indicator of radiotoxicity outcome in every instance. In addition, no significant difference in plasma citrulline concentration was observed between the grade 0-1 and grade 2+ toxicity patient groups, though a pattern of cituLline concentration level consistent with the pathogenesis of acute radiation toxicity was observed. As with the previous study in chapter 5 however, it may be too early to attempt prediction as the clinical status of a number of the grade 0-1 patients may progress to grade 2+ in the following years. These patients will be followed up every 6 months for up to 5 years with a minimum annual follow-up from 5-10 years, allowing the models to be updated as patient clinical status changes.

Chapter 7 – Summary and General Conclusions

7.1 Summary

The studies outlined in the preceding chapters demonstrate, for the first time, the novel application of Raman micro-spectroscopy to discriminate between RT patients based on late normal tissue toxicity. The primary aim of this study was to determine if spectral variations in blood lymphocytes from PCa patients may suggest Raman spectral bands that could be used in future research to identify spectral features associated with radiosensitivity. To this end, Raman micro-spectroscopy of lymphocytes taken *following* RT from PCa patients enrolled on the Cancer Trials Ireland ICORG 08-17 study was applied in conjunction with PLSDA to classify patients based on radiation toxicity grade (outlined in chapter 4). In addition, Raman micro-spectroscopy of lymphocytes taken *prior to* commencing RT was applied in conjunction with PLSDA in order to predict radiation toxicity outcome in PCa patients enrolled on the Cancer Trials Ireland ICORG 08-17 study and in a separate cohort of PCa patients enrolled on the Northern Ireland Cancer Trials Centre SPORT study (outlined in chapters 5 and 6, respectively).

This spectral data was examined in parallel with typically used biological assays for assessing radiosensitivity including the γH2AX DNA damage assay, the G2 chromosomal radiosensitivity assay and the citrulline assay. Following the application of the G2 chromosomal radiosensitivity assay to lymphocytes taken from PCa patients *following* RT, an increased mean G2 score was observed in the grade 2+ patients compared to the grade 0-1 patients, but this was not statistically significant due to inter-individual variability.

In contrast to the findings from this retrospective study however, a decreased mean G2 score was observed in the grade 2+ patients compared to the grade 0-1 patients following the application of the G2 chromosomal radiosensitivity assay to lymphocytes taken from PCa patients *prior to* commencing RT. This difference was again, not statistically significant however due to inter-individual variability, particularly in the grade 2+ group. Previous studies for breast cancer patients and for PCa patients also observed significant inter-individual variability in G2 radiosensitivity and no significant difference between patients with or without late adverse reactions (Brzozowska *et al*. 2012; Finnon *et al*., 2012).

An increase in γH2AX fluorescence in lymphocytes taken from PCa patients following RT was observed for both patient groups 1 hr following *in-vitro* irradiation to 0.05 Gy and 0.5 Gy but no statistically significant difference was found between the two groups due to the high level of inter-individual variability particularly in the grade 2+ group. However, while both groups from this retrospective study showed an increase in γH2AX fluorescence at each dose, only the grade 0-1 patient group showed an increase in γH2AX fluorescence at both irradiation doses following *in-vitro* irradiation of lymphocytes taken from PCa patients *prior to* commencing RT. Moreover, a low level of inter-individual variability was observed across each group in this study. Thus, while inter-individual variability in the early damage response may explain the lack of correlation to late normal tissue toxicity in the retrospective study, no correlation was found in the study using lymphocytes taken from PCa patients *prior to* commencing RT despite the low levels of inter-individual variability.

Other studies have shown correlations between residual γH2AX fluorescence and late normal tissue toxicity (Vandevoorde *et al*., 2016; Bourton *et al*., 2011; Chua *et al*., 2011) but these studies assessed γH2AX fluorescence >6 hr post-irradiation while the studies used here assessed γH2AX fluorescence at 1 hr post-irradiation to allow direct comparsion to the well established G2 radiosensitivity assay. However, while assessing γH2AX fluorescence >6 hr post-irradiation may have yielded lower inter-individual variability and therefore different results, several studies have failed to show correlations between residual γH2AX fluorescence and late normal tissue toxicity despite assessing γH2AX fluorescence >6 hr post-irradiation (Brzozowska *et al*., 2012; Finnon *et al*., 2012; Werbrouck *et al*., 2010). In addition, Felgentreff *et al*. (2021) demonstrated that the damage response capacity of lymphocyte subsets to irradation differs, particularly when comparing T- and B-lymphocytes to natural killer cells. Thus, any relationship between residual γH2AX fluorescence and late normal tissue toxicity may be masked by differing responses of lymphocyte subsets to irradiation. Thus, individual analyses of lymphocyte subsets may be necessary to identify any correlation between residual γH2AX fluorescence and late normal tissue toxicity.

In contrast to previous studies (Jäckel *et al.*, 2021; Onal *et al.*, 2011; Wedlake *et al.*, 2008 and Lutgens *et al*., 2004), no significant difference in plasma citrulline concentration from plasma taken *prior to* commencing RT was observed between the grade 0-1 and grade 2+ toxicity patient groups at any of the timepoints examined due to inter-individual variability, particularly in the grade 0-1 group. Plasma citrulline concentration was observed to be lower overall for all patients with grade 2+ toxicity 2 weeks after RT commencement before increasing at 4 weeks however.

This pattern of a decreasing plasma citrulline concentration level after 2 weeks of RT followed by an increase at 4 weeks is consistent with previous studies (Wedlake *et al.*, 2008; Lutgens *et al.*, 2004) and correlates with the pathogenesis of acute radiation toxicity. Maximal histological inflammation occurs within the irradiated rectum within the first 2 weeks of RT with GI symptoms peaking within 3-5 weeks of RT commencement and this is reflected in the plasma citrulline concentration at these timepoints (Wedlake *et al.* 2008; Hovdenak *et al*., 2000; Sedgewick *et al*., 1994; Gelfand *et al*., 1968).

The radiation response of the lymphocytes taken from PCa patients *following* RT from grade 0-1 and grade 2+ groups was investigated. Similar responses in spectral regions associated with DNA, RNA, proteins, and lipids were observed for the grade 0-1 and grade 2+ groups, relating to DNA damage and cellular response to that damage and correlating well with previous studies on normal and tumour cells irradiated *in-vitro* (Qiu *et al*., 2020; Meade *et al*., 2016; Harder *et al*., 2015; Maguire *et al*., 2015a; Matthews *et al*., 2011). More significant differences between unirradiated and irradiated lymphocytes were observed in the grade 2+ group, correlating well with the results of the *in-vitro* cellular radiosensitivity assays where more pronounced effects were also observed in the grade 2+ compared to the grade 0-1 group. These more pronounced effects observed in the grade 2+ group suggest an increased radiosensitivity compared to the grade 0-1 group.

The radiation response of the lymphocytes taken from PCa patients *prior to* commencing RT from grade 0-1 and grade 2+ groups was also investigated. Responses in spectral regions associated with nucleic acids, proteins, carbohydrates and lipids were observed after irradiation in lymphocytes from grade 0-1 patients.

Very few significant changes were observed after irradiation in lymphocytes from grade 2+ patients, however. Furthermore, significant differences between unirradiated and irradiated lymphocytes were observed in the grade 0-1 group than the grade 2+ group. These results correlate with the results of the *in-vitro* cellular radiosensitivity assays where more pronounced effects were observed in the grade 0-1 compared to the grade 2+ group and may be due to patients within the grade 0-1 group who have yet to progress to grade 2+ toxicity.

Furthermore, in a separate cohort of patients using lymphocytes also taken from PCa patients *prior to* commencing RT, significant intrinsic spectral differences were observed between patients with grade 0-1 and grade 2+ toxicity and these differences were related not only to DNA but also to proteins and lipids, again correlating well with the aforementioned studies (Qiu *et al*., 2020; Meade *et al*., 2016; Harder *et al*., 2015; Maguire *et al*., 2015a; Matthews *et al*., 2011). Moreover, CLS-R analysis of lymphocytes from this cohort found that patients with grade 2+ toxicity had lower levels of DNA, arachidonic acid, oleic acid, ceramide, cholesterol, L-α-lysophosphatidycholine, linoleic acid, palmitic acid, RNA and triglycerides compared with the lymphocytes from patients with grade 0-1 toxicity and these differences were found to be significant. In addition, signficantly higher levels of tyrosine, tryptophan and phenylalanine were also observed in the lymphocytes from patients with grade 2+ toxicity, correlating well with past studies (Qiu *et al*., 2020, Jafarzadeh *et al*., 2018; Harder *et al*., 2015; Yasser *et al*., 2014; Matthews *et al*., 2011). In contrast to these studies however, the differences here were observed without *in-vitro* irradiation.

Furthermore, the significant difference found in lysophosphatidycholine corroborates the finding that phosphatidylcholine may be an important variable in differentiating radiosensitive and radioresistant cell lines (Milligan *et al.*, 2021). Numerous fitted components were found to have moderate to strong positive correlation coefficients indicating collinearity between fitted components however, and this was particularly evident between the fitted lipid components. In addition, it was not possible to represent all expected biochemicals or to obtain spectra for these biochemcials in a similar microenvironment to that of a lymphocyte. Thus, the pure molecular reference species identified here are highly approximate and tentative.

Some separation between the grade 0-1 versus grade 2+ groups in this cohort was observed using PCA but, a significant amount of overlap was still observed between patient groups. Moreover, as with the previous cohort, no clustering was observed based on radiation toxicity outcome using *K*-means cluster analysis and no distinct clusters could be observed using PCA or *K*-means cluster analysis that correlated with radiation toxicity grade or any other clinically measurable outcome including PSA measurement, Gleason score or tumour grade. Classification of grade 0-1 versus grade 2+ groups yielded good accuracy using the PLSDA model for spectral data from lymphocytes taken from PCa patients *following* RT. Significantly, a high classification accuracy was achieved for the unirradiated lymphocytes from each group, suggesting that *in-vitro* irradiation may not be required for the future prediction of patient toxicity and that the intrinsic spectral phenotype of the patient may be sufficient to discriminate on radiation toxicity.

Classification of grade 0-1 versus grade 2+ groups yielded poor results using the PLSDA model for spectral data from both irradiated and unirradiated lymphocytes taken from PCa patients *prior to* commencing RT, however. In addition, no clustering was observed based on radiation toxicity outcome using PCA or *K*-means cluster analysis. Five patients were found to form distinct sub-clusters as radiation dose increased, however. These five patients appear to be more sensitive to radiation as the increasingly distinct clusters they formed as radiation dose increased, indicates a greater alteration in their spectral, and therefore molecular, profile.

The sub-clusters they formed however, did not correlate with any clinically measurable outcome analysed here, including radiation toxicity grade, PSA measurement, Gleason score or tumour grade. Classification of grade 0-1 versus grade 2+ groups yielded good accuracy using the PLSDA model in the second cohort of patients using lymphocytes also taken from PCa patients *prior to* commencing RT however. A high classification accuracy was achieved for the lymphocytes from each group, further suggesting that *in-vitro* irradiation may not be required for the future prediction of patient toxicity and that the intrinsic spectral phenotype of the patient may be sufficient to discriminate on radiation toxicity. High standard deviations associated with the sensitivity and specificity of the PLSDA model indicate that the model was not a reliable indicator of radiotoxicity outcome in every instance however, and the use of oversampling to handle the imbalance between patient groups in the dataset may also have had an influence on the model results by overfitting the data.

7.2 Limitations and Future Work

It is important to note, that the studies outlined in the preceding chapters have a number of limitations and much more work is needed if a predictive assay is to be developed. One of the main limitations with each of these studies is the low sample numbers. Low sample numbers can make it difficult to extrapolate findings and thus any findings here would need to be further validated in an independent set of patients. Furthermore, late radiation toxicity can take years to develop and, as a result, some of the patients included in the present studies may not be assigned the appropriate patient group label as they have not yet developed late radiation toxicity, making prediction challenging. Thus, it may be too early to attempt prediction based on the current clinical status of a number of the grade 0-1 patients. The data and models used in the current study will therefore be updated as patients from the study outlined in chapter 5 will undergo clinical follow-up at 6 monthly intervals until Year 9 and those from the study outlined in chapter 6 will be followed up every 6 months for up to 5 years with a minimum annual follow-up from 5-10 years.

Moreover, the samples obtained from healthy volunteers that were used in this study were taken from non-age matched males and females. Thus, the cohort of healthy samples contains confounding variables that may have had an impact on results. A database of healthy samples is currently being built to provide age and gender matched samples to use with the present data in order to provide more appropriate results. In addition, for each patient from the study outlined in chapter 5, samples have also been obtained post-hormonal treatment, during the last week of RT, 2 months post-RT and 8 months post-RT. Similarly, for each patient from the study outlined in chapter 6, samples have also been obtained throughout the course of RT treatment. These samples were obtained 1 hr post-RT, 24 hrs post-RT and at days 8, 15, 22 and 29 of RT treatment.

Samples for this cohort were also obtained 6 weeks post-RT and 3 months post-RT. Using the samples from these timepoints, the potential of Raman micro-spectroscopy to monitor radiotherapeutic response throughout RT treatment will be assessed in order to determine if the development of radiation toxicity can be identified at an early stage of treatment.

7.3 Conclusion

In conclusion, this thesis presents, for the first time, the novel application of Raman micro-spectroscopy to identify and predict RT patients with late normal tissue toxicity. Spectral differences were identified between lymphocytes from patients with severe (grade 2+) late radiation toxicity and those with no/minimal (grade 0-1) late radiation toxicity which allowed the classification of patients with a high degree of accuracy. Furthermore, while prediction could not be achieved based on late radiation toxicity in the first cohort of PCa patients, some success in predicting radiation toxicity could be achieved based on late radiation toxicity in the second cohort of PCa patients. The spectral analysis of the second cohort was not a reliable indicator of radiation toxicity outcome in every instance and in either case, it may be too early to attempt prediction as the clinical status of a number of the grade 0-1 patients may progress to grade 2+ in the following years. The patients from the first cohort will be followed up at 6 monthly intervals until Year 9 however, and those from the second cohort will be followed up every 6 months for up to 5 years with a minimum annual follow-up from 5-10 years, allowing the models to be updated as patient clinical status changes.

References

Abdi, H and Williams, LJ. Principal component analysis. *WIREs Computational Statistics* 2010; **2**: 433-459.

Adar, F. Evolution and revolution of Raman instrumentation – Application of available technologies to spectroscopy and microscopy. In Lewis, IR and Edwards, HGM. *Handbook of Raman spectroscopy: From the research laboratory to the process line* 2001. New York: Marcel Dekker Inc.

Adjakly, M *et al.* Prostate cancer: The main risk and protective factors – Epigenetic modifications. *Annales d'Endocrinologie* 2015; **76**: 25-41.

Agarwal, R, Tandon, P and Gupta, VD. Phonon dispersion in poly(dimethylsilane). *Journal of Organometallic Chemistry* 2006; **691**: 2902-8.

Ahnesorg, P, Smith, P and Jackson, SP. XLF interacts with the XRCC4-DNA ligase IV complex to promote DNA nonhomologous end-joining. *Cell* 2006; **124**: 301-13.

Alcorta, DA *et al*. Involvement of the cyclin-dependent kinase inhibitor p16 (INK4a) in replicative senescence of normal human fibroblasts. *Proceedings of the National Academy Sciences USA* 1996; **93**: 13742-7.

Alicikus, ZA *et al*. Ten-year outcomes of high-dose, intensity-modulated radiotherapy for localized prostate cancer. *Cancer* 2011; **117**(7): 1429-37.

An, J *et al*. DNA-PKcs plays a dominant role in the regulation of H2AX phosphorylation in response to DNA damage and cell cycle progression. *BMC Molecular Biology* 2010; **11**: 18.

Andreassen, CN. Searching for genetic determinants of normal tissue radiosensitivity--Are we on the right track? *Radiotherapy and Oncology* 2010; **97**(1): 1-8.

Andreassen, CN and Alsner, J. Genetic variants and normal tissue toxicity after radiotherapy: A systematic review. *Radiotherapy and Oncology* 2009; **92**(3): 299-309.

Andreassen, CN, Alsner, J, Overgaard, M and Overgaard, J. Prediction of normal tissue radiosensitivity from polymorphisms in candidate genes. *Radiotherapy and Oncology* 2003; **69**(2): 127-35.

Andreassen, CN, Alsner, J, Overgaard, M, Sørensen, FB and Overgaard, J. Risk of radiation-induced subcutaneous fibrosis in relation to single nucleotide polymorphisms in TGFB1, SOD2, XRCC1, XRCC3, APEX and ATM--A study based on DNA from formalin fixed paraffin embedded tissue samples. *International Journal of Radiation Biology* 2006; **82**(8): 577-86.

Andreassen, CN *et al*. ATM sequence variants and risk of radiation-induced subcutaneous fibrosis after postmastectomy radiotherapy. *International Journal of Radiation Oncology Biology Physics* 2006; **64**(3): 776-83.

Andrus, PGL and Strickland, RD. Cancer grading by Fourier transform infrared spectroscopy. Biospectroscopy 1998; 4: 37-46.

Auner, GW *et al*. Applications of Raman spectroscopy in cancer diagnosis. *Cancer Metastasis Reviews* 2018; **37**(4): 691-717.

Awad, M and Khanna, R. *Efficient Learning Machines: Theories, Concepts and Applications for Engineers and System Designers* 2015. New York: Apress.

Awal, A, Mostafa, SS and Ahmad, M. Performance analysis of Savitzky-Golay smoothing filter using ECG signal. *International Journal of Computer and Information Technology* 2011; **1**(2): 90-5.

Aykin-Burns, N *et al*. Sensitivity to low-dose/low-LET ionizing radiation in mammalian cells harbouring mutations in succinate dehydrogenase subunit C is governed by mitochondria-derived reactive oxygen species. *Radiation Research* 2011; **175**: 150-158.

Azria, D *et al*. Radiation-induced CD8 T-lymphocyte Apoptosis as a Predictor of Breast Fibrosis After Radiotherapy: Results of the Prospective Multicenter French Trial. *EBioMedicine* 2015; **2**(12): 1965-73.

Baade, PD, Youlden, DR and Krnjacki, LJ. International epidemiology of prostate cancer: Geographical distribution and secular trends. *Molecular Nutrition and Food Research* 2009; **53**: 171-84.

Baek, SJ, Park, A, Ahn, YJ and Choo, J. Baseline correction using asymmetrically reweighted penalized least squares smoothing. *Analyst* 2015; **140**: 250-7.

Baeyens, A, Thierens, H, Claes, K, Poppe, B, Messiaen, L, De Ridder, L and Vral, A. Chromosomal radiosensitivity in breast cancer patients with a known or putative genetic predisposition. *British Journal of Cancer* 2002; **87**: 1379-85.

Bähler, J. Cell-cycle control of gene expression in budding and fission yeast. *Annual Review of Genetics* 2005; **39**: 69-94.

Banasiak, D, Barnetson, AR, Odell, RA, Mameghan, H and Russell, PJ. Comparison between the clonogenic, MTT and SRB assays for determining radiosensitivity in a panel of human bladder cancer cell lines and a ureteral cell line. *Radiation Oncology Investigations* 1999; **7**(2): 77-85.

Barber, JBP *et al*. Relationship between *in vitro* chromosomal radiosensitivity of peripheral blood lymphocytes and the expression of normal tissue damage following radiotherapy for breast cancer. *Radiotherapy and Oncology* 2000; **55**: 179-86.

Baria, K, Warren, C, Roberts, SA, West CM and Scott, D. Chromosomal radiosensitivity as a marker of predisposition to common cancers? *British Journal of Cancer* 2001; **84**(7): 892-6.

Barnett, GC, Coles, CE and Elliott, RM *et al*. Independent validation of genes and polymorphisms reported to be associated with radiation toxicity: A prospective analysis study. Lancet Oncology 2012; 13: 65-77.

Barnett, GC *et al*. A genome wide association study (GWAS) providing evidence of an association between common genetic variants and late radiotherapy toxicity. *Radiotherapy and Oncology* 2014; **111**: 178-85.

Barnett, GC, West, CML, Dunning, AM, Elliott, RM, Coles, CE, Pharoah, PDP and Burnet, NG. Normal tissue reactions to radiotherapy: Towards tailoring treatment dose by genotype. *Nature Reviews Cancer* 2009; **9**(2): 134-42.

Barnum, KJ and O'Connell, MJ. Cell cycle regulation by checkpoints. *Methods in Molecular Biology* 2016; **1170**: 29-40.

Bartek, J and Lukas, J. DNA damage checkpoints: From initiation to recovery or adaptation. *Current Opinion in Cell Biology* 2007; **19**: 238-45.

Bartek, J, Lukas, C and Lukas, J. Checking on DNA damage in S phase. *Nature Reviews Molecular Cell Biology* 2004; **5**: 792-804.

Barzał, JA, Szczylik, C, Rzepecki, P, Jaworska, M and Anuszewska, E. Plasma citrulline level as a biomarker for cancer therapy-induced small bowel mucosal damage. *Acta Biochimica Polonica* 2014; **61**: 615-31.

Baskar, R, Lee, KA, Yeo, R and Yeoh, KW. Cancer and radiation therapy: Current advances and future directions. *International Journal of Medical Sciences* 2012; **9**(3): 193-99.

Basso, MS, Capriati, T, Goffredo, BM, Panetta, F and Diamanti, A. Citrulline as marker of atrophy in celiac disease. *Internal and Emergency Medicine* 2014; **9**: 705-7.

Beaton, LA, Ferrarotto, C and Marro, L *et al.* Chromosome damage and cell proliferation rates in *in vitro* irradiated whole blood as markers of late radiation toxicity after radiation therapy to the prostate. *International Journal of Radiation Oncology* 2013; **85**(5): 1346-52.

Beauséjour, CM *et al*. Reversal of human cellular senescence: Role of the p53 and p16 pathways. The *EMBO Journal* 2003; **22**: 4212-22.

Bedini *et al*. Evaluation of mediators associated with the inflammatory response in prostate cancer patients undergoing radiotherapy. *Disease Markers* 2018; **2018**: 9128128.

Begg, AC. Molecular targeting and patient individualization. In Joiner, M and van der Kogel, A (Eds.). *Basic clinical radiobiology* (4th Ed.) 2009. London: Hodder Arnold, pp. 316-31.

Begg, AC, Stewart, FA and Vens, C. Strategies to improve radiotherapy with targeted drugs. *Nature Reviews Cancer* 2011; **11**: 239-53.

Bekkar, M, Djemaa, HK and Alitouche, TA. Evaluation measures for models assessment over imbalanced data sets. *Journal of Information Engineering and Applications* 2013; **3**(10): 27-39.

Ben-David, U. Genomic instability, driver genes and cell selection: Projections from cancer to stem cells. *Biochimica et Biophysica Acta* 2015; **1849**: 427-35.

Bentzen, SM. Preventing or reducing late side effects of radiation therapy: Radiobiology meets molecular pathology. *Nature Reviews Cancer* 2006; **6**: 702-13.

Berghe, TV, Linkermann, A, Jouan-Lanhouet, S, Walczak, H and Vandenabeele, P. Regulated necrosis: The expanding network of non-apoptotic cell death pathways. *Nature Reviews Molecular Cell Biology* 2014; **15**: 135-47.

Bernstein, C, Prasad, AR, Nfonsam, V and Bernstein H. DNA damage, DNA repair and cancer. In Chen, C (Ed.). *New Res Directions* 2013. London: InTech.

Bertoli, C, Skotheim, JM and de Bruin, RAM. Control of cell cycle transcription during G1 and S phases. *Nature Reviews Molecular Cell Biology* 2013; **14**(8): 518-28.

Bhatti, S, Kozlov, S, Farooqi, AA, Naqi, A, Lavin, M and Khanna, KK. ATM protein kinase: The linchpin of cellular defenses to stress. *Cellular and Molecular Life Sciences* 2011; **68**: 2977-3006.

Binoy, J, Abraham, JP, Joe, IH, Jayakumar, VS, Petit, GR and Nielsen, OF. NIR-FT Raman and FT-IR spectral studies and ab initio calculations of the anti-cancer drug combretastatin-A4. Journal of Raman Spectroscopy 2004; 35: 939-46.

Björk-Eriksson, T *et al*. Tumor radiosensitivity (SF2) is a prognostic factor for local control in head and neck cancers. *International Journal of Radiation Oncology Biology Physics* 2000; **46**: 13-19.

Blekherman, G *et al*. Bioinformatics tools for cancer metabolomics. *Metabolomics* 2011; **7**: 329-43.

Bolla, M *et al*. Concurrent and adjuvant docetaxel with three-dimensional conformal radiation therapy plus androgen deprivation for high-risk prostate cancer: Preliminary results of a multicentre phase II trial. *Radiotherapy and Oncology* 2010; **97**: 312-7.

Bolla, M *et al*. Long-term results with immediate androgen suppression and external irradiation in patients with locally advanced prostate cancer (an EORTC study): A phase III randomised trial. *Lancet* 2002; **360**: 103-6.

Bonner, WM. Phenomena leading to cell survival values which deviate from linear-quadratic models. *Mutation Research* 2004; **568**: 33-9.

Borgmann, K *et al*. Indicators of late normal tissue response after radiotherapy for head and neck cancer: fibroblasts, lymphocytes, genetics, DNA repair, and chromosome aberrations. *Radiotherapy and Oncology* 2002; **64**(2): 141-52.

Boulesteix, AL and Strimmer, K. Partial least squares: a versatile tool for the analysis of high- dimensional genomic data. *Briefings in Bioinformatics* 2007; **8**: 32-44.

Bourton, EC, Plowman, PN, Smith, D, Arlett, D and Parris, CN. Prolonged expression of the γ-H2AX DNA repair biomarker correlates with excess acute and chronic toxicity from radiotherapy treatment. *International Journal of Cancer* 2011; **129**: 2928-34.

Boustani, J, Grapin, M, Laurent, PA, Apetoh, L and Mirjolet, C. The 6th R of radiobiology: Reactivation of anti-tumor immune response. *Cancers* 2019; **11**: 860.

Brandsma, I and Gent, DC. Pathway choice in DNA double strand break repair: Observations of a balancing act. *Genome Integrity* 2012; **3**: PMC3557175.

Brereton, RG and Lloyd GR. Partial least squares discriminant analysis: Taking the magic away. *Journal of Chemometrics* 2014; **28**: 213-25.

Brierley, JD, Gospodariwicz, M and Wittekind, C (Eds.). *TNM classification of malignant tumors. UICC International Union Against Cancer* (8th Ed.) 2016. NJ: Wiley-Blackwell.

Brown, V, Sridhar, T and Symonds, RP. Principles of chemotherapy and radiotherapy. *Obstetrics, Gynaecology and Reproductive Medicine* 2011; **21**(12): 339-45.

Bryant, PE *et al*. Technical report: The G2 chromosomal radiosensitivity assay. *International Journal of Radiation Biology* 2002; **78**(9): 863-6.

Brzozowska, K. *et al*. *In vivo* versus *in vitro* individual radiosensitivity analysed in healthy donors and in prostate cancer patients with and without severe side effects after radiotherapy. *International Journal of Radiation Biology* 2012; **88**(5): 405-13.

Buch, K, Peters, T, Nawroth, T, Snger, M, Schmidberger, H and Langguth, P. Determination of cell survival after irradiation via clonogenic assay versus multiple MTT Assay – A comparative study. *Radiation Oncology* 2012; **7**(1): PMC3274452.

Buck, D *et al*. Cernunnos, a novel nonhomologous end-joining factor, is mutated in human immunodeficiency with microcephaly. *Cell* 2006; **124**: 287-99.

Burke, JR, Hura, GL and Rubin, SM. Structures of inactive retinoblastoma protein reveal multiple mechanisms for cell cycle control. *Genes and Development* 2012; **26**(11): 1156-66.

Burkhart, DL and Sage, J. Cellular mechanisms of tumour suppression by the retinoblastoma gene. *Nature Reviews Cancer* 2008; **8**: 671-82.

Burmeister, JW and Joiner, MC. Physics of radiation therapy for the radiobiologist. In Joiner, M and van der Kogel, A (Eds.). *Basic clinical radiobiology* (5th Ed.) 2019. New York: Taylor and Francis Group, pp. 61-80.

Burnet, NG, Nyman, J, Turesson, I, Wurm, R, Yarnold, JR and Peacock, JH. Prediction of normal-tissue tolerance to radiotherapy from *in-vitro* cellular radiation sensitivity. *Lancet* 1992; **27**: 339: 1570-1.

Butler, HJ *et al*. Using Raman spectroscopy to characterize biological materials. *Nature Protocols* 2016; **11**(4): 664-87.

Byrne, HJ, Sockalingum, GD and Stone, N. In Moss, D (Ed.). *Biomedical applications of synchrotron infrared microspectroscopy: A practical approach* 2011. London: RSC Publishing, pp. 105-42.

Cadet, J and Wagner, JR. DNA base damage by reactive oxygen species, oxidizing agents, and UV radiation. *Cold Spring Harbor Perspectives in Biology* 2013; **5**: a012559.

Campisi, J and d'Adda di Fagagna, F. Cellular Senescence: When bad things happen to good cells. *Nature Reviews Molecular Cell Biology* 2007; **8**: 729-40.

Cancer Research UK. Decisions about your treatment. Retrieved 28 February 2017, from: *http://www.cancerresearchuk.org/about-cancer/prostate-cancer/treatment /decisions-about-your-treatment.*

Cande, C, Cecconi, F, Dessen, P and Kroemer, G. *Journal of Cell Science* 2002; **15**: 4727-34.

Cannan, WJ and Pederson, DS. Mechanisms and consequences of double-strand DNA break formation in chromatin. *Journal of Cellular Physiology* 2016; **231**(1): 3-14.

Carr, DF *et al*. Towards better models and mechanistic biomarkers for drug-induced gastrointestinal injury. *Pharmacology & Therapeutics* 2017; **172**: 181–94.

Caspers, PJ, Lucassen, GW, Carter, EA, Bruining, HA and Puppels, GJ. In vivo confocal Raman microspectroscopy of the skin: Non-invasive determination of molecular concentration profiles. *Journal of Investigative Dermatology* 2001; **116**(3): 434-42.

Castedo, M, Perfettini, JL, Roumier, T, Andreau, K, Medema, R and Kroemer, G. Cell death by mitotic catastrophe: A molecular definition. *Oncogene* 2004; **23**: 2825-37.

Castedo, M, *et al*. Mitotic catastrophe constitutes a special case of apoptosis whose suppression entails aneuploidy. *Oncogene* 2004; **23**(25): 4362-70.

Chan, JW, Taylor, DS, Zwerdling, T, Lane, SM, Ihara, K and Huser, T. Micro-Raman spectroscopy detects individual neoplastic and normal hematopoietic cells. *Biophysical Journal* 2006; **90**: 648-56.

Chang, AJ, Autio, KA, Roach, M and Scher, HI. High-risk prostate cancer – classification and therapy. *Nature* 2014; **11**: 308-23.

Chen, S, Lin, X, Yuen, C, Padmanabhan, S, Beuerman, RW and Liu, Q. Recovery of Raman spectra with low signal-to-noise ratio using Wiener estimation. *Optics Express* 2014; **22**(10): 12102-14.

Cheng, WT, Liu, MT, Liu, HN and Lin, SY. Micro-Raman spectroscopy used to identify and grade human skin pilomatrixoma. *Microscopy Research and Technique* 2005; **68**: 75-9.

Childs, BG, Durik, M, Baker, DJ and van Deursen, JM. Cellular senescence in aging and age-related disease: From mechanisms to therapy. *Nature Medicine* 2015; **21**(12): 1424-35.

Christensen, E *et al*. Longitudinal cytokine expression during IMRT for prostate cancer and acute treatment toxicity. *Clinical Cancer Research* 2009; **15**(17): 5576-83.

Christiakov, DA, Voronova, NV and Christiakov, PA. Genetic variations in DNA repair genes, radiosensitivity to cancer and susceptibility to acute tissue reactions in radiotherapy-treated cancer patients. *Acta Oncologica* 2008; **47**: 809-24.

Christin, C *et al*. A critical assessment of feature selection methods for biomarker discovery in clinical proteomics. *Molecular and Cellular Proteomics* 2013; **12**: 263-76.

Choquette, SJ, Etz, ES, Hurst, WS, Blackburn, DH and Leigh, SD. Relative Intensity Correction of Raman Spectrometers: NIST SRMs 2241 through 2243 for 785 nm, 532 nm, and 488 nm/514.5 nm Excitation. *Applied Spectroscopy* 2007; **61**(2):117-29.

Chu, K, Teele, N, Dewey, MW, Albright, N and Dewey, WC. Computerized video time lapse study of cell cycle delay and arrest, mitotic catastrophe, apoptosis and clonogenic survival in irradiated 14-3-3sigma and CDKN1A (p21) knockout cell lines. *Radiation Research* 2004; **162**(3): 270-86.

Chua, MLK, Somaiah, N, A'Hern, R, Davies, S, Gothard, L, Yarnold, J and Rothkamm, K. Residual DNA and chromosomal damage in *ex vivo* irradiated blood lymphocytes correlated with late normal tissue response to breast radiotherapy. *Radiotherapy and Oncology* 2011; **99**: 362-6.

Ciccia, A and Elledge, SJ. The DNA damage response: Making it safe to play with knives. *Molecular Cell* 2010; **40**: 179-204.

Ciervide *et al.* Five year outcome of 145 patients with ductal carcinoma in situ (DCIS) after accelerated breast radiotherapy. *International Journal of Radiation Oncology Biology Physics* 2012; **83**(2): 159-64.

Clemens, G, Hands, JR, Dorling, KM and Baker, MJ. Vibrational spectroscopic methods for cytology and cellular research. *Analyst* 2014; **139**: 4411-44.

Cogswell, JP, Brown, CE, Bisi, JE and Neill, SD. Dominant-negative polo-like kinase 1 induces mitotic catastrophe independent of cdc25C function. *Cell Growth and Differentiation* 2000; **11**(12): 615-23.

Collette, TW and Williams, TL. The role of Raman spectroscopy in the analytical chemistry of potable water. *Journal of Environmental Monitoring* 2002; **4**: 27-34.

Colthup, NB, Daly, LH and Wiberley, SE. *Introduction to infrared and Raman spectroscopy* 1990. London: Academic Press.

Cooper, GM. *The cell: A molecular approach* (2nd Ed.) 2000. Sunderland: Sinauer Associates.

Corsetti, S, Rabl, T, McGloin, D and Nabi, G. Raman spectroscopy for accurately characterizing biomolecular changes in androgen-independent prostate cancer cells. *Journal of Biophotonics* 2017; **11**(3): e201700166.

Cox, JD and Stetz, J. Toxicity criteria of the Radiation Therapy Oncology Group (RTOG) and the European Organisation for Research and Treatment of Cancer (EORTC). *International Journal of Radiation Oncology Biology Physics* 1995; **31**: 1341-6.

Cozma, AI *et al*. Relationship of urethral dose and genitourinary toxicity among patients receiving vaginal high dose rate interstitial brachytherapy. *Clinical Oncology* 2021; S0936-6555(21)00183-7.

Crenn, P, Messing, B and Cynober, L. Citrulline as a biomarker of intestinal failure due to enterocyte mass reduction. *Clinical Nutrition* 2008; **27**: 328-39.

Crenn, P, Vahedi, K, Lavergne-Slove, A, Cynober, L, Matuchansky, C and Messing, B. Plasma citrulline: A marker of enterocyte mass in villous atrophy-associated small bowel disease. *Gastroenterology* 2003; **124**: 1210–1219.

Crenn, P, Coudray-Lucas, C, Thuillier, F, Cynober, L and Messing, B (2000). Postabsorptive plasma citrulline concentration is a marker of absorptive enterocytemass and intestinal failure in humans. *Gastroenterology* 2000; **119**: 1496-505.

Crow, P, Barrass, B, Kendall, C, Hart-Prieto, M, Wright, M, Persad, R and Stone, N. The use of Raman spectroscopy to differentiate between different prostatic adenocarcinoma cell lines. *British Journal of Cancer* 2005b; **92**: 2166-70.

Crow, P, Molckovsky, A, Stone, A, Uff, J, Wilson, B and Wong Kee Song, LM. Assessment of fiberoptic near-infrared Raman spectroscopy for diagnosis of bladder and prostate cancer. *Urology* 2005a; **65**: 1126-30.

Crow, P, Stone, N, Kendall, CA, Uff, JS, Farmer, JAM, Barr, H and Wright, MPJ. The use of Raman spectroscopy to identify and grade prostatic adenocarcinoma *in vitro*. *British Journal of Cancer* 2003; **89**: 106-8.

Cuzick, J, Thorat, MA and Andriole, G. Prevention and early detection of prostate cancer. *Lancet Oncology* 2014; **15**(11): 484-92.

D'Amico, AV *et al.* Androgen suppression and radiation vs radiation alone for prostate cancer: A randomized trial. *JAMA* 2008; **299**: 289-95.

Dale, R. Use of the linear-quadratic radiobiological model for quantifying kidney response in targeted radiotherapy. *Cancer Biotherapy & Radiopharmaceuticals* 2004; **19**(3): 363-70.

Dal Pra, A, Cury, FL and Souhami, L. Combining radiation therapy and androgen deprivation therapy for localized prostate cancer. *Current Oncology* 2010; **17**(5): 28-38.

Degterev, A, Boyce, M and Yuan, J. *Oncogene* 2003; **22**: 8543-67.

Delahunt, B, Miller, RJ, Srigley, JR, Evans, AJ and Samaratunga, H. Gleason grading: Past, present and future. *Histopathology* 2012; **60**: 75-86.

Delaney, G, Jacob, S, Featherstone, C and Barton, M. The role of radiotherapy in cancer treatment: Estimating optimal utilisation from a review of evidence-based clinical guidelines. *Cancer* 2005; **104**: 1129-37.

De Meeleer, G *et al.* Intensity-modulated radiation therapy for prostate cancer: Late morbidity and results on biochemical control. *Radiotherapy and Oncology* 2007; **82**: 160-66.

Denham, JW and Hauer-Jensen, M. The radiotherapeutic injury--A complex 'wound'. *Radiotherapy and Oncology* 2002; **63**(2): 129-45.

De Ruyck, K *et al*. Chromosomal radiosensitivity in head and neck cancer patients: evidence for genetic predisposition? *British Journal of Cancer* 2008; **98**: 1723-8.

De Ruyck, K *et al*. TGFbeta1 polymorphisms and late clinical radiosensitivity in patients treated for gynecological tumors. *International Journal of Radiation Oncology Biology Physics* 2006; **65**(4): 1240-8.

Desai, S, Kumar, A, Laskar, S and Pandey, BN. Cytokine profile of conditioned medium from human tumor cell lines after acute and fractionated doses of gamma radiation and its effect on survival of bystander tumor cells. *Cytokine* 2013; **61**: 54-62.

Desouky, O, Ding, N and Zhou, G. Target and non-targeted effects of ionizing radiation. *Journal of Radiation Research and Applied Sciences* 2015; **8**: 247-54.

Di Maggio, FM *et al*. Portrait of inflammatory response to ionizing radiation treatment. *Journal of Inflammation* 2015; **12**: 10.1186/s12950-015-0058-3.

Doolittle, N. Cancer Genetics Ebook. Retrieved 19 December 2017, from: *http://www.cubocube.com/dashboard.php?a=1713&c=1.*

Dörr, W. Pathogenesis of normal tissue side effects. In Joiner, M and van der Kogel, A (Eds.). *Basic clinical radiobiology* (5th Ed.) 2019. New York: Taylor and Francis Group, pp. 152-70.

Dörr, W. Time factors in normal-tissue responses to irradiation. In Joiner, M and van der Kogel, A (Eds.). *Basic clinical radiobiology* (5th Ed.) 2019. New York: Taylor and Francis Group, pp. 136-42.

Dossin, O, Rupassara, SI, Weng, HY, Williams, DA, Garlick, PJ and Schoeman, JP. Effect of parvoviral enteritis on plasma citrulline concentration in dogs. *Journal of Veterinary Internal Medicine* 2011; **25**: 215–21.

Dovbeshko, GI, Gridina, NY, Kruglova, EB and Pashchuk, OP. FTIR spectroscopy studies of nucleic acid damage. *Talanta* 2000; **53**: 233-46.

Driessens, G *et al*. Micronuclei in detect *in vivo* chemotherapy damage in a p53 mutated solid tumour. *British Journal of Cancer* 2003; **89**(4): 727-9.

Dukor, RK. Vibrational spectroscopy in the detection of cancer. In Chalmers, JA and Griffiths, P (Eds.) *Handbook of Vibrational Spectroscopy* 2002. London: Wiley. 3335-61.

Dunne, AL, Price, ME, Mothersill, C, McKeown, SR, Robson, T and Hirst, DG. Relationship between clonogenic radiosensitivity, radiation-induced apoptosis and DNA damage/repair in human colon cancer cells. *British Journal of Cancer* 2003; **89**: 2277-83.

Dupré, A, Boyer-Chatenat, L and Gautier, J. Two-step activation of ATM by DNA and the Mre11-Rad50-Nbs1 complex. *Nature Structural and Molecular Biology* 2006; **13**(5): 451-7.

Duranska, NK, Sezen, D, Selek, U and Bolukbasi, Y. Toxicity management for pelvic tumors in radiation oncology. In Ozyigit, G and Selek, U (Eds.). *Prevention and management of acute and late toxicities in radiation oncology: Management of toxicities in radiation oncology* 2020. Switzerland: Springer Nature.

Durocher, D and Jackson, SP. DNA-PK, ATM and ATR as sensors of DNA damage: Variations on a theme? *Current Opinion Cell Biology* 2001; **13**: 225-31.

Eccles, LJ, O' Neill, P and Lomax, ME. Delayed repair of radiation induced clustered DNA damage: Friend or foe? *Mutation Research* 2011; **711**(1-2): 134-41.

Eldeeb, MA, Fahlman, RP, Esmaili, M and Ragheb, MA. Regulating apoptosis by degradation: The N-end rule-mediated regulation of apoptotic proteolytic fragments in mammalian cells. *International Journal of Molecular Sciences* 2018; **19**: 3414.

Elgedawy, MN. Prediction of breast cancer using random forest, support vector machines and naïve Bayes. *International Journal of Engineering and Computer Science* 2017; **6**(1): 19884-19889.

Ellis, DI, Cowcher, DP, Ashton, L, O' Hagan, S and Goodacre, R. Illuminating disease and enlightening biomedicine: Raman spectroscopy as a diagnostic tool. *Analyst* 2013; **138**: 3847-4204.

Encheva, E, Deleva, S, Hristova, R, Hadjidekova, V and Hadjieva, T. Investigating micronucleus assay applicability for prediction of normal tissue intrinsic radiosensitivity in gynecological cancer patients. *Reports of Practical Oncology and Radiotherapy* 2012; **17**: 24-31.

Epperly, MW, Epstein, CJ, Travis, EL and Greenberger, JS. Decreased pulmonary radiation resistance of manganese superoxide dismutase (MnSOD)-deficient mice is corrected by human human manganese superoxide dismutase-plasmid/liposome (SOD2-PL) intratracheal gene therapy. *Radiation Research* 2000; **154**: 365-74.

Epstein, JI *et al.* A contemporary prostate cancer grading system: A validated alternative to the Gleason score. *European Urology* 2016; **69**: 428-35.

Erickson, BA, Otterson, MF, Moulder, JE, Sarna, SK. Altered motility causes the early gastrointestinal toxicity of irradiation. *International Journal of Radiation Oncology Biology Physics* 1994; **28**(4): 905-12.

Eriksson, D and Stigbrand, T. Radiation-induced cell death mechanisms. *Tumor Biology* 2010; **31**(4): 363-72.

Eschwege, F *et al*. Predictive assays of radiation response in patients with head and neck squamous cell carcinoma: A review of the Institute of Gustave Roussy experience. *International Journal of Radiation Oncology Biology Physics* 1997; **39**: 849-53.

Fachal, L *et al*. A three-stage genome-wide association study identifies a susceptibility locus for late radiotherapy toxicity at 2q24.1. *Nature Genetics* 2014; **46**(8): 891-4.

Falck, J, Coates, J and Jackson, SP. Conserved modes of recruitment of ATM, ATR and DNA-PKcs to sites of DNA damage. *Nature* 2005; **434**: 605-11.

Falck, J, Mailand, N, Syljuasen, RG, Bartek, J and Lukas, J. The Atm-Chk2-Cdc25A checkpoint pathway guards against radioresistant DNA synthesis. *Nature* 2001; **410**: 842-7.

Fan, Z, Beresford, PJ, Oh, DY, Zhang, D and Lieberman, J. Tumor suppressor NM23-H1 is a granzyme A-activated DNase during CTL-mediated apoptosis, and the nucleosome assembly protein SET is its inhibitor. *Cell* 2003; **112**: 659-72.

Faolain, EO *et al*. A study examining the effects of tissue processing on human tissue sections using vibrational spectroscopy. Vibrational Spectroscopy 2005; 38: 121-7.

Farguharson, S, Shende, C, Inscore, FE, Maksymiuk, P and Gift, A. Analysis of 5-fluorouracil in saliva using surface-enhanced Raman spectroscopy. Journal of Raman Spectroscopy 2005; 36: 208-12.

Fawcett, T. An introduction to ROC analysis. *Pattern Recognition Letter* 2006; **27**(8): 861-74.

Felgentreff *et al*. Differential DNA damage response of peripheral blood lymphocyte populations. *Frontiers in Immunology* 2021; **12**: 739675.

Ferlay, J, Soerjomataram, I, Dikshit, R, Eser, S, Mathers, C, Rebelo, M, Parkin, DM, Forman, D and Bray, F. Cancer incidence and mortality worldwide: Sources, methods and major patterns in GLOBOCAN 2012. *International Journal of Cancer* 2015; **136**: E359-86.

Ferlazzo, ML, Bourguignon, M and Foray, N. Functional assays for individual radiosensitivity: A critical review. *Seminars in Radiation Oncology* 2017; **27**: 310-15.

Ferraro, JR, Nakamoto, K and Brown, CW. *Introductory Raman spectroscopy* 2003. London: Academic Press.

Finnon, *et al*. Correlation of *in vitro* lymphocyte radiosensitivity and gene expression with late normal tissue reactions following curative radiotherapy for breast cancer. *Radiotherapy and Oncology* 2012; **105**(3): 329-36.

Foray, N, Colin, C and Bourguignon, M. 100 years of individual radiosensitivity: How we have forgotten the evidence. *Radiology* 2012; **264**(3): 627-31.

Frank, CJ, McCreecy, RL and Redd, DCB. Raman spectroscopy of normal and diseased human breast tissues. *Analytical Chemistry* 1995; 67: 777-83.

Frappart, PO and McKinnon, PJ. Ataxia-telangiectasia and related diseases. *NeuroMolecular Medicine* 2006; **8**: 495-511.

Fulda, S and Debatin, KM. Extrinsic versus intrinsic apoptosis pathways in anticancer chemotherapy. *Oncogene* 2006; **25**: 4798-811.

Fung, MFK, Senterman, MK, Mikhael, NZ, Lacelle, S and Wong, PTT. Pressure-tuning Fourier transform infrared spectroscopic study of carcinogenesis in human endometrium. *Biospectroscopy* 1996; **2**: 155-65.

Galluzzi, L *et al*. Molecular definitions of cell death subroutines: Recommendations of the Nomenclature Committee on Cell Death 2012. *Cell Death and Differentiation* 2012; **19**: 107-20.

Gann, P. Risk factors for prostate cancer. *Reviews in Urology* 2002; **4**(5): S3-10.

Gazda, M and Coia, L. Principles of radiation therapy. In Pazdur, R *et al.* (Eds.). *Cancer management: A multidisciplinary approach* (9th Ed) 2005. Lawrence: CMP Healthcare Media, pp.11-22.

Gazi, E *et al*. Applications of Fourier transform infrared microspectroscopy in studies of benign prostate and prostate cancer: A pilot study. *Journal of Pathology* 2003; **201**: 99-108.

Geara, FB, Peters, LJ, and Ang, KK *et al.* Intrinsic radiosensitivity of normal human fibroblasts and lymphocytes after high- and low-dose-rate irradiation. *Cancer Research* 1992; **52**: 6348-52.

Geinitz, H, Zimmermann, FB, Thamm, R, Schumertl, A, Busch, R and Molls, M. 3D conformal radiation therapy for prostate cancer in elderly patients. *Radiotherapy and Oncology* 2005; **76**: 27-34.

Gelfand, M, Tepper, M, Katz, L, Binder, H, Yesner, R and Floch M. Acute radiation proctitis in man. *Gastroenterology* 1968; **54**: 401– 11.

Gerou-Ferriani, M, Allen, R, Noble, PM, German, AJ, Caldin, M and Batchelor, DJ. Determining optimal therapy of dogs with chronic enteropathy bymeasurement of serum citrulline. *Journal of Veterinary Internal Medicine* 2018; **32**: 993–8.

Ghosh, S, Ghosh, A and Krishna, M. Role of ATM in bystander signalling between human monocytes and lung adenocarcinoma cells. *Mutation Research* 2015; **794**: 39-45.

Giotopoulus, G *et al*. The late radiotherapy normal tissue injury phenotypes of telangiectasia, fibrosis and atrophy in breast cancer patients have distinct genotype-dependent causes. *British Journal of Cancer* 2007; **96**(6): 1001-7.

Gleizes, A, Cavaillés and Lapierre, M. Transcriptional regulation of the intestinal cancer stem cell phenotype. In Uchiumi, F (Ed.). *Gene expression and regulation in mammalian cells: Transcription toward the establishment of novel therapeutics*, pp. 273-295.

Gomella, LG. Effective testosterone suppression for prostate cancer: Is there a best castration therapy? *Reviews in Urology* 2009; **11**(2): 52-60.

Greve, B *et al*. Evaluation of Different Biomarkers to Predict Individual Radiosensitivity in an Inter-Laboratory Comparison–Lessons for Future Studies. *PLoS One* 2012; **7**(10): e47185.

Gromski PS *et al*. A tutorial review: Metabolomics and partial least squares-discriminant analysis – A marriage of convenience or a shotgun wedding. *Analytica Chimica Acta* 2015; **879**: 10-23.

Habash, M, Bohorquez, LC, Kyriakou, E, Kron, T, Martin, OA and Blyth, BJ. Clinical and functional assays of radiosensitivity and radiation-induced second cancer. *Cancers* 2017; **9**(11): E147.

Hall, EJ and Giaccia AJ. *Radiobiology for the radiologist* (8th Ed.) 2019. Philadelphia: Wolters Kluwer.

Han, D, Chan, L and Zhu, N. Flood forecasting using support vector machines. *Journal of hydroinformatics* 2007; **9**: 267-76.

Hanks, GE *et al.* Phase III trial of long-term adjuvant androgen deprivation after neoadjuvant hormonal cytoreduction and radiotherapy in locally advanced carcinoma of the prostate: The Radiation Therapy Oncology Group Protocol 92-02. *Journal of Clinical Oncology* 2003; **21**: 3972-8.

Hanlon, EB *et al*. Prospects for *in vivo* Raman Spectroscopy. *Physics in Medicine and Biology* 2000; **45**: 1-59.

Hansen, J and Bross, P. A cellular viability assay to monitor drug toxicity. *Methods in Molecular Biology* 2010; **648**: 303-11.

Harder, SJ, Matthews, Q, Isabelle, M, Brolo, AG, Lum, JJ and Jirasek, A. A Raman spectroscopic study of cell response to clinical doses of ionising radiation. *Applied Spectroscopy* 2015; **69**(2): 193-204.

Harder, SJ *et al*. Raman spectroscopy identifies radiation response in human non-small cell lung cancer xenografts. *Scientific Reports* 2016; **6**: 21006.

Harney, J *et al*. The evaluation of low-dose hyper-radiosensitivity in normal human skin. *Radiotherapy and Oncology* 2004; **70**: 319-29.

Harrington, K, Jankowska, P and Hingorani, M. Molecular biology for the radiation oncologist: The 5Rs of radiobiology meet the hallmarks of cancer. *Clinical Oncology* 2007; **19**: 561-71.

Hastie, T, Tibshirani, R and Friedman, J. *The elements of statistical learning: Data mining, inference and prediction* 2009. New York: Springer-Verlag.

Hata *et al.* Degarelix as a neoadjuvant hormonal therapy for acute urinary tract toxicity associated with external beam radiotherapy for intermediate- and high-risk prostate cancer: A propensity score matched analysis. *Japanese Journal of Clinical Oncology* 2021; **51**(3): 478-83.

Herskind, C *et al.* Biology of high single doses of IORT: RBE, 5 R's, and other biological aspects. *Radiation Oncology* 2017; **24**: 24-38.

Herskind, C, Talbot, CJ, Kerns, SL, Veldwijk, MR, Rosenstein, BS and West, CML. Radiogenomics: A systems biology approach to understanding genetic risk factors for radiotherapy toxicity? *Cancer Letters* 2016; **382**(1): 95-109.

Hoeller, U *et al*. Individual radiosensitivity measured with lymphocytes may be used to predict the risk of fibrosis after radiotherapy for breast cancer. *Radiotherapy and Oncology* 2003; **69**(2): 137-44.

Hoenicke, L and Zender, L. Immune surveillance of senescent cells – biological significance in cancer- and non-cancer pathologies. *Carcinogenesis* 2012; **33**: 1123-6.

Horsman, MR, Brown, JM, van der Kogel, AJ, Wouters, BG and Overgaard, J. The oxygen effect and therapeutic approaches to tumor hypoxia. In Joiner, M and van der Kogel, A (Eds.). *Basic clinical radiobiology* (5th Ed.) 2019. New York: Taylor and Francis Group, pp. 188-205.

Hovdenak, N, Fajardo, LF and Hauer-Jensen, M. Acute radiation proctitis: A sequential clinicopathologic study during pelvic radiotherapy. *International Journal of Radiation Oncology Biology Physics* 2000; **48**: 1111-7.

Howe, OL, Daly, PA, Seymour, C, Ormiston, W, Nolan, C and Mothersill, C. Elevated G2 chromosomal radiosensitivity in Irish breast cancer patients: A comparison with other studies. *International Journal of Radiation Biology* 2005; **81**(5): 373-8.

Howe, OL *et al.* Cell death mechanisms associated with G2 radiosensitivity in patients with prostate cancer and benign prostatic hyperplasia. *Radiation Research* 2005; **164**: 627-34.

Huang, Z, Lui, H, McClean, DI, Korbelik, M and Zeng, H. Raman spectroscopy in combination with background near-infrared autofluorescence enhances the in vivo assessment of malignant tissues. *Photochemistry and Photobiology* 2005; **81**: 1219-26.

Huang, Z, McWilliams, A, Lui, M, McLean, DI, Lam, S and Zeng, H. Near-infrared Raman spectroscopy for optical diagnosis of lung cancer. *International Journal of Cancer* 2003a; **107**: 1047-52.

Huang, Z, McWilliams, A, Lam, S, English, J, McLean, D, Lui, H and Zeng, H. Effect of formalin fixation on the near-infrared Raman spectroscopy of normal and cancerous human bronchial tissues. *International Journal of Oncology* 2003b; **23**: 649-55.

Hunter, GK *et al*. Long-term (10 year) gastrointestinal and genitourinary toxicity after treatment with external beam radiotherapy, radical prostatectomy, or brachytherapy for prostate cancer. *Prostate Cancer* 2012; **2012**: PMC3345236.

Igdem, S. Treatment of prostate cancer by hypofractionated radiotherapy. *Marmara Medical Journal* 2015; **28**: 21-3.

Illiakis, G, Wang, Y, Guan, J and Wang, H. DNA damage checkpoint control in cells exposed to ionizing radiation. *Oncogene* 2003; **22**: 5834-47.

Inagaki-Ohara, K *et al*. p53-dependent radiation-induced crypt intestinal epithelial cells apoptosis is mediated in part through TNF-TNFR1 system. *Oncogene* 2001; **20**(7): 812-8.

Jaal, J and Dörr, W. Radiation-induced damage to mouse urothelial barrier. *Radiotherapy and Oncology* 2006; **80**(2): 250-6.

Jäckel, S *et al*. l-citrulline: A preclinical safety biomarker for the small intestine in rats and dogs in repeat dose toxicity studies. *Journal of Pharmacological and Toxicological Methods* 2021; **110**: 107068.

Jackson, SP. Sensing and repairing DNA double-strand breaks. *Carcinogenesis* 2002; **23**: 687-96.

Jackson, SP and Bartek, J. The DNA-damage response in human biology and disease. *Nature* 2009; **461**: 1071-8.

Jafarzadeh, N, Mani-Varnosfaderani, A, Gilany, K, Eynali, S, Ghaznavi, H and Shakeri-Zadeh, A. The molecular cues for the biological effects of ionizing radiation dose and post-irradiation time on human breast cancer SKBR3 cell line: A Raman spectroscopy study. *Journal of Photochemistry and Photobiology B: Biology* 2018; **180**: 1-8.

James, G, Witten, D, Hastie, T & Tibshirani, R. *An introduction to statistical learning with applications in R* (1st Ed.) 2017. New York: Springer.

Jani, AB and Gratzle, J. Late radiotherapy toxicity after prostate cancer treatment: Influence of hormonal therapy. *Adult Urology* 2005; **66**(3): 566-570.

Jani, AB, Gratzle, J and Myers, M. Impact of hormone therapy on acute radiotherapy toxicity in the treatment of prostate cancer. *Prostate Cancer and Prostatic Diseases* 2005; **8**(3): 224-8.

Jeggo, PA and Lavin, MF. Cellular radiosensitivity: How much better do we understand it? *International Journal of Radiation Biology* 2009; **85**: 1061-81.

Jeggo, PA and Lobrich, M. Artemis links ATM to double strand break rejoining. *Cell Cycle* 2005; **4**: 359-62.

Jianfeng, G, Weiming, Z, Ning, L, Fangnan, L, Li, T, Nan, L and Jieshou, L. Serum citrulline is a simple quantitative marker for small intestinal enterocytes mass and absorption function in short bowel patients. *The Journal of Surgical Research* 2005; **127**: 177–82.

Jiang, Z, Li, C, Fischer, A, Dresser, K and Woda, BA. Using an AMACR (P504S)/34betaE12/p63 cocktail for the detection of small focal prostate carcinoma in needle biopsy specimens. *American Journal of Clinical Pathology* 2005; **123**(2): 231-6.

Johansen, J *et al*. Radiosensitivity of normal fibroblasts from breast cancer patients assessed by the micronucleus and colony assays. *International Journal of Radiation Biology* 1998; **73**(6): 671-8.

Joiner, MC. Models of radiation cell killing. In Steel, GG. *Basic clinical radiobiology* (3rd Ed.) 2002. London: Arnold.

Joiner, MC. Quantifying cell kill and cell survival. In Joiner, M and van der Kogel, A (Eds.). *Basic clinical radiobiology* (5th Ed.) 2019. New York: Taylor and Francis Group, pp. 32-43.

Joiner, MC and Bentzen, SM. Fractionation: The linear-quadratic approach. In Joiner, M and van der Kogel, A (Eds.). *Basic clinical radiobiology* (5th Ed.) 2019. New York: Taylor and Francis Group, pp. 99-111.

Jokiel-Rokita, A and Topolnicki, R. Estimation of the ROC curve from the Lehmann family. *Computational Statistics & Data Analysis* 2020; **142**: 106820.

Jones, CU *et al.* Radiotherapy and short-term androgen deprivation therapy for localized prostate cancer. *New England Journal of Medicine* 2011; **365**: 107-18.

Jones, JW *et al*. Citrulline as a biomarker in the non-human primate total- and partial-body irradiation models: Correlation of circulating citrulline to acute and prolonged gastrointestinal injury. *Health Physics* 2015; **109**: 440–451.

Jones, L, Hoban, P and Metcalfe, P. The use of the linear quadratic model in radiotherapy: A review. *Australasian Physical & Engineering Sciences in Medicine* 2001; **24**(3): 132-46.

Kaminaka, S, Ito, T, Yamazaki, H, Kohoda, E and Hamaguchi, H. Near-infrared multichannel Raman spectroscopy toward real-time *in vivo* cancer diagnosis. *Journal of Raman Spectroscopy* 2001; **33**: 498-502.

Kastan, MB and Bartek, J. Cell-cycle checkpoints and cancer. *Nature* 2004; **432**: 316-23.

Kateinen, E *et al*. Qualification of the amphetamine content in seized street samples by Raman spectroscopy. *Journal of Forensic Science* 2007; **52**(1): 88-92.

Keller, MD, Kanter, EM and Mahadevan-Jansen, A. *Spectroscopy* 2006; **21**: 33-9.

Kerns, SL *et al*. Meta-analysis of genome wide association studies identifies genetic markers of late toxicity following radiotherapy for prostate cancer. *EBioMedicine* 2016; **10**: 150-63.

Kerns, SL *et al*. Radiogenomics consortium genome-wide association study meta-analysis of late toxicity after prostate cancer radiotherapy. *Journal of the National Cancer Institute* 2020; **112**(2): djz075.

Kim, JE *et al*. The use of MTT assay, *in vitro* and *ex vivo* to predict the adiosensitivity of colorectal cancer. *The Journal of the Korean Society for Therapeutic Radiology and Oncology* 2008; **26**(3): 166-72.

Kim, JH, Jenrow, KA and Brown, SL. Mechanisms of radiation-induced normal tissue toxicity and implications for future clinical trials. *Radiation Oncology Journal* 2014; **32**(3): 103-15.

Kim, JJ and Tannock, IF. Repopulation of cancer cells during therapy: An important cause of treatment failure. *Nature Reviews Cancer* 2005; **5**: 516-25.

Kir, G, Seneldir, H and Gumus E. Outcomes of Gleason score 3+4=7 prostate cancer with minimal amounts (<6%) vs ≥6% of Gleason pattern 4 tissue in needle biopsy specimens (*sic*). *Annals of Diagnostic Pathology* 2016; **20**: 48-51.

Klionsky, DJ. Autophagy: From phenomenology to molecular understanding in less than a decade. *Nature Reviews Molecular Cell Biology* 2007; **8**: 931-7.

Kolijenovic, S, Scut, TB, Vincent, A, Kros, JM and Puppels, GJ. Detection of meningioma in dura mater by Raman spectroscopy. *Analytical Chemistry* 2005; **77**(24): 7958-65.

Kong, K, Kendall, C, Stone, N and Notingher, I. Raman spectroscopy for medical diagnostics – From *in-vitro* biofluid assays to *in-vivo* cancer detection. *Advanced Drug Delivery Reviews* 2015; **89**: 121-34.

Kouzarides, T. Chromatin modifications and their function. *Cell* 2007; **128**(4): 693-705.

Krafft, C, Neudert, L, Simat, T and Salzer, R. Near infrared Raman spectra of human brain lipids. *Spectrochimica Acta* 2005; **61**: 1529-35.

Kromer, G *et al*. Classification of cell death: Recommendations of the Nomenclature Committee on Cell Death. *Cell Death and Differentiation* 2005; **12**: 1463-7.

Krueger, SA, Wilson, GD, Piasentin, E, Joiner, MC and Marples, B. *International Journal of Radiation Oncology, Biology, Physics* 2010; **77**(5): 1509-17.

Ku, JY, Lee, CH and Ha, HK. Long-term oncologic outcomes of postoperative adjuvant versus radiotherapy in prostate cancer: Systemic review and meta-analysis of 5-year and 10-year follow-up data. *Korean Journal of Urology* 2015; **56**: 735-41.

Kumar, A, Adhikary, A, Shamoun, L and Sevilla, MD. Do solvated electrons (e_{aq}^-) reduce DNA bases? A Gaussian 4 and density functional theory-molecular dynamics study. The *Journal of Physical Chemistry B* 2016; **120**(9): 2115-23.

Kuo, LJ and Yang, LX. γ-H2AX – A novel biomarker for DNA double-strand breaks. *In Vivo* 2008; **22**: 305-10.

Kuptsova, N *et al*. Genetic predictors of long-term toxicities after radiation therapy for breast cancer. *International Journal of Cancer* 2008; **122**: 1333-9.

Lakshimi, RJ, Kartha, VB, Krishna, CM, Solomon, JGR, Ullas, G and Uma Devi, P. Tissue Raman spectroscopy for the study of radiation damage: Brain irradiation of mice. *Radiation Research* 2002; **157**: 175-82.

Larkin, PJ. *IR and Raman Spectroscopy* 2011. London: Elsevier.

Lau, DP *et al*. Raman spectroscopy for optical diagnosis in the larynx: Preliminary findings. *Lasers in Surgery and Medicine* 2005; **37**: 192-200.

Lau, DP *et al*. Raman spectroscopy for optical diagnosis in normal and cancerous tissue of the nasopharynx – Preliminary findings. Lasers in Surgery and Medicine 2003; 32: 210-4.

Lavazzo, C, Athanasiou, S, Pitsouni, E and Falagas, ME. Hyaluronic acid: An effective alternative treatment of interstitial cystitis, recurrent urinary tract infections, and hemorrhagic cystitis? *European Urology* 2007; **51**: 1534-41.

Lawton, CA *et al.* Updated results of the phase III Radiation Therapy Oncology Group (RTOG) trial 85-31 evaluating the potential benefit of androgen suppression following standard radiation therapy for unfavourable prognosis carcinoma of the prostate. *International Journal of Radiation Oncology Biology Physics* 2001; **49**(4): 937-46.

Leibowitz, BJ *et al*. Interferon β drives intestinal regeneration after radiation. *Science Advances* 2021; **7**: eabl5253.

Liberman, D, Mehus, B and Elliott, SP. Urinary adverse effects of pelvic radiotherapy. *Translational Andrology and Urology* 2014; **3**(2): 186-95.

Lieber, MR. The mechanism of double-stranded DNA break repair by the nonhomologous DNA end-joining pathway. *Annual Review of Biochemistry* 2010; **79**: 181-211.

Lieber, MR. The mechanism of human nonhomologous DNA end joining. *The Journal of Biological Chemistry* 2008; **283**: 1-5.

Lillicrap, SC, Owen, B, Williams, JR and Williams, PC. Code of practice for high-energy photon therapy dosimetry based on the NPL absorbed dose calibration service. *Physics in Medicine and Biology* 2002; **35**: 1355-60.

Limoli, CL, Kaplan, MI, Corcoran, J, Meyers, M, Boothman, DA and Morgan, WF. Chromosomal instability and its relationship to other end points of genomic instability. *Cancer Research* 1997; **57**: 5557-63.

Lin, J *et al*. Surface-enhanced Raman scattering spectroscopy for potential noninvasive nasopharyngeal cancer detection. *Journal of Raman Spectroscopy* 2012; **43**(4): 497-502.

Little, JB. Genomic instability and radiation. *Journal of Radiological Protection* 2003; **23**: 173-81.

Little, MP, Heidenreich, WF, Moolgavkar, SH Schollnberger, H and Thomas, DC. Systems biological and mechanistic modelling of radiation-induced cancer. *Radiation and Environmental Biophysics* 2008; **47**(1): 39-47.

Liu, J, Osadchy, M, Ashton, L, Foster, M, Solomon, CJ and Gibson, SJ. Deep convolutional neural networks for Raman spectrum recognition: A unified solution. *Analyst* 2017; **142**: 4067-74.

Liu, W, Sun, Z, Chen, Jing, C. Raman spectroscopy in colorectal cancer diagnostics: Comparison of PCA-LDA and PLS-DA models. *Journal of Spectroscopy* 2016; **2016**: 1603609.

Lomax, ME, Folkes, LK and O'Neill, P. Biological consequences of radiation-induced DNA damage: Relevance to radiotherapy. *Clinical Oncology* 2013; **25**: 578-85.

Long, DA. *The Raman effect: A unified treatment of the theory of Raman scattering by molecules* 2002. West Sussex: John Wiley and Sons Ltd.

Lopes, RM, Silveira, L, Silva, MA, Leite, KRM, Pasqualucci, CAG and Pacheco, MTT. Diagnostic model based on Raman spectra of normal, hyperplasia and prostate adenocarcinoma tissues *in vitro*. *Spectroscopy* 2011; **25**: 89-102.

Ludemann, L, Grieger, W, Wurm, R, Wust, P and Zimmer, C. Glioma assessment using quantitative blood volume maps generated by T1-weighted dynamic contrast-enhanced magnetic resonance imaging: A receiver operating characteristic study. *Acta Radiologica* 2006; **47**: 303-310.

Lutgens, LCHW, Blijlevens, NMA, Deutz, NEP, Donnelly, JP, Lambin, P amd de Pauw, BE. Monitoring myeloablative therapy-induced small bowel toxicity by serum citrulline concentration: a comparison with sugar permeability tests. *Cancer* 2005; **103**(1): 191-9.

Luzhna, L, Kathiria, P and Kovalchuk, O. Micronuclei in genotoxicity assessment: From genetics to epigenetics and beyond. *Frontiers in Genetics* 2013; **4**: PMC3708156.

Maguire, A, Vega-Carrascal, I, White, L, McClean, B, Howe, O, Lyng, FM and Meade, AD. Analyses of ionizing radiation effects *in vitro* in peripheral in peripheral blood lymphocytes with Raman spectroscopy. *Radiation Research* 2015a; **183**: 407-16.

Maguire, A, Vega-Carrascal, I, Bryant, J, White, L, Howe, O, Lyng, FM and Meade, AD. Competitive evaluation of data mining algorithms for use in classification of leukocyte subtypes with Raman microspectroscopy. *Analyst* 2015b; **140**(7): 2473-81.

Mahadevan-Jansen, A and Richards-Kortum, R. Raman spectroscopy for the detection of cancers and precancers. *Journal of Biomedical Optics* 1997; **1**(1): 31-70.

Malini, R, Venkatakrishma, K and Kurien, J *et al.* Discrimination of normal, inflammatory, premalignant and malignant oral tissue: A Raman spectroscopy study. *Biopolymers* 2006; **81**: 179-93.

Maréchal, A and Zou, L. DNA damage sensing by the ATM and ATR kinases. *Cold Spring Harbor Perspectives in Biology* 2013; **5**(9): a012716.

Marcu, LG, Dasu, IT and Dasu, Alexandru. The six Rs of head and neck cancer radiotherapy. In Marcu, LG (Ed.). *Contemporary issues in head and neck cancer management* 2015. London: InTech.

Mark, H and Workman, J. *Chemometrics in spectroscopy* (*2nd Ed.*) 2010. London: Elsevier.

Marples, B and Collis, SJ. Low-dose hyper-radiosensitivity: Past, present and future. *International Journal of Radiation Oncology Biology Physics* 2008; **70**: 1310-8.

Marples, B, Wouters, BG, Collis, SJ, Chalmers, AJ and Joiner, MC. Low dose hyper-sensitivity: A consequence of ineffective cell cycle arrest of radiation-damaged G2-phase cells. *Radiation Research* 2004; **161**: 247-55.

Martin, LM *et al*. DNA mismatch repair and the DNA damage response to ionizing radiation: Making sense of apparently conflicting data. *Cancer Treatment Reviews* 2010; **36**: 518-27.

Matsumoto, Y *et al*. Two unrelated patients with MRE11A mutations and Nijmegen breakage syndrome-like severe microcephaly. *DNA Repair* 2011; **10**: 314-21.

Matsuoka, S *et al*. ATM and ATR substrate analysis reveals extensive protein networks responsive to DNA damage. *Science* 2007; **316**: 1160-6.

Matthews, Q, Brolo, AG, Lum, J, Duan, X and Jirasek, A. Raman spectroscopy of single human tumour cells exposed to ionizing radiation *in vitro*. *Physics in Medicine and Biology* 2011; **56**: 19-38.

Maxwell, CA *et al*. Targeted and nontargeted effects of ionizing radiation that impact genomic instability. *Cancer Research* 2008; **68**(20): 8304-11.

McCarthy, MI, Hirschhorn, JN. Genome-wide association studies: Potential next steps on a genetic journey. *Human Molecular Genetics* 2008; **17**: R156–65.

McMillan, TJ and Begg, AC. Genetic control of the cellular response to ionizing radiation. In Steel, GG. *Basic clinical radiobiology* (3rd Ed.) 2002. London: Arnold, pp. 84-93.

McMillan, TJ and Steel, GG. In Steel, GG. *Basic clinical radiobiology* (3rd Ed.) 2002. London: Arnold, pp. 71-83.

Meade, AD *et al*. Prediction of DNA damage and G2 chromosomal radio-sensitivity ex vivo in peripheral blood mononuclear cells with label-free Raman micro-spectroscopy. *International Journal of Radiation Biology* 2019; **95**(1): 44-53.

Meade, AD, Howe, O, Unterreiner, V, Sockalingum, GD, Byrne, HJ and Lyng, FM. Vibrational spectroscopy in sensing radiobiological effects: Analyses of targeted and non-targeted effects in human keratinocytes. *Faraday Discussions* 2016; **187**: 213-34.

Meek, K, Gupta, S, Ramsden, DA and Lees-Miller, SP. The DNA-dependent protein kinase: The director at the end. *Immunological Reviews* 2004; **200**: 132-41.

Merritt, AJ *et al*. The role of p53 in spontaneous and radiation-induced apoptosis in the gastrointestinal tract of normal and p53-deficient mice. *Cancer Research* 1994; **54**(3): 614-7.

Migliore, L, Di Bucchianico, S and Uboldi, C. *Genotoxicity and DNA Repair* 2014. New York: Humana Press.

Milligan, K *et al*. Raman spectroscopy and group and basis-restricted non negative matrix factorisation identifies radiation induced metabolic changes in human cancer cells. *Scientific Reports* 2021; **11**: 3853.

Mirzayans, R, Andrais, B and Murray, D. Impact of premature senescence on radiosensitivity measured by high throughput cell-based assays. *International Journal of Molecular Sciences* 2017; **18**(7): E1460.

Mizushima, N. Autophagy in protein and organelle turnover. *Cold Spring Harbor Symposia Quantitative Biology* 2011; **76**: 397-402.

Mordechai, S *et al*. Possible common biomarkers from FTIR microspectroscopy of cervical cancer and melanoma. *Journal of Microscopy* 2004; **215**(1): 86-91.

Moreno-Herrero, F, de Jager, M, Dekker, NH, Kanaar, R, Wyman, C and Dekker, C. Mesoscale conformational changes in the DNA-repair complex Rad50/Mre11/Nbs1 upon binding DNA. *Nature* 2005; **437**: 440-3.

Morse, KF and Wolfe, CM. *Radiobiology* 2013. New York: Springer Science and Business Media.

Mottet, N *et al*. Guidelines on prostate cancer. *European Urology* 2014; **65**(1): 124-37.

Mundt, AJ, Roeske, JC, Chung, TD and Weichselbaum, RR. *Physical basis of radiation therapy* 2003. Hamilton: BC Decker Inc.

Nabha, SM *et al*. Combretastatin-A4 prodrug induces mitotic catastrophe in chronic lymphocytic leukemia cell line independent of caspase activation and poly(ADP-ribose) polymerase cleavage. *Clinical Cancer Research* 2002; **8**(8): 2735-41.

Nahum, AE and Uzan, J. (Radio)Biological optimization of external-beam radiotherapy. *Computational and Mathematical Methods in Medicine* 2012; **2**: 329214.

Natarajan, C and Takeda, K. Regulation of various DNA repair pathways by E3 ubiquitin ligases. *Journal of Cancer Research and Therapeutics* 2017; **13**: 157-69.

National Cancer Registry Ireland. Cancer factsheet: Prostate. Retrieved 13 November 2021, from: *https://ncri.ie/factsheets*.

Naumann, D. Infrared and NIR Raman spectroscopy in medical microbiology. Proceedings of the SPIE 1998; 3257: 245-57.

Newhauser, WD and Durante, M. Assessing the risk of second malignancies after modern radiotherapy. *Nature Reviews Cancer* 2011; **11**(6): 438-48.

Nias, AHW. *An introduction to radiobiology* (2nd Ed.) 2000. West Sussex: John Wiley & Sons Ltd.

Nickoloff, JA, Boss, MK, Allen, CP and LaRue, SM. Translational research in radiation-induced DNA damage signalling and repair. *Translational Cancer Research* 2017; **6**(5): S875-91.

Nickoloff, JA. Paths from DNA damage and signalling to genome rearrangements via homologous recombination. *Mutation Research* 2017; **806**: 64-74.

Nickoloff, JA. Recombination: Mechanisms and roles in tumorgenesis. In Bertrino, JR (Ed.). *Encyclopaedia of Cancer* (2nd Ed.) 2002. San Diego: Elsevier Science, pp. 49-59.

Notingher, I, Green, C and Dyer, C. Discrimination between ricin and sulphur mustard toxicity *in vitro* using Raman spectroscopy. *Journal of the Royal Society Interface* 2004; **1**: 79-90.

O' Driscoll, M, Gennery, AR, Seidel, J, Concannon, P and Jeggo, PA. An overview of three new disorders associated with genetic instability: LIG4 syndrome, RS-SCID and ATR-Seckel syndrome. *DNA Repair* 2004; **3**: 1227-35.

Oh, JH, Kerns, S, Ostrer, H, Powell, SN, Rosenstein, B and Deasy, JO. Computational methods using genome-wide association studies to predict radiotherapy complications and to identify correlative molecular processes. *Scientific Reports* 2017; **7**: 43381.

Ohri, N, Dicker, AP and Showalter, TN. Late toxicity rates following definitive radiotherapy for prostate cancer. *The Canadian Journal of Urology* 2012; **19**(4): 6373-80.

Okada, H and Mak, TW. Pathways of apoptotic and non-apoptotic death in tumour cells. *Nature Reviews Cancer* 2004; **4**: 592-603.

Oksman-Caldentey, KM and Inze, D. Plant cell factories in the post-genomic era: new ways to produce designer secondary metabolites. *Trends in Plant Science* 2004; **9**: 433-40.

Onal, C *et al*. Plasma citrulline levels predict intestinal toxicity in patients treated with pelvic radiotherapy. *Acta Oncological* 2011; **50**(8): 1167-74.

Orrenius, S, Nicotera, P and Zhivotovsky, B. Cell death mechanisms and their implications in toxicology. *Toxicological Sciences* 2011; **119**(1): 3-19.

Ozsahin, M *et al*. CD4 and CD8 T-Lymphocyte Apoptosis Can Predict Radiation-Induced Late Toxicity: A Prospective Study in 399 Patients. *Clinical Cancer Research* 2005; **11**(20): 7426-33.

Pajonk, F, Vlashi, E and McBride, WH. Radiation resistance of cancer stem cells: The 4 R's of radiobiology revisited. *Stem Cells* 2010; **28**(4): 639-48.

Pawlik, TM and Keyomarsi, K. Role of cell cycle in mediating sensitivity to radiotherapy. *International Journal of Radiation Oncology Biology Physics* 2004; **59**(4): 928-42.

Payne, H *et al*. Chemical- and radiation-induced haemorrhagic cystitis: Current treatments and challenges. *BJU International* 2013; **112**(7): 885-97.

Pechenizkiy, M, Tsymbal, A and Puuronen, S. On combining principal components with Fisher's linear discriminants for supervised learning. *Foundations of Computing and Decision Sciences* 2006; **31**: 59-73.

Pelletier, MJ. Raman instrumentation. In Pelletier, MJ (Ed.). *Analytical applications of Raman spectroscopy* 1999. Blackwell Science: Cornwall.

Podhorecka, M, Skladanowski, A and Bozko, P. H2AX phosphorylation: Its role in DNA damage response and cancer therapy. *Journal of Nucleic Acids* 2010; **2010**: ID 920161.

Poggioli, T, Sterpone, S, Palma, S, Cozzi, R and Testa, A. G_0 and G_2 chromosomal assays in the evaluation of radiosensitivity in a cohort of Italian breast cancer patients. *Journal of Radiation Research* 2010; **51**: 615-9.

Polo, SE and Jackson, SP. Dynamics of DNA damage response proteins at DNA breaks: A focus on protein modifications. *Genes and Development* 2011; **25**: 409-33.

Postow, MA *et al.* Immunologic correlates of the abscopal effect in a patient with melanoma. *New England Journal of Medicine* 2012; **366**: 925-31.

Pray, LA. Discovery of DNA structure and function: Watson and Crick. Nature Education 2008; **1**(1): 100.

Price, P and McMillan, TJ. Use of the tetrazolium assay in measuring the response of human tumor cells to ionizing radiation. *Cancer Research* 1990; **50**(5): 1392-6.

Proskuryakov, SY and Gabai, VL. Mechanisms of tumor cell necrosis. *Current Pharmaceutical Design* 2010; **16**(1): 56-68.

Qiu, S *et al*. Raman profile alterations of irradiated human nasopharyngeal cancer cells detected with laser tweezer Raman spectroscopy. *RSC Advances* 2020; **10**: 14368-73.

Quarmby, S *et al*. Association of transforming growth factor beta-1 single nucleotide polymorphisms with radiation-induced damage to normal tissues in breast cancer patients. *International Journal of Radiation Biology* 2003; **79**(2): 137-43.

Qu, M, Ren, SC and Sun, Y. Current early diagnostic biomarkers of prostate cancer. *Asian Journal of Andrology* 2014; **16**: 549-54.

Ramsay, J and Birrell, G. Normal tissue radiosensitivity in breast cancer patients. *International Journal of Radiation Oncology•Biology•Physics* 1995; **31**(2): 339-44.

Ray, KJ, Sibson, NR and Kiltie, AE. Treatment of breast and prostate cancer by hypofractionated radiotherapy: Potential risks and benefits. *Clinical Oncology* 2015; **27**(7): 420-6.

Read, DS and Whiteley, AS. Chemical fixation methods for Raman spectroscopy-based analysis of bacteria. *Journal of Microbiological Methods* 2015; **109**: 79-83.

Rencher, AC and Christensen, WF. *Methods of Multivariate Analysis* (3rd Ed.) 2012. New Jersey: John Wiley and Sons Ltd.

Rencher, AC. *Methods of Multivariate Analysis* 2002 (2nd Ed.). USA: Wiley-Interscience.

Rieder F, Brenmoehl J, Leeb S, Schölmerich and Rogler, G. Wound healing and fibrosis in intestinal disease. *Gut* 2007; **56**: 130-9.

Riedl, SJ and Shi, YG. Molecular mechanisms of caspase regulation during apoptosis. *Nature Reviews Molecular Cell Biology* 2004; **5**: 897-907.

Ringborg, U, Berggvist, D and Brorsson, B *et al.* The Swedish Council on Technology Assessment in Health Care (SBU) systematic overview of radiotherapy for cancer including a prospective survey of radiotherapy practice in Sweden 2001 – Summary and conclusions. *Acta Oncologica* 2003; **42**(5-6): 357-65.

Riss, TL *et al*. Cell viability assays. Retrieved 13 December 2017, from: https://www.ncbi.nlm.nih.gov/books/NBK144065/.

Rogakou, EP, Pilch, DR, Orr, AH, Ivanova, BS and Bonner, WM. DNA double-stranded breaks induce histone H2AX phosphorylation on serine 139. *Journal of Biological Chemistry* 1998; **273**: 5858-68.

Ronen, SM, Stier, A and Degani, H. NMR studies of the lipid metabolism of T47D human breast cancer spheroids. *FEBS Letter*s 1990; **266**: 147-9.

Roninson, I. Tumor cell senescence in cancer treatment. *Cancer Research* 2003; **63**: 2705-15.

Ruiz-Chica, AJ, Medina, MA, Sanchez-Jimenez, F and Ramirez, FJ. Characterisation by Raman spectroscopy of conformational changes on guanine-cytosine and adenine-thymine oligonucleotides induced by aminooxy analogues of spermidine. *Journal of Raman Spectroscopy* 2004; **35**: 93-100.

Sadikovic, B, Al-Romaih, K, Squire, JA and Zielenska, M. Cause and consequences of genetic and epigenetic alterations in human cancer. *Current Genomics* 2008; **9**: 394-408.

Saelens, X, Festjens, N, Walle, LV, van Gurp, M, van Loo, G and Vandenabeele, P. *Oncogene* 2004; **23**: 2861-74.

Sage, E and Shikazono, N. Radiation-induced clustered DNA lesions: Repair and mutagenesis. *Free Radical Biology and Medicine* 2017; **107**: 125-35.

Saha, GB. *Radiation biology in physics and radiobiology of nuclear medicine* 2013. New York: Springer Science and Business Media.

Saha, GB. *Physics and radiobiology of nuclear medicine* 2001. New York: Springer Science and Business Media.

Sartori, AA *et al*. Human CtIP promotes DNA end resection. *Nature* 2007; **450**: 509-14.

Sathya, JR *et al.* Randomized trial comparing iridium implant plus external-beam radiation therapy with external-beam radiation therapy alone in node-negative locally advanced cancer of the prostate. *Journal of Clinical Oncology* 2005; **23**: 1192-99.

Schafer, RW. What is a Savitzky-Golay filter? *IEEE Signal Processing Magazine* 2011; **111**: 111-7.

Scaife, JE, Barnett, GC, Noble, DJ, Jena, R, Thomas, SJ, West, CML and Burnet, NG. Exploiting biological and physical determinants of radiotherapy toxicity to individualize treatment. *The British Journal of Radiology* 2015; **88**(1051): 20150172.

Schafer, RW. What is a Savitzky-Golay Filter? *IEEE Signal Processing Magazine* 2011; **111**: 10.1109.

Schie, IW and Huser, T. Methods and applications of Raman microspectroscopy to single-cell analysis. *Applied Spectroscopy* 2013; **67**: 813-28.

Schmidt-Hansen, M, Hoskin, P, Kirkbride, P, Hasler, E and Bromham, N. Hormone and radiotherapy versus hormone or radiotherapy alone for non-metastatic prostate cancer: A systematic review with meta-analyses. *Clinical Oncology* 2014; **26**(10): e21-e46.

Schmitt, CA. Cellular senescence and cancer treatment. *Biochimica et Biophysica Acta* 2007; **1775**: 5-20.

Schnarr, K, Boreham, D, Sathya, J, Julian, J and Dayes, IS. Radiation-Induced Lymphocyte Apoptosis to Predict Radiation Therapy Late Toxicity in Prostate Cancer Patients. *International Journal of Radiation Biology* 2009; **74**(5): 1424-30.

Schulz, H and Baranska, M. Identification and qualification of valuable plant substances by IR and Raman spectroscopy. *Vibrational Spectroscopy* 2007; **43**: 13-25.

Scott, D, Barber, JBP, Spreadborough, AR, Burrill and Roberts, SA. Increased chromosomal radiosensitivity in breast cancer patients: A comparison of two assays. *International Journal of Radiation Biology* 1999; **75**: 1-10.

Seballos, L, Zhang, JZ and Sutphen, R. Surface-enhanced Raman scattering detection of lysophosphatidic acid. *Analytical and Bioanalytical Chemistry* 2005; **383**: 763-7.

Sedgewick, D, Howard, G and Ferguson, A. Pathogenesis of acute radiation injury in the rectum. *International Journal of Colorectal Disease* 1994; **9**: 23-30.

Shadad, AK, Sullivan, FJ, Martin, JD and Egan, LJ. Gastrointestinal radiation injury: Symptoms, risk factors and mechanisms. *World Journal of Gastroenterology* 2013; **19**(2): 185-98.

Shaltiel, IA, Krenning, L, Bruinsma, W and Medema, RH. The same, only different – DNA damage checkpoints and their reversal throughout the cell cycle. *Journal of Cell Science* 2015; **128**: 607-20.

Shaver, J. Chemometrics for Raman spectroscopy. In Lewis, IR and Edwards, H (Eds.). *Handbook of Raman Spectroscopy: From the Research Laboratory to the Process Line* 2001. New York: Marcel Dekker Inc., pp. 275-306.

Shaw, RA and Mantsch, HH. Vibrational biospectroscopy: From plants to animals to humans: A historical perspective. *Journal of Molecular Structure* 1999; **480-1**: 1-13.

Shen, Z and Nickoloff, JA. Mammalian homologous recombination repair and cancer intervention. In Wei, Q, Li, L and Chen, DJ (Eds.). *DNA Repair, Genetic Instability, and Cancer* 2007. Singapore: World Scientific Publishing Co., pp. 119-56.

Shetty, G, Kedall, C, Shepherd, N, Stone and Barr, H. Raman spectroscopy: Evaluation of biochemical changes in carcinogenesis of oesophagus. *British Journal of Cancer* 2006; **94**: 1460-4.

Shim, S *et al*. Development of a new minipig model to study radiation-induced gastrointestinal syndrome and its application in clinical research. *Rare* 2014; **181**: 387-95.

Shin, S *et al*. Simultaneous analysis of acetylcarnitine, proline, hydroxyproline, citrulline, and arginine as potential plasma biomarkers to evaluate NSAIDs-induced gastric injury by liquid chromatography-tandem mass spectrometry. *Journal of Pharmaceutical and Biomedical Analysis* 2019; **165**: 101-11.

Short, S, Mayes, C, Woodcock, M, Johns, H and Joiner, MC. Low dose hypersensitivity in the T98G human glioblastoma cell line. *International Journal of Radiation Biology* 1999; **75**: 847-55.

Sigurdsson, S, Philipsen, PA, Hansen, LK, Laesen, L, Gniadecka, M and Wulf, HC. Detection of skin cancer by classification of Raman spectra. *IEEE Transcriptions on Biomedical Engineering* 2004; **51**: 10.

Sil, S, Gautam, R and Umapathy, S. Applications of Raman and infrared microscopy to materials and biology. In Gupta, VP (Ed.). *Molecular and Laser Spectroscopy: Advances and Applications* 2017. London: Elsevier.

Silveira, L, Leite, KR, Silveira, FL, Srougi, M, Pacheco, MT, Zangaro, RA and Pasqualucci, CA. Discrimination of prostate carcinoma from benign prostate tissue fragments in vitro by estimating the gross biochemical alterations through Raman spectroscopy. *Lasers in Medical Science* 2014; **29**(4): 1469-77.

Silveira, L, Sathaiah, S and Zangaro, RA *et al*. Correlation between near-infrared Raman spectroscopy and the histopathological analysis of atherosclerosis in human coronary arteries. *Lasers in Surgery and Medicine* 2002; **30**: 290-7.

Siva *et al*. A pattern of early radiation-induced inflammatory cytokine expression is associated with lung toxicity in patients with non-small cell lung cancer. *PLoS One* 2014; **9**(10): e109560.

Slavotinek, A, McMillan, TJ and Steel, CM. Measurement of radiation survival using the MTT assay. *European Journal of Cancer* 1994; **30**(9): 1376-82.

Słonina, D, Biesaga, B, Urbański, K and Kojs, Z. Low-dose radiation response of primary keratinocytes and fibroblasts from patients with cervix cancer. *Radiation Research* 2007; **167**(3): 251-9.

Smit, SG and Heyns, CF. Management of radiation cystitis. *Nature Reviews Urology* 2010; **7**: 206-14.

Sowa, MG *et al*. Semi-parametric estimation in the compositional modelling of multicomponent systems from Raman spectroscopic data. *Applied Spectroscopy* 2006; **60**(8): 877-83.

Spratt, DE *et al*. Long-term survival and toxicity in patients treated with high-dose intensity modulated radiation therapy for localized prostate cancer. *International Journal of Radiation Oncology Biology Physics* 2012; **85**: 686-92.

Sprung, CN, Chao, M, Leong, T and McKay, MJ. Chromosomal radiosensitivity in two cell lineages derived from clinically radiosensitive cancer patients. *Clinical Cancer Research* 2005; **11**(17): 6352-8.

Srivastava, S, Gochhait, P, de Boer, P and Bamezai, RNK. Role of H2AX in DNA damage response and human cancers. *Mutation Research* 2009; **681**: 180-8.

Stanojković *et al*. Evaluation of cytokine expression and circulating immune cell subsets as potential parameters of acute radiation toxicity in prostate cancer patients. *Scientific Reports* 2020; **10**: 10.1038/s41598-020-75812-0.

Stausbøl-Gren, B and Overgaard, J. Relationship between tumour cell *in vitro* radiosensitivity and clinical outcome after curative radiotherapy for squamous cell carcinoma of the head and neck. *Radiotherapy and Oncology* 1999; **50**: 47-55.

Steel, GG. Radiobiology of tumours. In Mayles, P, Nahum, A and Rosenwald, JC (Eds.). *Handbook of Radiotherapy Physics: Theory and Practice* 2007. London: Taylor and Francis Group, pp. 127-48.

Steel, GG, McMillan, TJ and Peacock, JH. The 5Rs of radiobiology. *International Journal of Radiation Biology* 1989; **56**(6): 1045-8.

Stenmark *et al*. Combining physical and biologic parameters to predict radiation-induced lung toxicity in patients with non-small-cell lung cancer treated with definitive radiation therapy. *International Journal of Radiation Oncology•Biology•Physics* 2012; **84**(2): E217-22.

Stone, HB, Coleman, CN, Anscher, MS and McBride, WH. Effects of radiation on normal tissue: Consequences and mechanisms. *Lancet Oncology* 2003; **4**: 529-36.

Stone, N, Kendall, C, Shepherd, N, Crow, P and Barr, H. Near-infrared Raman spectroscopy for the classification of epithelial pre-cancers and cancers. *Journal of Raman Spectroscopy* 2002; **33**: 564-73.

Stone, N, Kendall, C, Smith, J, Crow, P and Barr, H. Raman spectroscopy for identification of epithelial cancers. *Faraday Discussions* 2004; **126**: 141.

Stone, N, Prieto, MCH, Crow, P, Uff, J and Ritchie, AW. The use of Raman spectroscopy to provide an estimation of the gross biochemistry associated with urological pathologies. *Analytical and Bioanalytical Chemistry* 2007; **387**: 1657-68.

Stracker, TH and Petrini, JH. The MRE11 complex: Starting from the ends. *Nature Reviews Molecular Cell Biology* 2011; **12**: 90-103.

Streffer, C, van Beuningen, D, Gross, E, Schabronath, J, Eigler, FW and Rebmann, A. Predictive assays for the therapy of rectum carcinoma. *Radiotherapy Oncology* 1986; **5**: 303-10.

Sugiyama, T, Zaitseva, EM and Kowalczykowski, SC. A single-stranded DNA-binding protein is needed for efficient presynaptic complex formation by the Saccharomyces cerevisiae Rad51 protein. *The Journal of Biological Chemistry* 1997; **272**: 7940-5.

Sung, H, Ferlay, J, Siegel, RL, Laversanne, M, Soerjomataram, I, Jemal, A and Bray, F. Global cancer statistics 2020: GLOBOCAN estimates of incidence and mortality worldwide for 36 cancers in 185 countries. *CA: A Cancer Journal for Clinicians* 2021; **7**(3): 209-49.

Szymanska, E, Saccenti, E, Smilde, AK and Westerhuis, JA. Double-check: validation of diagnostic statistics for PLS-DA models in metabolomics studies. *Metabolomics* 2012; **8**: S3-16.

Tabesh, A *et al*. Multifeature prostate cancer diagnosis and Gleason grading of histological images. *IEEE Transactions on Medical Imaging* 2007; **26**(10): 1366-78.

Taghian, A *et al*. Intrinsic radiation sensitivity may not be the major determinant of the poor clinical outcome of glioblastoma multiforme. *International Journal of Radiation Oncology Biology Physics* 1993; **46**: 13-9.

Tait, SWG, Ichim, G and Green, DR. Die another way – non-apoptotic mechanisms of cell death. *Journal of Cell Science* 2014; **127**: 2135-44.

Takahashi, A *et al*. Mitogenic signalling and the $p16^{Ink4a}$-Rb pathway cooperate to enforce irreversible cellular senescence. *Nature Cell Biology* 2006; **8**: 1291-7.

Talbot, CJ *et al*. Multi-centre technical evaluation of the radiation-induced lymphocyte apoptosis assay as a predictive test for radiotherapy toxicity. *Clinical and Translational Radiation Oncology* 2019; **18**: 1-8.

Taverna, SD, Li, H, Ruthenburg, AJ, Allis, CD and Patel, DJ. How chromatin-binding modules interpret histone modifications: Lessons from professional pocket pickers. *Nature Structural and Molecular Biology* 2007; **14**(11): 1025-40.

Taylor, AM *et al*. Ataxia telangiectasia: A human mutation with abnormal radiation sensitivity. *Nature* 1975; **258**: 427-9.

Taylor, RC, Cullen, SP and Martin, SJ. Apoptosis: Controlled demolition at the cellular level. *Nature Reviews Molecular Cell Biology* 2008; **9**(3): 231-41.

Thierens, H, Vral, A, Barbé, M, Meijlaers, M, Baeyens, A and De Ridder, L. Chromosomal radiosensitivity study of temporary nuclear workers and the support of the adaptive response induced by occupational exposure. *International Journal of Radiation Biology* 2002; **78**(2): 1117-26.

Tibbs, MK. Wound healing following radiation therapy: A review. *Radiotherapy and Oncology* 1997; **42**: 99-106.

Toress-Roca, JF and Stevens, CW. Predicting response to clinical radiotherapy: Past, present and future directions. *Cancer Control* 2008; **15**(2): 151-6.

Travers, A and Muskhelishvili, G. DNA structure and function. *The FEBS Journal* 2015; **282**: 2279-95.

Tu, WZ *et al*. γH2AX foci formation in the absence of DNA damage: Mitotic H2AX phosphorylation is mediated by the DNA-PKcs/CHK2 pathway. *FEBS Letters* 2013; **587**(21): 3437-43.

Utzinger, URS *et al*. Near-infrared Raman spectroscopy for in vivo detection of cervical precancers. *Applied Spectroscopy* 2001; **55**(8): 955-9.

Valicenti, RK *et al.* RTOG 94-06: Is the addition of neoadjuvant hormonal therapy to dose-escalated 3D conformal radiation therapy for prostate cancer associated with treatment toxicity? *International Journal of Radiation Oncology•Biology•Physics* 2003; **57**(3): 614-20.

Van den Berg, RA, Hoefsloot, HCJ, Westerhuis, JA, Smilde, AK and van der Werf, MJ. Centering, scaling, and transformations: Improving the biological information content of metabolomics data. *BMC Genomics* 2006; **7**: 142.

Van de Poll, MCG, Ligthart-Melis, GC, Boelens, PG, Deutz, NEP, van Leeuwen, PAM and Dejong, CHC. Intestinal and hepatic metabolism of glutamine and citrulline in humans. *The Journal of Physiology* 2007; **581**: 819–827.

Van der Flier, LG and Clevers, H. Stem cells, self-renewal, and differentiation in the intestinal epithelium. *Annual Review of Physiology* 2009; **71**: 241-60.

Vandevoorde, C *et al*. In vitro cellular radiosensitivity in relationship to late normal tissue reactions in breast cancer patients: A multi-endpoint case-control study. *International Journal of Radiation Biology* 2016; **92**(12): 823-36.

Varmuza, K and Filzmoser, P. *Introduction to multivariate statistical analysis in chemometrics* 2009. Florida: CRC Press.

Vasireddy, RS, Sprung, CN, Cempaka, NL, Chao, M and McKay, MJ. H2AX phosphorylation screen of cells from radiosensitive cancer patients reveals a novel DNA double-strand break repair cellular phenotype. *British Journal of Cancer* 2010; **102**: 1511-18.

Velcheti, V and Punekar, SR. *Handbook of cancer treatment-related symptoms and toxicities* 2021. New York: Elsevier.

Veldwijk, MR *et al*. Association of CD4+ radiation-induced lymphocyte apoptosis with fibrosis and telangiectasia after radiotherapy in 272 breast cancer patients with >10-year follow-up. *Precision Medicine and Imaging* 2019; **25**(2): 562-72.

Vens, C, Koritzinsky, M and Wouters, BG. Irradiation-induced damage and the DNA damage response. In Joiner, M and van der Kogel, A (Eds.). *Basic clinical radiobiology* (5th Ed.) 2019. New York: Taylor and Francis Group, pp. 21-31.

Viehoever, AR, Anderson, D, Jansen, D and Mahadevan-Jansen, A. Organotypic raft cultures as an effective in vitro tool for understanding Raman spectral analysis of tissues. *Photochemistry and Photobiology* 2003; **78**(5): 517-24.

Vignard, J, Mirey, G and Salles, B. Ionizing-radiation induced DNA double-strand breaks: A direct and indirect lighting up. *Radiotherapy and Oncology* 2013; **108**: 362-9.

Villarroel, M, Barreiro, P, Kettlewell, P, Farish, M and Mitchell, M. Time derivatives in air temperature and enthalpy as non-invasive welfare indicators during long distance animal transport. *Biosystems Engineering* 2011; **110**(3): 253-60.

Von Sontag, C. *Free-radical-induced DNA damage and its repair: A chemical perspective* 2006. Berlin: Springer.

Vral, A, Thierens, H, Baeyens, A and De Ridder, L. Chromosomal aberrations and *in vitro* radiosensitivity: Intra-individual versus inter-individual variability. *Toxicology Letters* 2004; **149**: 345-52.

Vral, A, Thierens, Baeyens, A and De Ridder, L. The Micronucleus and G2-Phase Assays for Human Blood Lymphocytes as Biomarkers of Individual Sensitivity to Ionizing Radiation: Limitations Imposed by Intraindividual Variability. *Radiation Research* 2002; **157**(4): 472-7.

Wardman, P. The importance of radiation chemistry to radiation and free radical biology (The 2008 Silvanus Thompson Memorial Lecture). *The British Journal of Radiology* 2009; **82**: 89-104.

Wartewig, S. *IR and Raman Spectroscopy* 2003. Halle-Wittenberg: Wiley-VCH.

Wasserman, TH and Twentyman, P. Use of a colorimetric microtiter (MTT) assay in determining the radiosensitivity of cells from murine solid tumors. *International Journal of Radiation Oncology Biology Physics* 1988; **15**(3): 699-702.

Wedlake, L *et al*. Can biological markers act as non-invasive, sensitive indicators of radiation-induced effects in the gastrointestinal mucosa? *Alimentary Pharmacology & Therapeutics* 2008; **27**: 980–7.

Weeks, T and Huser, T. Raman spectroscopy of living cells. In Jue, T (Ed.). *Biomedical Applications of Biophysics* 2010. NJ: Humana Press, pp. 185-210.

Wehrens, R. Chemometrics with R: *Multivariate data analysis in the natural sciences and life sciences* 2011. Berlin: Springer-Verlag.

Weinstock, DM, Richardson, CA, Elliott, B and Jasin, M. Modelling oncogenic translocations: Distinct roles for double-strand break repair pathways in translocation formation in mammalian cells. *DNA Repair* 2006; **5**: 1065-74.

Wenzel, WS and Singh, ATK. Cell-cycle checkpoints and aneuploidy on the path to cancer. *In Vivo* 2018; **32**(1): 1-5.

Werbrouck, J, De Ruyck, K, Beels, L, Vral, A, Van Eijkeren, M, De Neve, W and Thierens, H. Prediction of late normal tissue complications in RT treated gynaecological cancer patients: Potential of the γH2AX foci assay and association with chromosomal radiosensitivity. *Oncology Reports* 2010; **23**: 571-8.

West, CM and Barnett, GC. Genetics and genomics of radiotherapy toxicity: Towards prediction. *Genome Medicine* 2011; **3**(8): 52-67.

West, CML *et al*. Lymphocyte radiosensitivity is a significant prognostic factor for morbidity in carcinoma of the cervix. *International Journal of Radiation Oncology•Biology•Physics* 2001; **51**(1): 10-5.

West, CM *et al*. The independence of intrinsic radiosensitivity as a prognostic factor for patient response to radiotherapy of carcinoma of the cervix. *British Journal of Cancer* 1997; **76**: 1184-90.

West, CML, Elyan, SAG, Berry, P, Cowan, R and Scott, D. A Comparison of the Radiosensitivity of Lymphocytes from Normal Donors, Cancer Patients, Individuals with Ataxia-telangiectasia (A-T) and A-T Heterozygotes. *International Journal of Radiation Biology* 1995; **68**(2): 197-203.

Westerhuis, JA *et al*. Assessment of PLSDA cross validation. *Metabolomics* 2008; **4**: 81-9.

White, L *et al*. A Comparison of Radiobiological Response in Cells Exposed to Low LET Radiation with Different Beam Energies. *Radiation and Environmental Medicine* 2020; **9**(1): 1-6.

Widmark, A *et al*. Endocrine treatment, with or without radiotherapy, in locally advanced prostate cancer (SPCG-7/SFUO-3): An open randomised phase III trial. *Lancet* 2009; **373**: 301-8.

Willock, DJ. *Molecular Symmetry* 2009. West Sussex: John Wiley and Sons Ltd.

Windmueller, HG and Spaeth, AE. Source and fate of circulating citrulline. *American Journal of Physiology-Endocrinology and Metabolism* 1981; **241**: E473-80.

Winter, E, Chiaradia, LD, Silva, AH, Nunes, RJ, Yunes, RA and Creczynski-Pasa, TB. Involvement of extrinsic and intrinsic apoptotic pathways together with endoplasmic reticulum stress in cell death induced by naphthylchalcones in a leukemic cell line: Advatnages of multi-target action. *Toxicology in Vitro* 2014; **28**(5): 769-77.

Wold, S, Sjostrom, M and Eriksson, L. PLS-regression: A basic tool of chemometrics. *Chemometrics and Intelligent Laboratory Systems* 2001; **58**: 109-30.

Wouters, BG. Cell death after irradiation: How, when and why cells die. In Joiner, M and van der Kogel, A (Eds.). *Basic clinical radiobiology* (5th Ed.) 2019. New York: Taylor and Francis Group, pp. 21-31.

Wouters, BG and Begg, AC. Irradiation-induced damage and the DNA damage response. In Joiner, M and van der Kogel, A (Eds.). *Basic clinical radiobiology* (4th Ed.) 2009. London: Hodder Education, pp. 11-26.

Wu, H, Volponi, J, Oliver, AE, Parikh, AN, Simmons, BA and Singh, S. *In vivo* lipidomics using single-cell Raman spectroscopy. *Proceeding of the National Academy of Sciences* 2011; **108**(9): 3809-14.

Xue, L, Yu, D, Furusawa, Y, Cao, J, Okayasu, R and Fan, S. ATM-dependent hyper-radiosensitivity in mammalian cells irradiated by heavy ions. *International Journal of Radiation Oncology, Biology, Physics* 2009; **75**(1): 235-43.

Yan, C, *et al*. Benzo[a]pyrene induces complex H2AX phosphorylation patterns by multiple kinases including ATM, ATR, and DNA-PK. *Toxicology In Vitro* 2011; **25**(1): 91–9.

Yang, J, Yue, JB, Liu, J and Yu, JM. Repopulation of tumor cells during fractionated radiotherapy and detection methods (Review). *Oncology Letters* 2014; **7**: 1755-60.

Yasser, M, Shaikh, R, Chilakapati, MK and Teni, T. Raman spectroscopic study of radioresistant oral cancer sublines established by fractionated ionizing radiation. *PLoS ONE* 2014; **9**(5): e97777.

Yoshikawa, R *et al*. Dual antitumor effects of 5-fluorouracil on the cell cycle in colorectal carcinoma cells: A novel target mechanism concept for pharmacokinetic modulating chemotherapy. *Cancer Research* 2001; **61**(3): 1029-37.

You, Z, Chahwan, C, Bailis, J, Hunter, T and Russell, P. ATM activation and its recruitment to damaged DNA require binding to the C terminus of Nbs1. *Molecular and Cellular Biology* 2005; **25**(13): 5363-79.

Yu, JB. Hypofractionated radiotherapy for prostate cancer: Further evidence to tip the scales. *Journal of Clinical Oncology* 2017; **35**(17): 1867-70.

Yu, L, Chen, Y and Tooze, SA. Autophagy pathway: Cellular and molecular mechanisms. *Autophagy* 2018; **14**(2): 207-15.

Zelefsky, MJ *et al.* Predicting biochemical tumor control after brachytherapy for clinically localized prostate cancer: The Memorial Sloane-Kettering Cancer Center experience. *Brachytherapy* 2012; **11**: 245-9.

Zips, D. Tumour growth and response to radiation. In Joiner, M and van der Kogel, A (Eds.). *Basic clinical radiobiology* (5th Ed.) 2019. New York: Taylor and Francis Group, pp. 81-98.

Zwaans, BMM, Chancellor, MB and Lamb, LE. Modeling and treatment of radiation cystitis. *Urology* 2016; **88**: 14-21.

List of Publications

A 4-Gene Signature of CDKN1, FDXR, SESN1 and PCNA Radiation Biomarkers for Prediction of Patient Radiosensitivity. International Journal of Molecular Sciences 2021, 22(19), doi: 10.3390/ijms221910607

*Orla Howe, Lisa White, **Daniel Cullen**, Grainne O'Brien, Laura Shields, Jane Bryant, Emma Noone, Shirley Bradshaw, Marie Finn, Mary Dunne, Aoife M. Shannon, John Armstrong, Brendan McClean, Aidan Meade, Christophe Badie and Fiona M. Lyng*

Discrimination of immune cell activation using Raman micro-spectroscopy in an in-vitro and ex-vivo model. Spectrochimica Acta Part A: Molecular and Biomolecular Spectroscopy 2020, 248, doi: 10.1016/j.saa.2020.119118

*Neha Chaudhary, Thi Nguyet Que Nguyen, **Daniel Cullen,** Aidan D. Meade, Claire Wynne*

Vibrational spectroscopy of liquid biopsies for prostate cancer diagnosis. Therapeutic Advances in Medical Oncology 2020, 12, doi:10.1177/1758835920918499

*Dinesh K.R. Medipally, **Daniel Cullen**, Valérie Untereiner, Ganesh D Sockalingum, Adrian Maguire, Thi Nguyet Que Nguyen, Jane Bryant, Emma Noone, Shirley Bradshaw, Marie Finn, Mary Dunne, Aoife M. Shannon, John Armstrong, Aidan D. Meade and Fiona M. Lyng*

Raman spectroscopy of lymphocytes for the identification of prostate cancer patients with late radiation toxicity following radiotherapy. Translational Biophotonics 2020, 2(4), doi:10.1002/tbio.201900035

***Daniel Cullen**, Jane Bryant, Adrian Maguire, Dinesh Medipally, Brendan McClean, Laura Shields, Emma Noone, Shirley Bradshaw, Marie Finn, Mary Dunne, Aoife M. Shannon, John Armstrong, Orla Howe, Aidan D. Meade, Fiona M. Lyng*

Effect of hemolysis on Fourier transform infrared and Raman spectra of blood plasma. Journal of Biophotonics 2020, doi:10.1002/jbio.201960173

*Dinesh K.R. Medipally, **Daniel Cullen**, Valerie Untereiner, Jane Bryant, Ganesh D. Sockalingum, Thi N.Q. Nguyen, Emma Noone, Shirley Bradshaw, Marie Finn, Mary Dunne, Aoife M. Shannon, John Armstrong, Aidan D. Meade and Fiona M. Lyng*

Monitoring treatment toxicity in prostate cancer through vibrational spectroscopy of liquid biopsies. Cancers 2019, 11, 925, doi: 10.3390/cancers11070925

*Dinesh K.R. Medipally, Thi Nguyet Que Nguyen, Jane Bryant, Valerie Untereiner, Ganesh D. Sockalingum, **Daniel Cullen,** Emma Noone, Shirley Bradshaw, Marie Finn, Mary Dunne, Aoife M. Shannon, John Armstrong, Fiona M. Lyng and Aidan D. Meade*

Prediction of DNA damage and G2 chromosomal radio-sensitivity ex vivo in peripheral blood mononuclear cells with label-free Raman micro-spectroscopy. International Journal of Radiation Biology 2019, 95(1), doi: 10.1080/09553002.2018.1451006

*Aidan D. Meade, Adrian Maguire, Jane Bryant, **Daniel Cullen**, Dinesh Medipally, Lisa White, Brendan McClean, Laura Shields, John Armstrong, Mary Dunne, Emma Noone, Shirley Bradshaw, Marie Finn, Aoife M. Shannon, Orla Howe & Fiona M. Lyng*

Conference Presentations

Oral Presentations

- International Society for Clinical Spectroscopy Conference, Manchester University (2017)
- Association for Radiation Research Conference, Oxford University (2017)
- European Radiation Research Society Conference, University of Duisburg-Essen (2017)
- SPEC Conference, University of Strathclyde (Flash) (2018)
- Association for Radiation Research Conference, Queen's Univeristy Belfast (2018)
- International Congress of Radiation Research, Manchester Central (2019)

Poster Presentations

- Microscopy Society of Ireland Symposium, Dublin Institute of Technology (2016)
- Irish Radiation Research Society Scientific Meeting, Trinity College Dublin (2016)
- Institute of Physics Scientific Meeting, Gibson Hotel Dublin (2016)
- Irish Radiation Research Society Scientific Meeting, Environmental Protection Agency Wexford (2017)
- SPEC Conference, University of Strathclyde (2018)
- European Radiation Research Society Conference, University of Pécs Medical School (2018)
- Biophotonics and Imaging Graduate Summer School, NUI Galway (2018)
- European Conference on the Spectroscopy of Biological Molecules, UCD (2019)

Modules Completed

Module Name	ECTS
Applied Optics	5
Statistics with R	10
Biomathematics	5
Research Integrity	5
Data Visualisation	5
Big Data Analytics	3
Applied Spectroscopy	5
Introduction to Statistics	5
CLIRSPEC Summer School	3
Bioinformatics and Data Analysis	5
Applied Modelling in Environment, Food and Health	5
Multivariate Analysis and Data Mining for Biomedical Applications	5

Awards and Grants

Young Investigator Award (2017), European Radiation Research Society

Early Career Investigator Award (2018), Irish Radiation Research Society

Travel Award (2019), CONCERT - European Joint Programme for the Integration of Radiation Protection Research